Generation of Ultra-Short Electron Bunches and FEL Pulses, and Characterization of Their Longitudinal Properties at FLASH2

Dissertation
zur Erlangung des Doktorgrades
an der Fakultät für Mathematik, Informatik und Naturwissenschaften
Fachbereich Physik
der Universität Hamburg

vorgelegt von

Florian Christie

Hamburg

2019

Gutachter der Dissertation:	Prof. Dr. Wolfgang Hillert Dr. Mathias Vogt
Zusammensetzung der Prüfungskommission:	Prof. Dr. Wolfgang Hillert Dr. Mathias Vogt Dr. Juliane Rönsch-Schulenburg Prof. Dr. Peter Hauschildt Prof. Dr. Daniela Pfannkuche
Vorsitzende der Prüfungskommission:	Prof. Dr. Daniela Pfannkuche
Datum der Disputation:	25.10.2019
Vorsitzender Fach-Promotionsausschuss PHYSIK:	Prof. Dr. Michael Potthoff
Leiter des Fachbereichs Physik:	Prof. Dr. Wolfgang Hansen
Dekan der Fakultät MIN:	Prof. Dr. Heinrich Graener

Abstract

The free-electron laser in Hamburg (FLASH) is a soft X-ray user facility, delivering radiation for photon science since 2005. Since 2014, a second beam line for user operation, FLASH2, has been in operation. The beam for FLASH2 is accelerated using the same accelerating modules as for the initial FLASH beam line (FLASH1), but then deflected downstream of this shared linac (linear accelerator). The electron bunches generated at a photocathode have an rms (root mean square) length of 6.5 ps or 4.5 ps when the standard injector lasers are used. These bunches are then compressed in two bunch compressors in the linac to about 30 fs to 200 fs.

To shorten the bunch lengths even further, a short-pulse injector laser was installed at FLASH, which generates short, low charge electron bunches directly at the cathode. These short electron bunches with a length of about 1 ps can be further compressed in the linac to produce ultra-short FEL (Free-Electron Laser) pulses down to a few femtoseconds in the FLASH2 undulators. Measurements of such pulses as well as tracking simulations of the FLASH2 beam line are presented in this thesis. Both studies demonstrate the feasibility of ultra-short FEL pulses down to single-spike lasing at FLASH2.

Up until now, no hardware to directly measure the electron bunch length has been installed in the FLASH2 beam line. As exact knowledge of the pulse duration is essential for time-resolved user experiments, the beam line downstream of the FLASH2 undulators has been redesigned for the installation of a variable polarization Transverse Deflecting Structure (TDS). In combination with a dipole magnet it is possible to map the longitudinal phase space density of the electron bunches onto a beam screen. Additionally, the photon pulse duration as well as the slice emittance in both transverse planes can be measured using such a TDS. This thesis presents the final layout of the beam line, the accelerator optics, and also simulations for the aforementioned measurements.

However, the temporal resolution of an X-band TDS is limited to the order of 1 fs rms. In most cases, this is not sufficient to resolve single self-amplified spontaneous emission (SASE) spikes within one photon pulse for hard X-ray radiation. By adding the intensity spectrum from a high-resolution spectrometer to the temporal profile from the TDS the overall resolution can be enhanced. This is done by applying an iterative reconstruction algorithm that is presented in this thesis. Additionally, the algorithm is tested using simulation data of the Linac Coherent Light Source (LCLS) and applied to data taken at LCLS.

Zusammenfassung

Der Freie-Elektronen-Laser in Hamburg (FLASH) ist eine weiche Röntgenstrahlenquelle für Nutzer, die seit 2005 Strahlung für die Photonenforschung liefert. Seit 2014 ist ein zweiter Arm für den Nutzerbetrieb, FLASH2, in Betrieb. Der Strahl für FLASH2 wird in den gleichen Beschleunigungsmodulen wie jener für die ursprüngliche FLASH-Beamline (FLASH1) beschleunigt, aber dann stromabwärts dieses gemeinsamen Linacs (Linearbeschleuniger) abgelenkt. Die Elektronenpakete, die mittels der Standardinjektorlaser und einer Photokathode erzeugt werden, haben eine Länge von 6.5 ps qmw (quadratischer Mittelwert) oder 4.5 ps qmw. Diese Teilchenpakete können dann mittels zweier Bunchkompressoren im Linac auf Längen von 30 fs bis 200 fs komprimiert werden.

Um die Bunchlänge weiter zu reduzieren, wurde bei FLASH ein Kurzpulsinjektorlaser installiert, der direkt an der Kathode kurze Elektronenpakete erzeugt. Diese kurzen Elektronenpakete mit Längen von um 1 ps können im Linac weiter komprimiert werden, um ultrakurze FEL (Freie-Elektronen-Laser) Pulse bis zu einigen Femtosekunden Länge in den FLASH2-Undulatoren zu erzeugen. Messungen solcher Pulse sowie Simulation der Teilchentrajektorien bei FLASH2 werden in dieser Arbeit vorgestellt. Beide Studien zeigen die Machbarkeit von ultrakurzen FEL-Pulsen bei FLASH2 bis hin zu einem einzigen Puls.

Bisher wurde in der FLASH2-Beamline keine Hardware zur direkten Messung der Elektronenpaketlänge oder der Photonenpulsdauer installiert. Da für zeitaufgelöste Nutzerexperimente die genaue Kenntnis der Pulsdauer unerlässlich ist, wurde die Beamline stromabwärts der FLASH2-Undulatoren neu gestaltet und verfügt nun über eine transversal ablenkende Struktur (TDS) mit variabler Polarisation. In Kombination mit einem Dipolmagneten ist es möglich, die longitudinale Phasenraumdichte des Strahls auf einem Strahlmonitor abzubilden. Zusätzlich können die Photonenpulsdauer sowie die Slice-Emittanz in beiden transversalen Ebenen mit solch einer TDS gemessen werden. Diese Arbeit stellt das endgültige Layout der Beamline, die Beschleunigeroptik sowie Simulationen für die zuvor genannten Messungen vor.

Die zeitliche Auflösung einer X-Band-TDS ist jedoch auf Größenordnungen von 1 fs qmw beschränkt. In den meisten Fällen reicht dies nicht aus, um einzelne Pulse der Strahlung durch selbstverstärkte, spontane Emission (SASE) innerhalb eines harten Röntgenpulses aufzulösen. Durch die Messung des Intensitätsspektrums mittels eines hochauflösenden Spektrometers und der Kombination mit dem zeitlichen Profil aus der TDS kann die Gesamtauflösung erhöht werden. Dies geschieht durch die Anwendung eines iterativen Rekonstruktionsalgorithmus, der in dieser Arbeit vorgestellt wird. Zusätzlich wird der Algorithmus mit Hilfe von Simulationsdaten der Linac Coherent Light Source (LCLS) getestet und auf Daten von LCLS angewendet.

All you have to decide is what to do with the time that is given to you.

Gandalf.

Contents

1 Introduction **1**

2 Elements of Beam Dynamics in "Linac-driven FELs" **3**
2.1 Hamiltonian Systems . . . 3
2.2 Linear Hamiltonian Coupling . . . 4
2.2.1 Dispersive Extension . . . 6
2.2.2 Cavity Extension . . . 7
2.3 Equation of Motion in the Accelerator Coordinate System . . . 7
2.4 Transfer Matrices . . . 10
2.5 Invariant Ellipse of an Accelerator in Two-Dimensional Phase Space . . . 13
2.6 Acceleration and Bunch Compression . . . 15
2.7 Collective Effects in Free-Electron Lasers . . . 17
2.7.1 Space Charge . . . 17
2.7.2 Coherent Synchrotron Radiation . . . 18

3 Free-Electron Lasers **20**
3.1 FEL Principle . . . 20
3.2 Characteristics of SASE FEL Radiation . . . 22
3.2.1 Single-Spike Radiation . . . 23
3.3 FLASH . . . 24
3.4 LCLS . . . 26

4 Transverse Deflecting Structures **28**
4.1 TDS Principle . . . 28
4.2 Transformation Matrix of a TDS . . . 30
4.3 Longitudinal Diagnostics using a TDS . . . 31
4.3.1 Longitudinal Current Profile . . . 32
4.3.2 Longitudinal Phase Space Density . . . 33
4.3.3 Photon Pulse Reconstruction . . . 35
4.3.4 Slice Emittance Reconstruction . . . 36

5 Ultra-Short Electron Bunches and Photon Pulses at FLASH2 **39**
5.1 Experimental Results for Short-Pulse Operation at FLASH2 . . . 40
5.2 Simulation Results for Short-Pulse Operation at FLASH2 . . . 43
5.2.1 Ideal Gaussian Beam . . . 44
5.2.2 Start-to-End Simulation . . . 45
5.3 Simulation Results for Single-Spike Operation at FLASH2 . . . 51

6 Implementation of a TDS at FLASH2 **59**
6.1 Layout of the TDS Diagnostic Section at FLASH2 59
6.1.1 PolariX TDS 60
6.1.2 Kicker Magnet 62
6.1.3 Screen Station 63
6.2 Accelerator Optics 64
6.2.1 Longitudinal Phase Space Density Measurement 64
6.2.2 Slice Emittance Measurement 71
6.3 Tracking Simulation for FLASH2 PolariX TDSs 73
6.3.1 Longitudinal Phase Space Density Measurement 74
6.3.2 Reconstruction of Photon Pulses 82
6.3.3 Slice Emittance Measurement 88

7 Temporal X-Ray Reconstruction Using Temporal and Spectral Measurements **97**
7.1 Iterative Reconstruction Algorithm 97
7.1.1 Base Functions 98
7.1.2 Iteration Process and Minimizing 99
7.2 Applying the Iterative Reconstruction Algorithm to SASE Simulations 101
7.2.1 Blurred Temporal Measurement and Perfect Spectral Measurement . . 102
7.2.2 Blurred Temporal Measurement and Blurred Spectral Measurement . . 110
7.2.3 Capabilities and Limitations of the Reconstruction Algorithm 110
7.3 Iterative Reconstruction Algorithm Applied to Measurement Data Taken at LCLS 116
7.3.1 Reconstruction of Photon Pulses from Bunches with 30 pC Charge . . . 117
7.3.2 Reconstruction of Photon Pulses from Bunches with 20 pC Charge . . . 119

8 Summary **123**

A Momentum Compaction in Straight Beam Line Elements **124**

References **126**

List of Figures

2.1 Scheme of a C-chicane bunch compressor. 16
2.2 Scheme of CSR. 18
3.1 Electron passing through a planar undulator 20
3.2 Radiation power and microbunching along the undulator 21
3.3 Temporal X-ray profile of a long SASE pulse and of single-spike radiation . . . 23
3.4 Overview of the FLASH facility 24
3.5 Overview of the LCLS facility 26
5.1 Gain curve and fluctuations measured for $Q = 60\,\mathrm{pC}$, $\lambda_l = 15\,\mathrm{nm}$, and $E = 1150\,\mathrm{MeV}$ 41
5.2 Gain curve and fluctuations measured for $Q = 88\,\mathrm{pC}$, $\lambda_l = 40.5\,\mathrm{nm}$ and $\lambda_l = 20\,\mathrm{nm}$, and $E = 690\,\mathrm{MeV}$ 42
5.3 Gain curve and fluctuations measured for $Q = 70\,\mathrm{pC}$ and $Q = 38\,\mathrm{pC}$, $\lambda_l = 30\,\mathrm{nm}$, and $E = 760\,\mathrm{MeV}$ 43
5.4 Highest fluctuations measured for $Q = 70\,\mathrm{pC}$ and $Q = 38\,\mathrm{pC}$, $\lambda_l = 30\,\mathrm{nm}$, and $E = 760\,\mathrm{MeV}$ 43
5.5 Gain curves simulated for $Q = 88\,\mathrm{pC}$, $\lambda_l = 40.5\,\mathrm{nm}$, and $E = 690\,\mathrm{MeV}$ 44
5.6 Temporal and spectral distribution simulated for $Q = 88\,\mathrm{pC}$, $\lambda_l = 40.5\,\mathrm{nm}$, and $E = 690\,\mathrm{MeV}$ 45
5.7 Simulated slice parameters of the bunch for a charge of 70 pC at the start of the undulator section 47
5.8 Simulated longitudinal phase space density at the beginning of the undulator for 70 pC 47
5.9 Gain curves from start-to-end simulations for $Q = 70\,\mathrm{pC}$, $\lambda_l = 30\,\mathrm{nm}$, and $E = 760\,\mathrm{MeV}$ 48
5.10 Temporal X-ray profile using six undulators for $Q = 70\,\mathrm{pC}$, $\lambda_l = 30\,\mathrm{nm}$, and $E = 760\,\mathrm{MeV}$ 48
5.11 Simulated slice parameters of the bunch for a charge of 38 pC at the start of the undulator section 49
5.12 Simulated longitudinal phase space density at the beginning of the undulator for 38 pC 50
5.13 Simulated longitudinal phase space density at the entrance and exit of the second bunch compressor for 38 pC 50
5.14 Gain curves from start-to-end simulations for $Q = 38\,\mathrm{pC}$, $\lambda_l = 30\,\mathrm{nm}$, and $E = 760\,\mathrm{MeV}$ 51
5.15 Temporal X-ray profile using seven undulators for $Q = 38\,\mathrm{pC}$, $\lambda_l = 30\,\mathrm{nm}$, and $E = 760\,\mathrm{MeV}$ 51
5.16 Simulated slice parameters of the bunch for a charge of 20 pC along the accelerator for single-spike radiation 53

5.17 Simulated slice parameters of the bunch for a charge of 20 pC at the start of the undulator section for single-spike radiation 54
5.18 Simulated longitudinal phase space density at the beginning of the undulator for single-spike radiation 54
5.19 Gain curves from start-to-end simulations for single-spike radiation at 35.64 nm 55
5.20 Temporal X-ray profile using six undulators for single-spike radiation at 35.64 nm 55
5.21 Spectral X-ray profile using six undulators for single-spike radiation at 35.64 nm 56
5.22 Temporal X-ray profile using all undulators for single-spike radiation at 35.64 nm 56
5.23 Spectral X-ray profile using all undulators for single-spike radiation at 35.64 nm 56
5.24 Gain curves from start-to-end simulations for single-spike radiation at 16.95 nm 57
5.25 Temporal X-ray profile using seven undulators for single-spike radiation at 16.95 nm 58
5.26 Spectral X-ray profile using seven undulators for single-spike radiation at 16.95 nm 58
6.1 Shared RF system between FLASH2 and FLASH Forward 59
6.2 Layout of the variable polarization mode launcher 61
6.3 Technical drawings and photo of the PolariX prototype 62
6.4 Technical drawing of the supports for the two PolariX TDSs at FLASH2 62
6.5 Technical drawing of the kicker 63
6.6 Layout of the screen station at FLASH2 63
6.7 Drawing of modified TQA quadrupole 66
6.8 Layout of the FLASH2 dump beam line with THz undulator installed 67
6.9 Beta functions in both planes and horizontal dispersion between the last FLASH2 undulator and the last FLASH2 dipole D1FL2DUMP with no THz undulator installed 68
6.10 Layout of the FLASH2 dump beam line with no THz undulator installed 69
6.11 Beta functions in both planes and horizontal dispersion between the last FLASH2 undulator and the last FLASH2 dipole D1FL2DUMP with no THz undulator installed 70
6.12 Temporal resolution, energy resolution and induced energy spread versus the normalized emittance of the electron bunch for the three different optics 71
6.13 Temporal resolution, energy resolution and induced energy spread versus the deflecting voltage of the TDSs for the three different optics 72
6.14 Beam size at the screen plotted against the deflecting voltage of the TDS 73
6.15 TDS phase scan and dipole current scan for the calibration of longitudinal phase space measurements 75
6.16 Longitudinal phase space density reconstruction using the 70 pC bunch described in Section 5.2.2 as input 76
6.17 Longitudinal phase space density reconstruction using the 38 pC bunch described in Section 5.2.2 as input 77

6.18 Longitudinal phase space density reconstruction using the 20 pC bunch described in Section 5.3 as input . . . 78
6.19 Longitudinal phase space density reconstruction using a 20 pC bunch as input . 79
6.20 Longitudinal phase space density reconstruction using a 1 nC bunch as input . . 80
6.21 Photon pulse reconstruction of a Gaussian bunch with a bunch length of 100 fs rms at an energy of 1200 MeV . . . 83
6.22 Photon pulse reconstruction of a Gaussian bunch with a bunch length of 100 fs rms at an energy of 700 MeV . . . 84
6.23 Photon pulse reconstruction of a Gaussian bunch with a bunch length of 23 fs rms at an energy of 1200 MeV . . . 85
6.24 Photon pulse reconstruction of a Gaussian bunch with a bunch length of 23 fs rms at an energy of 700 MeV . . . 85
6.25 Photon pulse reconstruction of a 70 pC electron bunch . . . 86
6.26 Photon pulse reconstruction of a 38 pC electron bunch . . . 86
6.27 Photon pulse reconstruction of a 20 pC electron bunch at a wavelength of 35.64 nm 87
6.28 Photon pulse reconstruction of a 20 pC electron bunch at a wavelength of 16.95 nm 88
6.29 Horizontal slice emittance measurement of a 1 nC bunch . . . 89
6.30 Vertical slice emittance measurement of a 1 nC bunch . . . 90
6.31 Horizontal slice emittance measurement of the 70 pC bunch described in Section 5.2.2 . . . 91
6.32 Vertical slice emittance measurement of the 70 pC bunch described in Section 5.2.2 . . . 92
6.33 Horizontal slice emittance measurement of the 20 pC bunch described in Section 5.3 . . . 93
6.34 Vertical slice emittance measurement of the 20 pC bunch described in Section 5.3 94
6.35 Horizontal slice emittance measurement of a 20 pC bunch . . . 95
6.36 Vertical slice emittance measurement of a 20 pC bunch . . . 96
7.1 Reconstructions for 20 pC using TDS resolutions between 1.2 fs to 0.5 fs . . . 104
7.2 Reconstructions for 40 pC using TDS resolutions between 1.2 fs to 0.5 fs . . . 105
7.3 Reconstructions for 150 pC using TDS resolutions between 1.2 fs to 0.5 fs . . . 106
7.4 Reconstruction of 50 different SASE shots for 40 pC bunches with perfect spectral resolution . . . 107
7.5 Reconstructions for 40 pC using TDS resolutions between 1.2 fs to 0.5 fs . . . 108
7.6 Reconstructions for 40 pC using TDS resolutions between 1.2 fs to 0.5 fs . . . 109
7.7 Reconstructions for 20 pC using TDS resolutions between 1.2 fs to 0.5 fs . . . 112
7.8 Reconstructions for 40 pC using TDS resolutions between 1.2 fs to 0.5 fs . . . 113
7.9 Reconstructions for 150 pC using TDS resolutions between 1.2 fs to 0.5 fs . . . 114
7.10 Reconstruction of 50 different SASE shots for 40 pC bunches with a spectral resolution of 0.2 eV . . . 115

7.11 Reconstruction of 50 different SASE shots for 40 pC bunches with no spectral information . . . 115
7.12 Gain curve measured at LCLS . . . 116
7.13 Longitudinal phase space density at LCLS for 30 pC . . . 117
7.14 Photon pulse reconstruction at LCLS for 30 pC, Shot 1 . . . 118
7.15 Photon pulse reconstruction at LCLS for 30 pC, Shot 2 . . . 119
7.16 Photon pulse reconstruction at LCLS for 30 pC, Shot 3 . . . 119
7.17 Longitudinal phase space density at LCLS for 20 pC . . . 120
7.18 Photon pulse reconstruction at LCLS for 20 pC, Shot 1 . . . 121
7.19 Photon pulse reconstruction at LCLS for 20 pC, Shot 2 . . . 121
7.20 Photon pulse reconstruction at LCLS for 20 pC, Shot 3 . . . 122

List of Tables

1 Parameter Overview and Results of Short Pulse Measurements at FLASH2. . . . 41
2 PolariX TDS Parameters . . . 61
3 Values of Optical Functions and Resolutions for Longitudinal Phase Space Density Measurement Optics with THz Undulator. . . . 67
4 Values of Optical Functions and Resolutions for Longitudinal Phase Space Density Measurement Optics without THz Undulator. . . . 69
5 Values of Optical Functions and Resolutions for Slice Emittance Measurement in the Horizontal Plane. . . . 73
6 Values of Optical Functions and Resolutions for Slice Emittance Measurement in the Vertical Plane. . . . 74
7 Comparison of the Bunch Length at the Undulator End and the Reconstructed One Using the TDSs. . . . 81
8 Comparison of the Energy Spread at the Undulator End and the Reconstructed One Using the TDSs. . . . 81
9 Comparison of rms Photon Pulse Duration Given by Genesis 1.3 and the Reconstruction at the Undulator Exit and the Screen. . . . 88
10 Parameter Overview of Measurements for Iterative Reconstruction Algorithm at LCLS . . . 116

1 Introduction

Since their invention in 1971 by John Madey at Stanford University [1], Free-Electron Lasers (FELs) proved to be one of the most brilliant and powerful artificial light sources. An FEL is capable of producing small bandwidth radiation in a broad wavelength range, ranging from infrared to hard X-rays. Especially the production of brilliant X-ray radiation made FELs a powerful tool for observing microscopic structures in the order of a few nanometers. An advantage over the storage ring based radiation generation is the possibility to generate short photon pulses in the order of femtoseconds using an FEL. In the soft and hard X-ray regime pulses in the order of a few femtoseconds or even sub-femtoseconds can be generated [2], rendering it possible to observe ultra-fast dynamical processes [3, 4, 5].

To generate such ultra-short photon pulses knowledge about the beam dynamics in the accelerator is crucial. Simulations and studies of the latter help to understand the underlying processes and increase the efficiency with which these ultra-short photon pulses can be generated. A part of this thesis is dedicated to such studies and tracking simulations for the FEL user facility FLASH2[1].

As most of the lasing process in an FEL depends on the longitudinal parameters of the electron bunches the measurement of their longitudinal properties is of utmost importance to control the lasing process. This can for example be achieved by means of a Transverse Deflecting Structure (TDS). With this device it is possible to relate the longitudinal coordinate of an electron beam to a transverse one which then can be imaged using a screen. Additionally, an energy spectrometer, such as a dipole magnet, deflecting the beam in the plane transverse to the streaking plane of the TDS can be used to relate the beam energy to the other transverse coordinate. By combining both methods, the longitudinal phase space density of the electron bunches can be mapped onto a screen [6]. Such a measurement station is planned in the context of the FLASH midterm refurbishment and the FLASH2020+ upgrade plans [7]. It will be installed downstream of the FLASH2 undulators as an essential part of these to ensure high beam-qualities at FLASH2 and thereby also brilliant and high-quality photon pulses. The measurement station comprises a novel TDS with a variable polarization feature (PolariX TDS[2]) [8, 9, 10] and will be used as an indispensable diagnostic tool for short electron bunches and photon pulses at FLASH2. The second part of this thesis deals with the integration of this system downstream of the FLASH2 undulators.

Even the temporal structure of the photon pulses can be reconstructed from measurements of the longitudinal phase space density [11]. However, these measurements are limited by the temporal resolution of the TDS which is often not enough to resolve the many adjacent spikes within one hard X-ray SASE[3] pulse. Nonetheless, the temporal resolution can be significantly enhanced using an iterative reconstruction algorithm and combining spectral measurements of

[1] Free-Electron Laser in Hamburg
[2] Polarizable X-band TDS
[3] Self-Amplified Spontaneous Emission

the SASE radiation with the TDS measurement. Knowledge of the exact temporal structure can for example be interesting for applications such as "ghost imaging" [12, 13]. With this technique it is possible to perform pump-probe experiments using X-ray radiation with a single SASE pulse. To do so, different, single SASE spikes within one SASE pulse serve as both, pump and probe [13]. Therefore, such an iterative reconstruction algorithm to reconstruct the temporal structure of SASE X-ray pulses was developed and tested and is presented in this thesis.

We start with a recapitulation of beam dynamics for FELs including the description of collective effects in Section 2. The theory of FELs and ultra-short FEL pulses is described in Section 3, including the description of the two FEL user facilities, FLASH and the Linac Coherent Light Source (LCLS) at Stanford. In Section 4 the working principle of a TDS and the possible applications of such a device are described. The generation of ultra-short electron bunches and FEL pulses at FLASH2 is studied in Section 5 and the characterization of their longitudinal properties by integrating a TDS downstream of the FLASH2 undulator in Section 6. In Section 7 we conclude with the presentation of the iterative reconstruction algorithm developed to enhance the temporal resolution of the photon pulse reconstruction using a TDS.

2 Elements of Beam Dynamics in "Linac-driven FELs"

In this section, we will give a short introduction to various beam dynamics topics which are relevant for the description of linac[4]-driven FELs.

Firstly, we will describe Hamiltonian systems and their relevance for accelerators, outline how the equation of motion can be derived in the accelerator coordinate system, and discuss the description of an accelerator lattice using transfer matrices. Secondly, we will describe the invariant ellipses of a beam line lattice in two dimensions. Thirdly, we will show how the acceleration and bunch compression in an FEL is performed and lastly, we will give a brief introduction about collective effects in FELs.

2.1 Hamiltonian Systems

We will give in the following a summary of Hamiltonian systems found for example in [14, 15, 16, 17, 18, 19], where also the proofs for the following relations are given. These principles can be used to derive the accelerator coordinate system and solutions for the equation of motion in a particle accelerator, as shown in [19][5].

In what follows, we assume that all fields have the required smoothness.

The Hamiltonian equations of motion in their standard form can be written as

$$\frac{\mathrm{d}}{\mathrm{d}t}\vec{z} = \mathbf{J}\,\vec{\nabla}_z \mathcal{H}(\vec{z};t), \tag{2.1}$$

where

$$\vec{z}_i = \begin{pmatrix} q_i \\ p_i \end{pmatrix} \in \mathbb{R}^2,\ \vec{z} = \vec{z}_1 \oplus \vec{z}_2 \oplus \ldots \vec{z}_n \in \mathbb{R}^{2n}, \tag{2.2}$$

$$\mathbf{J}^{2\times 2} = \begin{pmatrix} 0 & 1 \\ -1 & 0 \end{pmatrix},\ \mathbf{J} \equiv \mathbf{J}_{2n} \equiv \underbrace{\mathbf{J}^{2\times 2} \oplus \ldots \oplus \mathbf{J}^{2\times 2}}_{n\times}, \tag{2.3}$$

t is the time, and $\mathcal{H}$ is the Hamiltonian of the system.

The left hand side of the differential in Eq. (2.1) may be interpreted as a vector field $\vec{F}$

$$\frac{\mathrm{d}}{\mathrm{d}t}\vec{z} = \vec{F}(\vec{z};t), \tag{2.4}$$

with the Jacobian matrix

$$\left(\mathbf{F}\left(\vec{z}_0;t\right)\right)_{ij} := \left.\frac{\partial F_i}{\partial z_j}\right|_{\vec{z}=\vec{z}_0,t}. \tag{2.5}$$

A matrix $\mathbf{F}$ is called Hamiltonian iff

$$\left(\mathbf{JF}\right)^T = \mathbf{JF} \ \text{ or equivalently } \mathbf{JF} + \mathbf{F}^T\mathbf{J} = 0. \tag{2.6}$$

[4]Linear accelerator

[5]The following sections contain excerpts from [19].

A vector field $\vec{F}(\vec{z};t)$ is Hamiltonian if $\mathbf{F}(\vec{z}_0;t)$ is Hamiltonian $\forall \vec{z}_0, t$ or equivalently if the Jacobian of $\mathbf{J}\vec{F}$ is symmetric

$$\left(\vec{\nabla}_z \left(\mathbf{J}\vec{F}\right)^T\right)^T = \vec{\nabla}_z \left(\mathbf{J}\vec{F}\right)^T. \tag{2.7}$$

The Hamiltonian matrices form a Lie-algebra with the corresponding Lie-group, which is the group of the symplectic matrices. A $2n \times 2n$ matrix $\mathbf{M}$ is symplectic ($\mathbf{M} \in \mathrm{Sp}(2n)$) iff

$$\mathbf{M}^T \mathbf{J} \mathbf{M} = \mathbf{J}. \tag{2.8}$$

The following relations are true for symplectic matrices $\mathbf{M} \in \mathrm{Sp}(2n)$.

1. The inverse of a symplectic matrix is given by

$$\mathbf{M}^{-1} = -\mathbf{J}\mathbf{M}^T\mathbf{J}. \tag{2.9}$$

2.

$$\det(\mathbf{M}) = +1. \tag{2.10}$$

3. If $\mathbf{M}$ is symplectic and $\lambda \in \mathbb{C}$ is an eigenvalue of $\mathbf{M}$ with multiplicity μ, then so is $1/\lambda$.

Linear Hamiltonian differential equations are solved by symplectic matrices, as we will see in the following. Let $\mathbf{F}$ be Hamiltonian, then

$$\mathbf{M}(t) \equiv \exp(t\,\mathbf{F}) = \sum_{n=1}^{\infty} \frac{(t\mathbf{F})^n}{n!} \tag{2.11}$$

is symplectic $\forall t \in \mathbb{R}$. If we have a linear Hamiltonian system with constant coefficients

$$\frac{\mathrm{d}}{\mathrm{d}t}\vec{z} = \mathbf{F}\vec{z},\ \vec{z}(0) = \vec{z}_0, \tag{2.12}$$

then we find for $\vec{z}(t)$

$$\vec{z}(t) = \exp(t\mathbf{F})\ \vec{z}_0. \tag{2.13}$$

This can be used to derive the formalism of transfer matrices as we will show in Section 2.4.

A nonlinear map $\vec{M}(\vec{z};t)$ is symplectic iff $\mathbf{M}(\vec{z}_0;t) \in \mathrm{Sp}(2n) \forall \vec{z}_0, t$, where $(\mathbf{M}(\vec{z}_0;t))_{ij} \equiv \left.\frac{\partial M_i}{\partial z_j}\right|_{\vec{z}=\vec{z}_0,t}$. A symplectic map is always injective. If it is also surjective, then $\vec{M} \in \mathrm{Symp}(\mathbb{R}^{2n})$.

It can be shown that if $\vec{F}(\vec{z};t)$ is a general (potentially non-linear) Hamiltonian vector field, the flow $\vec{M}(\vec{z}_0;t,t_0)$ is a general (potentially non-linear) symplectic map over the existence interval.

2.2 Linear Hamiltonian Coupling

In the following, we will discuss how linear symplectic (sub-)systems can be coupled in a way that preserves the symplectic structure for the combined system. Let $\mathbf{K} \in \mathrm{Sp}(2k) \Leftrightarrow \mathbf{K}^T\mathbf{J}_{2k}\mathbf{K} =$

$\mathbf{J}_{2k}$ and $\mathbf{L} \in \mathrm{Sp}(2l) \Leftrightarrow \mathbf{L}^T\mathbf{J}_{2l}\mathbf{L} = \mathbf{J}_{2l}$ be symplectic matrices. It is clear that $\mathbf{M}_0 = \mathbf{K} \oplus \mathbf{L} \in \mathrm{Sp}(2k+2l)$, if $\mathbf{M}_0^T\mathbf{J}_{2k+2l}\mathbf{M}_0 = \mathbf{J}_{2k+2l}$. Now, we try to find $\mathbf{C},\mathbf{D} \in \mathbb{R}^{2k\times 2l}$ ($\Rightarrow \mathbf{C}^T,\mathbf{D}^T \in \mathbb{R}^{2l\times 2k}$), so that

$$\mathbf{M} \equiv \begin{pmatrix} \mathbf{K} & \mathbf{C} \\ \mathbf{D}^T & \mathbf{L} \end{pmatrix} \tag{2.14}$$

is symplectic: $\mathbf{M} \in \mathrm{Sp}(2k+2l) \Leftrightarrow \mathbf{M}^T\mathbf{J}_{2k+2l}\mathbf{M} = \mathbf{J}_{2k+2l}$. Calculating the symplectic condition yields

$$\begin{aligned} \mathbf{M}^T\mathbf{J}_{2k+2l}\mathbf{M} &= \begin{pmatrix} \mathbf{K}^T & \mathbf{D} \\ \mathbf{C}^T & \mathbf{L}^T \end{pmatrix}\begin{pmatrix} \mathbf{J}_{2k} & \mathbf{0} \\ \mathbf{0}^T & \mathbf{J}_{2l} \end{pmatrix}\begin{pmatrix} \mathbf{K} & \mathbf{C} \\ \mathbf{D}^T & \mathbf{L} \end{pmatrix} = \begin{pmatrix} \mathbf{K}^T\mathbf{J}_{2k} & \mathbf{D}\mathbf{J}_{2l} \\ \mathbf{C}^T\mathbf{J}_{2k} & \mathbf{L}^T\mathbf{J}_{2l} \end{pmatrix}\begin{pmatrix} \mathbf{K} & \mathbf{C} \\ \mathbf{D}^T & \mathbf{L} \end{pmatrix} \\ &= \begin{pmatrix} \mathbf{K}^T\mathbf{J}_{2k}\mathbf{K} + \mathbf{D}\mathbf{J}_{2l}\mathbf{D}^T & \mathbf{K}^T\mathbf{J}_{2k}\mathbf{C} + \mathbf{D}\mathbf{J}_{2l}\mathbf{L} \\ \mathbf{C}^T\mathbf{J}_{2k}\mathbf{K} + \mathbf{L}^T\mathbf{J}_{2l}\mathbf{D}^T & \mathbf{C}^T\mathbf{J}_{2k}\mathbf{C} + \mathbf{L}^T\mathbf{J}_{2l}\mathbf{L} \end{pmatrix} \\ &= \begin{pmatrix} \mathbf{J}_{2k} + \mathbf{D}\mathbf{J}_{2l}\mathbf{D}^T & \mathbf{K}^T\mathbf{J}_{2k}\mathbf{C} + \mathbf{D}\mathbf{J}_{2l}\mathbf{L} \\ \mathbf{C}^T\mathbf{J}_{2k}\mathbf{K} + \mathbf{L}^T\mathbf{J}_{2l}\mathbf{D}^T & \mathbf{C}^T\mathbf{J}_{2k}\mathbf{C} + \mathbf{J}_{2l} \end{pmatrix} \stackrel{!}{=} \begin{pmatrix} \mathbf{J}_{2k} & \mathbf{0} \\ \mathbf{0}^T & \mathbf{J}_{2l} \end{pmatrix}, \end{aligned} \tag{2.15}$$

with $\mathbf{0} \in \mathbb{R}^{2k\times 2l}$. Equation (2.15) yields three conditions as two equalities are equivalent

$$\mathbf{D}\mathbf{J}_{2l}\mathbf{D}^T \stackrel{!}{=} \mathbf{0}_{2k} \tag{2.16}$$

$$\mathbf{C}^T\mathbf{J}_{2k}\mathbf{C} \stackrel{!}{=} \mathbf{0}_{2l} \tag{2.17}$$

$$\mathbf{K}^T\mathbf{J}_{2k}\mathbf{C} + \mathbf{D}\mathbf{J}_{2l}\mathbf{L} \stackrel{!}{=} \mathbf{0} \Leftrightarrow \left(\mathbf{C}^T\mathbf{J}_{2k}\mathbf{K} + \mathbf{L}^T\mathbf{J}_{2l}\mathbf{D}^T\right)^T \stackrel{!}{=} \mathbf{0}. \tag{2.18}$$

Evaluating Eq. (2.18) yields

$$\mathbf{D}\mathbf{J}_{2l}\mathbf{L} \stackrel{!}{=} -\mathbf{K}^T\mathbf{J}_{2k}\mathbf{C} \tag{2.19}$$

$$\Leftrightarrow \quad \mathbf{D}\mathbf{J}_{2l} \stackrel{!}{=} -\mathbf{K}^T\mathbf{J}_{2k}\mathbf{C}\mathbf{L}^{-1} = +\mathbf{K}^T\mathbf{J}_{2k}\mathbf{C}\mathbf{J}_{2l}\mathbf{L}^T\mathbf{J}_{2l} \tag{2.20}$$

$$\Leftrightarrow \quad \mathbf{D} \stackrel{!}{=} \mathbf{K}^T\mathbf{J}_{2k}\mathbf{C}\mathbf{J}_{2l}\mathbf{L}^T \tag{2.21}$$

$$\Rightarrow \quad \mathbf{D}^T \stackrel{!}{=} \mathbf{L}\mathbf{J}_{2l}\mathbf{C}^T\mathbf{J}_{2k}\mathbf{K}. \tag{2.22}$$

Inserting Eqs. (2.21) and (2.22) in Eq. (2.16) gives

$$\begin{aligned} \mathbf{D}\mathbf{J}_{2l}\mathbf{D}^T &= \mathbf{K}^T\mathbf{J}_{2k}\mathbf{C}\mathbf{J}_{2l}\mathbf{L}^T\mathbf{J}_{2l}\mathbf{L}\mathbf{J}_{2l}\mathbf{C}^T\mathbf{J}_{2k}\mathbf{K} \\ &= \mathbf{K}^T\mathbf{J}_{2k}\mathbf{C}\mathbf{J}_{2l} \quad \mathbf{J}_{2l} \quad \mathbf{J}_{2l}\mathbf{C}^T\mathbf{J}_{2k}\mathbf{K} \\ &= \mathbf{K}^T\mathbf{J}_{2k}\mathbf{C} \quad (-\mathbf{J}_{2l}) \quad \mathbf{C}^T\mathbf{J}_{2k}\mathbf{K} \stackrel{!}{=} \mathbf{0}_{2k}. \end{aligned} \tag{2.23}$$

As $\mathbf{K}^T\mathbf{J}_{2k} \neq \mathbf{0}_{2k}$ and $\mathbf{J}_{2k}\mathbf{K} \neq \mathbf{0}_{2k}$, the only way to fulfill this equation, is if

$$\mathbf{C}\,(-\mathbf{J}_{2l})\,\mathbf{C}^T \stackrel{!}{=} \mathbf{0}_{2k}. \tag{2.24}$$

We now have two constraints on $\mathbf{C}$, which are found in Eqs. (2.17) and (2.24) and a definition of $\mathbf{D}$ by means of $\mathbf{C}$, $\mathbf{K}$, and $\mathbf{L}$ in Eq. (2.21) so that $\mathbf{M} \in \mathrm{Sp}(2k+2l)$. We will now apply the above result to examples crucial to beam line elements, and in particular TDSs.

2.2.1 Dispersive Extension

For the special case of the dispersive extension, we will set $2l = 2$,

$$\mathbf{C} \equiv \begin{pmatrix} \vec{0} & \vec{c} \end{pmatrix}, \text{ and } \mathbf{L} \equiv \begin{pmatrix} 1 & \alpha \\ 0 & 1 \end{pmatrix}. \tag{2.25}$$

The name dispersive extension is motivated by an example where $\vec{c}$ is the dispersive vector and α is the momentum compaction factor. Calculating Eq. (2.17), we obtain

$$\begin{aligned} \mathbf{C}^T \mathbf{J}_{2k} \mathbf{C} &= \begin{pmatrix} \vec{0}^T \\ \vec{c}^T \end{pmatrix} \mathbf{J}_{2k} \begin{pmatrix} \vec{0} & \vec{c} \end{pmatrix} = \begin{pmatrix} \vec{0}^T \\ \vec{c}^T \end{pmatrix} \begin{pmatrix} 0 & 1 & 0 & 0 & \cdots \\ -1 & 0 & 0 & 0 & \cdots \\ 0 & 0 & 0 & 1 & \cdots \\ 0 & 0 & -1 & 0 & \cdots \\ \vdots & \vdots & \vdots & \vdots & \ddots \end{pmatrix} \begin{pmatrix} 0 & c_1 \\ 0 & c_2 \\ 0 & c_3 \\ 0 & c_4 \\ \vdots & \vdots \end{pmatrix} \\ &= \begin{pmatrix} \vec{0}^T \\ \vec{c}^T \end{pmatrix} \begin{pmatrix} 0 & c_2 \\ 0 & -c_1 \\ 0 & c_4 \\ 0 & -c_3 \\ \vdots & \vdots \end{pmatrix} = \begin{pmatrix} \vec{0}^T \\ \vec{c}^T \end{pmatrix} \begin{pmatrix} \vec{0} & \vec{\tilde{c}} \end{pmatrix} = \begin{pmatrix} \vec{0}^T\vec{0} & \vec{0}^T\vec{\tilde{c}} \\ \vec{c}^T\vec{0} & \vec{c}^T\vec{\tilde{c}} \end{pmatrix} = \mathbf{0}_2, \end{aligned} \tag{2.26}$$

with $\tilde{c}_{2i-1} = c_{2i}$ and $\tilde{c}_{2i} = -c_{2i-1}$ for $i = 1, 2, \ldots, 2k$, and therefore Eq. (2.17) holds for our choice of $\mathbf{C}$. Verifying Eq. (2.24), we get

$$\mathbf{C}\mathbf{J}_2\mathbf{C}^T = \begin{pmatrix} \vec{0} & \vec{c} \end{pmatrix} \begin{pmatrix} 0 & 1 \\ -1 & 0 \end{pmatrix} \begin{pmatrix} \vec{0}^T \\ \vec{c}^T \end{pmatrix} = \begin{pmatrix} \vec{0} & \vec{c} \end{pmatrix} \begin{pmatrix} \vec{c}^T \\ \vec{0}^T \end{pmatrix} = \mathbf{0}_{2k} \tag{2.27}$$

and also this equation holds. We will now calculate $\mathbf{D}$ by using Eq. (2.21)

$$\begin{aligned} \mathbf{D} &= \mathbf{K}^T \mathbf{J}_{2k} \begin{pmatrix} \vec{0} & \vec{c} \end{pmatrix} \begin{pmatrix} 0 & 1 \\ -1 & 0 \end{pmatrix} \begin{pmatrix} 1 & 0 \\ \alpha & 1 \end{pmatrix} = \mathbf{K}^T \mathbf{J}_{2k} \begin{pmatrix} \vec{0} & \vec{c} \end{pmatrix} \begin{pmatrix} \alpha & 1 \\ -1 & 0 \end{pmatrix} \\ &= -\mathbf{K}^T \mathbf{J}_{2k} \begin{pmatrix} \vec{c} & \vec{0} \end{pmatrix} = -\mathbf{K}^T \begin{pmatrix} \vec{\tilde{c}} & \vec{0} \end{pmatrix} = \begin{pmatrix} -\mathbf{K}^T\vec{\tilde{c}} & \vec{0} \end{pmatrix}. \end{aligned} \tag{2.28}$$

Using this relation, we can calculate

$$\mathbf{D}^T = \begin{pmatrix} -\vec{\tilde{c}}^T\mathbf{K} \\ \vec{0}^T \end{pmatrix} \tag{2.29}$$

and found conditions for $\mathbf{C}$ and $\mathbf{D}^T$ so that our map $\mathbf{M}$ defined in Eq. (2.14) is symplectic for a dispersive map. The vanishing first column of $\mathbf{C}$ and the drift type form of $\mathbf{L}$ are essential for the vanishing second row of $\mathbf{D}^T$. An example for such a dispersive map is a dipole with a transversely focusing block and the dispersive sixth column and fifth row such as the transversely decoupled matrix found in Eq. (2.54).

2.2.2 Cavity Extension

We will now do the same exercise for a cavity extension, where $2l = 2$,

$$\mathbf{C} \equiv \begin{pmatrix} \vec{c} & \vec{0} \end{pmatrix}, \text{ and } \mathbf{L} \equiv \begin{pmatrix} 1 & 0 \\ \kappa & 1 \end{pmatrix}. \tag{2.30}$$

The name cavity extension is motivated by an example where $\vec{c}$ is the "streak" vector and κ is the cavity kick. Calculating Eq. (2.17) for this new choice of $\mathbf{C}$, we obtain

$$\mathbf{C}^T\mathbf{J}_{2k}\mathbf{C} = \begin{pmatrix} \vec{c}^T \\ \vec{0}^T \end{pmatrix} \mathbf{J}_{2k} \begin{pmatrix} \vec{c} & \vec{0} \end{pmatrix} = \begin{pmatrix} \vec{c}^T \\ \vec{0}^T \end{pmatrix} \begin{pmatrix} \vec{\tilde{c}}^T & \vec{0}^T \end{pmatrix} = \begin{pmatrix} \vec{c}^T\vec{\tilde{c}} & \vec{c}^T\vec{0} \\ \vec{0}^T\vec{\tilde{c}} & \vec{0}^T\vec{0} \end{pmatrix} = \mathbf{0}_2, \tag{2.31}$$

so also for this choice the condition is fulfilled. Verifying Eq. (2.24), we get

$$\mathbf{C}\mathbf{J}_2\mathbf{C}^T = \begin{pmatrix} \vec{c} & \vec{0} \end{pmatrix} \begin{pmatrix} 0 & 1 \\ -1 & 0 \end{pmatrix} \begin{pmatrix} \vec{c}^T \\ \vec{0}^T \end{pmatrix} = \begin{pmatrix} \vec{0} & \vec{c} \end{pmatrix} \begin{pmatrix} \vec{0}^T \\ -\vec{c}^T \end{pmatrix} = \mathbf{0}_{2k}. \tag{2.32}$$

Both conditions for $\mathbf{C}$ hold and we can now calculate $\mathbf{D}$ by using Eq. (2.21)

$$\begin{aligned} \mathbf{D} &= \mathbf{K}^T\mathbf{J}_{2k} \begin{pmatrix} \vec{c} & \vec{0} \end{pmatrix} \begin{pmatrix} 0 & 1 \\ -1 & 0 \end{pmatrix} \begin{pmatrix} 1 & \kappa \\ 0 & 1 \end{pmatrix} = \mathbf{K}^T\mathbf{J}_{2k} \begin{pmatrix} \vec{0} & \vec{c} \end{pmatrix} \begin{pmatrix} 0 & 1 \\ -1 & -\kappa \end{pmatrix} \\ &= -\mathbf{K}^T\mathbf{J}_{2k} \begin{pmatrix} \vec{0} & \vec{c} \end{pmatrix} = \mathbf{K}^T \begin{pmatrix} \vec{0} & \vec{\tilde{c}} \end{pmatrix} = \begin{pmatrix} \vec{0} & \mathbf{K}^T\vec{\tilde{c}} \end{pmatrix}. \end{aligned} \tag{2.33}$$

From this, we can calculate

$$\mathbf{D}^T = \begin{pmatrix} \vec{0}^T \\ \vec{\tilde{c}}^T\mathbf{K} \end{pmatrix} \tag{2.34}$$

and found our conditions for $\mathbf{C}$ and $\mathbf{D}^T$ so that our map $\mathbf{M}$ defined in Eq. (2.14) is symplectic for a cavity map. The vanishing second column of $\mathbf{C}$ and the kick type form of $\mathbf{L}$ are essential for the vanishing first row of $\mathbf{D}^T$. An example of such a cavity map is the thick lens matrix of a TDS which can be found in Eq. (4.13).

2.3 Equation of Motion in the Accelerator Coordinate System

In this section, we will introduce the coordinates used in this thesis, summarizing the treatment in [19, 20, 21] and restricting ourselves to the case of straight beam lines and constant reference momentum P_0.

The standard Hamiltonian of classical relativistic electrodynamics in Cartesian coordinates reads

$$\mathcal{H}(X,P_X,Y,P_Y,Z,P_Z;t) = \sqrt{m_e^2c^4 + \left(\vec{P} - e\vec{A}(X,Y,Z;t)\right)^2 c^2} + e\phi(X,Y,Z;t), \tag{2.35}$$

where X, Y, and Z are the Cartesian coordinates, P_X, P_Y, and P_Z the corresponding conjugate momenta, $m_e = 0.511\,\mathrm{MeV/c^2}$ is the mass of an electron, e is the elementary charge, c is the speed of light, $\vec{A}$ is the vector potential, and ϕ is the scalar potential. We can subtract the coordinates of the reference trajectory which are marked by the index 0 from the coordinates of a particle

$$\begin{pmatrix} x \\ p_x \\ y \\ p_y \\ z \\ p_z \end{pmatrix}(t) := \begin{pmatrix} X - X_0 \\ P_x \\ Y - Y_0 \\ P_y \\ Z - Z_0 \\ -(P_z - P_0) \end{pmatrix}(t). \tag{2.36}$$

We assume here that the reference trajectory is in the direction of the unit vector $\hat{Z}$. In the absence of acceleration, the relation $s - s_i = \beta c\,(t - t_i)$, with t_i and s_i being the initial time and the initial position in the lattice, $\beta = v/c$ and c the speed of light, holds. Following the prescription in [19, 20, 21] we change the free parameter from t to s obtaining a new set of canonical variables for the longitudinal motion (originally along $\hat{Z}$)

$$\begin{pmatrix} x \\ p_x \\ y \\ p_y \\ -(t - t_0) \\ T - T_0 \end{pmatrix}(s). \tag{2.37}$$

Here $T = E - m_e c^2$ is the kinetic energy, and E is the total energy of the free particle.

These momenta can be rescaled by a so-called "improper canonical transformation" [19] which preserves the Hamiltonian structure of the system. Following [19], we obtain the canonical accelerator coordinates for a straight beam line

$$\begin{pmatrix} x \\ a \equiv p_x/P_0 \\ y \\ b \equiv p_y/P_0 \\ -(t - t_0)\cdot T_0/P_0 \equiv \tau \\ (T - T_0)/T_0 \equiv \delta \end{pmatrix}(s). \tag{2.38}$$

The Hamiltonian in these coordinates, in the ultra-relativistic limit, and in Weyl gauge ($\phi \equiv 0$) reads

$$\begin{aligned}\mathcal{K}(x,a,y,b,\tau,\delta;s) = &-\frac{1}{T_0}\sqrt{(1+\delta)^2-(a-\frac{e}{P_0}A_x)^2-(b-\frac{e}{P_0}A_y)^2} \\ &-\frac{eT_0}{P_0}A_\tau+\frac{1}{T_0}(1+\delta).\end{aligned} \tag{2.39}$$

In the SCOFF[6] approximation and in the absence of solenoids A_x and A_y are identical zero. $A_\tau(x,y)$ describes the standard (upright as well as skew) magnetic beam line elements. In the presence of cavities A_τ would in addition also depend on τ. Expanding $-\sqrt{1-a^2-b^2}$ for $a,b \ll 1$ and expanding A_τ around $x,y=0$ gives the usual transverse Hamiltonian.

In the transverse phase space, it is common practice to use $x' = \frac{\mathrm{d}x}{\mathrm{d}s} = \frac{p_x}{p_s}$ and $y' = \frac{\mathrm{d}y}{\mathrm{d}s} = \frac{p_y}{p_s}$ instead of $a = \frac{p_x}{P_0}$ and $b = \frac{p_y}{P_0}$. One reason is, that the map for a free space drift is exactly linear in (x,x') and (y,y') while in (x,a) and (y,b) it inherits higher order contributions. For $P_0 = \text{const}$ and $p_x, p_y \ll p_s$ we obtain

$$\begin{aligned}|P_0| &= \sqrt{p_x^2+p_y^2+p_s^2} \\ &= |p_s|\sqrt{1+\frac{p_x^2+p_y^2}{p_s^2}} \\ &= |p_s|\left(1+\frac{1}{2}\frac{p_x^2+p_y^2}{p_s^2}-\mathcal{O}\left(\left(p_x^2+p_y^2\right)^2\right)\right) \\ &= |p_s|+\mathcal{O}\left(p_x^2+p_y^2\right).\end{aligned} \tag{2.40}$$

Therefore, at first order the canonical momenta a and b, are equal to the slopes x' and y'. We will thus in the following write the transverse phase space vectors as

$$\vec{u}(s) = \begin{pmatrix} u(s) \\ u'(s) \end{pmatrix} = \begin{pmatrix} u \\ u' \end{pmatrix}_s, \tag{2.41}$$

where u is one of x and y and s is the position.

In this thesis, we will deal with electrons in the ultra-relativistic limit, i.e. $\beta \approx 1$ and the Lorentz factor $\gamma = 1/\sqrt{1-\beta^2} \gg 1$. Due to the rest mass of electrons m_e being smaller than the reference momentum $m_e c^2 \ll P_0$ we will use the terms energy $E^2 = (P_0 c)^2 + \left(m_e c^2\right)^2 \approx (P_0 c)^2$, kinetic energy $T = m_e c^2 - E \approx E$, and reference momentum P_0 analogously. Also the difference in kinetic energy, defined as the sixth coordinate in Eq. (2.38), can be the total energy difference or the momentum difference, respectively

$$\delta \equiv \frac{T-T_0}{T_0} \approx \frac{E-E_0}{E_0} \approx \frac{P_z-P_0}{P_0}. \tag{2.42}$$

[6] Sharp Cut-OFF

2.4 Transfer Matrices

Starting from the general equation of motion for a particle with no momentum offset $\delta = 0$ and with no dipoles present, we obtain Hill's equation of motion for the transverse plane [22]

$$u''(s) - k(s)u(s) = 0, \tag{2.43}$$

where $k(s)$ is the quadrupole strength as function of the position s. The Hill's type equations found in Eq. (2.43) can be solved for piecewise constant k, e.g. in a quadrupole or a drift. Setting $k(s) = k$, $u(s) \equiv q$, and $u'(s) \equiv p$ one can rewrite Eq. (2.43)

$$\left\{ \begin{array}{c} q' = p \\ p' - k\, q = 0 \end{array} \right\} \Leftrightarrow \left\{ \begin{array}{c} q' = p \\ p' = k\, q \end{array} \right\}, \tag{2.44}$$

or in vector notation

$$\begin{pmatrix} q' \\ p' \end{pmatrix} = \begin{pmatrix} 0 & 1 \\ k & 0 \end{pmatrix} \begin{pmatrix} q \\ p \end{pmatrix} = \mathbf{K} \begin{pmatrix} q \\ p \end{pmatrix}, \tag{2.45}$$

where $\mathbf{K}$ is Hamiltonian.

In fact Eq. (2.45) follows to first order from Eq. (2.39) in coordinates found in Eq. (2.41).

We can find a solution for

$$\vec{u}(s) = \mathbf{M}_{s \leftarrow s_0}(s)\ \vec{u}(s_0) \tag{2.46}$$

by setting

$$\mathbf{M}_{s \leftarrow s_0}(s) = \exp(s\mathbf{K}) = \sum_{n=1}^{\infty} \frac{(s\mathbf{K})^n}{n!}, \tag{2.47}$$

as stated in Eqs. (2.12) and (2.13) with $\mathbf{M}_{s \leftarrow s_0} \in \mathrm{Sp}(2)$. For $k = 0$ we obtain $s\mathbf{K} = \left(\begin{smallmatrix} 0 & s \\ 0 & 0 \end{smallmatrix}\right)$ and therefore

$$\mathbf{M}_{s \leftarrow s_0} = \begin{pmatrix} 1 & s \\ 0 & 1 \end{pmatrix}, \tag{2.48}$$

which is the transfer matrix of a drift space. For $k > 0$, $s\mathbf{K} = \left(\begin{smallmatrix} 0 & s \\ ks & 0 \end{smallmatrix}\right)$, which yields

$$\begin{aligned} \mathbf{M}_{s \leftarrow s_0} &= \mathbb{1} + \begin{pmatrix} 0 & \frac{1}{\sqrt{k}}(\sqrt{k}s)^1 \\ \sqrt{k}(\sqrt{k}s)^1 & 0 \end{pmatrix} + \frac{1}{2!} \begin{pmatrix} (\sqrt{k}s)^2 & 0 \\ 0 & (\sqrt{k}s)^2 \end{pmatrix} \\ &\quad + \frac{1}{3!} \begin{pmatrix} 0 & \frac{1}{\sqrt{k}}(\sqrt{k}s)^3 \\ \sqrt{k}(\sqrt{k}s)^3 & 0 \end{pmatrix} + \frac{1}{4!} \begin{pmatrix} (\sqrt{k}s)^4 & 0 \\ 0 & (\sqrt{k}s)^4 \end{pmatrix} + \dots \\ &= \begin{pmatrix} \sum_{n=0}^{\infty} \frac{(\sqrt{k}s)^{2n}}{(2n)!} & \frac{1}{\sqrt{k}} \sum_{n=0}^{\infty} \frac{(\sqrt{k}s)^{2n+1}}{(2n+1)!} \\ \sqrt{k} \sum_{n=0}^{\infty} \frac{(\sqrt{k}s)^{2n+1}}{(2n+1)!} & \sum_{n=0}^{\infty} \frac{(\sqrt{k}s)^{2n}}{(2n)!} \end{pmatrix} \\ &= \begin{pmatrix} \cosh(\sqrt{k}s) & \frac{1}{\sqrt{k}} \sinh(\sqrt{k}s) \\ \sqrt{k} \sinh(\sqrt{k}s) & \cosh(\sqrt{k}s) \end{pmatrix}. \end{aligned} \tag{2.49}$$

For the case with $k < 0$ we replace k with $-|k|$ and make use of $\sqrt{-|k|} = i\sqrt{|k|}$,

$\sinh(ix) = i\sin(x)$, and $\cosh(ix) = \cos(x)$ thus resulting in

$$\mathbf{M}_{s\leftarrow s_0} = \begin{pmatrix} \cos(\sqrt{|k|}s) & \frac{1}{\sqrt{|k|}}\sin(\sqrt{|k|}s) \\ -\sqrt{|k|}\sin(\sqrt{|k|}s) & \cos(\sqrt{|k|}s) \end{pmatrix}. \tag{2.50}$$

For a quadrupole with the constant strength k of the length L, we find

$$\mathbf{M}_{s\leftarrow s_0} = \begin{cases} \begin{pmatrix} \cos\left(\sqrt{|k|}L\right) & \frac{1}{\sqrt{|k|}}\sin\left(\sqrt{|k|}L\right) \\ -\sqrt{|k|}\sin\left(\sqrt{|k|}L\right) & \cos\left(\sqrt{|k|}L\right) \end{pmatrix} & \text{if } k < 0 \\ \begin{pmatrix} 1 & L \\ 0 & 1 \end{pmatrix} & \text{if } k = 0 \\ \begin{pmatrix} \cosh\left(\sqrt{k}L\right) & \frac{1}{\sqrt{k}}\sinh\left(\sqrt{k}L\right) \\ \sqrt{k}\sinh\left(\sqrt{k}L\right) & \cosh\left(\sqrt{k}L\right) \end{pmatrix} & \text{if } k > 0. \end{cases} \tag{2.51}$$

To calculate the particle trajectory through an element, it is possible to use the previously defined matrices

$$\vec{u}(s) = \mathbf{M}_{s\leftarrow s_0}\,\vec{u}(s_0). \tag{2.52}$$

Since in general, a beam line consists of more than one element, we can use successive matrix multiplication, to obtain $\vec{x}_n$ [22].

We will now extend the 2×2-dimensional transfer matrices to 6×6 dimensions. If the initial phase space vector of a particle at the position s_0 is given as $\vec{z}(s_0) = (x, x', y, y', \zeta, \delta)^T_{s_0}$, with the internal bunch coordinate ζ, we can write the evolution of this phase space vector to an arbitrary point in the beam line s as

$$\vec{z}(s) = \mathbf{M}_{s\leftarrow s_0}\cdot\vec{z}(s_0), \tag{2.53}$$

where $\mathbf{M}_{s\leftarrow s_0}$ now is the 6×6-dimensional transfer matrix. For a decoupled beam line, i.e. there is no correlation between the transverse planes, we can write the transfer matrix in its decoupled form

$$\mathbf{M}_{\text{decoupled}} = \begin{pmatrix} M_{11} & M_{12} & 0 & 0 & 0 & M_{16} \\ M_{21} & M_{22} & 0 & 0 & 0 & M_{26} \\ 0 & 0 & M_{33} & M_{34} & 0 & M_{36} \\ 0 & 0 & M_{43} & M_{44} & 0 & M_{46} \\ M_{51} & M_{52} & M_{53} & M_{54} & M_{55} & M_{56} \\ 0 & 0 & 0 & 0 & 0 & M_{66} \end{pmatrix}. \tag{2.54}$$

As we have shown in Section 2.2.1, this dispersive map $\mathbf{M}_{\text{decoupled}}$ can be symplectic if[7] $\mathbf{K} \in \text{Sp}(4)$, $\mathbf{L} \in \text{Sp}(2)$, and $\mathbf{D}^T$ is defined by means of Eq. (2.29). The transfer matrices for a

[7] See Eq. (2.14).

drift space $\mathbf{M}_{\mathrm{D}}$, a horizontally focusing quadrupole magnet $\mathbf{M}_{\mathrm{QF}}$, and a vertically focusing quadrupole magnet $\mathbf{M}_{\mathrm{QD}}$ are given by [22]

$$\mathbf{M}_{\mathrm{D}} = \begin{pmatrix} 1 & L & 0 & 0 & 0 & 0 \\ 0 & 1 & 0 & 0 & 0 & 0 \\ 0 & 0 & 1 & L & 0 & 0 \\ 0 & 0 & 0 & 1 & 0 & 0 \\ 0 & 0 & 0 & 0 & 1 & \frac{L}{(\gamma+1)^2} \\ 0 & 0 & 0 & 0 & 0 & 1 \end{pmatrix}, \tag{2.55}$$

$$\mathbf{M}_{\mathrm{QF}} = \begin{pmatrix} \cos\left(\sqrt{|k|}L\right) & \frac{1}{\sqrt{|k|}}\sin\left(\sqrt{|k|}L\right) & 0 & 0 & 0 & 0 \\ -\sqrt{|k|}\sin\left(\sqrt{|k|}L\right) & \cos(\sqrt{|k|}L) & 0 & 0 & 0 & 0 \\ 0 & 0 & \cosh\left(\sqrt{|k|}L\right) & \frac{1}{\sqrt{|k|}}\sinh\left(\sqrt{|k|}L\right) & 0 & 0 \\ 0 & 0 & \sqrt{|k|}\sinh\left(\sqrt{|k|}L\right) & \cosh\left(\sqrt{|k|}L\right) & 0 & 0 \\ 0 & 0 & 0 & 0 & 1 & \frac{L}{(\gamma+1)^2} \\ 0 & 0 & 0 & 0 & 0 & 1 \end{pmatrix}, \tag{2.56}$$

and

$$\mathbf{M}_{\mathrm{QD}} = \begin{pmatrix} \cosh\left(\sqrt{k}L\right) & \frac{1}{\sqrt{k}}\sinh\left(\sqrt{k}L\right) & 0 & 0 & 0 & 0 \\ \sqrt{k}\sinh\left(\sqrt{k}L\right) & \cosh(\sqrt{k}L) & 0 & 0 & 0 & 0 \\ 0 & 0 & \cos\left(\sqrt{k}L\right) & \frac{1}{\sqrt{k}}\sin\left(\sqrt{k}L\right) & 0 & 0 \\ 0 & 0 & -\sqrt{k}\sin\left(\sqrt{k}L\right) & \cos\left(\sqrt{k}L\right) & 0 & 0 \\ 0 & 0 & 0 & 0 & 1 & \frac{L}{(\gamma+1)^2} \\ 0 & 0 & 0 & 0 & 0 & 1 \end{pmatrix}, \tag{2.57}$$

where L is the length of the element, $k < 0$ is the strength of a focusing quadrupole, and $k > 0$ is the strength of a defocusing quadrupole. More transfer matrices for all beam line elements exist, the full form of some of them can be found in [21, 22].

One of the most important perturbations of the beam orbit is caused by the fact, that particle beams are not monochromatic but posses a finite momentum spread around the reference energy δ [21]. As can already be seen in Eq. (2.54) this momentum deviation will already cause a coupling into the transverse planes at first order if the M_{16} to M_{46} elements are non-zero, as it is the case for a dispersive beam line incorporating dipoles. The M_{16} element of a transfer matrix is called the horizontal dispersion η_x and the M_{36} element the vertical dispersion η_y. Where the dispersion is non-zero a particle with a momentum offset of δ has a transverse position of [22]

$$u(s) = u_0(s) + u_\eta(s) = u_0(s) + \eta_u(s)\delta, \tag{2.58}$$

where $u_0(s)$ is the transverse position of a particle without momentum offset, $u_\eta(s)$ is the dis-

placement due to the momentum offset, and $\vec{u}(s) = (x, x')_s^T$ or $\vec{u}(s) = (y, y')_s^T$.

2.5 Invariant Ellipse of an Accelerator in Two-Dimensional Phase Space

We will follow [21, 22] in this section to derive the invariant ellipse of an accelerator in two-dimensional phase space. To obtain a general solution of Eq. (2.43) one can make the s-dependent ansatz for u [22]

$$u(s) = \sqrt{\varepsilon_u}\sqrt{\beta_u(s)}\cos\left[\Psi_u(s) - \Psi_{u0}\right] \tag{2.59}$$

which following [21, 22] indeed satisfies Hill's equation of motion. Here, $\beta_u(s)$ is the beta function or amplitude function in the u plane,

$$\Psi_u(s) = \int_0^s \frac{\mathrm{d}\sigma}{\beta_u(\sigma)} \tag{2.60}$$

is the phase function and Ψ_{u0} is an integration constant [22]. The constant ε_u is the Courant-Snyder invariant and will be explained in the following. The first derivative of the trajectory function can be written in the form [22]

$$u'(s) = -\frac{\sqrt{\varepsilon_u}}{\sqrt{\beta_u(s)}}\left[\alpha_u(s)\cos\left(\Psi_u(s) - \Psi_{u0}\right) + \sin\left(\Psi_u(s) - \Psi_{u0}\right)\right] \tag{2.61}$$

with

$$\alpha(s) \equiv -\frac{\beta_u'(s)}{2}. \tag{2.62}$$

The optical functions $\beta_u(s)$ and $\alpha_u(s)$ with the phase $\Psi_u(s)$ together with the dispersion $\eta_u(s)$ and its derivative $\eta_u'(s)$ fully describe the linear beam optics in the u plane [22]. Furthermore, the transverse transfer matrix $\mathbf{M}_{s\leftarrow s_0}$ in the chosen plane transporting the trajectory from s_0 to s

$$\begin{pmatrix} u(s) \\ u'(s) \end{pmatrix} = \mathbf{M}_{s\leftarrow s_0} \cdot \begin{pmatrix} u(s_0) \\ u'(s_0) \end{pmatrix} \tag{2.63}$$

can be expressed by the optical functions: [22]

$$\mathbf{M}_{s\leftarrow s_0} = \begin{pmatrix} \sqrt{\frac{\beta_u(s)}{\beta_u(s_0)}}\left[\cos\left(\Delta\Psi_u\right) + \alpha_u(s_0)\sin\left(\Delta\Psi_u\right)\right] & \sqrt{\beta_u(s)\beta_u(s_0)}\sin\left(\Delta\Psi_u\right) \\ \frac{(\alpha_u(s_0) - \alpha_u(s))\cos(\Delta\Psi_u) - (1 + \alpha_u(s)\alpha_u(s_0))\sin(\Delta\Psi_u)}{\sqrt{\beta_u(s)\beta_u(s_0)}} & \sqrt{\frac{\beta_u(s_0)}{\beta_u(s)}}\left[\cos\left(\Delta\Psi_u\right) - \alpha_u(s)\sin\left(\Delta\Psi_u\right)\right] \end{pmatrix}, \tag{2.64}$$

with the phase advance $\Delta\Psi_u = \Psi_u(s) - \Psi_u(s_0)$. Therefore, the transfer matrix between two points can also be calculated if the optical functions are known at the start point and at the end point.

To describe the invariant curves in the u-u' phase space plane, it is necessary to eliminate the phase $\Psi_u(s)$ in Eqs. (2.59) and (2.61). Following [21, 22] one obtains a constant of motion

which is referred to as Courant-Snyder invariant [23]

$$\gamma_u(s)u^2(s) + 2\alpha_u(s)u(s)u'(s) + \beta_u(s)u'^2(s) = \varepsilon_u \tag{2.65}$$

with

$$\gamma_u(s) \equiv \frac{1+\alpha_u^2(s)}{\beta_u(s)}. \tag{2.66}$$

Equation (2.65) is the general equation of an ellipse. The quantity ε_u which was originally introduced in Eq. (2.59) as a constant parameter now has a physical interpretation. The quantity $\pi\varepsilon_u$ is the area of the phase space ellipse often called the enclosed emittance. This is a key parameter of particle beams as in particular it is a figure of merit for many derived quantities, e.g. for luminosity and brilliance. The fact that ε_u is constant is a linear specialization of Liouville's theorem [24] which states that under Hamiltonian flows the phase space density stays constant along trajectories. Liouville's theorem in its most general form implies that arbitrary symplectic maps preserve Lebesgue measure on phase space [25]. In the linear case, the Courant-Snyder ellipses are invariant sets of the linear flow and their area is preserved. In order to apply Liouville's theorem to the acceleration process, one has to use coordinates for which the momenta are proper canonical conjugates to the spatial coordinates for all beam reference momenta. In particular, the scaled momenta in Eq. (2.38) do not fulfill this constraint. However, the normalized Courant-Snyder invariant

$$\varepsilon_{u,n} = \beta\gamma\varepsilon_u, \tag{2.67}$$

is an adiabatic invariant of acceleration from one reference momentum to another one. It has become common practice in accelerator physics [26] to refer to the Courant-Snyder invariant as emittance and denoting both quantities as ε_u. In what follows, we will also use this definition.

The representation of particle beams via the phase-space ellipse is advantageous, as all particles contained in that ellipse stay within that ellipse under linear maps [21]. Thus, instead of mapping each individual particle we will map the optical functions.

Let $\vec{u}(s) = (u, u')_s^T$ be the two-dimensional phase space vector of a particle, then

$$\vec{u}^T(s)\sigma^{-1}\vec{u}(s) = 1 \tag{2.68}$$

is the representation of a 2-dimensional ellipse with a symmetric matrix σ to be determined [21]. Evaluating Eq. (2.68) yields

$$\sigma_{22}u^2(s) + 2\sigma_{12}u(s)u'(s) + \sigma_{11}u'^2(s) = \det\sigma. \tag{2.69}$$

Comparing this equation with Eq. (2.65), we see [21]

$$\sigma(s) = \begin{pmatrix} \sigma_{11}(s) & \sigma_{12}(s) \\ \sigma_{21}(s) & \sigma_{22}(s) \end{pmatrix} = \varepsilon_u \begin{pmatrix} \beta_u(s) & -\alpha_u(s) \\ -\alpha_u(s) & \gamma_u(s) \end{pmatrix}, \tag{2.70}$$

which is the so-called beam matrix, and $\varepsilon_u = \sqrt{\det \sigma}$.

Furthermore, using Eqs. (2.59) and (2.61) and forming the average values of all particles within a previously defined fraction of the beam, we obtain [21]

$$\begin{aligned} \left\langle u^2(s) \right\rangle &= \varepsilon_u \beta_u(s) = \sigma_{11}(s) \equiv \sigma_u^2(s) \\ \left\langle u'^2(s) \right\rangle &= \varepsilon_u \gamma_u(s) = \sigma_{22}(s) \equiv \sigma_{u'}^2(s) \\ \left\langle u(s)u'(s) \right\rangle &= -\varepsilon_u \alpha_u(s) = \sigma_{12}(s) = \sigma_{21}(s) \equiv \sigma_{uu'}(s). \end{aligned} \tag{2.71}$$

With this definition we obtain

$$\varepsilon_u = \sqrt{\left\langle u^2(s) \right\rangle \left\langle u'^2(s) \right\rangle - \left\langle u(s)u'(s) \right\rangle^2}. \tag{2.72}$$

The here-described formalism for a two-dimensional phase space vector can of course be transferred to higher dimensional cases, in particular to $\vec{z}(s) = (x, x', y, y', \zeta, \delta)_s^T$ which is used to describe particle beams.

After some simple calculations, which can be found e.g. in [22], we find, that also the beta matrix can be evolved along the beam line using the transfer matrices defined in Eq. (2.53). Given the beam matrix $\sigma(s_0)$ at the starting point s_0, the beam matrix at s is given by

$$\sigma(s) = \mathbf{M}_{s \leftarrow s_0} \sigma(s_0) \mathbf{M}_{s \leftarrow s_0}^T. \tag{2.73}$$

2.6 Acceleration and Bunch Compression

The energy gain of a particle at a longitudinal position ζ relative to the reference particle at $\zeta = 0$ within an electron bunch when passing through a radio frequency (RF) accelerating cavity is given by [27]

$$\Delta E = eV \cos\left(\Phi_{\mathrm{RF}} + k_{\mathrm{RF}} \zeta\right) \tag{2.74}$$

where e is the elementary charge, V is voltage amplitude, Φ_{RF} is the phase of the RF, and k_{RF} is the RF wave number. The final energy after the acceleration is then $E_f = E_i + \Delta E$ with the initial energy E_i. The acceleration is maximum for $\Phi_{\mathrm{RF}} = 0$ and if the reference particle of a particle beam is accelerated at this phase, the beam is "on-crest" of the RF wave [27]. As we will see in the following, for bunch compression a linear dependence of the energy on the longitudinal position in the bunch is necessary. This can be achieved by accelerating the beam "off-crest", i.e. at an RF phase of $-\pi < \Phi_{\mathrm{RF}} < 0$ or $0 < \Phi_{\mathrm{RF}} < \pi$. The correlation describing the dependence of energy and the longitudinal position in the bunch is called linear energy chirp and is calculated by expanding the energy gain defined in Eq. (2.74) up to first order in ζ [27]

$$\begin{aligned} h &= \frac{1}{E_f} \frac{\mathrm{d}E_f}{\mathrm{d}\zeta} \approx \frac{1}{E_i + eV\cos\left(\Phi_{\mathrm{RF}}\right)} \frac{\mathrm{d}}{\mathrm{d}\zeta} \left[E_i + eV\cos\left(\Phi_{\mathrm{RF}}\right) - eVk_{\mathrm{RF}}\zeta \sin\left(\Phi_{\mathrm{RF}}\right) + \mathscr{O}\left(\zeta^2\right) \right] \\ &= -\frac{eVk_{\mathrm{RF}} \sin\left(\Phi_{\mathrm{RF}}\right)}{E_i + eV\cos\left(\Phi_{\mathrm{RF}}\right)}. \end{aligned} \tag{2.75}$$

Thus, the energy deviation of a particle at a position ζ relative to the energy of the reference particle E_0 at $\zeta = 0$ can be approximated by [28]

$$\delta = \frac{\Delta E}{E_0} = h\zeta + \delta_i, \tag{2.76}$$

where δ_i is the uncorrelated intrinsic energy deviation independent of ζ.

Equating the Lorentz force with the centripetal force for a particle moving with a longitudinal momentum p_z through a dipole with a uniform vertical magnetic field B_0 yields [22]

$$B_0\rho = \frac{p_z}{e}, \tag{2.77}$$

where ρ is the bending radius. This suggests that for highly-relativistic particles, i.e. the longitudinal velocity is independent of the momentum of the particles ($\beta \approx 1$), particles with a higher momentum will follow a shorter path in a dipole than particles with a lower momentum. This enables the possibility to build magnetic chicanes, where particles with a higher momentum in the tail of the bunch catch up with particles with a lower momentum in the head of the bunch.

As in linac-driven FELs one usually wants to maintain a straight trajectory, the magnetic chicanes used for bunch compression are arranged in a way that downstream of the chicane the beam travels on the same orbit as upstream of the chicane [27]. This can e.g. be achieved by utilizing a four-dipole C-chicane such as the one shown in Fig. 2.1. More complex arrangements such as a six-dipole S-chicane are also possible.

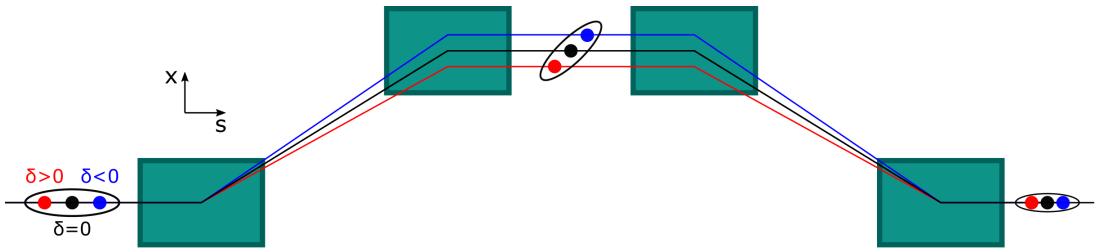

Figure 2.1: Scheme of a C-chicane bunch compressor. Particles with a higher momentum (marked in red) in the tail of the bunch catch up with particles with a lower momentum (marked in blue) in the head of the bunch. The dipoles are plotted in teal.

From Eq. (2.54) we see, that the longitudinal position of a particle with a momentum offset of $\delta \neq 0$ when passing through a beam line element with $M_{56} \neq 0$ changes according to

$$\Delta\zeta = M_{56}\delta \tag{2.78}$$

in first order of δ. When passing through a chicane the longitudinal position of a particle at the exit of the chicane is given by [27]

$$\zeta_f = \zeta_i + M_{56}\delta = \zeta_i\,(1 + M_{56}h) + M_{56}\delta_i \equiv \frac{\zeta_i}{C} + M_{56}\delta_i, \tag{2.79}$$

where $C \equiv (1+M_{56}h)^{-1}$ is the compression factor. Taking the average over all particles in the bunch, the rms bunch length in a bunch compressor changes according to

$$\sigma_{\zeta_f}^2 = \frac{\sigma_{\zeta_i}^2}{C^2} + M_{56}^2 \sigma_{\delta_i}^2. \tag{2.80}$$

In the limit of $C \to \infty$, the bunch length reaches a minimum of $\sigma_{\zeta_{f,\min}} \approx |M_{56}|\,\sigma_{\delta_i}$ [27].

2.7 Collective Effects in Free-Electron Lasers

Collective effects such as space charge and coherent synchrotron radiation can have a significant influence on the beam dynamics and seriously degrade the beam quality. We will give a brief introduction to these effects in the following.

2.7.1 Space Charge

Due to the necessarily high beam current and therefore the high particle densities in FELs, space charge (SC) forces can have a significant influence on the beam dynamics in particular at low energies. The space charge forces acting on the particles can lead to a notable degradation of the beam quality. We will outline the most important aspects of space charge forces in the following, for a more detailed view on space charge we refer to [29, 30, 31, 32].

The radial space charge force of a radial symmetric Gaussian beam with a total current of $I = \beta c \lambda$, where λ is the line charge density, is given by [33, 34]

$$F_r(r) = \frac{eI}{2\pi\varepsilon_0 \beta c \gamma^2} \frac{1}{r} \left(1 - e^{-r^2/2\sigma_{x,y}^2}\right), \tag{2.81}$$

with the vacuum permittivity ε_0, $r = \sqrt{x^2+y^2}$ and $\sigma_{x,y}$ is the rms radial beam size. It is repulsive and can lead, especially for beams at low energies, i.e. $\gamma \approx 1$, to a radial blowup of the particle beam [32]. For beams with higher energies, i.e. $\gamma \gg 1$, the influence of the transverse space charge force becomes less significant due to the $1/\gamma^2$ dependency and vanishes in the limit of $\gamma \to \infty$.

The longitudinal electric field of a round Gaussian beam with a charge of Q, an rms radial beam size of σ_r, and a bunch length of σ_ζ, for linear motion is given by [35]

$$E_z(\zeta) = \frac{-Q}{4\pi\varepsilon_0 \gamma \sigma_r \sigma_\zeta} \int_{-\infty}^{\infty} g'(x+\zeta) G(x\gamma \frac{\sigma_\zeta}{\sigma_r}) \mathrm{d}x, \tag{2.82}$$

with

$$G(\xi) = \sqrt{\frac{\pi}{2}} e^{\frac{\xi^2}{2}} \left(1 - \mathrm{erf}\left(\frac{|\xi|}{\sqrt{2}}\right)\right) \approx \frac{1}{\sqrt{1+\xi^2}} \text{ for } |\xi| \gg 1, \tag{2.83}$$

$$\mathrm{erf}(x) = \frac{2}{\sqrt{\pi}} \int_0^x e^{-t^2} \mathrm{d}t, \tag{2.84}$$

and

$$g(x) = \frac{1}{\sqrt{2\pi}} e^{-\frac{x^2}{2}} \tag{2.85}$$

the Gaussian normal distribution. Due to this longitudinal electric field particles in the head of the bunch are accelerated by the high charge in the center, whereas particles in the tail of the bunch are decelerated [28].

To mitigate space charge effects particles should be accelerated fast to higher energies and the charge density should be kept small at low energies.

2.7.2 Coherent Synchrotron Radiation

Relativistic electrons moving on a curved path emit synchrotron radiation tangentially to their movement [36]. If the curvature radius of the trajectory is small, radiation emitted by the particles can "overtake" them on a shorter, straight trajectory and interact with them [37], c.f. Fig. 2.2.

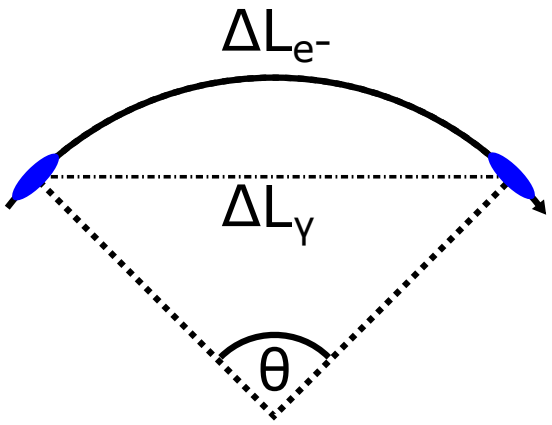

Figure 2.2: Scheme of CSR. The electron bunch (blue) emits radiation when following a curved path that travels on a shorter part through the curve and catches up with the electron bunch.

In the following, we will briefly describe the effects of synchrotron radiation acting on the particle beam while passing through a deflecting magnet. For a much more detailed description, we refer to [36, 37, 38, 39, 40, 41, 42].

Three radiation regimes can be distinguished in the description of synchrotron radiation. If the longitudinal distance between the particles is large, i.e. the bunch length $\sigma_\zeta > N^{\frac{3}{4}}\sigma_0$, where N is the number of particles and $\sigma_0 = \rho/\gamma^3$ is the critical bunch length, particles radiate independently or incoherently [38]. The radiated power is then [38]

$$P_{\mathrm{ic}} = N\frac{1}{6\pi}\frac{e^2 c}{\varepsilon_0}\frac{\gamma^4}{\rho^2}. \tag{2.86}$$

If the bunch length is shorter than the critical bunch length, the particles radiate fully coherent, independent of finer structures in the longitudinal distribution [38]. The radiated power in this

fully coherent regime is given by [38]

$$P_{\mathrm{fc}} = N \cdot P_{\mathrm{ic}} = N^2 \frac{1}{6\pi} \frac{e^2 c}{\varepsilon_0} \frac{\gamma^4}{\rho^2}. \tag{2.87}$$

Between these two extremes, we speak of the regime of coherent synchrotron radiation (CSR), where there radiation power grows with N^2 and is independent of the energy γ, but depends on σ_ζ [38]. The radiated power of CSR is [38]

$$P_{\mathrm{CSR}} \approx 0.028 N^2 \frac{e^2 c}{\varepsilon_0} \frac{1}{\rho^{2/3} \sigma_\zeta^{4/3}}. \tag{2.88}$$

Radiation emitted by electrons slips through the bunch by the slippage length [28, 40]

$$L_{\mathrm{sl}} = \Delta L_{e^-} - \Delta L_\gamma = \frac{\rho \theta^3}{24} \tag{2.89}$$

where ΔL_{e^-} and ΔL_γ are the lengths traveled by the electron and photons, respectively, and θ is the bending angle of the dipole. The overtaking length L_0 is defined as the length on which the radiation from the tail of the bunch passes through the complete bunch and is given by [37]

$$L_0 = \sqrt[3]{24 \rho^2 \sigma_\zeta}. \tag{2.90}$$

If the length of the dipole is larger than the overtaking length, the radiation emitted from the tail of the bunch is able to interact with the particles in the head of the bunch.

The energy change of an electron due to CSR is given by [40]

$$\frac{\mathrm{d}E}{\mathrm{d}(ct)} = N \frac{2e^2}{3^{1/3} \sqrt{2\pi} \rho^{2/3} \sigma_\zeta^{4/3}} G(\xi, \chi), \tag{2.91}$$

with

$$G(\xi, \chi) = \frac{1}{\sqrt[3]{\chi}} \left[e^{-(\xi-\chi)^2} - e^{-(\xi-4\chi)^2/2} \right] + \int_{\xi-\chi}^{\xi} \frac{\mathrm{d}\xi'}{(\xi-\xi')^{1/3}} \frac{\mathrm{d}}{\mathrm{d}\xi'} e^{-(\xi')^2/2}, \tag{2.92}$$

$\xi = \zeta/\sigma_\zeta$, and $\chi = L_{\mathrm{sl}}/\sigma_\zeta$. This energy exchange causes particles to gain or lose energy to the light wave. Following [38, 41] it can be seen, that particles in the head of the bunch tend to gain energy and particles in the tail of the bunch tend to lose energy due to CSR. Additionally, the projected emittance as well as the slice emittance can be increased by CSR as it is outlined in [38].

To reduce CSR small bending radii in bunch compressors should be avoided. As a consequence, the M_{56} of a bunch compressor is limited. To achieve strong compression without introducing an energy chirp h which causes the energy of the beam to exceed the bandwidth for the FEL process, c.f. Eq. (3.7), several cascaded bunch compressor stages should be used.

3 Free-Electron Lasers

In this section, the theory of Free-Electron Lasers is briefly summarized with a strong focus on the production and the properties of ultra-short FEL pulses. For further reading on FEL theory we refer to [32, 43, 44, 45]. Additionally, the layout of two FEL facilities, the Free-Electron Laser in Hamburg (FLASH) and the Linac Coherent Light Source (LCLS), are described in more detail in Sections 3.3 and 3.4, respectively.

3.1 FEL Principle

Free-Electron Lasers were invented by John Madey in the 1970s [1] and demonstrated experimentally for the first time by his group at Stanford University [46].

One possibility to create radiation from moving particles is sending them through an "undulator". This is a magnetic chicane with a sinusoidally varying magnetic field. For a planar undulator with a horizontal gap the vertical magnetic field along the z direction can be expressed as

$$B_y = B_0 \sin(k_u z), \tag{3.1}$$

where B_0 is the magnetic pole field, $k_u = 2\pi/\lambda_u$, and λ_u is the undulator period. Relativistic electrons passing through such an undulator, c.f. Fig. 3.1, will wiggle in the horizontal direction and spontaneously emit radiation at the resonant wavelength [21, 45]

$$\lambda_r = \frac{\lambda_u}{2\gamma^2}\left(1 + \frac{K^2}{2} + \gamma^2\theta^2\right), \tag{3.2}$$

where γ is the Lorentz factor,

$$K = \frac{eB_0}{m_e c k_u} \tag{3.3}$$

is the dimensionless undulator strength parameter, and θ is the observation angle to the z axis.

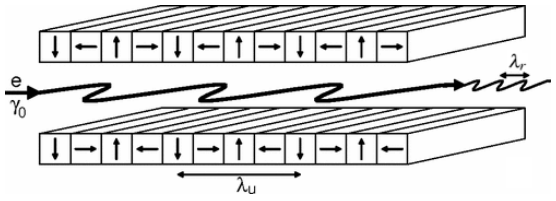

Figure 3.1: An electron passing through a planar undulator emits undulator radiation. Image from [45].

The radiation emitted in forward direction copropagates with the electrons and may exchange energy with the electrons. In an undulator, the light wave overtakes the electrons in one undulator period by one resonant wavelength in forward direction

$$\lambda_l = \lambda_r(\theta = 0) = \frac{\lambda_u}{2\gamma^2}\left(1 + \frac{K^2}{2}\right). \tag{3.4}$$

Depending on the relative phase between the electron bunch and the light wave, the electrons lose energy to the light wave or gain energy from the light wave. This energy modulation at a periodicity of λ_l within the bunch leads to a density modulation of the electron bunch, as electrons with a higher energy travel on a shorter path than electrons with a lower energy. This is the so-called "microbunching" process which can lead to a coherent emission of radiation and finally result in the light wave gaining energy from the electron bunch. [45]

In a high-gain FEL, i.e. a bright electron beam traveling through a long undulator, an exponential growth of the radiation power along large parts of the undulator can be observed. This process is illustrated in Fig. 3.2. At the beginning of the undulator, no microbunching can be observed. To start the microbunching process an initial electromagnetic wave is needed. This can either be an external radiation field in a so-called seeded FEL or the spontaneous undulator radiation interacting with the resonant Fourier component of the electron shot noise in a so-called SASE FEL. After passing a couple of undulator periods the microbunching in the electron beam evolves and the electrons start to radiate coherently leading to an exponential growth of the radiation power. Therefore, this is often called the exponential regime. At some point, the exponential gain stops as the electrons lost so much energy to the light wave, the resonant condition in Eq. (3.4) is no longer fulfilled due to γ being significantly lower than initially. Additionally, the microbunches are fully developed. Further interaction with the light wave causes a withdrawal of energy from the light wave. The radiation power reaches a saturation level and we speak of the saturation regime.

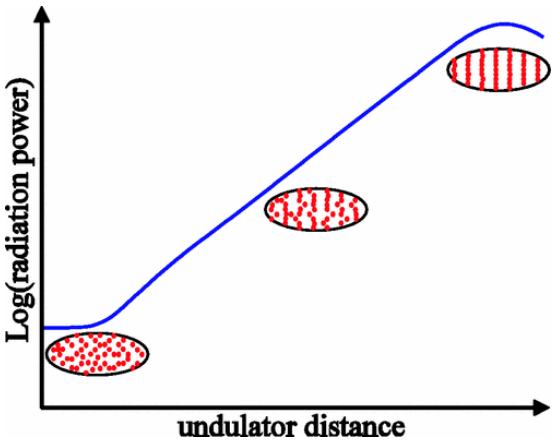

Figure 3.2: Radiation power growth and the evolution of the microbunching process along the undulator in the 1D theory. Image from [45].

A fundamental parameter for the high-gain FEL is the dimensionless Pierce or FEL parameter ρ_{FEL} [47]

$$\rho_{\mathrm{FEL}} = \left[\frac{K^2\,[JJ]^2}{32}\frac{k_p^2}{k_u^2}\right]^{\frac{1}{3}} = \left[\frac{1}{16}\frac{I_e}{I_A}\frac{K^2\,[JJ]^2}{\gamma^3\sigma_x^2 k_u^2}\right]^{\frac{1}{3}}, \tag{3.5}$$

where $[JJ] = [J_0(\xi) - J_1(\xi)]$ with $\xi = K^2/\left(4+2K^2\right)$ for a planar undulator, $k_p = \sqrt{2I_e/\left(\gamma^3 I_A \sigma_x^2\right)}$ is the longitudinal plasma oscillation wave number, I_e is the peak current of the electron beam, $I_A = ec/r_e \approx 17\,\mathrm{kA}$ is the Alfvén current, $r_e \approx 2.8\times10^{-15}\,\mathrm{m}$ is the

classical electron radius, and σ_x is the rms horizontal beam size of the electron beam.

In the 1D FEL theory, the distance required to increase the radiation power by a factor of e in the exponential regime is described by the power gain length

$$L_{G0} = \frac{\lambda_u}{4\pi\sqrt{3}\rho_{\mathrm{FEL}}}. \tag{3.6}$$

In order to limit the increase of the 1D power gain length L_{G0} to less than 25 %, the energy spread of the electron beam σ_δ has to fulfill [32]

$$\frac{\sigma_E}{E} = \sigma_\delta < \frac{\rho_{\mathrm{FEL}}}{2}. \tag{3.7}$$

The actual gain length L_G differs from the 1D gain length L_{G0}, e.g. due to the beam emittance and the energy spread of the beam. A degradation factor η was calculated in [48] to account for 3D effects. The actual gain length is then given by

$$L_G = L_{G0}\,(1+\eta)\,. \tag{3.8}$$

3.2 Characteristics of SASE FEL Radiation

In this section, the characteristics of radiation created by a high-gain SASE FEL are briefly presented, summarizing the findings of [43, 45, 49, 50].

Several of the main properties of SASE radiation are characterized by the FEL parameter ρ_{FEL}. The relative FEL bandwidth at saturation according to the 1D theory is close to ρ_{FEL}, and the saturation power of the radiation is about ρ_{FEL} times the electron beam power [45, 47].

The transverse coherence of the radiation of a SASE FEL in the start-up regime is very poor due to the non-negligible beam emittance which excites many transverse modes [45]. During the amplification process in the exponential regime, the degree of transverse coherence in the photon pulse grows, due to the self-focusing of the electromagnetic wave by the electron beam, which is referred to as optical guiding [45, 51], until it reaches its maximum close to the saturation point [49]. SASE radiation can achieve almost full transverse coherence, even if the beam emittance ε_u is larger than the diffraction-limited radiation emittance $\varepsilon_{r0} = \lambda_l/(4\pi)$, also due to optical guiding [45]. In the deep saturation regime the transverse coherence of the radiation is again poor. There is a correlation between the increase of the radiation power and the degradation of the transverse coherence [49].

As the SASE process is initiated by shot noise the temporal property of a SASE FEL follows that of chaotic light [52]. An important parameter for the determination of the temporal or longitudinal coherence is the cooperation length [52]

$$L_c = \frac{\lambda_l}{4\pi\sqrt{3}\rho_{\mathrm{FEL}}} = \frac{\lambda_l}{\lambda_u} L_{G0}. \tag{3.9}$$

This is the length over which the electrons and the light wave interact with each other due to

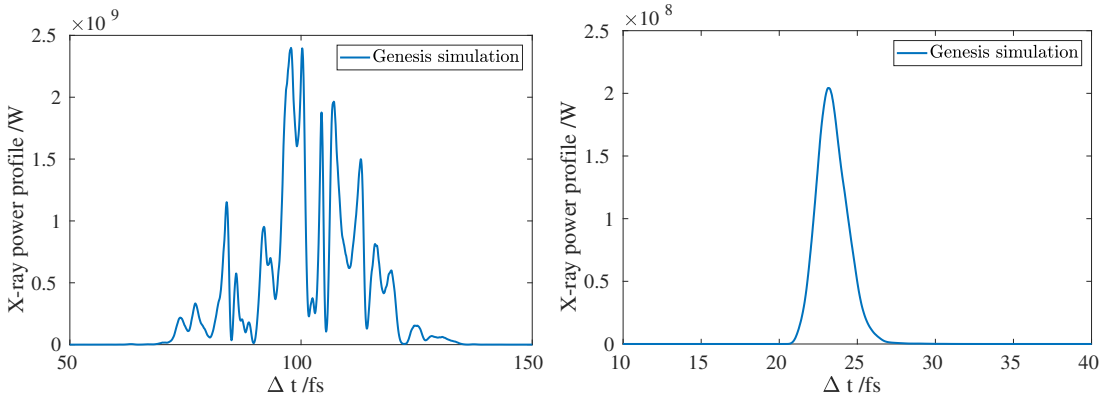

(a) Long SASE pulse.

(b) Single-spike radiation.

Figure 3.3: Temporal X-ray profile of a long SASE pulse and of single-spike radiation.

slippage in one gain length and characterizes the first order longitudinal coherence [50]. As usually the bunch length is much larger than the cooperation length, the radiation pulse consists of many spikes with a maximum duration of about $2\pi L_c/c$ [52]. An example of such a longer SASE pulse is shown in Fig. 3.3(a).

The probability distribution of the radiation energy W follows a gamma-distribution [53, 54]

$$p\left(\frac{W}{\langle W\rangle}\right) = \frac{M^M}{\Gamma(M)}\left(\frac{W}{\langle W\rangle}\right)^{M-1}\exp\left(-M\frac{W}{\langle W\rangle}\right), \tag{3.10}$$

where $M = \langle W\rangle^2/\sigma_W^2$ is the number of modes in the radiation pulse, $\Gamma(M)$ is the gamma function, and $\sigma_W^2 = \left\langle (W-\langle W\rangle)^2\right\rangle$.

3.2.1 Single-Spike Radiation

As discussed before, mostly the electron bunch length is much longer than the cooperation length and many independent radiation modes arise within the radiation pulse. Nonetheless, for some applications a much higher longitudinal coherence is desired up to the extreme case of fully coherent radiation.

Such a high degree of longitudinal coherence can for example be achieved by seeding the FEL pulse, as it is described e.g. in [55, 56].

Additionally, some applications require extremely short photon pulses. Also this can be achieved by seeding [55, 56] or spoiling the emittance in most parts of the bunch [2]. However, this is not efficient, as only a small fraction of the electron bunch is used to produce radiation [57]. One possibility to achieve both requirements simultaneously and utilize the whole beam to produce radiation is to only have one radiation mode being radiated by the electron bunch. An example for single-spike radiation is shown in Fig. 3.3(b). This can be achieved by significantly decreasing the bunch length, so that it satisfies [52, 57]

$$\sigma_\zeta \lesssim 2L_c = \frac{\lambda_l}{2\pi\sqrt{3}\rho_{\mathrm{FEL}}}. \tag{3.11}$$

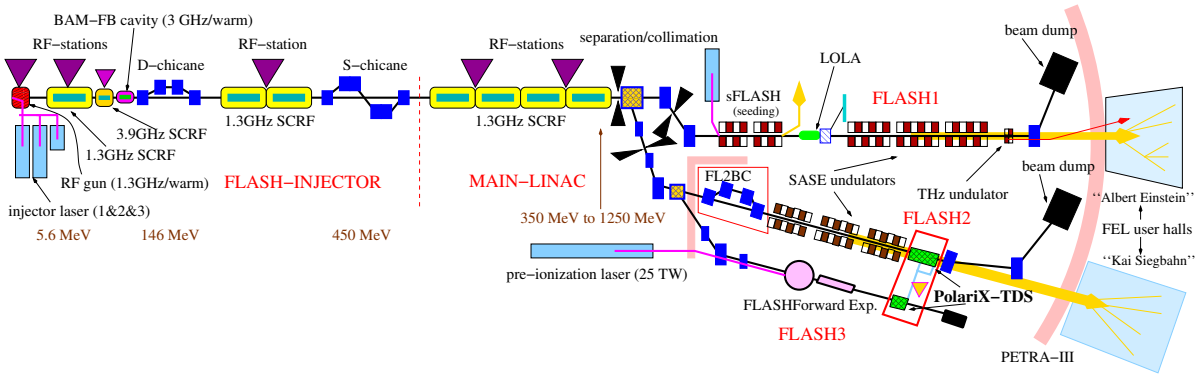

Figure 3.4: Overview of the FLASH facility (not to scale). Courtesy of M. Vogt.

If the electron bunch is longer than given by these conditions, multiple optical modes arise in the bunch, thus resulting in a not-fully coherent radiation pulse, which is also longer than one single-spike. If the electron bunch is much shorter than given by the condition in Eq. (3.11), the radiation wave may slip out of the electron bunch before the microbunching process is saturated. Additional radiation modes can form, resulting again in longer, not-fully coherent radiation. Therefore, ideally the electron bunch length should be in the order of the cooperation length. However, this single-spike radiation is only present close to the point, where saturation is reached. Before that, additional modes are visible as not all of the electrons interacted with the light wave and the fundamental mode is not built up, yet. In the saturation regime, the single spike slips ahead of the electron bunch and again, additional radiation modes begin to form along the electron bunch. [28]

3.3 FLASH

The Free-Electron Laser in Hamburg (FLASH) is an FEL user facility delivering soft X-ray radiation since 2005 [58, 59]. In 2007, wavelengths in the water window were achieved, enabling the possibility to perform *in vitro* (and potentially *in vivo*) experiments on biological samples [60]. In 2015, a second beam line, called FLASH2, was commissioned enabling to supply two users with radiation at the same time at different wavelengths, beam patterns, and FEL pulse properties [61, 62, 63, 64]. The newest upgrade to the FLASH facility is the plasma-wakefield experiment FLASHForward which is currently under commissioning [65].

A schematic overview of the FLASH accelerator is shown in Fig. 3.4.

The electrons used for acceleration are extracted from a Cs_2Te cathode [66] by using one of the three independent UV[8] injector lasers [67]. The two lasers used for "regular" operation produce UV pulses with an rms pulse duration of 4.5 ps and 6.5 ps, respectively [68]. These two lasers are used to create bunches with a charge of up to 2 nC with a repetition rate of up to 1 MHz [68]. The third injector laser is the so-called "short-pulse" injector laser [69, 70], which is capable of producing UV pulses with a variable rms pulse duration of 0.8 ps to 1.6 ps.

[8] Ultra-Violet

With this laser, short bunches can be created directly at the cathode, reducing the compression factor to achieve short photon pulses significantly. The bunch charges created by the short-pulse injector laser typically range from 20 pC to 120 pC [71].

The RF gun used to accelerate the particles from the cathode is a 1.5-cell normal conducting 1.3 GHz L-band copper cavity [72]. It is pulsed at 10 Hz with an RF pulse duration of up to 800 µs. With the repetition rate of the injector laser of up to 1 MHz it is therefore possible to accelerate up to 800 electron bunches in one bunch train or 8000 bunches per second. Using this RF gun, the electrons are accelerated to energies of about 5.6 MeV.

The normal conducting RF gun is followed by the superconducting linac. It comprises seven superconducting modules each consisting of eight 1 m long 9-cell standing wave pure niobium cavities [72]. They are operated at the same frequency as the RF gun. The maximum beam energy possible is 1.25 GeV, the lowest beam energy reasonably achievable is 350 MeV. The first accelerating module called ACC1 is followed by a third-harmonic module comprising four third-harmonic cavities operated at 3.9 GHz [72]. This module is used to linearize the energy chirp to achieve efficient bunch compression in the following bunch compressors.

The two bunch compressors are installed downstream of the third-harmonic module and the third accelerating module, respectively, c.f. Fig. 3.4. The first bunch compressor is a C-chicane with an M_{56} of 180 mm operating at a nominal beam energy of 146 MeV. The second bunch compressor is an S-chicane with an M_{56} of nominal 43 mm but typically set to 77 mm operating at a nominal beam energy of 450 MeV [73]. In the context of the FLASH midterm refurbishment and the FLASH2020+ upgrade plans, a third bunch compressor will be installed downstream of the FLASH2 extraction arc (FL2BC) [7, 74]. This bunch compressor allows a bunch compression at the highest beam energy, reducing space charge effects by reducing the compression in the first two bunch compressors. Additionally, the compression takes place downstream of the FLASH2 extraction arc, thereby reducing CSR effects. This idea was developed in parallel to this thesis, therefore the FLASH layout used in Section 5 still comprises only two bunch compressors.

After the final acceleration the electron bunches are transported to the undulators where the radiation for the users is generated. Until 2014 only one undulator beam line was available and therefore only one user experiment at a time could be performed. As FLASH is capable of delivering up to 8000 electron bunches per second due to its superconducting linac, a second beam line was built which uses a part of these electron bunches to supply a second undulator beam line to enable the simultaneous operation of two experiments [61, 75]. Downstream of the main linac the beam line is split. A part of the bunch train is then sent to the initial undulator beam line, nowadays called FLASH1. The other part is extracted using a kicker and a Lambertson-septum [41, 76] and is sent to the newly built FLASH2 undulator beam line.

The FLASH1 undulator beam line consists of six fixed-gap undulators with a length of 4.5 m each [72]. The maximum magnetic pole field is 0.47 T, the undulator period is 27.3 mm, and the undulator parameter is 1.27 [72]. As FLASH1 is equipped with fixed-gap undulators, the only possibility to tune the radiation wavelength is by changing the beam energy. With an energy

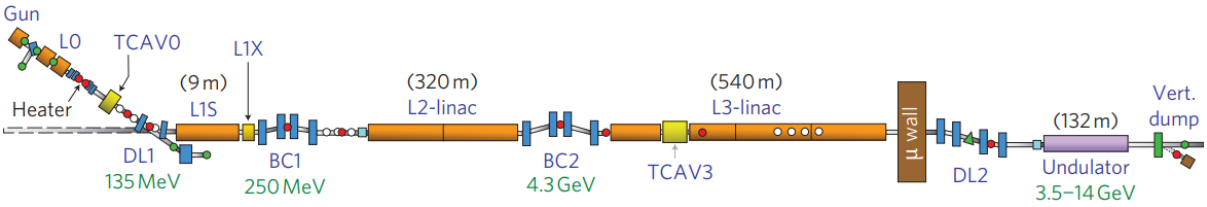

Figure 3.5: Overview of the LCLS facility (not to scale). Reprinted by permission from [82].

range of 350 MeV to 1.25 GeV the corresponding wavelength range is 52 nm to 4.1 nm [72]. In contrary, FLASH2 is equipped with twelve variable-gap undulators with a length of 2.5 m, each [77, 78]. The maximum magnetic pole field is 0.92 T, the undulator period is 31.4 mm, and the undulator parameter can be adjusted in the range from 1.0 to 2.7 by opening or closing the undulator gap. With these variable gap undulators, FLASH2 covers wavelengths in the range from 4 nm to 90 nm [61]. This enables the set-up of different wavelengths simultaneously at both undulator beam lines. If FLASH runs at a beam energy of 700 MeV, the corresponding wavelength at FLASH1 is 13.5 nm, which is quite popular among users [78]. At the same time, the wavelength that can be covered at FLASH2 spans from 10 nm to 40 nm [78], thus enabling a variety of additional experiments. Additionally, a third undulator line is integrated at FLASH1. Between the SASE undulators described above and the FLASH2 extraction additional undulators are integrated for a seeding experiment called sFLASH [55, 79]. Lasing at all three beam lines was achieved simultaneously [80].

Various diagnostics are integrated in the FLASH facility, for example to measure the bunch charge or the FEL pulse energy. An overview of the available diagnostics to characterize ultrashort photon pulses at FLASH1 is given in [81].

3.4 LCLS

The Linac Coherent Light Source (LCLS) is an X-ray free electron laser for soft and hard X-rays [82]. It was the first hard X-ray FEL in operation and delivers radiation to users since 2009 [82]. The electron accelerator driving the LCLS is based on the last kilometer of the Stanford two-mile accelerator initially operated to drive high energy physics experiments [83]. The initial linac was capable of delivering electrons with energies of up to 50 GeV by using an S-band copper linac at 2.856 GHz [82].

A schematic overview of the LCLS is shown in Fig. 3.5.

To create the electrons for the LCLS, a new injector was built [84]. It is driven by a UV injector laser [85] that extracts electrons from a copper cathode. The FWHM pulse duration of the laser can be varied in the range of 3 ps to 20 ps with a repetition rate of up to 120 Hz [84]. The electrons are accelerated using a 1.6-cell normal conducting 2.856 GHz S-band RF gun, capable of reaching field strengths of up to 140 MV/m [86]. The design energy of the electrons when leaving the gun is about 6 MeV [84], the maximum repetition rate is 120 Hz.

The RF gun is immediately followed by a modified version of two S-band linac sections

(L0) formerly used in the old two-mile accelerator [84]. Using these cavities, the electrons reach energies of 135 MeV.

Directly downstream of this first linac section, a laser heater follows [87, 88] introducing a controlled amount of energy spread ($\sim$ 20 keV rms). This is done to "Landau damp" possible micro-bunching instabilities that might disrupt the high-brightness beam [82, 88]. The laser heater successfully showed to overcome this instability and improve the FEL performance [89].

The beam is then injected on the axis of the main linac, where it is accelerated using three S-band accelerating structures (L1S), directly followed by a X-band fourth-harmonic module (11.424 GHz) to linearize the longitudinal phase space for the following bunch compression [84]. Two more accelerating sections follow. The first one (L2-linac) is situated between the first and the second bunch compressor, the second one (L3-linac) is placed downstream of the second bunch compressor. Using all of these accelerating modules the maximum achievable beam energy is 14 GeV [82].

The bunches are compressed in two bunch compressors. The first bunch compression (BC1) takes place at an energy of 250 MeV with $M_{56} = 39$ mm [90]. The second bunch compression (BC2) is performed at an energy of 4.3 GeV with an M_{56} of 24.7 mm [91]. Both bunch compressors comprise four dipole magnets arranged in a C-shape and are designed to minimize CSR effects [40, 92]. Using both bunch compressors, compression factors of about 100 can be achieved, yielding peak currents of up to 3.5 kA [82].

After the final acceleration, the electron bunch is transported to the undulators. The LCLS undulator section comprises 33 3.4 m-long planar undulator segments with a undulator period of 30 mm [82, 93]. The undulator magnet poles are canted [94] to allow for tapering of the undulators to compensate the energy loss of the electrons. The effective K-value varies from 3.500 to 3.485 [95]. The final electron beam energy at the undulator is in the range of 3.5 GeV to 14 GeV, resulting in photon wavelengths of 22 Å to 1.5 Å, respectively [82].

Downstream of the undulators, LCLS is equipped with an X-band TDS called XTCAV[9] operating at a frequency of 11.424 GHz to enable longitudinal phase space measurements in the following dispersive section [96]. The principle of a TDS and possible applications are discussed in detail in Section 4. The installation of such a device downstream of the FEL undulators enables to reconstruct the temporal profile of photon pulses [11].

[9] X-band Transverse Deflecting Cavity

4 Transverse Deflecting Structures

Transverse Deflecting Structures (TDS) are a widely used tool in particle accelerators since the 1960s. Based on the findings in [97], TDSs were initially used for high energy physics to identify and separate high energy particles [98, 99].

In 2000, the first ideas to use a TDS as a tool for bunch length and phase space diagnostics were brought forward [6]. Due to the high achievable resolutions of a TDS, this application proved especially useful to measure short electron bunches at FELs and is used at many facilities [100, 101, 102, 103].

In this section, we will show the basics of the TDS principle, derive the transfer matrix of such a device, and will show the possible applications to longitudinal diagnostics.

4.1 TDS Principle

Here, we will describe the working principle of a TDS closely following the derivations given in [6, 99, 102]. In the following, the transverse plane in which the TDS is deflecting is denoted as u, the plane perpendicular to the streaking direction is denoted as v, as a TDS can have an arbitrary streaking direction. In particular, the streak of a PolariX TDS, c.f. Section 6.1.1, is not limited to the horizontal or vertical plane, but can be set to any transverse direction.

The electric and magnetic field inside a TDS excited in the $\mathrm{TM}_{1,1}$ mode are given in [6, 99]. The Lorentz force experienced by a particle of charge e when passing through such a device in cartesian coordinates (u, v, ζ) is given by [102]

$$\begin{aligned} F_u &= e\mathscr{E}_0 \sin(\Phi_{\mathrm{RF}} + k_{\mathrm{RF}}\zeta), \\ F_v &= 0, \\ F_z &= e\mathscr{E}_0 \cos(\Phi_{\mathrm{RF}} + k_{\mathrm{RF}}\zeta) k_{\mathrm{RF}} u, \end{aligned} \tag{4.1}$$

where Φ_{RF} is the RF phase at the bunch center ($\zeta = 0$) relative to the zero-crossing, $\mathscr{E}_0$ is the amplitude of the traveling electromagnetic wave $\mathscr{E} = \mathscr{E}_0 e^{i(k_{\mathrm{RF}}\zeta - \omega_{\mathrm{RF}} t)}$, and $k_{\mathrm{RF}} = \omega_{\mathrm{RF}}/c$ are the wave number and the frequency of the RF, respectively. The slope u' in the deflecting plane after passing through a TDS will now be calculated under the approximation that the total momentum P_0 remains constant, there is no phase slippage of the RF, and in the paraxial approximation ($u' = \mathrm{d}u/\mathrm{d}s = \approx p_u/P_0$). As $\zeta \ll \lambda/2\pi$ [6], we approximate the sine and cosine of the RF phase by a Taylor series around $k_{\mathrm{RF}}\zeta = 0$

$$\begin{aligned} F_u &\approx e\mathscr{E}_0 \left[k_{\mathrm{RF}}\zeta \cos(\Phi_{\mathrm{RF}}) + \sin(\Phi_{\mathrm{RF}})\right], \\ F_v &= 0, \\ F_z &\approx e\mathscr{E}_0 \left[\cos(\Phi_{\mathrm{RF}}) - k_{\mathrm{RF}}\zeta \sin(\Phi_{\mathrm{RF}})\right] k_{\mathrm{RF}} u. \end{aligned} \tag{4.2}$$

After passing through the cavity for a distance of $s < L$, where L is the total length of the cavity,

the change of the slope by the TDS is added to the initial slope $u'(s_0)$ [102]

$$\begin{aligned} u'(s) &= u'(s_0) + \int_0^{P_u(s)} \frac{\mathrm{d}P_u}{P_0} = u'(s_0) + \int_0^s \frac{1}{P_0} F_u \frac{\mathrm{d}s}{c} = u'(s_0) + \frac{F_u}{P_0 c} s \\ &\approx u'(s_0) + \frac{e\mathscr{E}_0 \left(k_{\mathrm{RF}} \zeta \cos(\Phi_{\mathrm{RF}}) + \sin(\Phi_{\mathrm{RF}})\right)}{P_0 c} s. \end{aligned} \tag{4.3}$$

As a linear dependence of the deflection on the longitudinal position ζ in the bunch is beneficial, a TDS is usually operated at the zero-crossing phase, i.e. $\Phi_{\mathrm{RF}} = 0, \pi$ [102]. The slope is then

$$u'(s) = u'(s_0) \pm \frac{e\mathscr{E}_0 k_{\mathrm{RF}} \zeta}{P_0 c} s, \tag{4.4}$$

where $+$ and $-$ refer to $\Phi_{\mathrm{RF}} = 0$ and $\Phi_{\mathrm{RF}} = \pi$, respectively.

The total displacement of the particle can be calculated by means of Eq. (4.4) [102]

$$u(s) = u(s_0) + \int_0^s u'(s)\mathrm{d}s = u(s_0) + u'(s_0)s \pm \frac{e\mathscr{E}_0 k_{\mathrm{RF}} \zeta}{P_0 c} s^2. \tag{4.5}$$

As can be seen in Eqs. (4.1) and (4.2), particles with an offset in the cavity experience a longitudinal force changing their longitudinal momentum p_z. By combining Eqs. (4.2) and (4.5) we obtain for the momentum change $\Delta p_z(s)$ for a particle after traveling through the cavity for a length s [102]

$$\begin{aligned} \Delta p_z(s) &= \int_0^s F_z \frac{\mathrm{d}s}{c} = \int_0^s e\mathscr{E}_0 k_{\mathrm{RF}} \left(u(s_0) + u'(s_0)s \pm \frac{e\mathscr{E}_0 k_{\mathrm{RF}} \zeta}{P_0 c} s^2 \right) \frac{\mathrm{d}s}{c} \\ &= \frac{e\mathscr{E}_0 k_{\mathrm{RF}}}{c} \left(s u(s_0) + \frac{1}{2} s^2 u'(s_0) \pm \frac{1}{6} s^3 \zeta \frac{e\mathscr{E}_0 k_{\mathrm{RF}}}{P_0 c} \right). \end{aligned} \tag{4.6}$$

Finally, the momentum change after traveling through the whole structure of length L is given by

$$\Delta p_z = \Delta p_z(L) = \frac{e\mathscr{E}_0 k_{\mathrm{RF}}}{c} \left(L u(s_0) + \frac{1}{2} L^2 u'(s_0) \pm \frac{1}{6} L^3 \zeta \frac{e\mathscr{E}_0 k_{\mathrm{RF}}}{P_0 c} \right). \tag{4.7}$$

The transverse deflection also changes the momentum in u direction. As F_u is constant over the structure, we obtain for the momentum change in u [102]

$$\Delta p_u = \Delta p_u(L) = \frac{F_u}{c} \cdot u(L) = \frac{e\mathscr{E}_0 k_{\mathrm{RF}}}{c} \left(\zeta u(s_0) + \frac{1}{2} \zeta L u'(s_0) \pm \frac{1}{6} L^2 \zeta^2 \frac{e\mathscr{E}_0 k_{\mathrm{RF}}}{P_0 c} \right). \tag{4.8}$$

Comparing Eqs. (4.7) and (4.8) we observe, that $\Delta p_z \gg \Delta p_u$ as typically $L \gg \zeta$. Thus, the total momentum gain Δp is dominated by the gain of the longitudinal momentum $\Delta p \approx \Delta p_z$ [102]. Using

$$\mathscr{K} = \frac{eV_0 k_{\mathrm{RF}}}{P_0 c} = \frac{eV_0 \omega_{\mathrm{RF}}}{P_0 c^2} \tag{4.9}$$

with the total deflecting voltage $V_0 = \mathscr{E}_0 L$, the total momentum change of a particle is

$$\Delta\delta = \frac{\Delta p_z}{P_0} = \mathscr{K} u(s_0) + \frac{1}{2}\mathscr{K} L u'(s_0) \pm \frac{1}{6}\mathscr{K}^2 L\zeta. \tag{4.10}$$

For a particle bunch, the first term in Eq. (4.10) results in an induced rms momentum spread due to the finite beam size of the particle bunch [104, 105]

$$\sigma_{\mathrm{IES}} = \mathscr{K} \cdot \sigma_u(s_0). \tag{4.11}$$

The second term also results in an rms momentum spread due to the angular spread, but is usually neglected for the case of a short TDS [105]. The third term in Eq. (4.10) results in a linear momentum chirp along the bunch [104, 105]

$$\frac{\mathrm{d}}{\mathrm{d}\zeta}\delta = \frac{1}{6}\mathscr{K}^2 L. \tag{4.12}$$

4.2 Transformation Matrix of a TDS

Using Eqs. (4.4), (4.5) and (4.10) and the fact, that the TDS acts as a drift space in the non-deflecting plane v, the transfer matrix for a thick TDS of length L and using the approximation $\gamma \gg 1$ is given by [102, 106]

$$\mathbf{M}_{\mathrm{TDS,thick}} = \begin{pmatrix} 1 & L & 0 & 0 & \pm\frac{\mathscr{K}L}{2} & 0 \\ 0 & 1 & 0 & 0 & \pm\mathscr{K} & 0 \\ 0 & 0 & 1 & L & 0 & 0 \\ 0 & 0 & 0 & 1 & 0 & 0 \\ 0 & 0 & 0 & 0 & 1 & 0 \\ \pm\mathscr{K} & \pm\frac{\mathscr{K}L}{2} & 0 & 0 & \pm\frac{\mathscr{K}^2 L}{6} & 1 \end{pmatrix}, \tag{4.13}$$

if the phase space vector in front of the TDS at s_0 is written as $\vec{z}(s_0) = (u, u', v, v', \zeta, \delta)^T_{s_0}$. Again, the $+$ and $-$ refer to the two zero-crossing phases, c.f. Eq. (4.4). For $\gamma \ll \infty$ the M_{56} term would not vanish, which results in additional terms in the sixth column and the fifth row, c.f. Section 2.2.2. This matrix is indeed symplectic, as can be shown using the relations shown in Section 2.2.2 for

$$\mathbf{K} = \begin{pmatrix} 1 & L & 0 & 0 \\ 0 & 1 & 0 & 0 \\ 0 & 0 & 1 & L \\ 0 & 0 & 0 & 1 \end{pmatrix}, \ \mathbf{L} = \begin{pmatrix} 1 & 0 \\ \pm\frac{\mathscr{K}^2 L}{6} & 1 \end{pmatrix}, \text{ and } \vec{c} = \begin{pmatrix} \pm\frac{\mathscr{K}L}{2} \\ \pm\mathscr{K} \\ 0 \\ 0 \end{pmatrix}. \tag{4.14}$$

For $\mathbf{M}_{\mathrm{TDS,thick}}$ to be symplectic, Eq. (2.34) has to be true. This is indeed the case, as

$$\vec{\tilde{c}}^T \mathbf{K} = \begin{pmatrix} \pm\mathscr{K} & \pm\mathscr{K}L \mp \frac{\mathscr{K}L}{2} & 0 & 0 \end{pmatrix} = \begin{pmatrix} \pm\mathscr{K} & \pm\frac{\mathscr{K}L}{2} & 0 & 0 \end{pmatrix}, \tag{4.15}$$

which yields that the correct form of $\mathbf{B}^T$ is given in Eq. (4.13).

Equation (4.13) considers the finite length of the TDS and is therefore called the "thick lens form" [102]. If only the transverse motion of the particles is of interest, a thin lens approximation is made for $L \to 0$. The transfer matrix is then a drift matrix of length $L/2$, followed by the thick lens matrix for $L \to 0$ and another drift matrix of length $L/2$ [102, 106]

$$\begin{aligned}\mathbf{M}_{\text{TDS,thin}} &= \mathbf{M}_{\text{D}}\left(\frac{L}{2}\right) \cdot \mathbf{M}_{\text{TDS,thick},L\to 0} \cdot \mathbf{M}_{\text{D}}\left(\frac{L}{2}\right) \\ &= \mathbf{M}_{\text{D}}\left(\frac{L}{2}\right) \cdot \begin{pmatrix} 1 & 0 & 0 & 0 & 0 & 0 \\ 0 & 1 & 0 & 0 & \pm\mathscr{K} & 0 \\ 0 & 0 & 1 & 0 & 0 & 0 \\ 0 & 0 & 0 & 1 & 0 & 0 \\ 0 & 0 & 0 & 0 & 1 & 0 \\ \pm\mathscr{K} & 0 & 0 & 0 & 0 & 1 \end{pmatrix} \cdot \mathbf{M}_{\text{D}}\left(\frac{L}{2}\right).\end{aligned} \tag{4.16}$$

4.3 Longitudinal Diagnostics using a TDS

Knowledge about longitudinal parameters of a particle beam is crucial for the operation of particle accelerators. Especially in high-gain FELs, where the lasing process strongly depends on e.g. the peak current or the slice energy spread, knowledge of these parameters can significantly enhance the ability to optimize the lasing process.

A TDS offers the possibility to gain direct access to the longitudinal coordinate of electron bunches. As we will see in Eq. (4.18), the longitudinal coordinate of the electron bunch is mapped linearly to a transverse one when using a TDS. The measurement of the transverse coordinates in an accelerator can be easily achieved, e.g. by using scintillator screens [107] or optical transition radiation (OTR) screens [108]. For this reason, TDSs are widely used for longitudinal diagnostics. While other methods, such as the electro-optics (EO) method [109, 110] or the coherent radiation spectroscopy [111, 112], exist for the measurement of the longitudinal current profile, these methods cannot be used for the measurement of the longitudinal phase space density or the slice emittance as they are indirect methods. Given that a TDS provides a direct measurement of the longitudinal coordinate, this measurement can be combined with a variety of other measurements, yielding access to many longitudinal bunch properties including the longitudinal phase space density and the slice emittance. The longitudinal phase space density can be mapped by combining the streak of a TDS with a dipole deflecting the beam in the plane transverse to the streaking direction of the TDS. On a subsequent screen, one coordinate (u) is then related to the longitudinal position and the other (v) to the beam energy [6]. Additionally, a TDS comprises a wide dynamical range: Electron bunches with bunch lengths of picoseconds down to a few femtoseconds can be characterized using a TDS [11, 102].

In the following, we will show how the measurement of the longitudinal current profile, the longitudinal phase space and subsequently the FEL photon pulse reconstruction, and the slice emittance can be performed using a TDS.

4.3.1 Longitudinal Current Profile

In FELs a high-peak current is required for the lasing process, c.f. Eq. (3.5). To monitor the evolution of the longitudinal current profile downstream of bunch compressors, a TDS can be used. Additionally, the electron bunch length can serve as an estimate for the upper radiation pulse length [113]. We follow [102] in our derivation of the longitudinal current profile measurement.

For the measurement of the longitudinal current profile, only transverse motions are of interest, we consider the TDS to be described by the thin lens form found in Eq. (4.16) [100]. The transport of an electron beam with the 6D-phase space vector $\vec{z}(s_0) = (u, u', v, v', \zeta, \delta)^T_{s_0}$ from the center of the TDS at s_0 to a screen station at s_1 is described to first order by

$$\vec{z}(s_1) = \mathbf{M}_{s \leftarrow s_0} \cdot \mathbf{M}_{\text{TDS,thin}} \cdot \vec{z}(s_0). \tag{4.17}$$

Evaluating this expression yields for the position of a particle in the streaking plane

$$u(s_1) = u_0(s_1) + S \cdot \left(\zeta + \frac{\sin(\Phi_{\text{RF}})}{\cos(\Phi_{\text{RF}})} \cdot \frac{c}{\omega_{\text{RF}}} \right) \tag{4.18}$$

with the initial particle position $u_0(s_1)$, the Shear-parameter

$$S = \sqrt{\beta_u(s_0)\beta_u(s_1)} \cdot \sin(\Delta\Psi_u) \cdot \frac{eV_0\omega_{\text{RF}}}{P_0 c^2} \cdot \cos(\Phi_{\text{RF}}) = \sqrt{\beta_u(s_0)\beta_u(s_1)} \cdot \sin(\Delta\Psi_u) \cdot \mathscr{K} \cdot \cos(\Phi_{\text{RF}}), \tag{4.19}$$

the beta function in the streaking plane at the center of the TDS $\beta_u(s_0)$, the beta function in the streaking plane at the screen $\beta_u(s_1)$, and the phase advance in the streaking plane between the center of the TDS and the screen $\Delta\Psi_u = \Psi(s_1) - \Psi(s_0)$.

As there is usually more than one particle passing through the cavity, we are interested in the second moments of the particle distribution. In the following, we will treat electron bunches without an initial correlation in (u, ζ) and (u', ζ). Cases where this is not true can of course also be treated and are described in detail in [102, 114]. Additionally, the TDS is operated at the zero-crossing, i.e. $\Phi_{\text{RF}} = 0$.

Going from the single-particle motion in Eq. (4.18) to the squared rms beam size in the streaking plane on the screen yields

$$\sigma_u^2(s_1) = \sigma_{u_0}^2(s_1) + S^2 \sigma_\zeta^2(s_0). \tag{4.20}$$

When the intrinsic beam size $\sigma_{u_0}(s_1)$ is known, e.g. by performing a measurement with the TDS switched off, the rms bunch length $\sigma_\zeta(s_0)$ can be determined by means of Eq. (4.20).

The longitudinal resolution is usually defined as the bunch length making the two terms on the right-hand side of Eq. (4.20) equal [115]

$$R_\zeta = \frac{\sigma_{u_0}(s_1)}{S} = \frac{\sqrt{\varepsilon_u} \cdot P_0 c^2}{\sqrt{\beta_u(s_0)} \cdot \sin(\Delta\Psi_u) \cdot eV_0\omega_{\text{RF}} \cdot \cos(\Phi_{\text{RF}})}. \tag{4.21}$$

In accelerator physics, it is common to indicate the length of ultra-relativistic particle bunches not in units of meters but rather in seconds by dividing the bunch length by c

$$\sigma_t = \frac{\sigma_\zeta}{c}. \tag{4.22}$$

The corresponding equivalent for the longitudinal resolution defined in Eq. (4.21) can also be stated in seconds

$$R_t = \frac{R_\zeta}{c}. \tag{4.23}$$

It is then sometimes also referred to as "temporal" resolution of a TDS measurement.

For the measurement of the longitudinal current profile using a TDS, the transverse coordinate u has to be translated to the arrival time t. This is achieved by applying Eq. (4.18) for the difference of the transverse position $\Delta u(s_1) = u(s_1) - u_0$ and $\Delta t = t - t_0$

$$\Delta t = \frac{\Delta u(s_1)}{Sc}. \tag{4.24}$$

The offsets u_0 and t_0 are usually not of interest and can be defined arbitrarily. Common definitions are the center of the screen, the mean of the bunch distribution or the beginning of the bunch distribution.

To be able to use Eq. (4.24) the Shear parameter S has to be known. If the optical functions at the TDS center and the screen are known, this can be done easily by using Eq. (4.19). As in reality this is mostly not the case, another way to calculate S is using a phase-scan of the TDS. The RF phase Φ_{RF} is varied by small amounts around the zero-crossing and the centroid position of the beam $\langle u(s_1)\rangle$ at the screen is recorded. S can then be obtained by a linear fit of Eq. (4.18) for small deviations of Φ_{RF}

$$\Delta\langle u(s_1)\rangle = S\frac{c}{\omega_{\mathrm{RF}}}\Delta\Phi_{\mathrm{RF}}. \tag{4.25}$$

4.3.2 Longitudinal Phase Space Density

As a TDS is only streaking the beam in one plane, the other remains unaffected. It is therefore possible to combine the streak of the TDS in the u plane with an energy spectrometer, such as a dipole, bending the beam in the v plane. With such an arrangement, additionally to the current profile, the energy profile can be extracted and finally, the longitudinal phase space density can be measured [6].

The position of a particle at a screen at s_1 in the deflecting plane v of the dipole at s_0 is given by, c.f. Eq. (2.58), [22, 104, 116]

$$v(s_1) = v_0(s_1) + \eta_v(s_1)\delta. \tag{4.26}$$

It is worth noting, that by using a TDS the momentum deviation of a particle changes according to Eq. (4.10), which is of course added to the initial momentum spread δ_0. In the above equation,

the total momentum deviation responsible for the change of the particle position when using a TDS is $\delta = \delta_0 + \Delta\delta$.

Again, going from the single particle motion described in Eq. (4.26) to the rms beam size as in the previous section, we obtain

$$\sigma_v^2(s_1) = \sigma_{v_0}^2(s_1) + \eta_v^2(s_1)\sigma_\delta^2. \tag{4.27}$$

If the intrinsic beam size $\sigma_{v_0}^2(s_1)$ is known, the momentum spread σ_δ of the bunch including the induced momentum spread by the TDS, c.f. Eq. (4.11), can be determined. As we have seen before, the TDS induces an momentum spread to the bunch, therefore the measured momentum spread is $\sigma_\delta^2 = \sigma_{\delta_0}^2 + \mathscr{K}^2\sigma_u^2$. The induced momentum spread is not homogeneous along the bunch, but depends on the slice beam size. However, the determination of the exact momentum spread σ_δ would require a measurement with the dipole switched off or setting the dispersion at the screen to zero. The first option requires a duplicate of the dispersive beam line continuing straight through the dipole, which is hardly feasible at any facility. The second option requires very precise matching of the optical functions which in real machines is very difficult to achieve and is therefore seldom used.

The resolution of the measurement is defined analogously to the previous section as the momentum spread σ_δ making both terms on the right-hand side in Eq. (4.27) equal

$$R_\delta = \frac{\sigma_v(s_1)}{\eta_v(s_1)} = \frac{\sqrt{\beta_v(s_1)\varepsilon_v}}{\eta_v(s_1)}. \tag{4.28}$$

For the measurement of the longitudinal phase space density, not only the transverse coordinate u has to be translated to the arrival time t by applying Eq. (4.24), but also the transverse coordinate v has to be translated to the momentum deviation δ. This is achieved by applying Eq. (4.26) for the momentum deviation δ and the difference of the transverse position $\Delta v(s_1) = v(s_1) - v_0$

$$\delta = \frac{\Delta v(s_1)}{\eta_v(s_1)}. \tag{4.29}$$

The offset v_0 is usually chosen in a way that a particle with the momentum P_0 arrives at the screen at this position. If the dispersion at the screen is known, Eq. (4.29) can be applied with ease. As in reality, this is mostly not the case, a momentum scan can be used to determine the dispersion on the screen. The design deflection angle of a dipole is defined by [22, 102]

$$\alpha_0 = \frac{L}{\rho_0} = \frac{eB_0L}{P_0} \propto \frac{eI_0L}{P_0}, \tag{4.30}$$

where L is the length of the dipole magnet, B_0 the magnetic field and I_0 the current corresponding to the magnetic field B_0. For a particle with a slightly higher momentum $P = P_0(1+\varepsilon_\delta)$, $\varepsilon_\delta \ll 1$ the deflection angle is

$$\alpha = \alpha_0 - \Delta\alpha. \tag{4.31}$$

The change of the deflection angle is

$$\Delta\alpha = \alpha_0 - \alpha = \alpha_0 - \alpha_0 \frac{P_0}{P_0(1+\varepsilon_\delta)} = \alpha_0 \frac{\varepsilon_\delta}{1+\varepsilon_\delta} \approx \alpha_0 \varepsilon_\delta. \tag{4.32}$$

Therefore, if we scan the mean momentum of the particle beam in steps of ε_δ and record the corresponding centroid position of the beam in the v plane $\langle v(s_1)\rangle$, we can obtain the dispersion via Eq. (4.26) [102]

$$\Delta\langle v(s_1)\rangle = \eta_v(s_1)\Delta\varepsilon_\delta. \tag{4.33}$$

As in a real machine changing the momentum with the required precision for the calibration is usually not feasible and practicable, a different approach is used. The same variation of the deflection angle can be achieved by changing the current of the dipole from I_0 to $I_0(1+\varepsilon_I)$, $\varepsilon_I \ll 1$. The change of deflection angle is then

$$\Delta\alpha = \alpha - \alpha_0 = \alpha_0 \frac{I_0(1+\varepsilon_I)}{I_0} - \alpha_0 = \alpha_0 \varepsilon_I. \tag{4.34}$$

Therefore, the same displacement as with a momentum scan can be achieved and the centroid position varies with the current change as

$$\Delta\langle v(s_1)\rangle = \eta_v(s_1)\Delta\varepsilon_I. \tag{4.35}$$

Performing this scan and fitting the applying a linear fit yields the dispersion $\eta_v(s_1)$ at the screen.

4.3.3 Photon Pulse Reconstruction

If a TDS is installed downstream of the FEL undulators, the temporal profile of photon pulses can be reconstructed [11, 96, 117, 118]. To accomplish this, the longitudinal phase space density of an electron bunch producing light (lasing on) has to be compared to one where the lasing process is suppressed (lasing off). This can for example be achieved by opening the undulators (in the case of variable gap undulators), moving the undulators out or offsetting the orbit in the undulator. Here, it is assumed that the stability of the machine suffices to guarantee that the bunches with lasing on and off are identical at the undulator entrance.

The longitudinal phase space densities are then divided into slices along the time dimension to get the time-dependent beam parameters such as the mean energy $E_{\mathrm{on,off}}(t_i)$, the energy spread $\sigma_{E_{\mathrm{on,off}}}(t_i)$, and the current $I(t_i)$ in each time slice t_i [11, 117]. The subscript denotes, whether the quantity was taken from a measurement with lasing on or lasing off. The influence of the FEL process on the bunch current is negligible, therefore, this quantity does not have a subscript. For each time slice, the energy loss and the energy spread increase comparing the lasing-on and lasing-off measurement is then calculated

$$\Delta E(t_i) = E_{\mathrm{on}}(t_i) - E_{\mathrm{off}}(t_i), \tag{4.36}$$

$$\sigma_E(t_i) = \sqrt{\sigma^2_{E_{\text{on}}}(t_i) - \sigma^2_{E_{\text{off}}}(t_i)}. \tag{4.37}$$

From these quantities the radiation power in each slice can be determined. When using the energy loss method, the radiation power in each slice is [11, 96, 117]

$$P(t_i) = \Delta E(t_i) \cdot \frac{I(t_i)}{e}. \tag{4.38}$$

When using the energy spread method, the radiation power in each slice is [11, 117, 119]

$$P(t_i) \propto \sigma_E(t_i)^2 \cdot I(t_i)^{\frac{2}{3}}. \tag{4.39}$$

To determine the total radiation power an additional, independent measurement of the total pulse energy is necessary. This can for example be accomplished using a calibrated gas detector [120, 121, 122].

The reconstruction of the temporal radiation power profile using these to methods generally only works in the linear FEL regime and at the beginning of the saturation regime. In deep saturation, the radiation created in the exponential regime slips ahead of the position where the actual energy transfer from the electron bunch to the light wave happened. Therefore, the position of the energy loss and the energy spread increase is not related to the position where it is actually stored in the light wave anymore. Additionally, the temporal resolution of the TDS blurs the reconstruction of the temporal power profile. In good approximation, this process can be modeled by a convolution of the actual power profile $P(t)$ with a Gaussian $G(t)$ of fixed standard deviation R_t

$$(P * G)(t) = \tilde{P}(t), \tag{4.40}$$

yielding the reconstructed blurred power profile $\tilde{P}(t)$, see Section 7.

4.3.4 Slice Emittance Reconstruction

As described in Section 2.5, the emittance is an important quantity in particle accelerators. Especially in FELs, low emittances can significantly enhance the lasing process by lowering the transverse beam size and thereby enlarging the FEL parameter, c.f. Eq. (3.5). Even more important for the FEL process than the projected emittance is the slice emittance, as not all of the bunch contributes to the lasing process and the slice emittance in the core part of the bunch can be significantly smaller than the projected emittance. The combination of an emittance measurement with a TDS can be used to measure the slice emittance. We will describe the emittance measurement in the following, which is used for both, the measurement of the projected emittance and the slice emittance.

Again in this section, u is the transverse plane in which the TDS is streaking, v is the plane perpendicular to u. If no TDS is used, the equations are valid for both planes. The indices $\{q, p\}$ are $\{1,2\}$ for the horizontal plane and $\{3,4\}$ for the vertical plane. Applying the matrix for a

decoupled beam line defined in Eq. (2.54) to Eq. (2.73) yields for the transverse beam size [123]

$$\begin{aligned}\left\langle v^2(s_1)\right\rangle = \sigma_v^2(s_1) =& M_{qq}^2\left\langle v^2(s_0)\right\rangle + 2M_{qq}M_{qp}\left\langle v(s_0)v'(s_0)\right\rangle + M_{qp}^2\left\langle v'^2(s_0)\right\rangle \\ &+ 2M_{qq}M_{q6}\left\langle v(s_0)\delta(s_0)\right\rangle + 2M_{qp}M_{q6}\left\langle v'(s_0)\delta(s_0)\right\rangle + M_{q6}^2\left\langle \delta^2(s_0)\right\rangle,\end{aligned} \tag{4.41}$$

where M_{qp} is the q,p element of the transfer matrix $\mathbf{M}_{s_1\leftarrow s_0}$ from the reconstruction point at s_0 to the screen at s_1. If one uses six different, known, and independent transfer matrices $\mathbf{M}^i_{s_1\leftarrow s_0}$ and measures the corresponding beam sizes using e.g. OTR screens [108, 124] or wire scanners [125], all unknown quantities in Eq. (4.41) can be determined.

When the M_{q6} element vanishes, Eq. (4.41) simplifies to

$$\left\langle v^2(s_1)\right\rangle = \sigma_v^2(s_1) = M_{qq}^2\left\langle v^2(s_0)\right\rangle + 2M_{qq}M_{qp}\left\langle v(s_0)v'(s_0)\right\rangle + M_{qp}\left\langle v'^2(s_0)\right\rangle. \tag{4.42}$$

This can for example be accomplished by performing the measurement in a dispersion free beam line or letting the dispersion at the measurement screen vanish. With this equation, only three different measurements are needed to determine $\left\langle v^2(s_0)\right\rangle$, $\langle v(s_0)v'(s_0)\rangle$, and $\left\langle v'^2(s_0)\right\rangle$. From these quantities, the emittance and also the Twiss functions can be calculated via [126, 127]

$$\varepsilon_v = \sqrt{\langle v^2(s_0)\rangle\langle v'^2(s_0)\rangle - \langle v(s_0)v'(s_0)\rangle}, \tag{4.43}$$

$$\beta_v(s_0) = \frac{\left\langle v^2(s_0)\right\rangle}{\varepsilon_v}, \tag{4.44}$$

$$\alpha_v(s_0) = -\frac{\langle v(s_0)v'(s_0)\rangle}{\varepsilon_v}. \tag{4.45}$$

Additionally, the mismatch between the design and the measured beam ellipse can be expressed by the mismatch parameter or beta matching parameter B_{mag} and the mismatch amplitude λ_{mag} [128]

$$B_{\mathrm{mag}} = \frac{1}{2}\left(\beta_v(s_0)\gamma_{v_0}(s_0) - 2\alpha_v(s_0)\alpha_{v_o}(s_0) + \beta_{v_0}(s_0)\gamma_v(s_0)\right), \tag{4.46}$$

$$\lambda_{\mathrm{mag}} = B_{\mathrm{mag}} + \sqrt{B_{\mathrm{mag}}^2 - 1}, \tag{4.47}$$

where $\beta_v(s_0)$, $\alpha_v(s_0)$, and $\gamma_v(s_0)$ are the measured Twiss parameters, and $\beta_{v_0}(s_0)$, $\alpha_{v_0}(s_0)$, and $\gamma_{v_0}(s_0)$ are the design parameters.

Although three measurements with different, known, and independent $\mathbf{M}^i_{s_1\leftarrow s_0}$ suffice to determine the three unknown second moments in Eq. (4.42), in reality they are subject to errors. Therefore, more than just three measurements should be used. The different M^i can be chosen by performing the measurement at subsequent screens (multi-screen method) or varying the quadrupole strengths between the measurement point and the screen or a combination of both [126].

To determine the second moments $\left\langle v^2(s_0)\right\rangle$, $\langle v(s_0)v'(s_0)\rangle$, and $\left\langle v'^2(s_0)\right\rangle$ one has to

solve [126, 127]

$$\begin{pmatrix} \Sigma_1 \\ \vdots \\ \Sigma_n \end{pmatrix} = \mathbf{N} \cdot \begin{pmatrix} \left\langle v^2(s_0) \right\rangle \\ \langle v(s_0)v'(s_0) \rangle \\ \left\langle v'^2(s_0) \right\rangle \end{pmatrix}, \tag{4.48}$$

where $n \geq 3$ is the number of measurements,

$$\Sigma_i = \frac{\left\langle \left(v^i(s_1)\right)^2 \right\rangle}{\sigma_{\left\langle (v^i(s_1))^2 \right\rangle}}, \tag{4.49}$$

$i \in [1,n]$ is the measurement index, $\sigma_{\left\langle (v^i(s_1))^2 \right\rangle}$ is the error of the measured, squared beam size $\left\langle \left(v^i(s_1)\right)^2 \right\rangle$, and the i-th row of the $n \times 3$ matrix $\mathbf{N}$ is given by

$$N_i = \frac{1}{\sigma_{\left\langle (v^i(s_1))^2 \right\rangle}} \begin{pmatrix} \left(M^i_{qq}\right)^2 & 2M^i_{qq}M^i_{qp} & \left(M^i_{qp}\right)^2 \end{pmatrix}. \tag{4.50}$$

This can for example be accomplished by calculating the inverse of $\mathbf{N}$ with approaches like SVD or the Gauss-Jordan algorithm [127].

To determine the slice emittance, additionally a TDS has to be used streaking the beam in the u plane [129]. For each measurement i the beam image is then sliced into m slices along the u axis. For each of the m slices the corresponding beam size $\left\langle \left(v^i_m(s_1)\right)^2 \right\rangle$ is measured and Eq. (4.48) is solved m times (once for each slice). This yields via Eq. (4.43) the m slice emittances $\varepsilon_{v,j}$, where $j \in [1,m]$.

5 Ultra-Short Electron Bunches and Photon Pulses at FLASH2

To study the dynamics of ultra-fast processes users of FELs often require very short X-ray pulses. These are fundamental for experiments which depend strongly on a high temporal resolution, e.g. to study ultra-fast process. This can be indeed achieved by using ultra-short electron bunches for the radiation production, c.f. Section 3.2.1, however at the cost of a reduced pulse energy, as we will see in the following. The main concern of other experiments is a large number of photons per time. Although by using short electron bunches the radiation pulse length is drastically reduced, the total amount of photons in the pulse might be too low for these experiments. A third reason to use short X-ray pulses is their longitudinal coherence, c.f. Section 3.2.1, though this can also be achieved by seeded FELs.

To provide short X-ray pulses for these users a short pulse injector laser was installed at FLASH [69], c.f. Section 3.3. This short pulse injector laser is designed to generate electron bunches with a bunch length of about 1 ps rms directly at the cathode. The generation of ultra-short electron bunches and photon pulses at FLASH1 using this short-pulse injector laser has been studied extensively in [28]. However, these studies cannot be directly transferred to FLASH2 as the layout of the two beam lines differs: The extraction arc of FLASH2 has a different geometry than the FLASH1 dogleg and FLASH2 is equipped with variable gap undulators, offering the possibility to vary the undulator K parameter. In the following, we show that at FLASH2 we are also able to generate ultra-short electron bunches and photon pulses down to a few or even a single longitudinal mode.

In Section 5.1 experimental data taken at FLASH2 is presented, showing that radiation pulses containing close to only one longitudinal radiation mode can be generated.

These measurement results are further investigated in Section 5.2. Genesis 1.3 simulations using an ideal Gaussian beam as input are shown in Section 5.2.1. Start-to-end simulations from the FLASH gun to the FLASH2 undulators are shown in Section 5.2.2. To get an insight on the beam dynamics of the short pulse creation, these simulations are based on three main simulation codes:

- the tracking algorithm ASTRA [130] models transverse and longitudinal space charge forces on the bunch in straight sections including external and internal fields
- the code CSRtrack [131] includes the coherent synchrotron radiation effects on the bunch in the bunch compressors and the FLASH2 extraction arc
- the 3D time-dependent FEL code Genesis 1.3 [132] simulates the lasing process in the undulators.

Additionally, the possibility to generate single-spike radiation at FLASH2 at different wavelengths using start-to-end simulations is demonstrated in Section 5.3.

These simulation results of short pulses will be used in Section 6.3 to understand the performance and limits of the TDSs that will be installed at FLASH2.

5.1 Experimental Results for Short-Pulse Operation at FLASH2

Short electron bunches were sent through the FLASH2 undulators. The goal was to obtain short photon pulses comprising only few radiation modes. The results have already been partly published in [133].

During the measurements gain curves were recorded using a gas monitor detector (GMD) [120, 121] for SASE pulse energies above 2 µJ. With only a few undulators used, the GMD resolution was limited by the reduced SASE pulse energy. Therefore, these measurements were performed using a micro channel plate (MCP) based radiation detector [134], which was calibrated with GMD values at high pulse energies.

In addition to the gain curves, the fluctuations of the SASE radiation were measured. As discussed in Section 3.2, the probability distribution of the radiation energy follows a gamma-distribution. Using Eq. (3.10) the number of modes in the radiation pulse can be determined. The full width-half maximum (FWHM) photon pulse duration $\tau_{\mathrm{ph}}^{\mathrm{min}}$ and the rms photon pulse duration $\sigma_{t,\mathrm{ph}}^{\mathrm{min}}$ at the end of the exponential regime[10] for the number of longitudinal modes $M \gtrsim 2$ is then given by [113]

$$2\sqrt{2\ln 2}\sigma_{t,\mathrm{ph}}^{\mathrm{min}} = \tau_{\mathrm{ph}}^{\mathrm{min}} \simeq \frac{M\lambda_l}{5\rho_{\mathrm{FEL}}} \simeq \frac{M\lambda_l L_{\mathrm{sat}}}{5c\lambda_u}, \tag{5.1}$$

where L_{sat} is the saturation length. Additionally, the rms bunch length $\sigma_{t,\mathrm{lasing}}$ of the "potential lasing part" of the electron bunch can be linked to this photon pulse duration

$$\tau_{\mathrm{ph}}^{\mathrm{min}} \simeq \sigma_{t,\mathrm{lasing}}. \tag{5.2}$$

In this case, following [113], the "potential lasing part" of the bunch is referred to as the Gaussian-core region of the bunch. The actual bunch length can be larger, as e.g. parts with a high slice-emittance or high energy spread do not contribute to the lasing process. These two procedures were the only available photon pulse duration diagnostics at FLASH2 during the measurements.

The FEL parameter ρ_{FEL} and the coherence time τ_c are related to the saturation length L_{sat} by [113]

$$\rho_{\mathrm{FEL}} \approx \frac{\lambda_u}{L_{\mathrm{sat}}}, \qquad \tau_c \approx \frac{\lambda_l L_{\mathrm{sat}}}{2\sqrt{\pi}c\lambda_u}. \tag{5.3}$$

Multiple measurement shifts were conducted at FLASH2 to demonstrate the feasibility of the short-pulse operation at FLASH2 as well as the integrability of short-pulse operation at FLASH2 during regular operation at FLASH1. In each shift gain curves were recorded at different electron beam and undulator settings and the SASE radiation fluctuations were measured.

[10] See Section 3.1.

Table 1: Parameter Overview and Results of Short Pulse Measurements at FLASH2.

λ_l /nm	Q /pC	E /MeV	$\sigma_{W,\max}$	M	$\tau_{\mathrm{ph}}^{\mathrm{min}}$ /fs	τ_c /fs	Date
15	60	1150	0.70 ± 0.03	2.0 ± 0.2	13.0 ± 1.5	9.0 ± 0.6	26.08.16
40.5	88	690	$\mathbf{0.97} \pm 0.09$	$\mathbf{1.1} \pm 0.2$	14.7 ± 2.8	19.7 ± 1.5	27.08.16
20	88	690	0.57 ± 0.04	3.1 ± 0.5	34.8 ± 5.3	15.7 ± 0.7	27.08.16
30	70	760	0.67 ± 0.03	2.2 ± 0.2	24.7 ± 2.8	15.7 ± 1.1	11.03.17
30	38	760	0.79 ± 0.05	1.6 ± 0.2	20.4 ± 2.7	18.0 ± 1.1	11.03.17

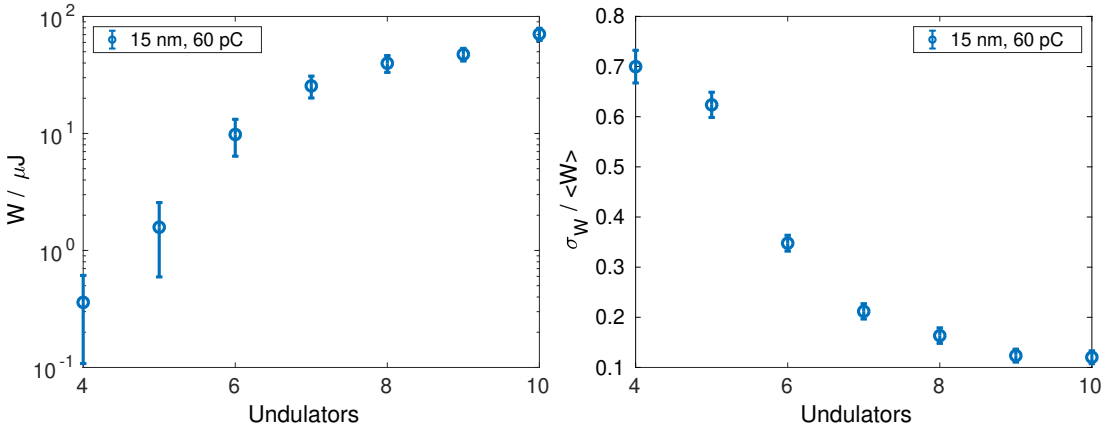

(a) Gain curve. (b) Fluctuations.

Figure 5.1: Measurement at FLASH2 for a bunch charge of 60 pC and a radiation wavelength of 15 nm. The beam energy was 1150 MeV.

An overview of the parameters and results is shown in Table 1 and detailed information is presented in the following.

During all of the shifts in August 2016, i.e. the first three rows in Table 1, FLASH1 was running in parallel for other users.

For the first shift on 26.08.16, we set up FLASH2 for a radiation wavelength of 15 nm. The measured gain curve and the corresponding measured fluctuations can be found in Fig. 5.1. The maximum of the relative fluctuations was 0.70 ± 0.03 corresponding to 2.0 ± 0.2 modes in the radiation pulse. The calculated mean radiation pulse duration using Eq. (5.1) is (13.0 ± 1.5) fs FWHM which is only 1.4 times higher than the coherence length, c.f. Eq. (3.9), of (9.0 ± 0.6) fs for this wavelength.

In the second shift on 27.08.16, we attempted to achieve a single radiation mode in the photon pulse. The bunch charge was raised to 88 pC to achieve a higher peak current compared to the first shift. Additionally, a wavelength of 20 nm was set up to observe how many radiation modes we obtain with the same settings but for half of the radiation wavelength. The measured gain curves and the corresponding measured fluctuations are displayed in Fig. 5.2 for both radiation wavelengths. For a radiation wavelength of 40.5 nm almost single mode lasing was accomplished, there were on average only 1.1 ± 0.2 radiation modes present in the photon pulse. This gave a theoretical minimal FWHM photon pulse duration of (14.7 ± 2.8) fs which is even below the coherence length of (19.7 ± 1.5) fs, as for this case $M < 2$ and Eq. (5.1) is only a rough approximation of the photon pulse duration. Genesis 1.3 simulations for this case using

an ideal Gaussian electron beam as input are shown in Section 5.2.1. For a radiation wavelength of 20 nm and a slightly changed compression the number of modes tripled in comparison to the measurement at 40.5 nm. Due to the shorter coherence length not only one single mode is amplified in the bunch but multiple independent ones.

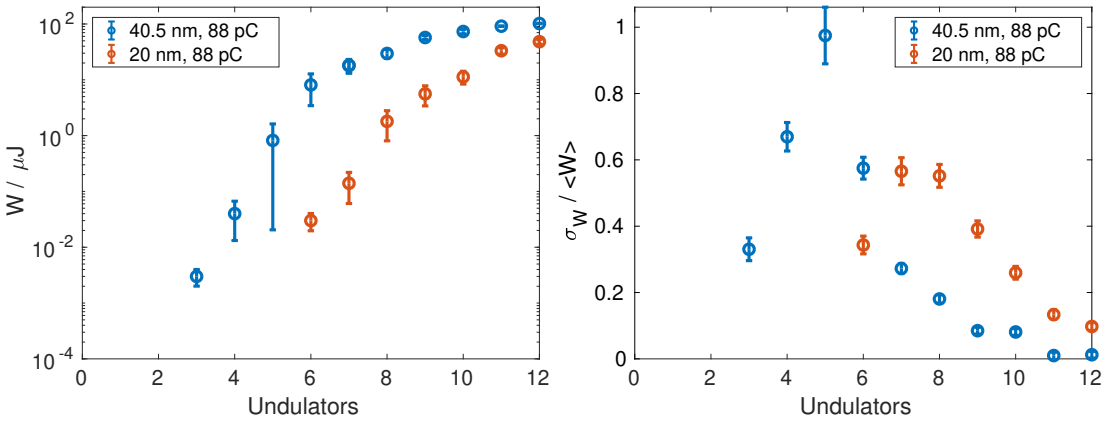

(a) Gain curves. (b) Fluctuations.

Figure 5.2: Measurement at FLASH2 for a bunch charge of 88 pC and radiation wavelengths of 40.5 nm and 20 nm. The beam energy was 690 MeV.

In the third shift, a wavelength of 30 nm was selected at FLASH2. For this wavelength electron bunches with charges of 70 pC and 38 pC were sent through the undulators. The gain curve measurement and the corresponding fluctuations are shown in Fig. 5.3. Start-to-end simulations from the cathode to the end of the undulator section are shown in Section 5.2.2. For a bunch charge of 70 pC there were in the mean 2.2 ± 0.2 modes present in the radiation pulse, a histogram for the highest fluctuations of 0.67 ± 0.03 is shown in Fig. 5.4(a). The FWHM photon pulse duration and the rms electron bunch length were therefore in the order of (24.7 ± 2.8) fs. By selecting a smaller laser beam spot on the cathode and slightly retuning the machine, e.g. to compensate phase drifts in the accelerating modules, the bunch charge decreased to 38 pC and the number of modes in the radiation pulse to 1.6 ± 0.2. The corresponding histogram is shown in Fig. 5.4(b). The FWHM photon pulse duration was in the order of (20.4 ± 2.7) fs, although of course in this case $M < 2$ and therefore Eq. (5.1) is only a rough approximation. Additionally, as can be seen in Fig. 5.3(a) the saturation length increases when the charge is reduced, which according to Eq. (5.1) leads to a longer photon pulse duration. The shorter electron bunch length is achieved by reducing the charge, as the (longitudinal) space charge forces in the bunch are also reduced. Therefore, the electron bunch stays shorter after compression.

The values for the minimal photon pulse duration are shorter than in [133], since the saturation length was determined differently. For the calculation here, the findings from the start-to-end simulations shown in Section 5.2.2 are also considered.

In summary, these measurement results show that ultra-short pulses at FLASH2 can be generated at different beam energies, bunch charges, and wavelengths. Even nearly single-spike lasing could be achieved. In the following, we will show simulation results supporting these findings and show, that single-spike lasing at lower wavelengths is also feasible.

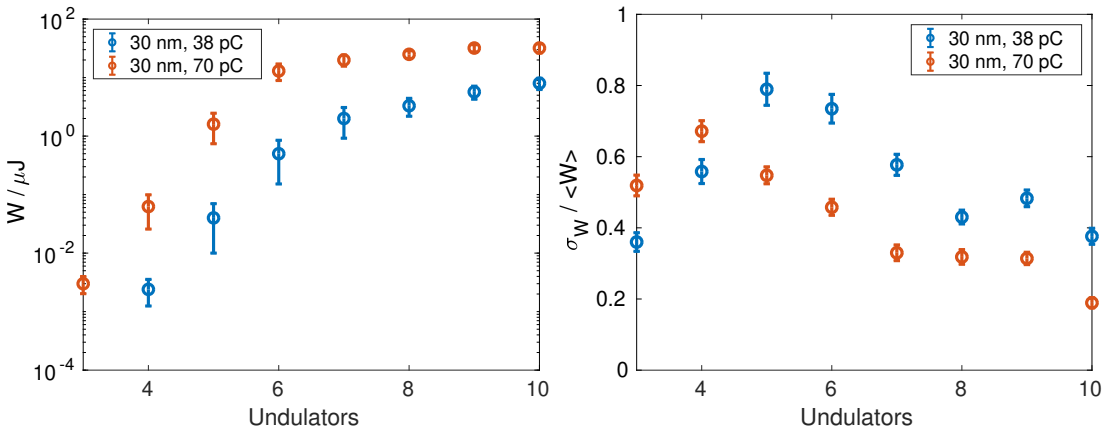

(a) Gain curves. (b) Fluctuations.

Figure 5.3: Measurement at FLASH2 for bunch charges of 70 pC and 38 pC and a radiation wavelength of 13.5 nm. The beam energy was 760 MeV.

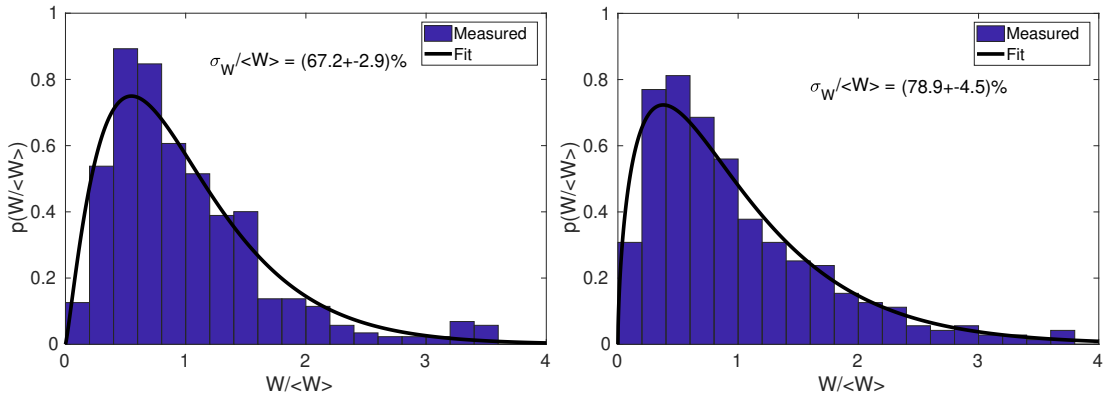

(a) $Q = 70$ pC. (b) $Q = 38$ pC.

Figure 5.4: Highest fluctuations measured at FLASH2 for bunch charges of 70 pC and 38 pC and a radiation wavelength of 13.5 nm. The beam energy was 760 MeV.

5.2 Simulation Results for Short-Pulse Operation at FLASH2

To investigate the measurement results further, simulations are used based on three main simulation codes explained in Section 5. Genesis 1.3 simulations using an ideal Gaussian beam as input are shown in Section 5.2.1. Start-to-end simulations from the FLASH gun to the FLASH2 undulators using all three simulation codes are shown in Section 5.2.2.

To model the statistic nature of SASE, Genesis 1.3 was ran with various random initial conditions for the start-up processes of the radiation. The runs with these "seeds" will be presented in the following images. They are not to be confused with the laser pulse seed for a seeded FEL. For the simulations using an ideal Gaussian beam in Section 5.2.1 a total of four different initial conditions was used, as this study was done to complement the measurements. For the simulations shown in Sections 5.2.2 and 5.3 a total of ten initial seeds was used, to obtain a more detailed view on the radiation emission.

5.2.1 Ideal Gaussian Beam

In this section, results of Genesis 1.3 simulations using an ideal Gaussian beam are shown for one of the examples. The 88 pC case producing radiation with a wavelength of 40.5 nm is selected, as this setting produced radiation which was the closest to single-spike lasing. Some input parameters such as the bunch length and the beam energy are taken from the measurements. Others have to be estimated or iterated, as there is no direct way to measure those properties at FLASH2, yet.

To model the 88 pC case a beam energy of 690 MeV, a peak current of 0.9 kA at the undulator entrance, a normalized emittance of 0.6 mm mrad, an rms bunch length of 14.7 fs, and an energy spread of 0.5 MeV is assumed for the simulations. The temporal and radial distributions are assumed to be Gaussian. The rms electron bunch length for the potential lasing part is estimated from the measurements according to Eq. (5.2), although, as stated before, this is a rough approximation in this case. For this setting, four different random initial conditions are used to model the statistical nature of SASE. A comparison of the measured and the simulated gain curves for the 88 pC case is shown in Fig. 5.5. In the exponential regime the simulated gain curves are a little above the measured curve, as there were no errors assumed for the simulation. In the saturation regime the radiation power stops to grow for the simulation because the photon pulse slips out of the electron bunch. This is because only the core part of the electron bunch was modeled for the simulation as we are most interested in the radiation produced in the exponential regime. Figure 5.6 shows the temporal and spectral distribution at the end of the exponential regime, i.e. at the sixth undulator. Three of the pulses show a temporal single-spike, one of the pulses shows a small side peak. The spectral distribution shows a single-spike for all cases. These results support the measured nearly single-spike radiation at a wavelength of 40.5 nm at FLASH2. The generation of single-spike radiation at other wavelengths is studied in Section 5.3.

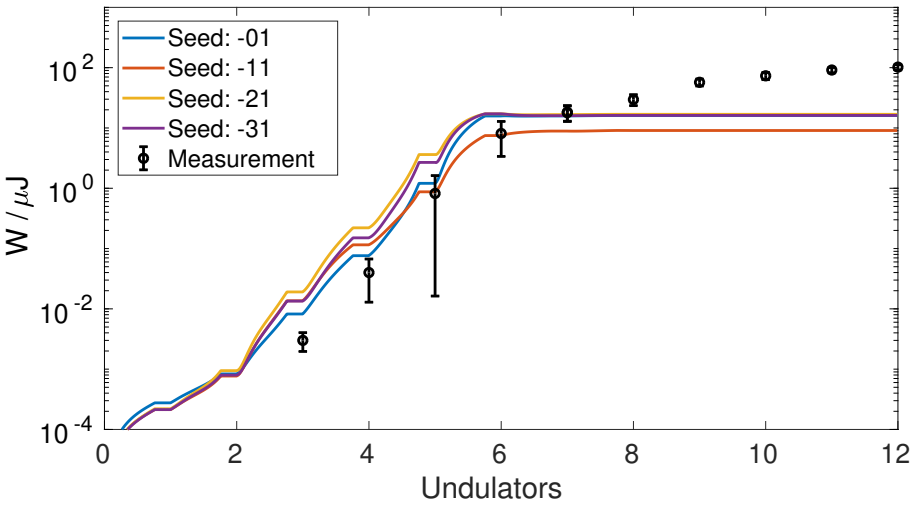

Figure 5.5: Comparison of gain curves measured and simulated for 88 pC and a radiation wavelength of 40.5 nm. The beam energy is 690 MeV. Four different initial conditions are used for the radiation pulse.

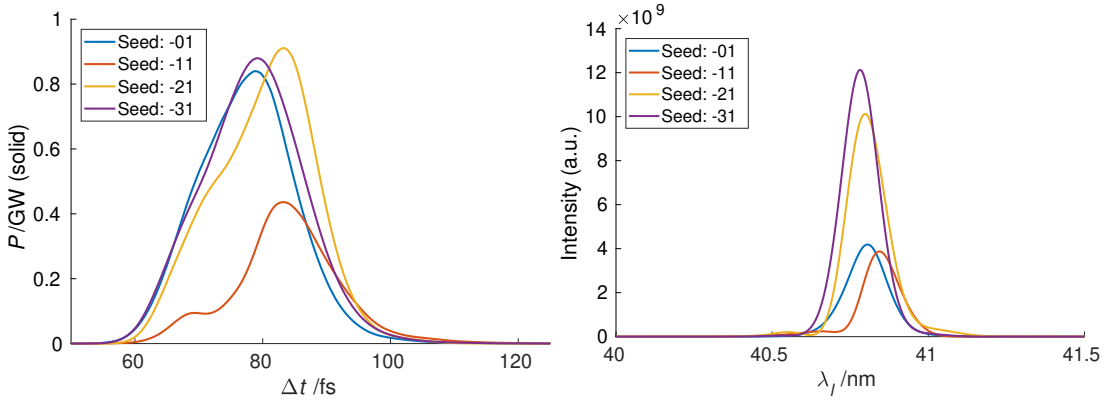

(a) Temporal distribution.

(b) Spectral distribution.

Figure 5.6: Simulated distributions of the FEL pulse at the sixth undulator for 88 pC and a radiation wavelength of 40.5 nm. The beam energy is 690 MeV. Four different initial conditions are used for the radiation pulse.

5.2.2 Start-to-End Simulation

During the shifts in March 2017, c.f. Table 1, we carefully recorded the machine parameters. This enables the possibility to perform meaningful start-to-end-simulations for the measurements to get a better understanding of the beam dynamics.

Some assumptions for the simulations are made. If one tries to directly use the theoretical current values as actual values for the magnets at FLASH2, the beam does not follow the theory optics. This is not yet fully understood. However, one reason is that the design optics are valid only in the limit of no space charge. To overcome this, matching routines are applied in the FLASH matching sections to match the beam to the theoretical Twiss parameters. Therefore, the beam optic used for the simulation is the theory optic as this is the one the machine is set up for. Additionally, the RF phases are subject to phase drifts. The on-crest phases were measured 4 hours before the shift, therefore phase differences in the on-crest phases of $\pm 1°$ can occur. The RF phase of ACC1 has the biggest influence on the compression in the FLASH linac. This phase is adjusted empirically using RFTweak [135] in the given range. Offsets of 0.15° and 0.3° in the ACC1 phase for the 70 pC and the 38 pC bunch, respectively, yield results reproducing the gain curve measurements shown in Fig. 5.3.

70 pC bunch

Figure 5.7 shows the simulated bunch parameters for a charge of 70 pC at the start of the undulator section.

It is worth noting, that the peak current for this bunch charge is only ∼600 A although the same compression settings as for the 38 pC bunch are applied and also the initial bunch length is the same. Nonetheless, the 38 pC bunch yields a peak current of more than 1.1 kA, c.f. Fig. 5.11. This happens because of strong space charge effects before the compression chicanes for the 70 pC bunch which elongate the bunch. The bunch length at the undulator is 54 fs. This value

is higher than the electron bunch length calculated according to Eq. (5.2) of (24.7 ± 2.8) fs as Eq. (5.2) is an approximation and only takes the potential lasing part of the bunch into account.

The slice emittance is between 0.4 mm mrad and 1.2 mm mrad, c.f. Fig. 5.7(a). Interestingly, the lowest slice emittance is in the region of 100 fs and not around the current peak. This is due to space charge induced emittance growth in the region of the current peak, as the electron density is higher there.

Nonetheless, the radiation is emitted around the current peak but slightly shifted towards regions with lower emittance and energy spread, as can be seen from the temporal profiles at the end of the exponential regime in Fig. 5.10. This is because not only the emittance is important for the lasing process, but also the peak current, the energy spread, and how well the electron beam is matched to the undulator. Figure 5.7(b) shows the slice-beta matching parameter indicating how well the slices are matched to the undulator. In the region from -50 fs to 50 fs, which is also where the current peak is, B_{mag} is close to one in both transverse planes. In the region of the lowest slice emittance, $B_{\mathrm{mag,y}}$ grows and the slices are not matched very well to the undulator. All of these effects add up in the lasing process.

The slice energy spread is below 180 keV for the whole bunch as can be seen in Fig. 5.7(d). This low energy spread is due to the fact that the machine was operated at undercompression for this bunch charge, which can also be seen in the longitudinal phase space density shown in Fig. 5.8.

Figure 5.9 shows the measured and the simulated gain curves using the bunch described above as input. It can be seen that the simulated gain curves tend to have more pulse energy than the measured ones. This is due to the aperture of 2 mm we used for the measurement which cut the outer part of the radiation and also because the simulation does not consider orbit or undulator errors.

The temporal distribution of the photon pulses at the end of the exponential regime, i.e. using the first six undulators is shown in Fig. 5.10. It can be seen that the pulses consist of 2 to 4 modes, which is in the order of the measured number of modes of 2.9. The simulated photon pulse durations are in the order of 10 fs to 35 fs with a mean value of (24.1 ± 10.5) fs. This value is in good agreement the measured value of (24.7 ± 2.8) fs.

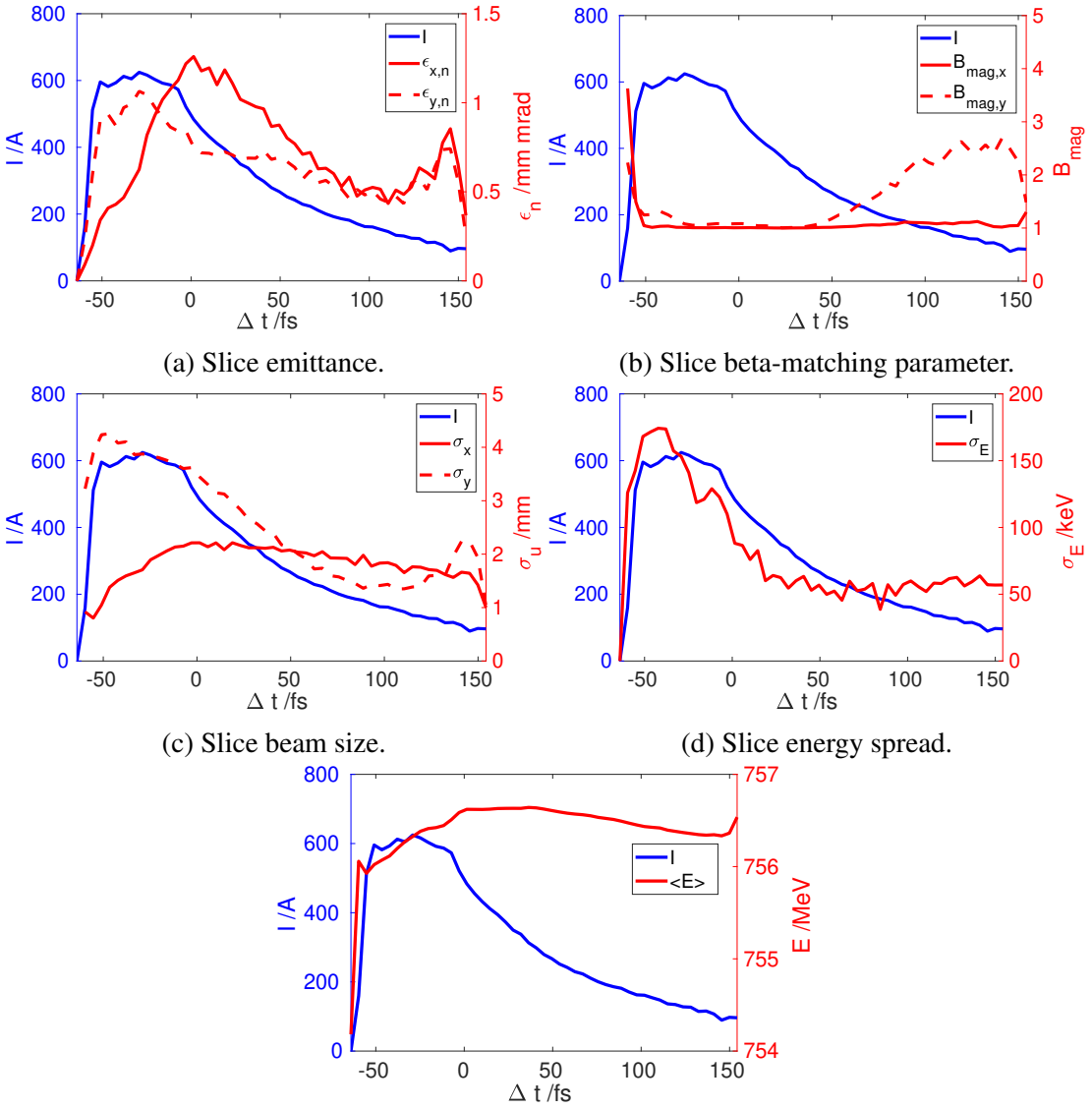

Figure 5.7: Simulated slice parameters of the bunch for a charge of 70 pC at the start of the undulator section. The current profile is plotted in blue, the slice parameters in red. The head of the bunch is to the right.

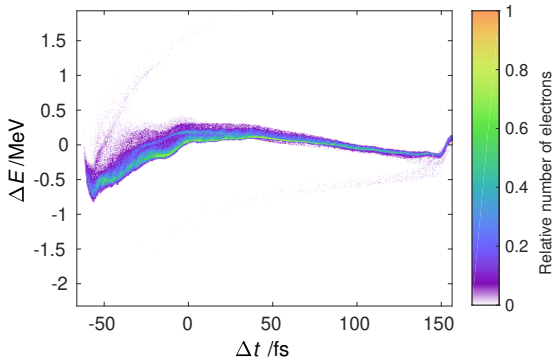

Figure 5.8: Simulated longitudinal phase space density at the beginning of the undulator for 70 pC at a beam energy of 760 MeV. The head of the bunch is to the right.

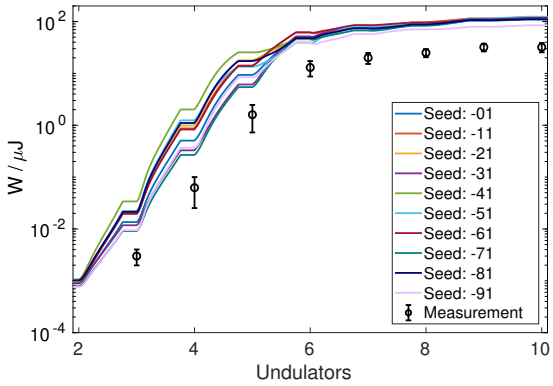

Figure 5.9: Comparison of gain curves measured and obtained from start-to-end simulations for 70 pC and a radiation wavelength of 30 nm. The beam energy is 760 MeV. Ten different initial conditions are used for the radiation pulse.

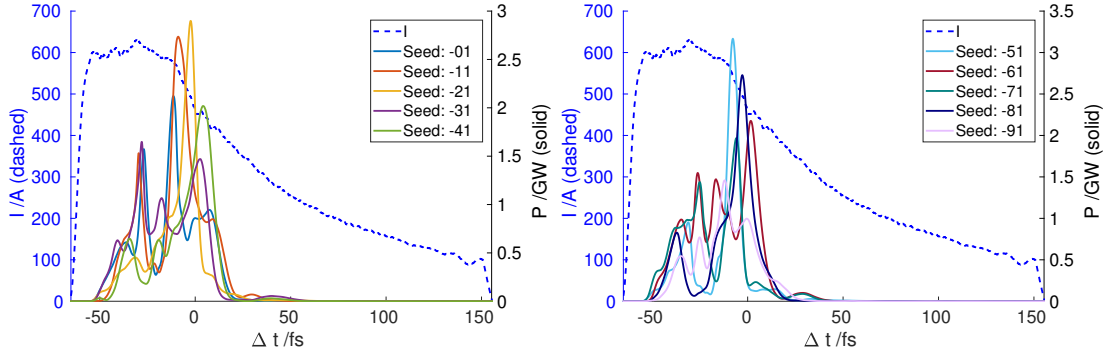

Figure 5.10: Temporal X-ray profile using six undulators obtained from start-to-end simulations for 70 pC and a radiation wavelength of 30 nm. The beam energy is 760 MeV. Ten different initial conditions are used for the radiation pulse. The bunch current is plotted using a dashed blue line.

38 pC bunch

Figure 5.11 shows the simulated bunch parameters for a charge of 38 pC at the start of the undulator section.

Using the same compression settings as for the 70 pC bunch, the peak current at the undulator entrance is about 1.15 kA for 38 pC. This is twice as large as the peak current that was achieved using the 70 pC bunch, since the elongation due to space charge effects for the 38 pC bunch is smaller due to the lower particle density.

The slice emittance, which can be seen in Fig. 5.11(a), for the tail of the bunch is very small and grows strongly around the position of the current peak to values of 1.5 mm mrad in the horizontal plane. Behind the current peak the emittance decreases. The increase around the current peak stems from transverse space charge effects due to the high particle density in this region. Nonetheless, the beta-matching parameter in both planes is about 1 in the region from 0 fs to 40 fs, c.f. Fig. 5.11(b). Most parts of the bunch are matched to the undulator and contribute to the lasing process, see also Fig. 5.15.

The slice energy spread is shown in Fig. 5.11(d) and ranges from 200 keV to 400 keV. This is four to eight times higher than for the 70 pC bunch as the 38 pC bunch is strongly

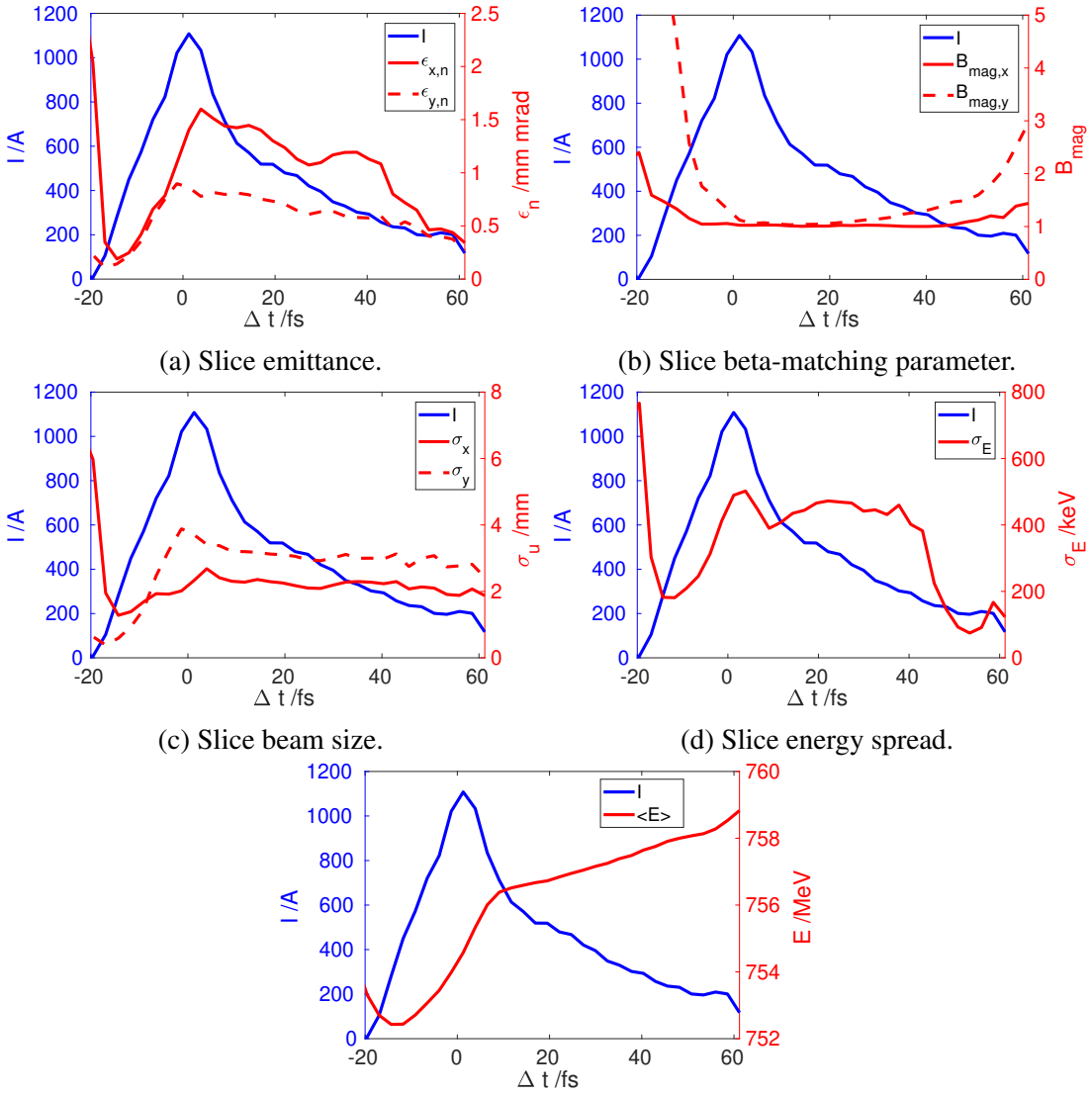

(a) Slice emittance.

(b) Slice beta-matching parameter.

(c) Slice beam size.

(d) Slice energy spread.

(e) Slice mean energy.

Figure 5.11: Simulated slice parameters of the bunch for a charge of 38 pC at the start of the undulator section. The current profile is plotted in blue, the slice parameters in red. The head of the bunch is to the right.

overcompressed, which can also be seen in the longitudinal phase space density at the beginning of the undulator in Fig. 5.12. This strong overcompression is also the reason why during this shift no single-spike lasing was achieved. According to [28, 136], the best possibility to achieve single-spike lasing is at slight overcompression. Additionally, due the strong overcompression there are two main energies at the same longitudinal position within the bunch. The tail of the bunch is compressed stronger than the head of the bunch due to nonlinearities, space charge effects, and CSR, especially in the second bunch compressor. The longitudinal phase space density at the entrance and the exit of the second bunch compressor are shown in Fig. 5.13. Due to CSR and space charge effects, the electrons in the head of the bunch are accelerated, c.f. Section 2.7, resulting in a smaller compression than for the rest of the bunch. Space charge effects between the second bunch compressor and the undulator and the compression in the

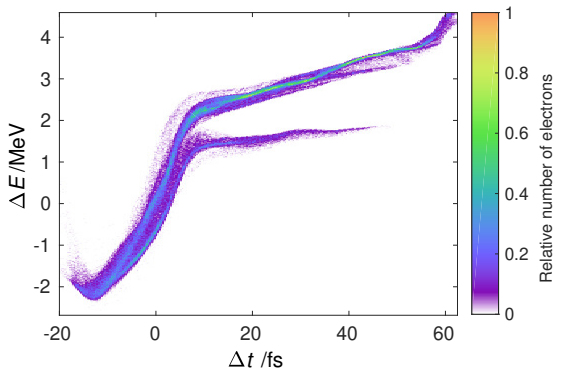

Figure 5.12: Simulated longitudinal phase space density at the beginning of the undulator for 38 pC at a beam energy of 760 MeV. The electron bunch is overcompressed. The head of the bunch is to the right.

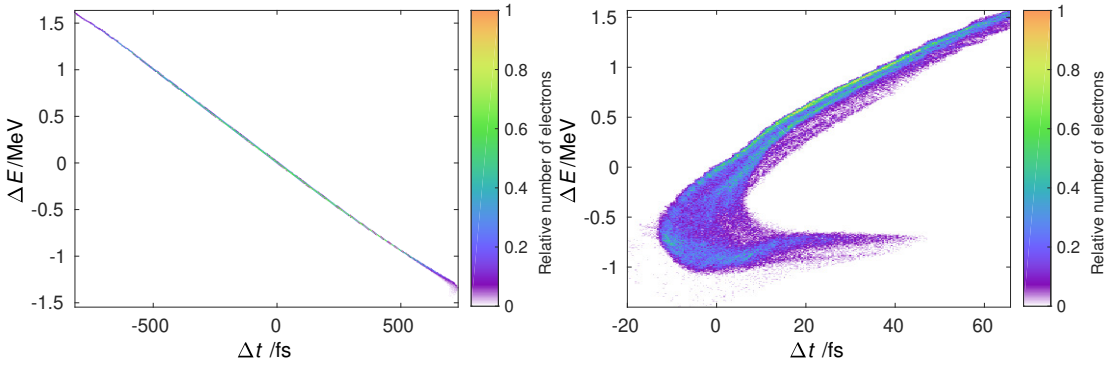

(a) Entrance of second bunch compressor.

(b) Exit of second bunch compressor.

Figure 5.13: Simulated longitudinal phase space density at the entrance and exit of the second bunch compressor for 38 pC at a beam energy of 450 MeV. The electron bunch is overcompressed. The head of the bunch is to the right.

FLASH2 extraction chicane cause these effect to become more severe, resulting in the phase space density at the undulator displayed in Fig. 5.12. A similar phase space density was also observed in simulations for FLASH1 [53].

Figure 5.14 shows the measured and the simulated gain curves using the bunch described above as input. In the exponential regime, most of the ten different gain curves are within the errors of the measurement. In saturation the simulated gain curves are a factor three to six higher than the measured ones. This is again due to the aperture of 2 mm we used for the measurement which cut the outer part of the radiation and also because the simulation does not consider orbit or undulator errors.

The temporal distribution of the photon pulses at the end of the exponential regime, i.e. using the first six undulators is shown in Fig. 5.15. The photon pulses are created in the region of the current peak and then slip ahead within the electron bunch, where they are then amplified. The simulated pulse durations range from 10.1 fs to 27.6 fs with a mean of (15.8 ± 5.5) fs FWHM which is within the error range of the mean measured photon pulse duration of (20.4 ± 2.7) fs FWHM. The slightly lower simulated pulse duration may stem from the idealized model for the undulator and beam orbit in the simulations and also the uncertainty in the accelerating phases.

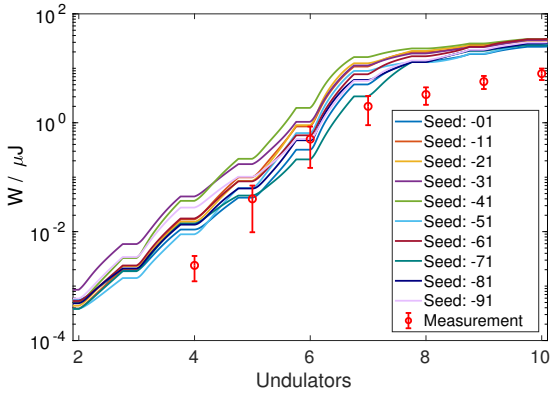

Figure 5.14: Comparison of gain curves measured and obtained from start-to-end simulations for 38 pC and a radiation wavelength of 30 nm. The beam energy is 760 MeV. Ten different initial conditions are used for the radiation pulse.

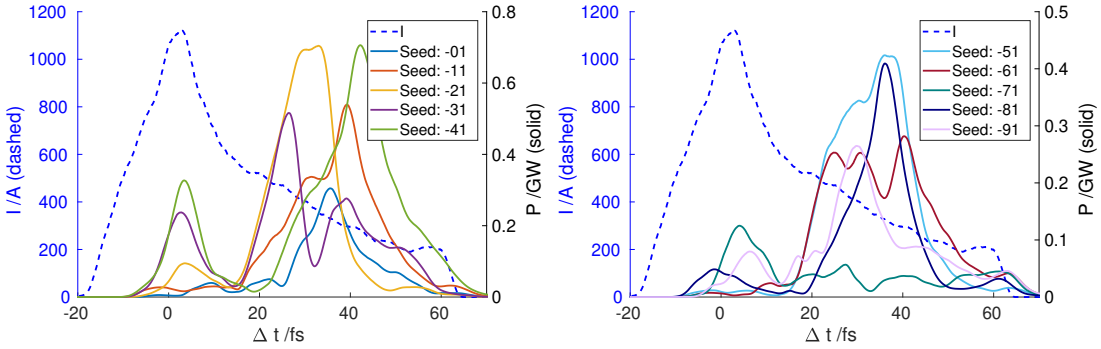

Figure 5.15: Temporal X-ray profile using seven undulators obtained from start-to-end simulations for 38 pC and a radiation wavelength of 30 nm. The beam energy is 760 MeV. Ten different initial conditions are used for the radiation pulse.

Also, Eq. (5.1) holds for $M \gtrsim 2$ which is not the case here. Additionally, only ten different SASE pulses were simulated, which is a lot lower than the 500 measured SASE pulses.

5.3 Simulation Results for Single-Spike Operation at FLASH2

A feasibility study for the generation of single-spike radiation, c.f. Section 3.2.1, at FLASH2 is conducted, similarly to the one for FLASH1 described in [28]. The goal is to show, that single-spike operation at FLASH2 is possible and that we can reach single-spike radiation at different wavelengths.

The bunch charge used to create single-spike radiation is 20 pC. With such a low bunch charge the space charge forces are minimized, yet there are enough electrons to produce radiation. The laser pulse duration is set to 1 ps rms to create a short electron bunch directly at the cathode, which is feasible using the short-pulse injector laser. Figures 5.16(a) and 5.16(b) show the slice emittance and the energy spread downstream of the gun, respectively. Due to space charge in the gun and the first accelerating module, the bunch length grows to 1.277 ps rms at the first dipole of the first bunch compressor.

In the first bunch compressor the electron bunch is compressed by a factor of 4 to 302 fs rms. The slice emittance, shown in Fig. 5.16(c), in the central part is unchanged, the slice

energy spread, shown in Fig. 5.16(d) grows a little due to the acceleration.

The second bunch compressor compresses the bunch by a factor of 16 to 19 fs rms. The horizontal slice emittance in the region of the current peak grows slightly due to CSR and space charge effects in the bunch compressor, as can be seen in Fig. 5.16(e). The slice energy spread also increases, as the bunch is strongly compressed and most of the electrons are in the region of the current spike, c.f. Fig. 5.16(f).

The final compression takes place in the FLASH2 extraction, resulting in a bunch length of 12 fs rms at the undulator entrance. Strong space charge effects blow up the emittance around the current spike, see Fig. 5.17(a). Additionally, CSR effects and the further compression lead to an increase in the slice energy spread to values of up to 1.5 MeV rms in the region of the current spike, c.f. Fig. 5.17(d). This results in the main spike not contributing to the lasing process as will be shown in the following. The slice energy spread and the slice emittance are too large in the region of the current spike to sustain lasing. The longitudinal phase space density at the undulator entrance is shown in Fig. 5.18, the slice parameters and current distribution are displayed in Fig. 5.17. The mean energy of this bunch is 694 MeV.

This electron bunch is used to create radiation at different wavelengths as described in the following.

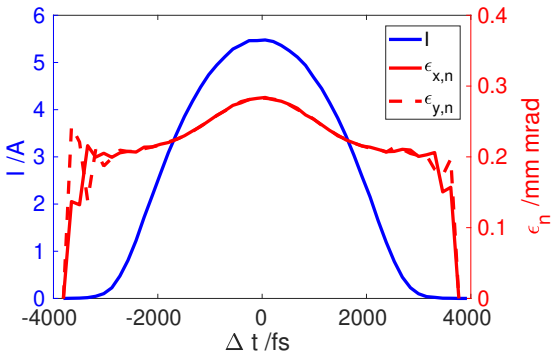

(a) Slice emittance downstream of the gun.

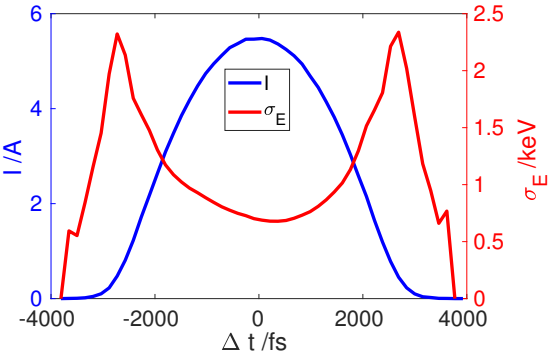

(b) Slice energy spread downstream of the gun.

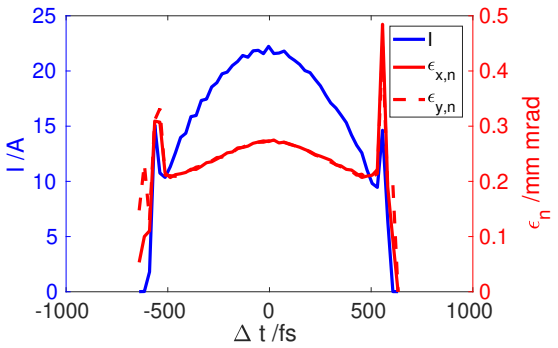

(c) Slice emittance downstream of the first bunch compressor.

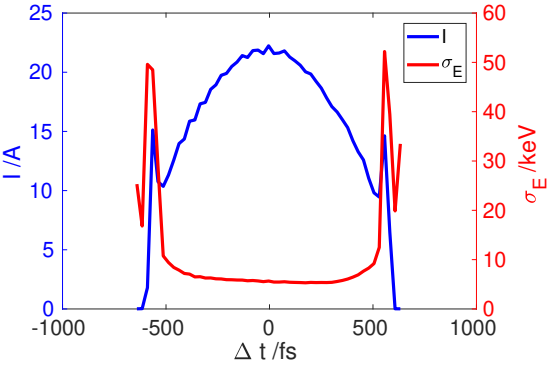

(d) Slice energy spread downstream of the first bunch compressor.

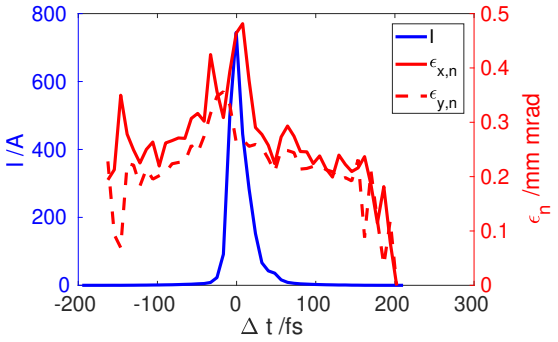

(e) Slice emittance downstream of the second bunch compressor.

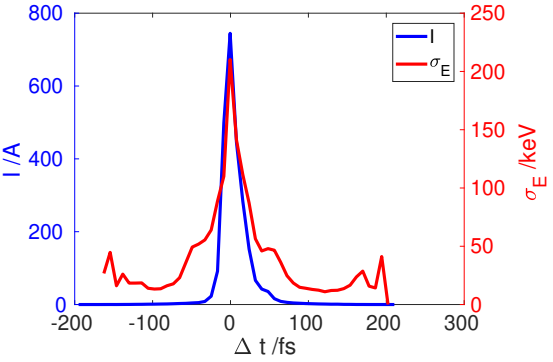

(f) Slice energy spread downstream of the second bunch compressor.

Figure 5.16: Simulated slice parameters of the bunch for a charge of 20 pC along the accelerator for single-spike radiation. The current profile is plotted in blue, the slice parameters in red. The head of the bunch is to the right.

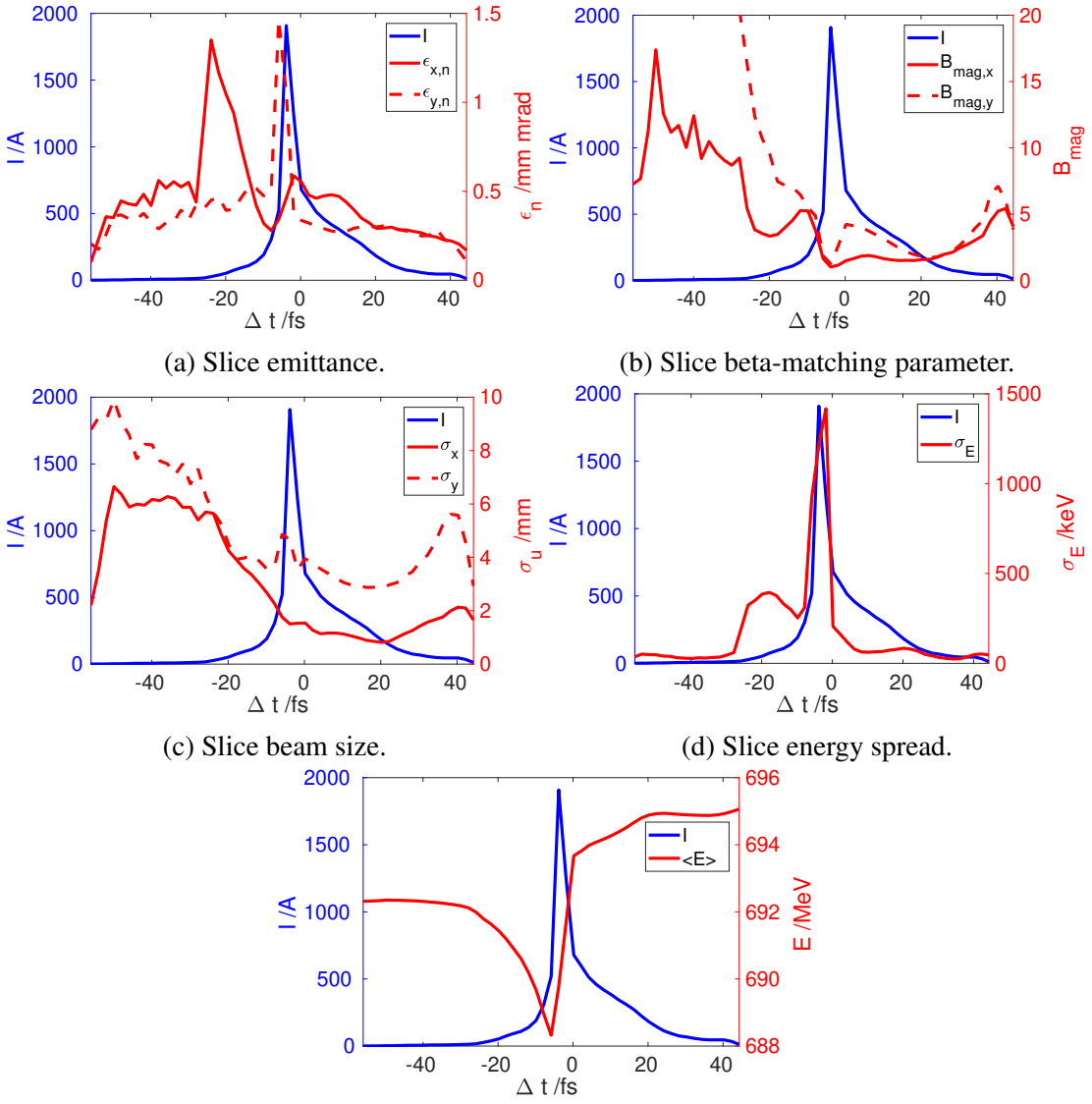

(a) Slice emittance.

(b) Slice beta-matching parameter.

(c) Slice beam size.

(d) Slice energy spread.

(e) Slice mean energy.

Figure 5.17: Simulated slice parameters of the bunch for a charge of 20 pC at the start of the undulator section for single-spike radiation. The current profile is plotted in blue, the slice parameters in red. The head of the bunch is to the right.

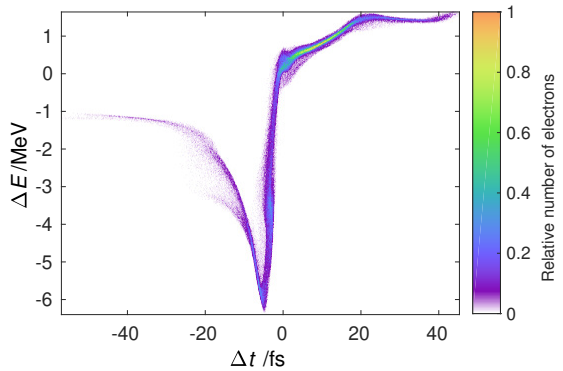

Figure 5.18: Simulated longitudinal phase space density at the beginning of the undulator for single-spike radiation at beam energy of 694 MeV. The head of the bunch is to the right.

35.64 nm

The first radiation wavelength at which the production of single-spike radiation using the electron bunch described before is simulated is 35.64 nm. The mean energy of this bunch is 694 MeV. The K-value of the variable gap undulators has to be set to 2.52 to yield this radiation wavelength.

Figure 5.19 shows the gain curves obtained from the Genesis 1.3 simulations for the ten different statistical seeds. The according temporal and spectral X-ray profiles just before saturation, i.e. downstream of the sixth undulator, are displayed in Figs. 5.20 and 5.21, respectively. The SASE pulse duration for these simulations is 10 fs to 20 fs and all but two temporal profiles show a single spike. However, the single spikes are not in the region of the main current spike but are created by electrons in the head of the electron bunch. This is due to the high slice emittance and slice energy spread of the current spike, c.f. Figs. 5.17(d) and 5.17(d), resulting in no lasing in this region. In the spectral domain all but one radiation pulses consist of a single spike, one profile shows a negligible side peak.

These simulation results encourage the possibility to produce single-spike radiation at a wavelength of 35.64 nm at pre-saturation. To achieve this in reality, the first six undulators at FLASH2 have to be opened. Otherwise, the beam will produce radiation in the saturation

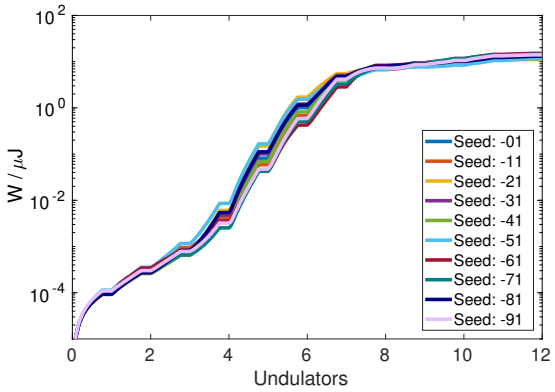

Figure 5.19: Gain curves from start-to-end simulations for single-spike radiation at 35.64 nm. Ten different initial conditions are used for the radiation pulse.

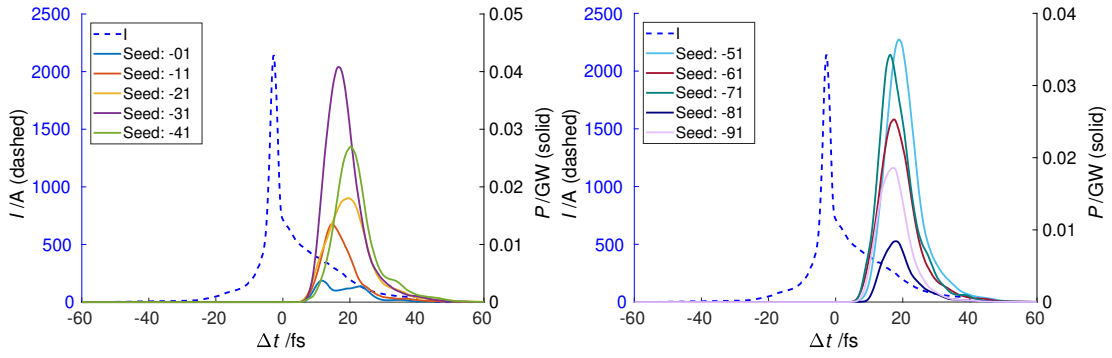

Figure 5.20: Temporal X-ray profile using six undulators obtained from start-to-end simulations for single-spike radiation at 35.64 nm. Ten different initial conditions are used for the radiation pulse.

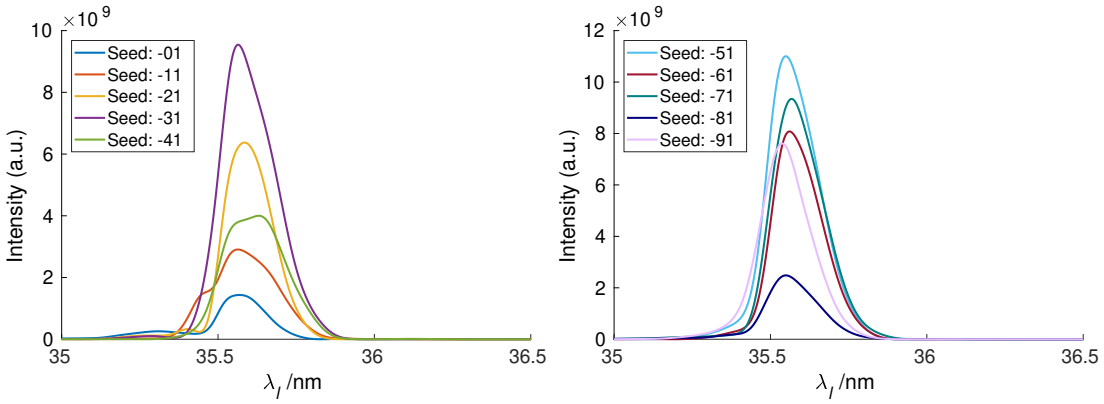

Figure 5.21: Spectral X-ray profile using six undulators obtained from start-to-end simulations for single-spike radiation at 35.64 nm. Ten different initial conditions are used for the radiation pulse.

regime, where multiple additional modes in the radiation pulse arise due to slippage effects, as can be seen in the temporal and spectral X-ray profiles at the end of the undulator section shown in Figs. 5.22 and 5.23, respectively.

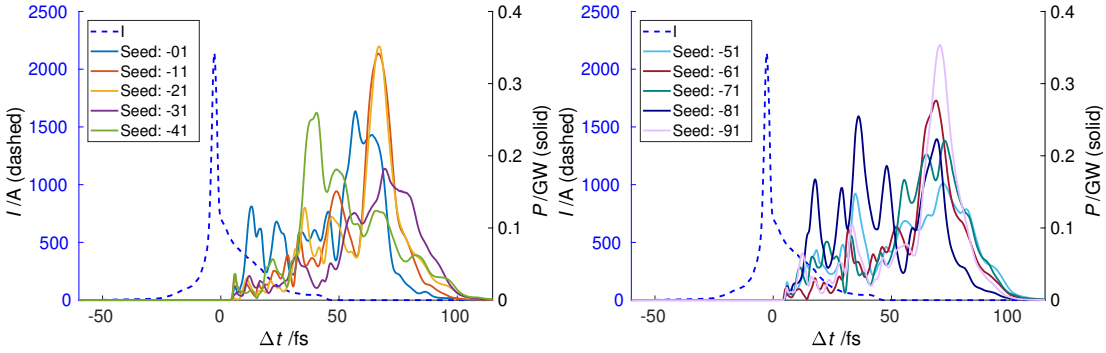

Figure 5.22: Temporal X-ray profile using all undulators obtained from start-to-end simulations for single-spike radiation at 35.64 nm. Ten different initial conditions are used for the radiation pulse.

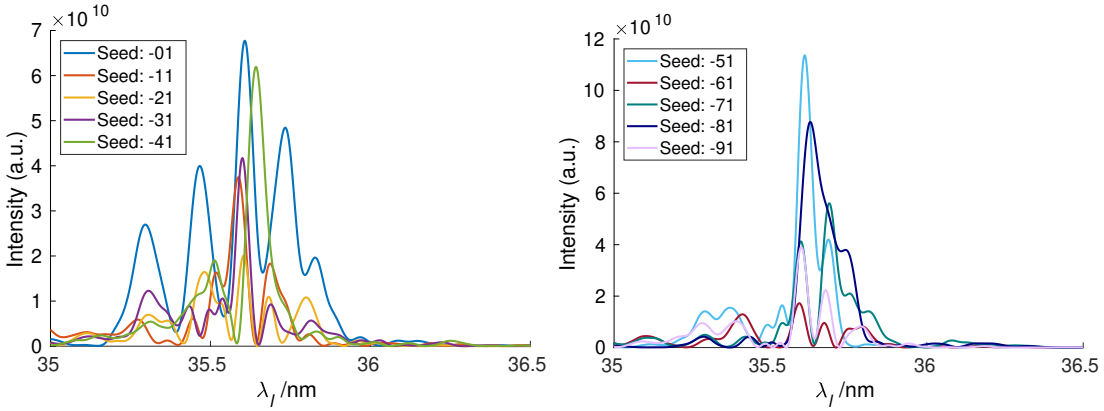

Figure 5.23: Spectral X-ray profile using all undulators obtained from start-to-end simulations for single-spike radiation at 35.64 nm. Ten different initial conditions are used for the radiation pulse.

16.95 nm

The second radiation wavelength at which the production of single-spike radiation is simulated is 16.95 nm which is less than half of the wavelength used in the first case. Again, the same electron bunch, described above, is used to create the radiation in the undulators. As FLASH2 consists of variable gap undulators only the K-value has to be adjusted to 1.40 by slightly enlarging the undulator gap to yield radiation at this wavelength.

Figure 5.24 shows the gain curves at this radiation wavelength obtained from Genesis 1.3 simulations for the ten different statistical seeds. Saturation is reached using about eight undulators. The temporal and spectral X-ray profile in the pre-saturation regime, i.e. using seven undulators in this case, are displayed in Figs. 5.25 and 5.26. At this radiation wavelength, most of the temporal X-ray profiles consist of a single spike. Some profiles comprise a large main spike and a smaller side spike due to the shorter cooperation length at this wavelength. This leads to more possible modes fitting in the bunch. Nonetheless, six pure single-spikes are produced. The same is true for the spectral domain. The FWHM X-ray pulse duration is in the range of 5 fs to 15 fs. Again, the radiation is not produced by the main spike due to its poor beam quality as discussed before.

Also these simulation results are very encouraging, as they demonstrate the feasibility of single-spike radiation at FLASH2 at this shorter wavelength. They could be further optimized by changing the compression in the bunch compressors so that less slice energy spread in the core part of the bunch is present, for example by performing further parameter scans of the accelerating phases. This was not done in this thesis, as the feasibility of single-spikes at FLASH2 is sufficiently demonstrated.

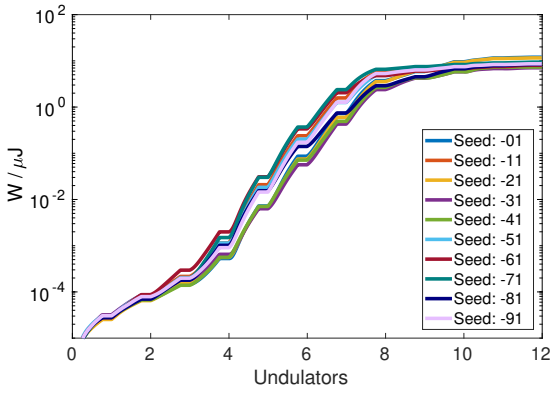

Figure 5.24: Gain curves from start-to-end simulations for single-spike radiation at 16.95 nm. Ten different initial conditions are used for the radiation pulse.

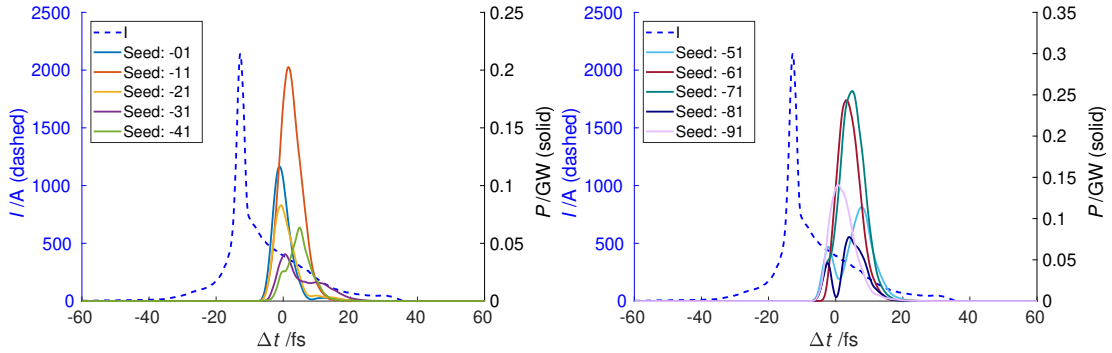

Figure 5.25: Temporal X-ray profile using seven undulators obtained from start-to-end simulations for single-spike radiation at 16.95 nm. Ten different initial conditions are used for the radiation pulse.

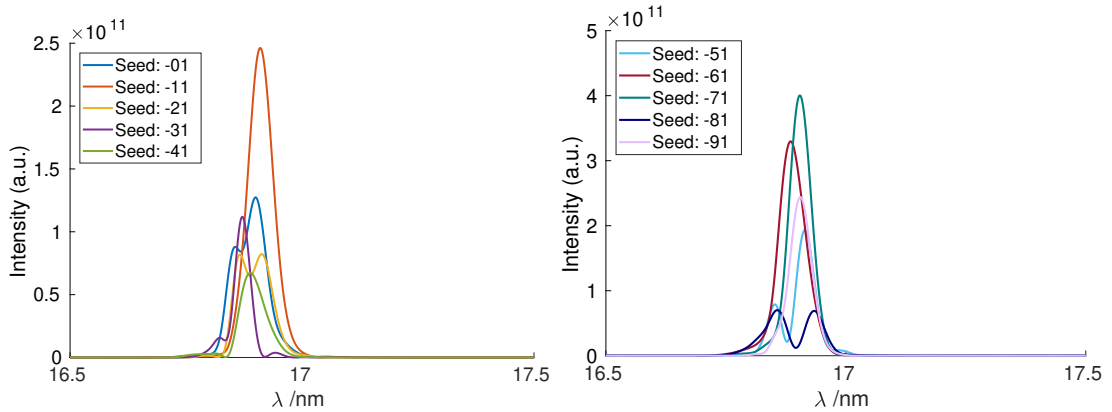

Figure 5.26: Spectral X-ray profile using seven undulators obtained from start-to-end simulations for single-spike radiation at 16.95 nm. Ten different initial conditions are used for the radiation pulse.

6 Implementation of a TDS at FLASH2

FLASH2 will be equipped with a longitudinal diagnostics section downstream of the FLASH2 undulators. Up until now, the only possibility to estimate the electron bunch lengths was to perform statistics measurements as described in the previous section. Additionally, a coherent transition radiation intensity spectrometer (CRISP) [137] is currently under commissioning at the FLASH2 beam line upstream of the undulators [138].

In this section, we describe the implementation of a TDS downstream of the undulators to enable direct measurements of the longitudinal phase space density, photon pulse reconstructions, as well as slice emittance measurements.

6.1 Layout of the TDS Diagnostic Section at FLASH2

The TDS diagnostic section is situated directly downstream of the FLASH2 undulators. It will feature two PolariX TDSs [10], which are X-band transverse deflecting structures ($f_{\mathrm{RF}} \approx 12\,\mathrm{GHz}$), and a kicker to deflect the beam onto an off-axis screen station as described in the following.

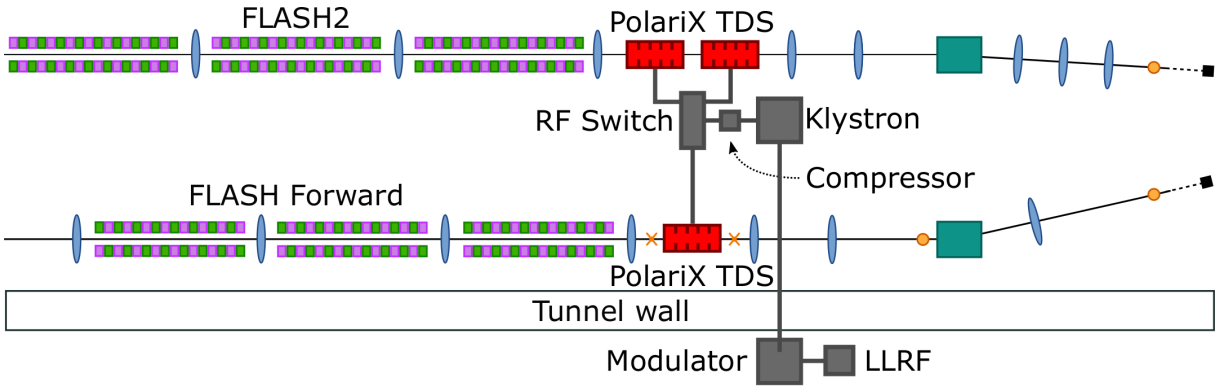

Figure 6.1: Shared RF system between FLASH2 and FLASH Forward. Courtesy of P. González Caminal.

The installation of the TDSs downstream of the FLASH2 undulators shares an RF station with FLASH Forward [65] as both experiments share the need for longitudinal diagnostics [9]. The waveguide distribution and RF components can be seen in Fig. 6.1. The TDSs at both experiments are connected via an RF switch to the same RF source. This installation scheme prohibits the simultaneous operation, but requires only one RF station and therefore reduces costs and space. The RF source comprises a 6 MW Toshiba E37113A klystron with an Ampegon Type μ, S-Class modulator [10] and is similar to the CERN[11] Xbox3 design [139]. To minimize the attenuation in the waveguides and achieve high deflecting powers, it was decided to place the klystron as close to the FLASH2 TDSs as possible. Therefore, the klystron is placed inside of the tunnel while the radiation sensitive modulator and LLRF[12]-rack are placed

[11] Conseil Européen pour la Recherche Nucléaire
[12] Low-Level RF

outside. The klystron and the modulator are connected by 15 m-long pulse cables. The total waveguide length from the klystron to the cavities is about 5 m. In the final stage, a compressor will be installed between the TDSs and the klystron, approximately raising the input power for the TDSs by a factor of four. Possible pulse compressors under discussion are a SLED cavity developed at CERN [140, 141] or an X-band version of the PSI[13] C-band barrel open cavity (BOC) [142].

6.1.1 PolariX TDS

The TDSs that will be installed downstream of the FLASH2 undulators are called PolariX TDS. They were originally designed for CLIC[14] at CERN [8] and have been further developed in a collaboration between CERN, PSI, and DESY [9]. Cavities of this type will be installed at FLASH2 [133], FLASH Forward [143], SINBAD[15] [115, 144], and at SwissFEL [145]. This novel design of a TDS will allow for variable polarization of the deflecting field and thus arbitrary streaking directions. This enables for example the possibility of a 3D charge reconstruction [146, 147] or slice emittance measurements in both planes using the same TDS, c.f. Section 6.3.3. This innovative CERN design requires highest manufacturing precision to guarantee the azimuthal symmetry of the structure and avoid the deterioration of the polarization of the streaking field [9, 10]. To ensure this, the high-precision tuning-free assembly procedures developed at PSI for the production of the C-band and X-band accelerating structures [148] are used for the manufacturing of the PolariX TDS.

The working principle of the variable polarization of the TDS is shown in Fig. 6.2. The incoming power is split using an E-hybrid [8] and distributed in two branches. The RF phase in one branch can be varied using a variable phase shifter. The power of both circularly polarized modes is then combined in an E-rotator, where a linearly polarized $TM_{1,1}$ mode is formed. By changing the phase difference between the two incoming modes by 180°, the polarization of the deflecting field is rotated by 90°, i.e. from horizontal to vertical [8]. Arbitrary streaking directions can therefore be selected by varying the phase difference between the two modes. The linearly polarized deflecting mode is fed into the TDS at the downstream end, since it is a backward traveling wave structure.

The parameters for the Polarix TDS are summarized in Table 2. There are two designs available: a long one and a short one. FLASH2 will be equipped with two short ones, since the deflecting voltage should be maximized given the available space. Two of the longer cavities do not fit, and the total voltage is lower if only one long cavity is built in. The parameters are given for the design temperature of 30 °C. For FLASH2 the RF frequency needs to be 11.9888 GHz, therefore the cavity is operated at a temperature of 62 °C. Additionally, the option with a TDS and the previously discussed BOC pulse compressor is indicated in the table, which is currently under development at PSI.

[13] Paul-Scherrer Institut
[14] Compact Linear Collider
[15] Short and INovative Bunches At DESY

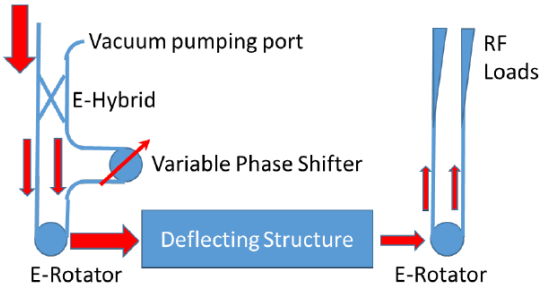

Figure 6.2: Layout of the variable polarization mode launcher. A variable phase shifter controls the RF phase between the two incoupling ports which enables to rotate the polarization of the deflecting field. Image from [8].

Table 2: PolariX TDS Parameters for the Long and the Short Version and a Temperature of 30 °C [10].

Cell parameter		
Frequency /MHz	11 995.2	
Phase advance/cell /°	120	
Iris radius /mm	4	
Iris thickness /mm	2.6	
Group velocity $/(\%c)$	-2.666	
Quality factor	6490	
Shunt impedance /(MΩ/m)	50	
TDS parameter	Short	Long
Number of cells	96	120
Filling time /ns	104.5	129.5
Active length /mm	800	1000
Total length /mm	960	1160
Power-to-voltage /(MV/MW$^{0.5}$)	5.225	6.124
TDS + BOC	Short	Long
Power-to-voltage /(MV/MW$^{0.5}$)	12.010	13.626

For FLASH2, the maximum deflecting voltage for two short cavities assuming an output power of 6 MW from the klystron and 5 m of waveguides with an attenuation of −0.1 dB/m is 39.28 MV. Nonetheless, in the following chapters we will mostly show parameters and simulations for a deflecting voltage of 34 MV to give more realistic values for the operation later, as additional losses in the waveguide bends can occur and also the pulse compressor is not yet finally developed. Only one bunch out of a FLASH2 bunch train can be streaked using the TDSs, due to the maximum length of the RF pulse produced by the klystron and the maximum repetition rate of the klystron.

Technical drawings of the Polarix TDS, the input coupler and a regular disc can be found in Fig. 6.3(a), a photo of the PolariX TDS prototype at the test stand at CERN is shown in Fig. 6.3(b). A technical drawing of the supports for the two cavities at FLASH2 is displayed in Fig. 6.4.

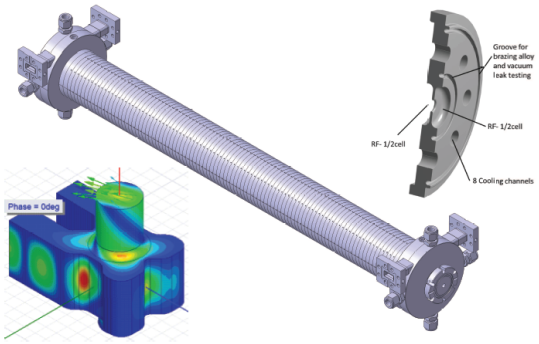

(a) Left: Input/output coupler. Middle: Drawing of the TDS prototype. Right: Regular disc. Image from [10].

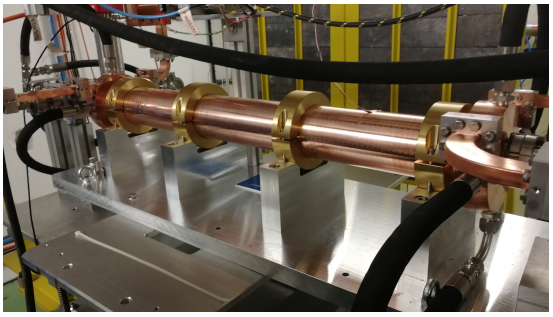

(b) Photo of the prototype.

Figure 6.3: Technical drawings and photo of the PolariX prototype.

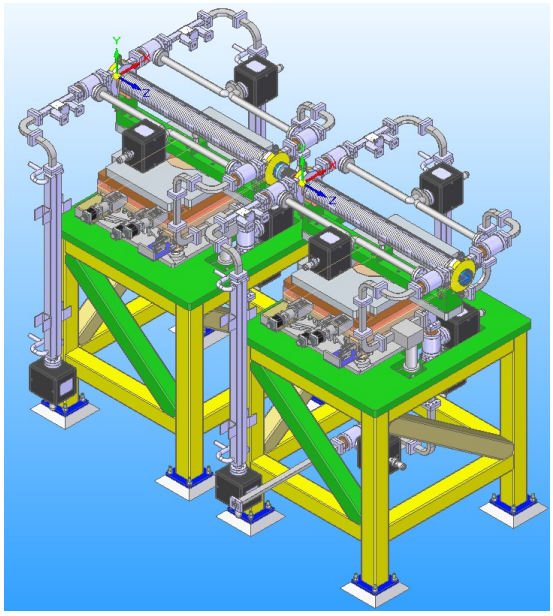

Figure 6.4: Technical drawing of the supports for the two PolariX TDSs at FLASH2. Courtesy of M. Föse.

6.1.2 Kicker Magnet

The kicker magnet that will be used to deflect the streaked bunch onto the off-axis screen is similar to the ones used at European XFEL[16] and described in [102]. The kicker consists of a ceramic vacuum chamber that is sputtered with a 1 µm thick layer of stainless steel. The deflecting pulse is produced by two copper air coils and has a pulse duration of less than 2 µs. It is thus possible, to deflect a single bunch at the full maximum repetition rate of 1 MHz. The high voltage for the deflection is generated by a pulser directly attached to the kicker at a repetition rate of 10 Hz and a maximum deflecting voltage of 20 kV. A technical drawing of the kicker is shown in Fig. 6.5.

[16] X-ray Free-Electron Laser

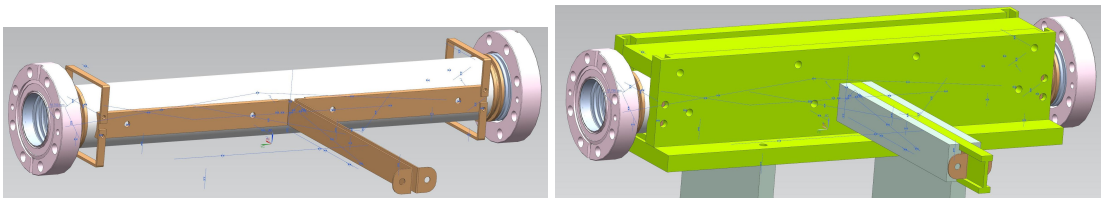

(a) Copper bars. (b) Housing.

Figure 6.5: Technical drawing of the kicker. Courtesy of F. Obier.

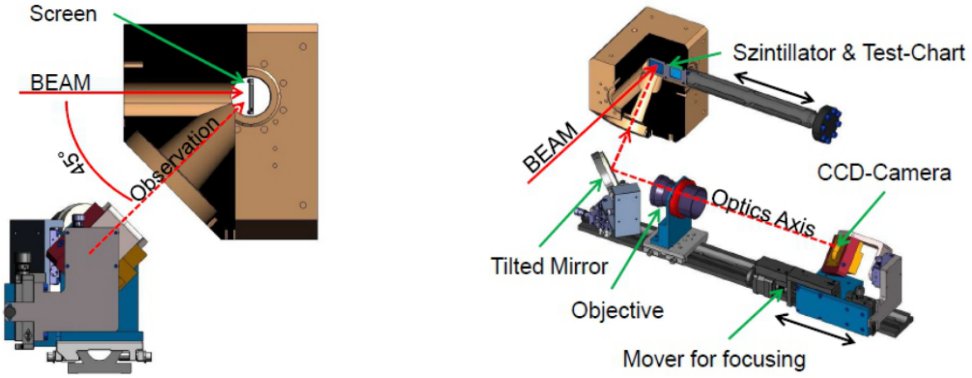

(a) Observation geometry. (b) Imaging optics.

Figure 6.6: Layout of the screen station that will be installed at FLASH2. The beam hits a screen and the radiation is observed under an angle of 45°. A movable CCD camera is used to digitize the image. Image from [149].

6.1.3 Screen Station

The screen station that will be installed for the FLASH2 longitudinal diagnostics section is already in use at the European XFEL and several other positions at FLASH [102, 149]. A technical drawing of the screen station and imaging system can be found in Fig. 6.6. The beam hits the screen frontally, the observation of the radiation produced by the beam on the screen is observed under an angle of 45°. The screen material is not yet decided, as non-linearities in the conventionally used scintillators were observed [150].

The imaging system is placed outside of the vacuum tube and comprises a CCD[17] Basler aviator avA2300-25gm camera and a focusing lens. Magnification ratios of 1:1 or 2:1 are possible. The size of the 2330×1750 pixels is $5\,\mu\text{m} \times 5\,\mu\text{m}$ leading to a field of view of $12.815\,\text{mm} \times 9.625\,\text{mm}$ for a magnification of 1:1 and $25.63\,\text{mm} \times 19.25\,\text{mm}$ for a magnification of 2:1, respectively [102, 149]. To correct perspective distortion arising from the observation of the screen under an angle of 45°, the Scheimpflug principle is applied [149, 151]. The CCD chip is tilted to accommodate the tilt of the screen so that the depth of field is not lost over the whole screen [102].

The spatial resolution of the whole imaging system was tested to be about $R_{\text{camera}} = 10\,\mu\text{m}$ [149].

[17] Charge Coupled Device

6.2 Accelerator Optics

As shown in Section 4.3.1, the temporal resolution of measurements using a TDS depends strongly on the accelerator optics. Therefore, the temporal resolution is optimized by modifying the accelerator optics downstream of the FLASH2 undulators within the constraints defined by the available space and the required optics at the FLASH2 dump.

Different optics are needed for the longitudinal phase space density measurement and the slice emittance measurement in both transverse planes using the same cavity. This versatility is a unique feature of the PolariX TDS, as described in Section 6.1.1. The accelerator optics are presented in the following.

Unless otherwise stated, resolutions are given for electron bunches with a normalized 1σ emittance in both planes of $\varepsilon_n = 3\,\mathrm{mm\,mrad}$ and a reference energy of $E = 1.2\,\mathrm{GeV}$ for standard operation, $\varepsilon_n = 1\,\mathrm{mm\,mrad}$ and $E = 1.2\,\mathrm{GeV}$ for low charge operation, and TDS parameters of $V_0 = 34\,\mathrm{MV}$ and $\omega_{\mathrm{rf}} = 2\pi \cdot 11.9888\,\mathrm{GHz}$.

6.2.1 Longitudinal Phase Space Density Measurement

For two lattices three sets of optics (see below) are matched, as the final layout of the beam line and the components in the beam line were subject to change. Initially, the installation of a THz undulator between the TDSs and the screen station was planned. This, however, would have resulted in strong boundary conditions on the possible number of magnets for the matching of the accelerator optics and the beam pipe diameter.

The plan to install a THz undulator at this position was later abandoned due to various reasons. We still present the optics, as they show that also with more rigorous bounds, the operation of a TDS at FLASH2 is possible. Therefore, additional magnets between the TDSs and the screen station may potentially be installed and for this case, a new set of accelerator optics is matched.

For each of these two cases, three sets of accelerator optics were matched:

Regular operation: In regular operation all quadrupoles between the last FLASH2 undulator and the beam dump can be used for matching. The constraints at the entrance to the FLASH2 dump have to be fulfilled in order to be able to safely dump up to 800 bunches in a bunch train. The constraints were specified as: $\beta_{x,y} > 1000\,\mathrm{m}$ and $\left|\eta_{x,y}\right| < 0.1\,\mathrm{m}$.

Regular operation with Delta undulator: The installation of a circular undulator directly upstream of the TDSs is planned for the future. When the Delta undulator is installed and in use, the quadrupole upstream of it cannot be used for matching into the TDSs. And of course in regular operation, the dump constraints have to be fulfilled.

Single bunch operation: When only one single bunch is used for the measurements, the dump constraints no longer have to be fulfilled, as this single bunch is not transported to the dump. This operation mode should be used when a very high resolution in the order of

1 fs is needed, e.g. for short pulse operation using the short pulse injector laser, c.f. Section 3.3.

The different optics are presented in the following. The matching was done using MAD8 [152] with the extension LMAD [153]. The goal was to minimize the temporal resolution while maintaining an energy resolution in the order of 10^{-4}. Therefore, according to Eqs. (4.21) and (4.28), the vertical phase advance has to be close to $\Delta\Psi_y = \pi/2 + n \cdot \pi, n \in \mathbb{N}_0$, the vertical beta function at the TDSs $\beta_y(s_1)$ has to be maximized, the horizontal beta function at the screen $\beta_x(s_2)$ has to be minimized, and the horizontal dispersion at the screen $\eta_x(s_2)$ has to be maximized. Additionally, the vertical beta function at the screen has to be $\beta_y(s_2) > 2\,\mathrm{m}$, so that the camera system is able to resolve the electron bunch.

Accelerator Optics with THz Undulator

The installation of a THz undulator between the TDSs and the measurement screen imposes limitations on the remodeling of the beam line and the accelerator optics.

The planned installation of a kicker, c.f. Section 6.1.2, is not possible with the THz undulator, as there is no space. However, the longitudinal phase space density measurements should be done parasitically, i.e. without disturbing the other bunches in the bunch train. Hence, the use of an off-axis screen is necessary. Instead of using a kicker, the intention was to use the streak of the TDSs to deflect the beam onto the screen. The displacement of a particle in the streaking direction can be calculated by Eq. (4.18). If the TDSs are operated at the zero-crossing, i.e. at $\Phi_{\mathrm{RF}} = 0°$, the centroid particle at $\zeta = 0\,\mathrm{fs}$ does not change its transverse position $u_0(s_2) = 0\,\mathrm{mm}$. However, when the TDSs are operated a few degrees away from the zero-crossing, the centroid particle is deflected. This deflection can be used to kick the beam onto the off-axis screen. For the highest and lowest Shear parameter, $S = 110$ and $S = 64$, of the matched optics in Table 3, one has to operate the TDSs at $\Phi_{\mathrm{RF}} = 1.31°$ and $\Phi_{\mathrm{RF}} = 2.25°$, respectively, to deflect the centroid of the beam 1 cm in vertical direction. Yet, we can see from Eq. (4.21) that the longitudinal resolution grows by a factor of $1/\cos(\Phi_{\mathrm{RF}})$. For the previously calculated phases, this amounts to a diminishing of the longitudinal resolution by a factor of 1.0003 and 1.0008. This effect is therefore negligible and the TDSs can be used to kick the beam onto the off-axis screen. Nonetheless, without a kicker the measurements cannot be performed completely parasitically. To obtain the longitudinal resolution, one needs to measure the unstreaked beam size $\sigma_{u_0}(s_2)$. As the only way to kick the beam onto the off-axis screen is to switch the TDSs on, the measurement of the unstreaked beam size cannot be performed using the off-axis screen. For this measurement an on-axis screen has to be used, which prevents the usage of long bunch trains for a short period of time.

As the dispersion inside the THz undulator should be kept as small as possible, because of the blow-up of the source point and the divergence of the photon beam, one needs to install a quadrupole directly between the dipole and the THz undulator. The angle between the photon beam line of the main undulators and the electron beam line is merely 3.5°. Therefore, a regular

quadrupole with an appropriate gap would only fit between the electron beam line and the photon beam line when placed at least 3 m downstream of the dipole. As the THz undulator should be as long as possible to enable highest output power this was not considered tolerable. Hence, a regular FLASH quadrupole of type "TQA" is modified by moving the iron yoke further away from the beam line. This enables the photon beam line to pass through the magnet within the iron yoke. A drawing of this modified TQA quadrupole is shown in Fig. 6.7.

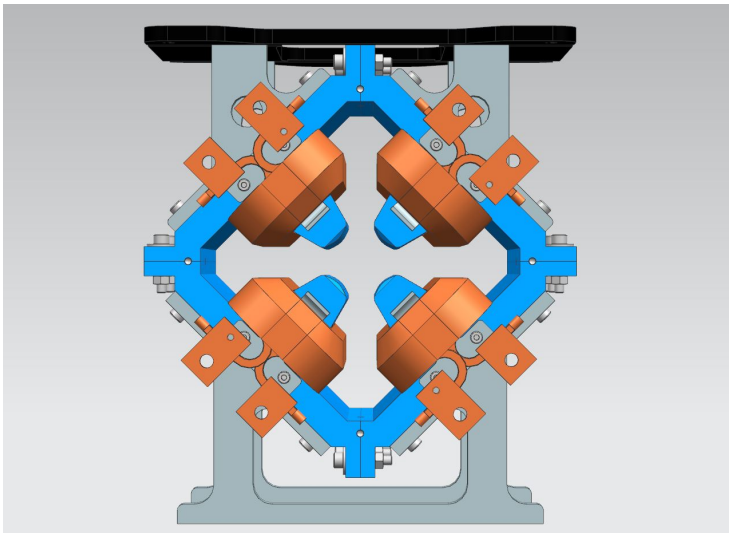

Figure 6.7: Drawing of modified TQA quadrupole. The photon beam line fits inside the iron yoke. Courtesy of J. Kuhlmann.

Furthermore, the beam pipe inside the THz undulator is limited to be 25 mm in diameter perpendicular to the orientation of the undulator to ensure that the deflecting field is strong enough for the electrons to radiate. An installation of the THz undulator with the gap in the horizontal plane precludes the previously discussed use of an off-axis screen. As the dispersive dipole orientation is fixed to the horizontal plane due to global geometrical constraints of the beam line, the TDSs have to deflect the beam vertically. Since it is planned to use the TDSs to kick the beam onto the off-axis screen, the displacement has to be in the vertical direction. If the beam pipe inside the undulator was restricted to 25 mm in diameter, large parts of the streaked and kicked beam would be scraped off by the beam pipe and be lost inside the undulator before reaching the screen. As this is not tolerable, the installation of a horizontal THz undulator would prevent the parasitical use without an on-axis screen of the TDS, which is not the case with a vertical THz undulator.

With the installation of a THz undulator the optics matching can be done with three quadrupoles upstream of the TDSs (two if the Delta undulator is used), three between the TDSs and the screen and four quadrupoles in between the screen and the dump, c.f. Fig. 6.8.

The design optical functions between the last FLASH2 undulator and the FLASH2 dump are plotted in Fig. 6.9. The values of the optical functions at the TDSs and at the screen as well as the resolutions for all three cases are shown in Table 3. For low charge operation a temporal resolution of 1.5 fs and an energy resolution of $1.7 \cdot 10^{-4}$ can be achieved simultaneously when

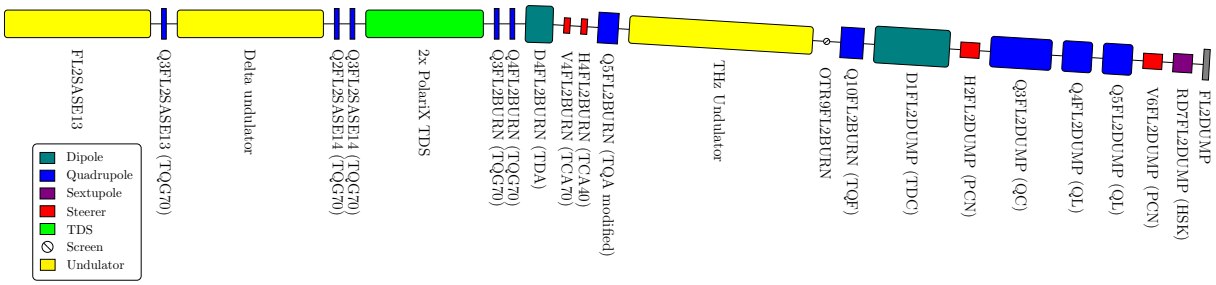

Figure 6.8: Layout of the FLASH2 dump beam line with THz undulator installed. The elements are plotted to scale, the drift spaces are not plotted to scale. The name of each element is indicated below each element. For magnets the name of the magnet type is indicated in parentheses. The electron beam travels from left to right.

Table 3: Values of Optical Functions and Resolutions for Longitudinal Phase Space Measurement Optics with THz Undulator. The Center of the TDSs is at s_1, the Screen is at s_2.

Optics	Regular operation		Delta undulator operation		Single bunch operation	
Mode	Standard	Low charge	Standard	Low charge	Standard	Low Charge
$\beta_y(s_1)$ /m	11.6		7.3		39.6	
$\beta_y(s_2)$ /m	19.9		23.7		2.0	
$\Delta\Psi_y$ /2π	0.25		0.25		0.25	
$\beta_x(s_2)$ /m	2.3		3.2		2.0	
$\eta_x(s_2)$ /m	0.200		0.194		0.171	
S	107.9		93.5		63.9	
R_t /fs	4.9	2.8	6.2	3.6	2.7	1.5
R_δ /10^{-4}	2.7	1.6	3.3	1.9	3.0	1.7

the single bunch optics are used.

Accelerator Optics without THz Undulator

As, currently, the THz undulator cannot be integrated in the FLASH2 beam line, the beam line in this section can be optimized for the PolariX TDSs. The previously modified TQA magnet, see Fig. 6.7, is kept and one additional quadrupole is inserted into the beam line. With this the optics matching can be done with two quadrupoles upstream of the TDSs (one if the Delta undulator is used), five quadrupoles between the TDSs and the screen, and four quadrupoles in between the screen and the dump, c.f. Fig. 6.10. The quadrupole upstream of the TDSs which would have been inserted with the THz undulator is no longer needed. In its place, two steerers will be inserted to control the beam orbit at the TDS entrance and ensure the beam passes on-axis through the two cavities.

The design optical functions between the last FLASH2 undulator and the FLASH2 dump are plotted in Fig. 6.11. The values of the optical functions at the TDSs and at the screen as well as the resolutions for all three cases are shown in Table 4. For low charge operation a temporal resolution of 1.7 fs and an energy resolution of $1.6 \cdot 10^{-4}$ can be achieved simultaneously when the single bunch optics are used.

As described in Section 4.1 the TDSs induce an energy spread in the electron bunch. In the

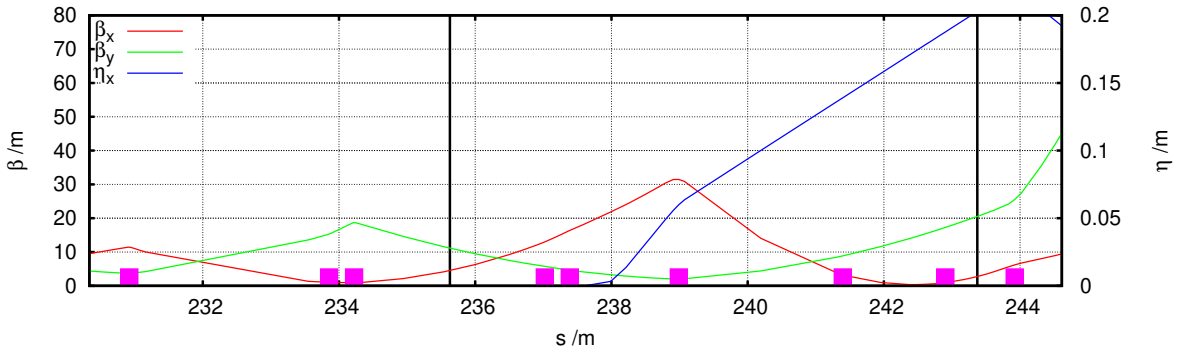

(a) Regular operation.

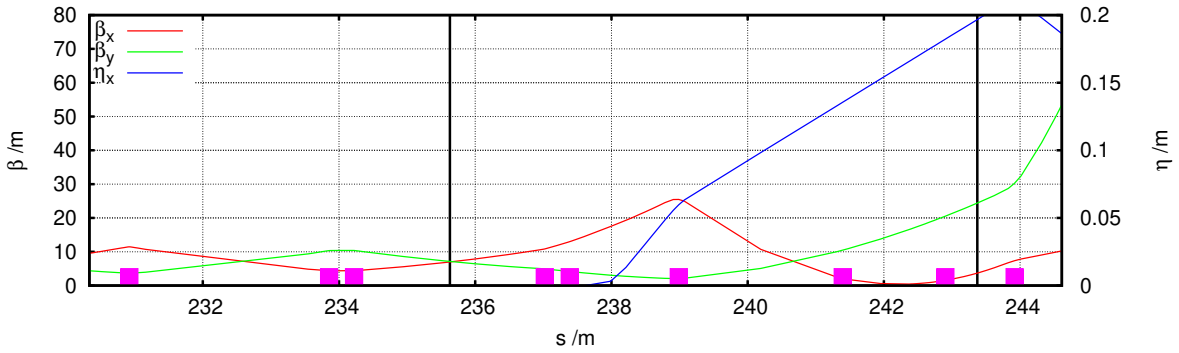

(b) Regular operation with Delta undulator.

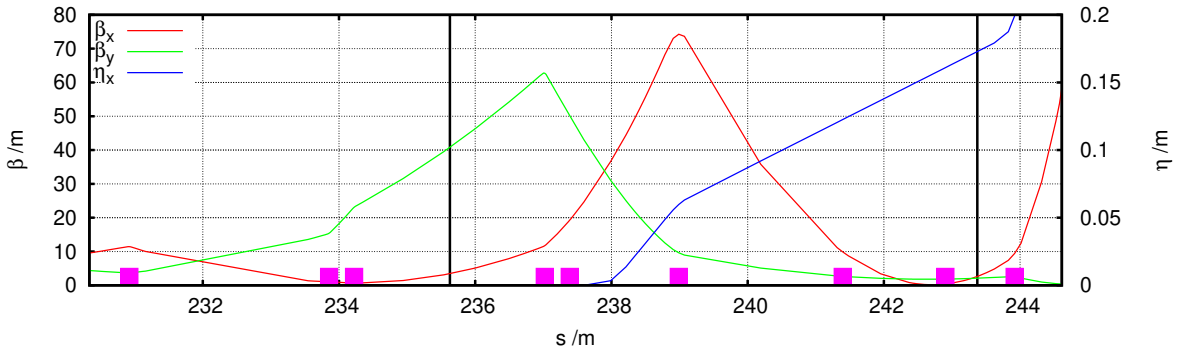

(c) Single bunch operation.

Figure 6.9: Beta functions in both planes and horizontal dispersion between the last FLASH2 undulator and the last FLASH2 dipole D1FL2DUMP with THz undulator installed. The center of the TDSs is at the first vertical black line, the screen at the second. The position of the quadrupoles is shown as pink boxes.

measurement, this induced energy spread σ_{IES} is added to the initial energy spread σ_δ when the TDSs are used. The main contribution of the induced energy spread is calculated using Eq. (4.11). The total measured slice energy spread is then $\sigma_{\delta,\mathrm{meas}} = \sqrt{\sigma_\delta^2 + R_E^2 + \sigma_{\mathrm{IES}}^2}$, for FLASH2 $\sigma_\delta \approx 5 \cdot 10^{-4}$.

Figures 6.12 and 6.13 show the temporal resolution, the energy resolution, and the induced energy spread against the normalized, vertical emittance of the electron bunch and the total deflecting voltage of the cavities, respectively. As can be seen in these figures, the measured slice energy spread is dominated by the induced energy spread. When the TDSs are operated at the maximum deflecting voltage, the induced energy spread can be two to three times higher

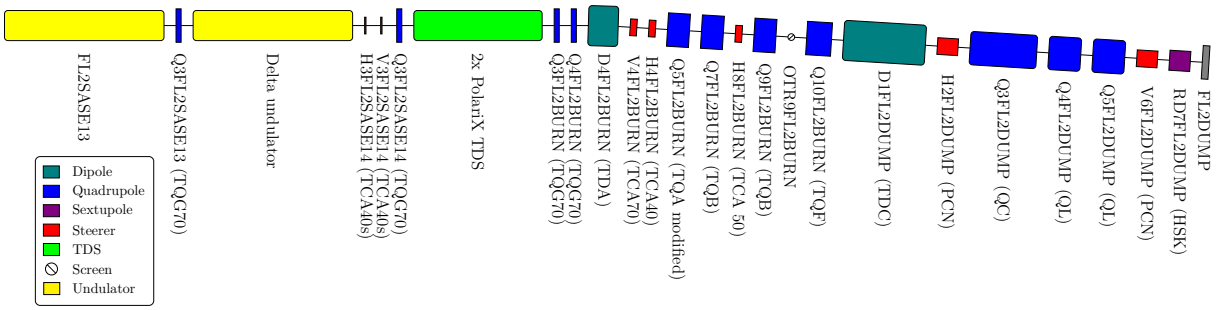

Figure 6.10: Layout of the FLASH2 dump beam line with no THz undulator installed. The elements are plotted to scale, the drift spaces are not plotted to scale. The name of each element is indicated below each element. For magnets the name of the magnet type is indicated in parentheses. The electron beam travels from left to right.

Table 4: Values of Optical Functions and Resolutions for Longitudinal Phase Space Measurement Optics without THz Undulator. The Center of the TDSs is at s_1, the Screen is at s_2.

Optics	Regular operation		Delta undulator operation		Single bunch operation	
Mode	Standard	Low charge	Standard	Low charge	Standard	Low Charge
$\beta_y(s_1)$ /m	17.5		11.0		31.2	
$\beta_y(s_2)$ /m	10.3		16.2		2.5	
$\Delta\Psi_y$ /2π	0.25		0.25		0.25	
$\beta_x(s_2)$ /m	1.0		1.0		1.8	
$\eta_x(s_2)$ /m	0.156		0.169		0.180	
S	95.6		94.8		62.5	
R_t /fs	4.0	2.3	5.1	2.9	3.0	1.7
R_δ /10^{-4}	2.3	1.3	2.1	1.2	2.7	1.6

than the slice energy spread of the bunches. This is an issue when reconstructing the longitudinal phase space densities of the electron bunches. The deflecting voltages can be lowered to accurately measure the slice energy spread directly by using the TDSs. As a trade-off, the longitudinal resolution is lowered, c.f. Fig. 6.13. Nonetheless, for the reconstruction of photon pulses this is only a minor issue, as both, the lasing-on and lasing-off electron bunches, are affected by the induced energy spread in the same way, c.f. Section 6.3.2.

The streaked beam size on the screen should be large enough to be resolved easily by the imaging system with a spatial resolution of $R_{\text{camera}} = 10\,\mu\text{m}$ [149], c.f. Section 6.1.3. The measured beam size by the imaging system can be approximated by $\sigma_{\text{measured}} \approx \sqrt{\sigma_0^2(s_2) + R_{\text{camera}}^2}$, where $\sigma_0(s_2)$ is the actual beam size at the screen.

Figure 6.14 shows the rms vertical beam size plotted against the deflecting voltage of the cavity for long and short bunches and for the three different optics. Bunches with a length of 100 fs rms streaked at the highest deflecting voltage are in the order of 1 mm rms when hitting the screen. These can be easily resolved. However, the screen size of 2 cm imposes a limit for longer bunches. When a 500 fs rms bunch is streaked using the highest deflecting voltage, the vertical beam size at the screen is more than 1.4 cm rms, and therefore the beam does not fit on the screen completely. As a result, these bunches have to be streaked using a lower deflecting

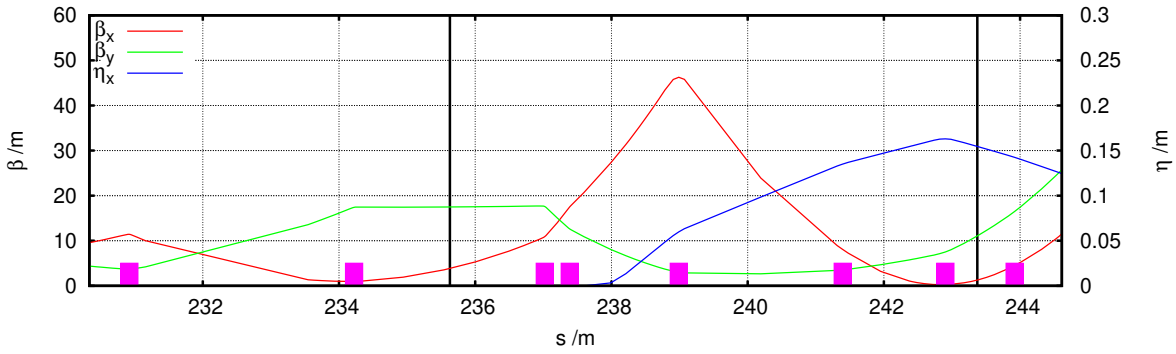

(a) Regular operation.

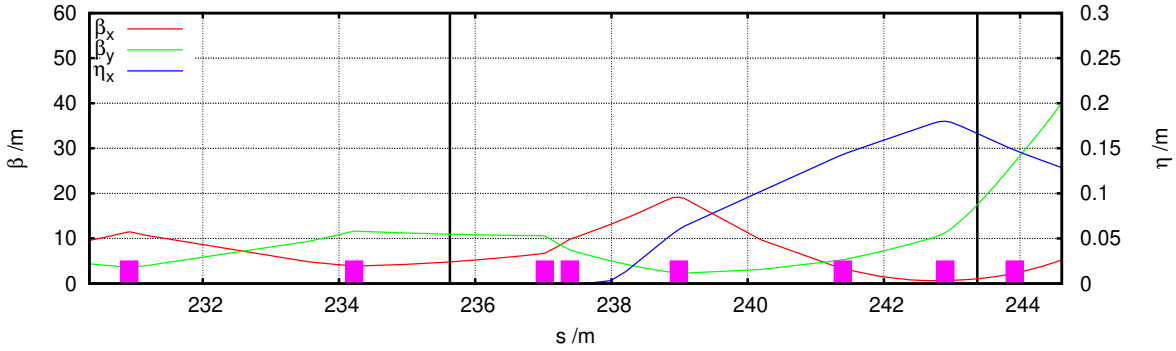

(b) Regular operation with Delta undulator.

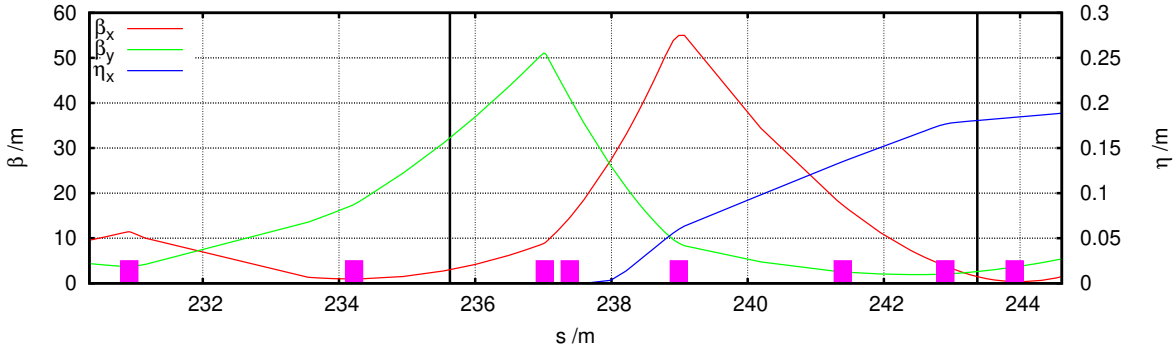

(c) Single bunch operation.

Figure 6.11: Beta functions in both planes and horizontal dispersion between the last FLASH2 undulator and the last FLASH2 dipole D1FL2DUMP with no THz undulator installed. The center of the TDSs is at the first vertical black line, the screen at the second. The position of the quadrupoles is shown as pink boxes.

voltage, which results in a lower temporal resolution. In contrast, short electron bunches with a length of 5 fs rms and a vertical rms beam size of 91 µm on the screen. Using the above given relation for the measured beam size, $\sigma_{\text{measured}} = 91.6\,\mu\text{m}$. The deviation between actual and measured beam size is less than 0.7 %. In general, the optical resolution of the imaging system does not impose any limits on the measurements.

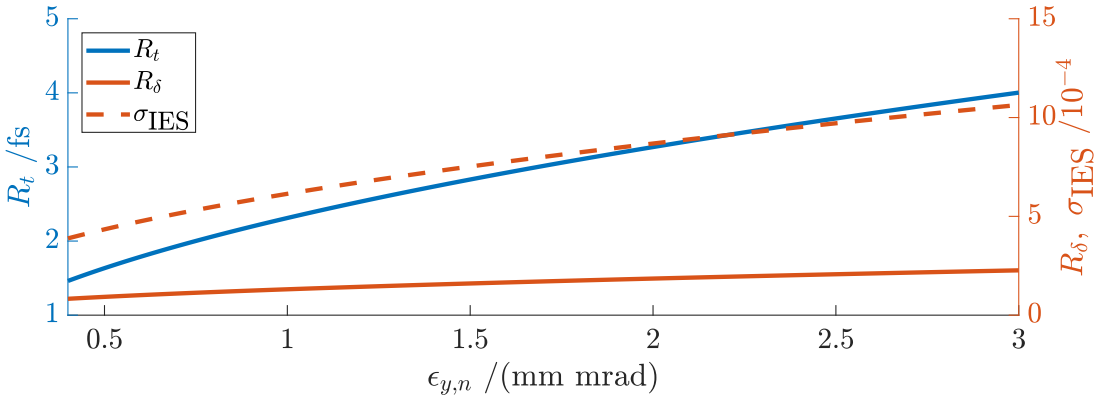

(a) Regular operation.

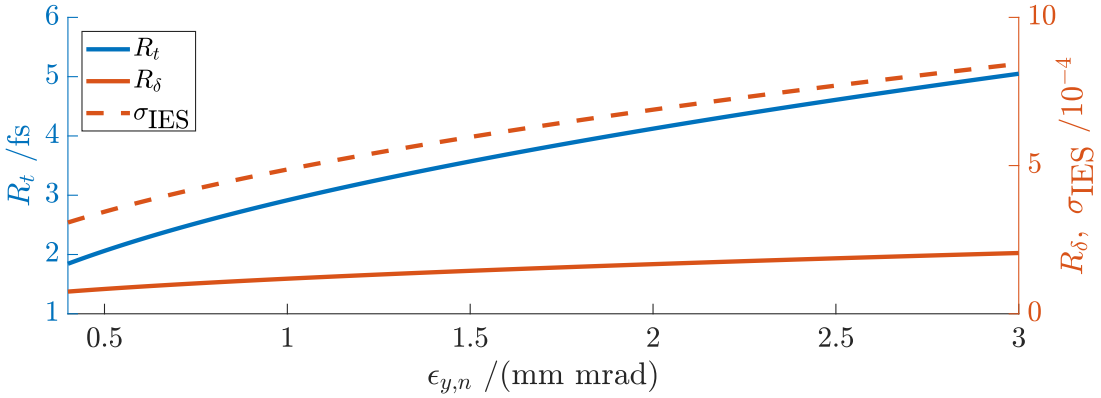

(b) Regular operation with Delta undulator.

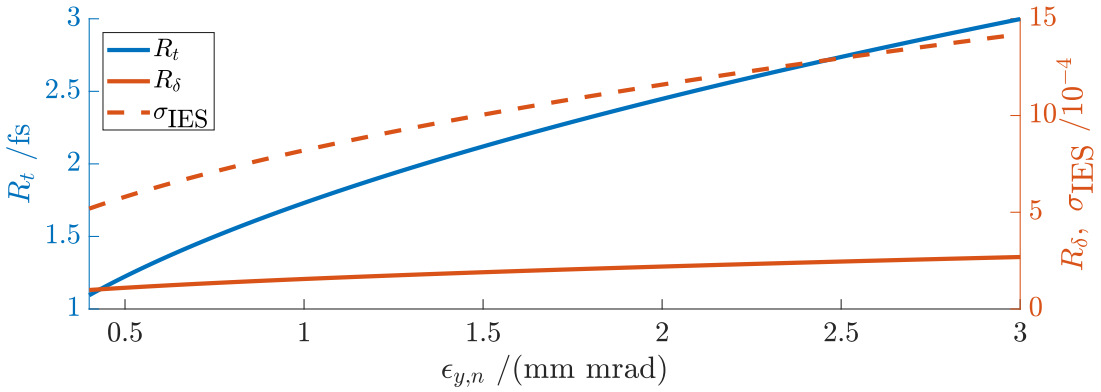

(c) Single bunch operation.

Figure 6.12: Temporal resolution, energy resolution and induced energy spread versus the normalized emittance of the electron bunch for the three different optics. The TDSs are operated at the maximum deflecting voltage of 34 MV.

6.2.2 Slice Emittance Measurement

The PolariX TDS comprises a variable polarization feature, as described in Section 6.1.1. This enables the possibility to perform slice emittance measurements in both planes using the same TDS. This is a unique feature of the PolariX TDS. To fully avail of this feature some design limitations of the beam line have to be considered. As only one screen station is available for the slice emittance measurement, a quadrupole scan has to be performed. Furthermore, the screen station is placed in a horizontally dispersive section of the beam line. In order to have

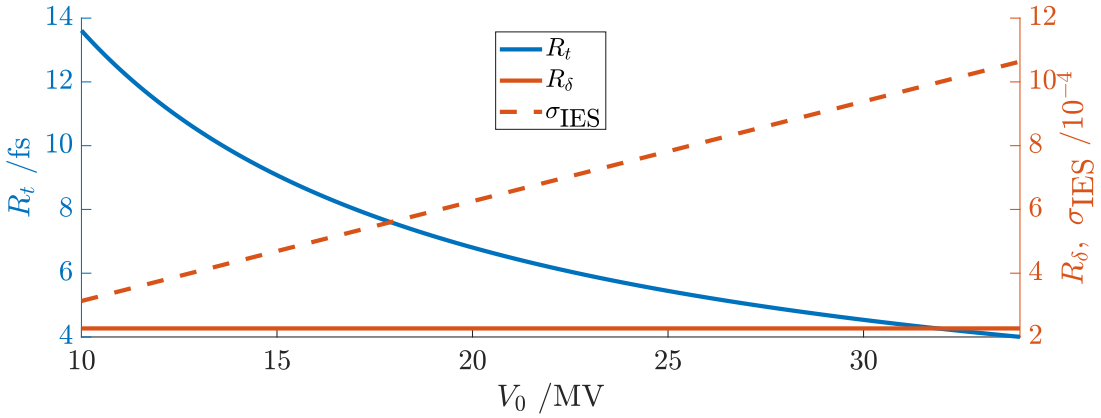

(a) Regular operation.

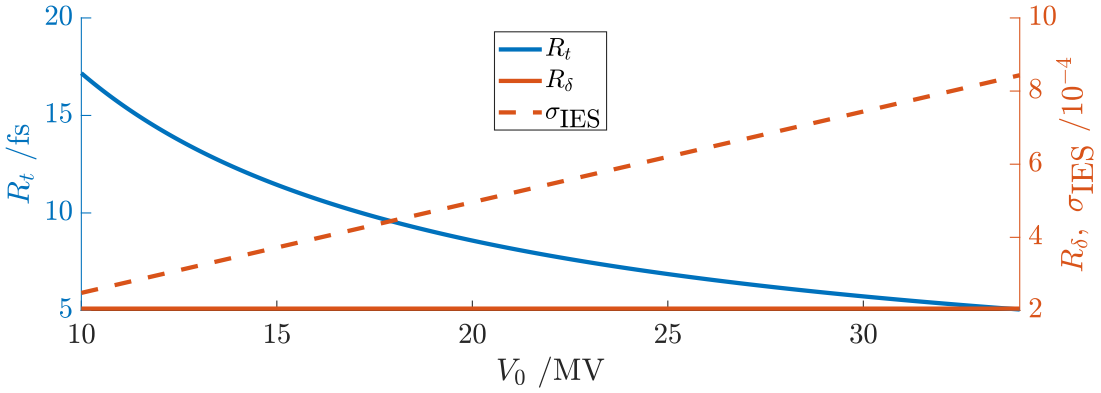

(b) Regular operation with Delta undulator.

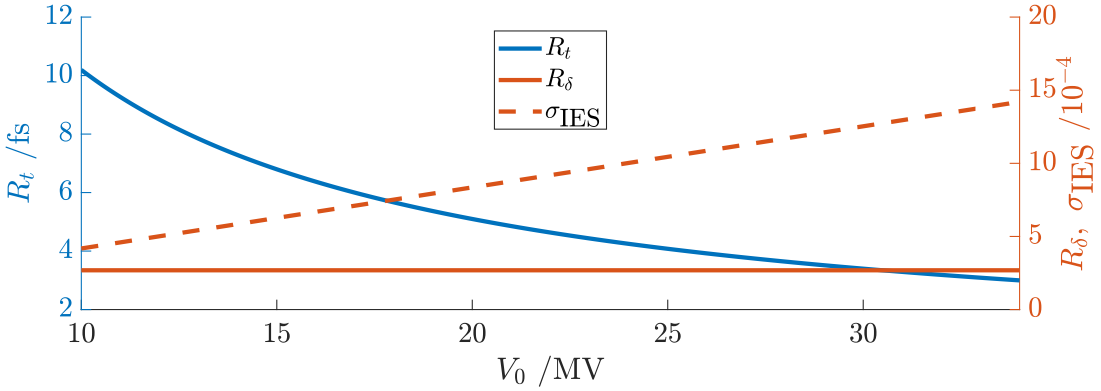

(c) Single bunch operation.

Figure 6.13: Temporal resolution, energy resolution and induced energy spread versus the deflecting voltage of the TDSs for the three different optics. The normalized emittance of the electron bunch is $\varepsilon_n = 3\,\mathrm{mm\,mrad}$.

a vanishing M_{16} and therefore be able to use Eq. (4.42) instead of Eq. (4.41), the horizontal dispersion at the screen at s_2 has to vanish: $\eta_x(s_2) = 0$.

For the optics matching, all quadrupoles between the last FLASH2 SASE undulator (FL2SASE13, c.f. Fig. 6.10) and the screen station are used. The emittance reconstruction point is directly upstream of the first quadrupole at s_0. To increase the accuracy of the measurement, seven different optics covering a total phase advance in the slice emittance measurement plane v between the screen s_2 and the reconstruction point s_0 of $\Delta\Psi_{v,\mathrm{total}} = \frac{3}{5}\pi$ are matched. In the streak direction u a high longitudinal resolution is required. This is again accomplished

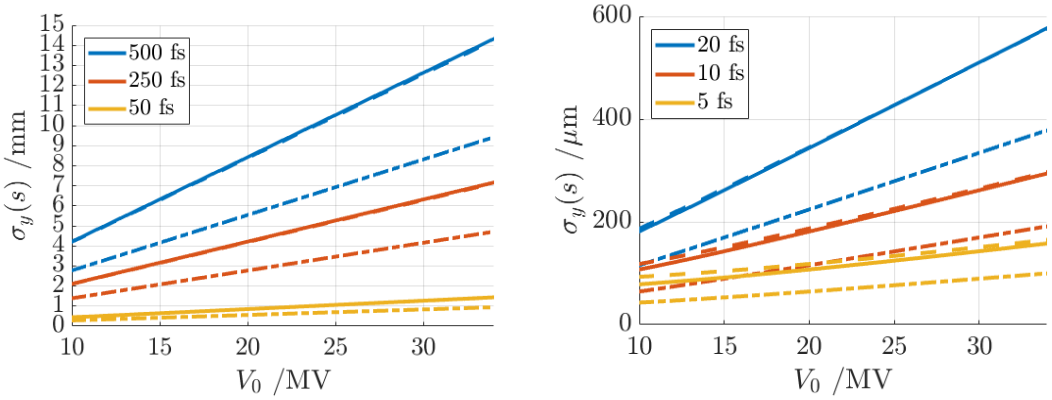

(a) Long bunches.

(b) Short bunches.

Figure 6.14: Beam size at the screen plotted against the deflecting voltage of the TDSs for long and short bunches and for all three different optics. The bunch length and the respective color are indicated in the legend. The beam sizes for the regular operation are plotted using solid lines, for the regular operation with Delta undulator using dashed lines, and for the single bunch operation using dashed-dotted lines, respectively.

by maximizing the beta function at the TDSs $\beta_u(s_1)$ and setting the phase advance between the screen s_2 and the TDSs s_1 in the streaking direction close to $\Delta\Psi_u = \pi/2 + n \cdot \pi, n \in \mathbb{N}_0$.

Tables 5 and 6 list the most important parameters for the slice emittance measurement in the horizontal and the vertical plane, respectively. In the vertical plane, the longitudinal resolution is comparable for all of the optics and is in the order of 4 fs. In the horizontal plane, the longitudinal resolutions differ slightly. They are in the range of 3.8 fs to 4.9 fs. The resolution of the emittance is given by the measurement error of the beam size at the screen. Simulations showing the slice emittance reconstruction are presented in Section 6.3.3.

Table 5: Values of Optical Functions and Resolutions for Slice Emittance Measurement in the Horizontal Plane. The Screen is at s_2.

$\Delta\Psi_x\ /2\pi$	$\beta_x(s_2)$ /m	$\eta_x(s_2)$ /m	R_t /fs	S
0.60	50.0	$1.9 \cdot 10^{-7}$	4.9	134
0.65	50.0	$5.4 \cdot 10^{-8}$	4.4	134
0.70	50.0	$2.3 \cdot 10^{-8}$	4.2	140
0.75	50.0	$1.5 \cdot 10^{-8}$	4.1	147
0.80	50.0	$1.1 \cdot 10^{-8}$	4.0	158
0.85	50.0	$8.7 \cdot 10^{-9}$	3.9	174
0.90	10.3	$2.1 \cdot 10^{-12}$	3.8	101

6.3 Tracking Simulation for FLASH2 PolariX TDSs

In the following, tracking simulations for the PolariX TDSs at FLASH2 are presented. The tracking simulations are carried out in elegant [154] and use a 1D CSR model but do not include space charge.

Table 6: Values of Optical Functions and Resolutions for Slice Emittance Measurement in the Vertical Plane. The Screen is at s_2.

$\Delta\Psi_y\ /2\pi$	$\beta_y(s_2)$ /m	$\eta_x(s_2)$ /m	R_t /fs	S
0.45	15.3	$-8.7\cdot10^{-7}$	4.0	-94
0.50	12.1	$-1.2\cdot10^{-6}$	4.1	-92
0.55	9.6	$-2.2\cdot10^{-7}$	4.0	-93
0.60	10.5	$-8.6\cdot10^{-7}$	4.1	-93
0.65	9.9	$-3.2\cdot10^{-9}$	4.1	-93
0.70	11.8	$-9.4\cdot10^{-10}$	4.2	-145
0.75	38.5	$-4.6\cdot10^{-11}$	4.2	-177

The lattices used for the tracking simulations are the ones described in the previous section without THz undulator. The start point is the end of the last FLASH2 SASE undulator (FL2SASE13, c.f. Fig. 6.10). Tracking simulations of longitudinal phase space density measurements, the reconstruction of photon pulses and slice emittance measurements using the PolariX TDSs at FLASH2 are presented in the following.

6.3.1 Longitudinal Phase Space Density Measurement

For the longitudinal phase space density reconstruction, different input distributions at the undulator exit are used. These are tracked through the TDSs and the following beam line up to the screen used for the measurements.

The vertical coordinate y, which is the streaking plane, at the screen at s_2 is converted to the arrival time Δt by applying Eq. (4.24). The horizontal coordinate $x(s_2)$ at the screen is converted to energy deviation ΔE by using $\Delta E = \Delta x(s_2)\cdot P_0 c/\eta_x(s_2)$, c.f. Eq. (4.29). The Shear parameter S is obtained by a phase scan of the TDSs. The vertical offset of the beam centroid is recorded against the phase of the TDSs and a linear fit yields the Shear parameter by using Eq. (4.18). An example for a phase scan is shown in Fig. 6.15(a). The dispersion at the screen $\eta_x(s_2)$ is obtained by a scan of the dipole current, i.e. by varying the dipole current I by small amounts of ε_I, and recording the horizontal offset of the beam centroid. The dispersion at the screen can then be obtained by a linear fit of Eq. (4.35). An example of a dipole current scan is shown in Fig. 6.15(b). The obtained values of $S = 95.6$ and $\eta_x(s_2) = 0.156\,\mathrm{m}$ are very close to the theoretical values found in Table 4.

In the following, tracking simulations of longitudinal phase space density measurements are presented. The input distributions used for Figs. 6.16 to 6.18 are the ones presented in Section 5.2. These were selected, as the 70 pC and the 38 pC cases show real bunches in the machine. The 20 pC case is one of the shortest bunches in the machine, and therefore used to show the limitations of the TDSs. As the emittance and the energy spread for this bunch were not optimized, another 20 pC bunch [155] is tracked, to demonstrate the possibilities of the TDSs when a low emittance bunch is reconstructed. Since FLASH is capable not only of producing short electron bunches with low charge but also long electron bunches with charges

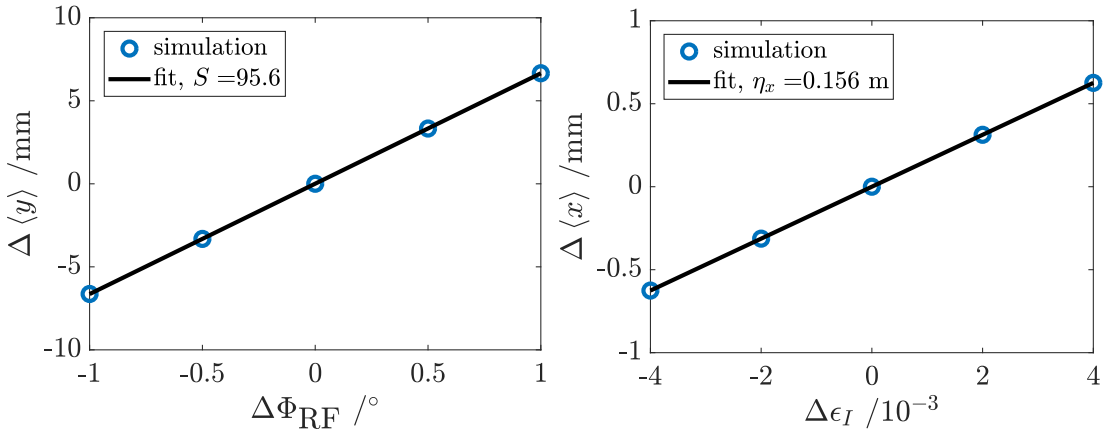

(a) TDS phase scan.

(b) Dipole current scan.

Figure 6.15: TDS phase scan and dipole current scan for the calibration of longitudinal phase space measurements.

of up to 1 nC, one example for a long 1 nC bunch is also shown.

The result of tracking simulations for the 70 pC bunch described in Section 5.2.2 is shown in Fig. 6.16. The initial slice energy spread of this electron bunch is in the order of $2.4 \cdot 10^{-4}$. As discussed before, c.f. Fig. 6.13 the energy measurement especially at high deflecting voltages is mainly dominated by the induced energy spread of the TDS. This effect can be seen in Fig. 6.16(b) which shows longitudinal phase space density at the TDS exit using the maximum deflecting voltage of 34 MV. Clearly, this also limits the reconstruction of the longitudinal phase space density at the screen. The reconstruction in Fig. 6.16(c) perfectly resembles the longitudinal phase space density at the TDS exit, but also here, the influence of the induced energy spread is visible. By reducing the deflecting voltage, this influence of the induced energy spread can be reduced at the cost of a lower resolution, c.f. Fig. 6.13. Figures 6.16(d) and 6.16(e) show the longitudinal phase space density at the TDS exit and the reconstruction at the screen using a deflecting voltage of 10 MV, respectively. Although still visible, the influence of the induced energy spread is reduced and the longitudinal phase space density can be measured more accurately.

The result of tracking simulations for the 38 pC bunch described in Section 5.2.2 are shown in Fig. 6.17. The longitudinal phase space density at the undulator exit is plotted in Fig. 6.17(a). This electron bunch has a stronger energy chirp compared to the 70 pC bunch shown before, although the slice energy spread for most parts of the bunch is still in the order of $5.2 \cdot 10^{-4}$. Using high deflecting voltages, see Figs. 6.17(b) and 6.17(c), the measurement is still largely dominated by the induced energy spread, although the energy chirp can be reconstructed. By reducing the deflecting voltage to 20 MV this effect can again be reduced. By doing so, the two horns in the region of 0 fs to 40 fs become slightly visible, even though the influence of the induced energy spread is still clearly notable, c.f. Figs. 6.17(d) and 6.17(e). Additionally, the lower temporal resolution of 2.9 fs is not negligible for this bunch anymore. In the region from −40 fs to 0 fs the blurring leads to a widening of the reconstructed beam at the screen, the

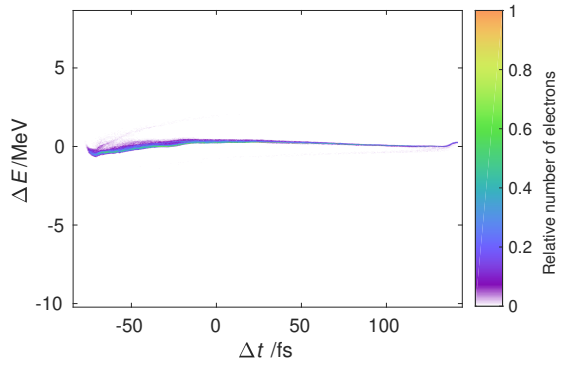

(a) At undulator exit.

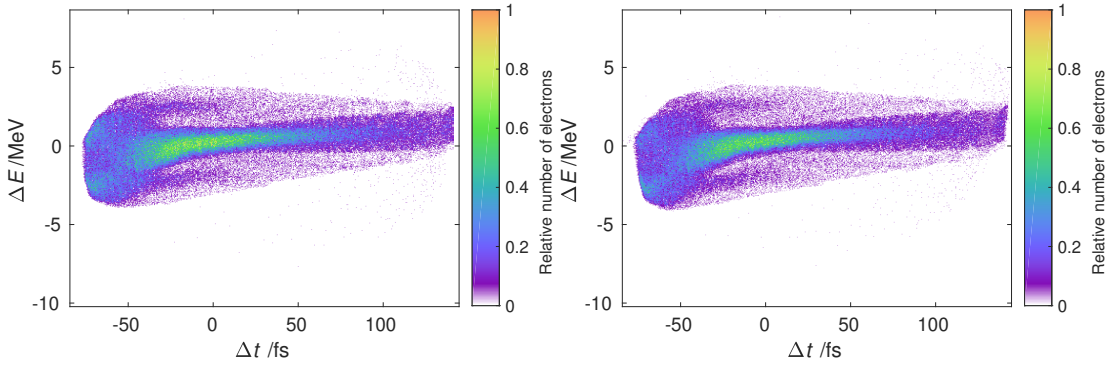

(b) At TDS exit, $V_0 = 34\,\mathrm{MV}$.

(c) Reconstructed, $V_0 = 34\,\mathrm{MV}$, single bunch operation. $R_t = 1.4\,\mathrm{fs}$, $R_\delta = 1.9 \cdot 10^{-4}$.

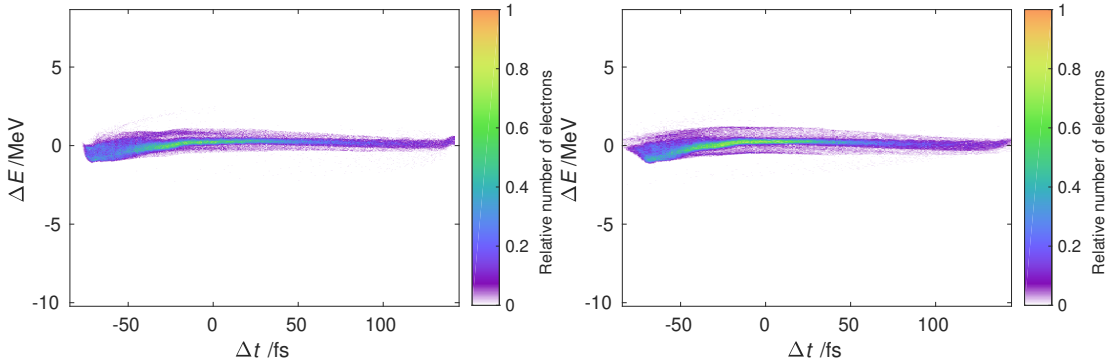

(d) At TDS exit, $V_0 = 10\,\mathrm{MV}$.

(e) Reconstructed, $V_0 = 10\,\mathrm{MV}$, regular operation. $R_t = 6.1\,\mathrm{fs}$, $R_\delta = 1.6 \cdot 10^{-4}$.

Figure 6.16: Longitudinal phase space density reconstruction using the 70 pC bunch described in Section 5.2.2 as input:
The longitudinal phase space density at the undulator exit is shown in (a). The longitudinal phase space density at the exit of the TDSs, i.e. including the induced energy spread, is shown in (b) and (d) for deflecting voltages of $V_0 = 34\,\mathrm{MV}$ and $V_0 = 10\,\mathrm{MV}$, respectively. The reconstructed longitudinal phase space density at the screen is shown in (c) and (e) for deflecting voltages of $V_0 = 34\,\mathrm{MV}$ and $V_0 = 10\,\mathrm{MV}$, respectively.

longitudinal phase space density at the exit of the TDSs and the reconstruction at the screen look slightly different in this region.

Figures 6.18 and 6.19 show the result of tracking simulations for bunches with a charge of 20 pC. The first bunch is described in Section 5.3, the second one has a bunch length of 13.8 fs rms, the mean energy is 1 GeV, and its longitudinal phase space density at the undulator exit can

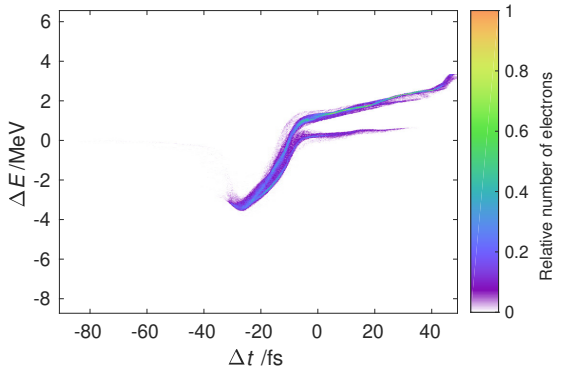

(a) At undulator exit.

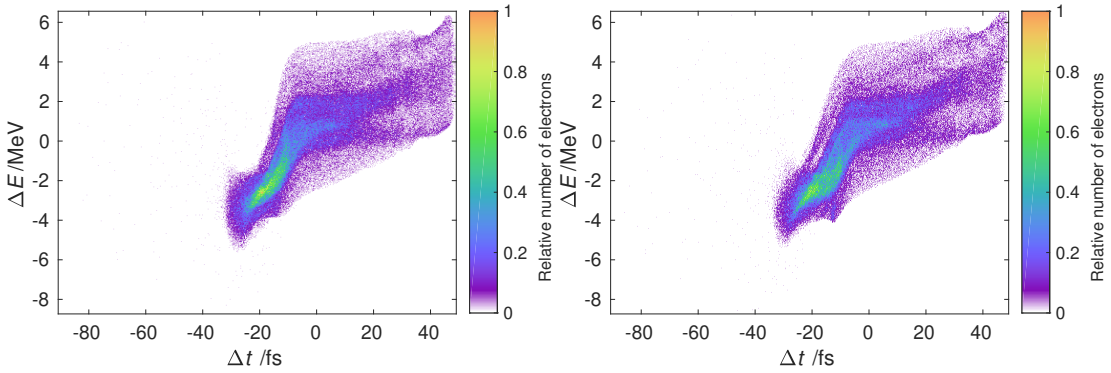

(b) At TDS exit, $V_0 = 34\,\mathrm{MV}$.

(c) Reconstructed, $V_0 = 34\,\mathrm{MV}$, single bunch operation. $R_t = 1.3\,\mathrm{fs}$, $R_\delta = 2.3 \cdot 10^{-4}$.

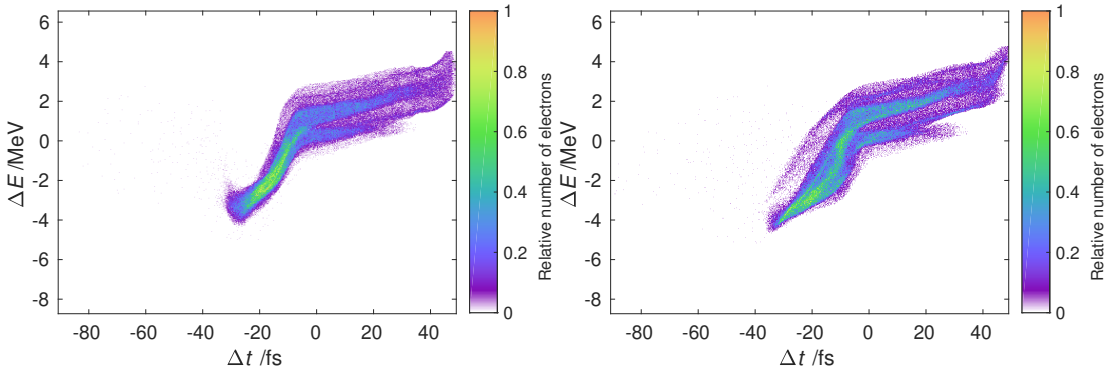

(d) At TDS exit, $V_0 = 20\,\mathrm{MV}$.

(e) Reconstructed, $V_0 = 20\,\mathrm{MV}$, regular operation. $R_t = 2.9\,\mathrm{fs}$, $R_\delta = 1.9 \cdot 10^{-4}$.

Figure 6.17: Longitudinal phase space density reconstruction using the 38 pC bunch described in Section 5.2.2 as input:
The longitudinal phase space density at the undulator exit is shown in (a). The longitudinal phase space density at the exit of the TDSs, i.e. including the induced energy spread, is shown in (b) and (d) for deflecting voltages of $V_0 = 34\,\mathrm{MV}$ and $V_0 = 20\,\mathrm{MV}$, respectively. The reconstructed longitudinal phase space density at the screen is shown in (c) and (e) for deflecting voltages of $V_0 = 34\,\mathrm{MV}$ and $V_0 = 20\,\mathrm{MV}$, respectively.

be seen in Fig. 6.19(a). As these bunches are very short, the temporal resolution plays a crucial role. When using a deflecting voltage of 34 MV the energy measurement is again dominated by the induced energy spread, although less severe than for the bunches before due to the low emittance of the bunches. The longitudinal phase space densities at the TDS exit are shown in Figs. 6.18(b) and 6.19(b). Again, the induced energy spread at the TDS exit is clearly visible in

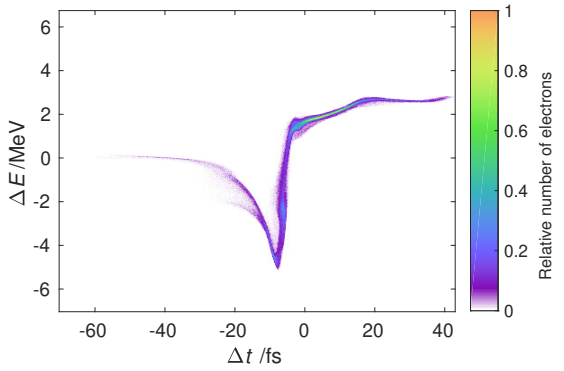

(a) At undulator exit.

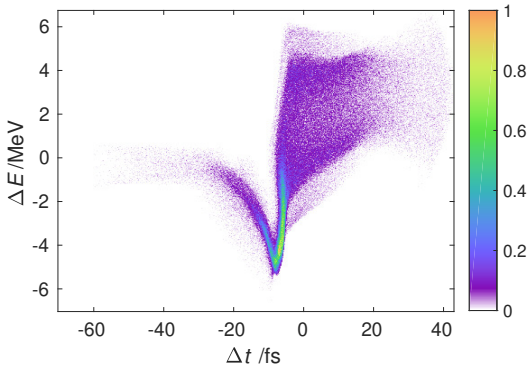

(b) At TDS exit, $V_0 = 34\,\mathrm{MV}$.

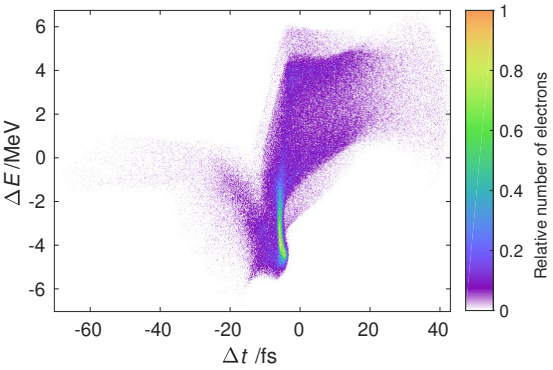

(c) Reconstructed, $V_0 = 34\,\mathrm{MV}$, single bunch operation. $R_t = 1.6\,\mathrm{fs}$, $R_\delta = 2.0 \cdot 10^{-4}$.

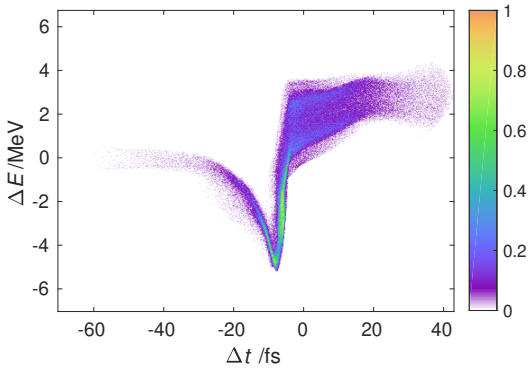

(d) At TDS exit, $V_0 = 20\,\mathrm{MV}$.

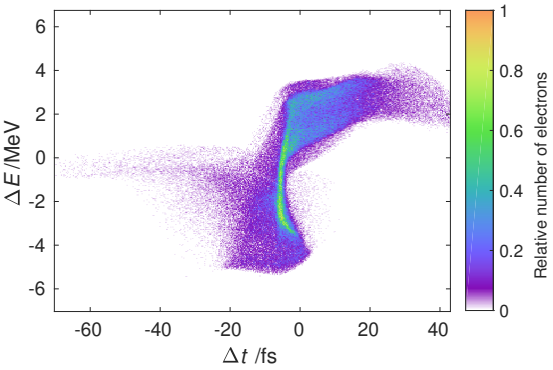

(e) Reconstructed, $V_0 = 20\,\mathrm{MV}$, regular operation. $R_t = 3.6\,\mathrm{fs}$, $R_\delta = 1.7 \cdot 10^{-4}$.

Figure 6.18: Longitudinal phase space density reconstruction using the 20 pC bunch described in Section 5.3 as input:
The longitudinal phase space density at the undulator exit is shown in (a). The longitudinal phase space density at the exit of the TDSs, i.e. including the induced energy spread, is shown in (b) and (d) for deflecting voltages of $V_0 = 34\,\mathrm{MV}$ and $V_0 = 20\,\mathrm{MV}$, respectively. The reconstructed longitudinal phase space density at the screen is shown in (c) and (e) for deflecting voltages of $V_0 = 34\,\mathrm{MV}$ and $V_0 = 20\,\mathrm{MV}$, respectively. This is bunch "A" in Tables 7 and 8.

comparison to the undulator exit. Additionally, even for resolutions of 1.6 fs and 0.8 fs differences between the longitudinal phase space density at the TDS exit and the reconstructions at the screen are visible, c.f. Figs. 6.18(c) and 6.19(c), respectively. In the core part of both bunches, i.e. between −20 fs and 0 fs for the first bunch and −10 fs and 10 fs for the second bunch, the longitudinal resolution limits the resolving capacity of the measurement. The measurement is

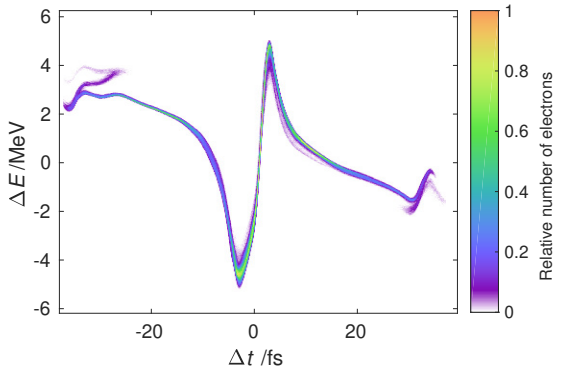

(a) At undulator exit.

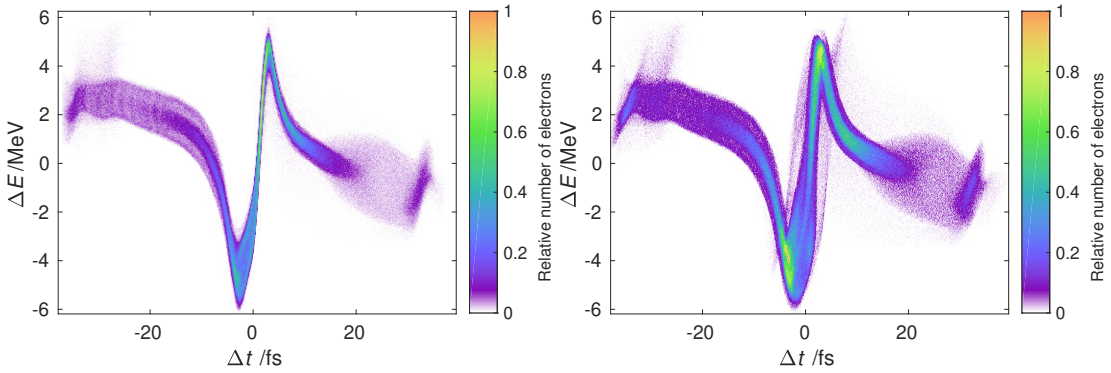

(b) At TDS exit, $V_0 = 34\,\mathrm{MV}$.

(c) Reconstructed, $V_0 = 34\,\mathrm{MV}$, single bunch operation. $R_t = 0.8\,\mathrm{fs}$, $R_\delta = 1.4 \cdot 10^{-4}$.

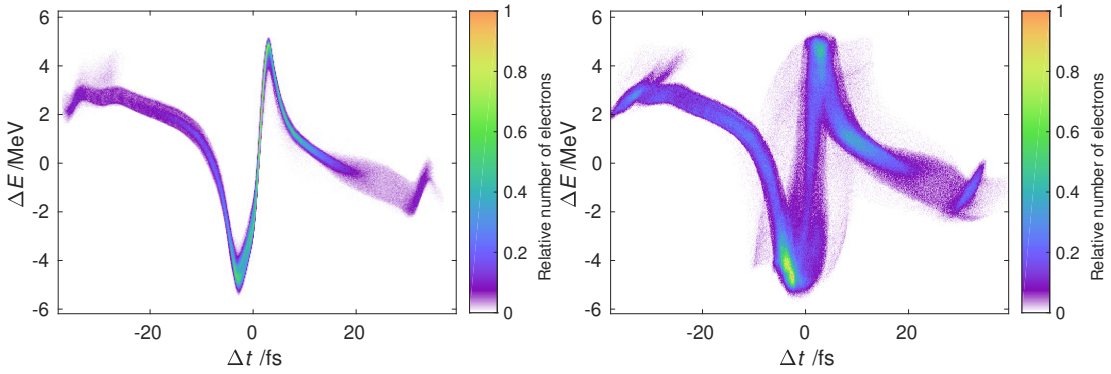

(d) At TDS exit, $V_0 = 20\,\mathrm{MV}$.

(e) Reconstructed, $V_0 = 20\,\mathrm{MV}$, regular operation. $R_t = 1.9\,\mathrm{fs}$, $R_\delta = 1.2 \cdot 10^{-4}$.

Figure 6.19: Longitudinal phase space density reconstruction using a 20 pC bunch [155] as input:
The longitudinal phase space density at the undulator exit is shown in (a). The longitudinal phase space density at the exit of the TDSs, i.e. including the induced energy spread, is shown in (b) and (d) for deflecting voltages of $V_0 = 34\,\mathrm{MV}$ and $V_0 = 20\,\mathrm{MV}$, respectively. The reconstructed longitudinal phase space density at the screen is shown in (c) and (e) for deflecting voltages of $V_0 = 34\,\mathrm{MV}$ and $V_0 = 20\,\mathrm{MV}$, respectively. This is bunch "B" in Tables 7 and 8.

blurred when compared to the longitudinal phase space density at the TDS exit. Lowering the streaking voltage to 20 MV does not ameliorate the blurring of the energy distribution at the screen, since the bunches are short and the temporal resolutions is lowered to 3.6 fs and 1.9 fs. As we will also see in Table 8, the measured mean energy spread of the reconstruction is the same for the bunch reconstructions in Figs. 6.19(c) and 6.19(e), although the induced energy

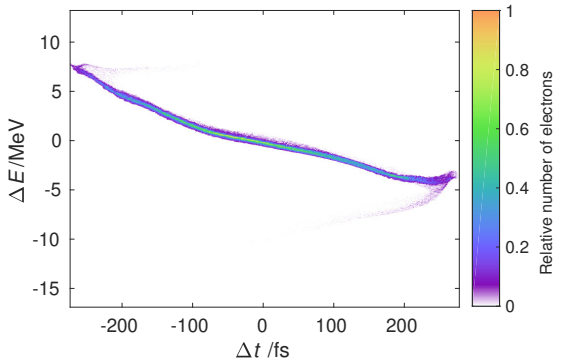

(a) At undulator exit.

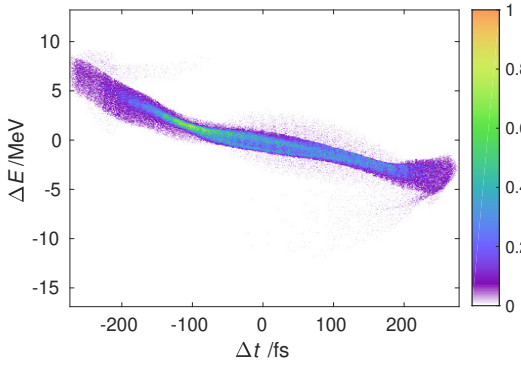

(b) At TDS exit, $V_0 = 20\,\mathrm{MV}$.

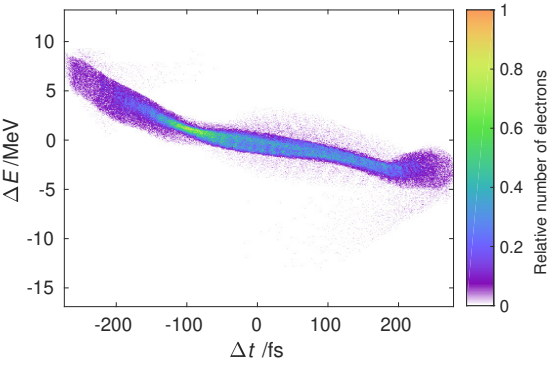

(c) Reconstructed, $V_0 = 20\,\mathrm{MV}$, regular operation. $R_t = 4.6\,\mathrm{fs}$, $R_\delta = 2.7 \cdot 10^{-4}$.

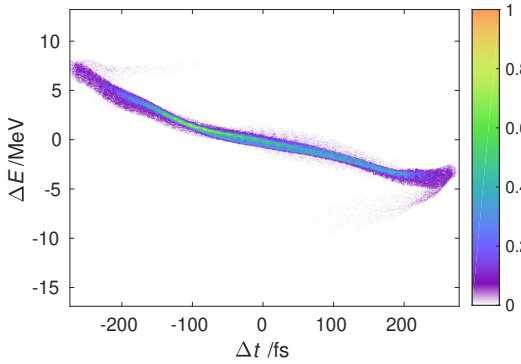

(d) At TDS exit, $V_0 = 10\,\mathrm{MV}$.

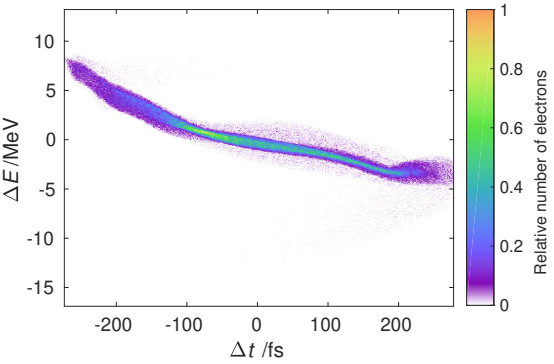

(e) Reconstructed, $V_0 = 10\,\mathrm{MV}$, regular operation. $R_t = 9.3\,\mathrm{fs}$, $R_\delta = 2.7 \cdot 10^{-4}$.

Figure 6.20: Longitudinal phase space density reconstruction using a 1 nC bunch [155] as input: The longitudinal phase space density at the undulator exit is shown in (a). The longitudinal phase space density at the exit of the TDSs, i.e. including the induced energy spread, is shown in (b) and (d) for deflecting voltages of $V_0 = 20\,\mathrm{MV}$ and $V_0 = 10\,\mathrm{MV}$, respectively. The reconstructed longitudinal phase space density at the screen is shown in (c) and (e) for deflecting voltages of $V_0 = 20\,\mathrm{MV}$ and $V_0 = 10\,\mathrm{MV}$, respectively.

spread is reduced, which can be seen when comparing Figs. 6.19(b) and 6.19(d). Due to the limited longitudinal resolution of the measurement, electrons move to adjacent slices in the reconstruction. Since the energy depends strongly on the longitudinal position for this particular bunch, this leads to an increase of the measured energy spread at the screen, regardless of the lower induced energy spread by the TDS. Such short electron bunches should be measured at the highest deflecting voltage, yielding the highest temporal resolution, at the cost of worsening

the energy resolution.

Figure 6.20 shows the result of tracking simulations for a bunch with a charge of 1 nC. The mean energy of the electron bunch is 1 GeV, the bunch length is 135.2 fs, and the longitudinal phase space density can be found in Fig. 6.20(a). As this bunch is rather long, one does not need to have the highest achievable resolution, also as the beam might be too large to fit on the screen, c.f. Fig. 6.14. At a deflecting voltage of 20 MV the resolution is 4.2 fs and the influence of the induced energy spread is not negligible, c.f. Figs. 6.20(b) and 6.20(c). By lowering the voltage to 10 MV, the resolution decreases to 8.5 fs, which is still sufficient to resolve the basic structures of this rather long electron bunch. However, the slice energy spread is only increased by a factor of about 2, the longitudinal phase space density for such long bunch can be accurately reconstructed, c.f. Figs. 6.20(d) and 6.20(e).

To summarize, the bunch length and the mean energy spread at the undulator exit and reconstructed using the TDSs are compared in Tables 7 and 8. The deviations of the reconstructed bunch lengths are minute. However, the mean energy spread reconstructed at the screen increases up to a factor of 13 when using a deflecting voltage of 34 MV due to the induced energy spread by the TDS. As previously discussed, this can be reduced by lowering the deflecting voltage.

Table 7: Comparison of the Bunch Length at the Undulator End and the Reconstructed One Using the TDSs.

	σ_t/fs at undulator	σ_t/fs reconstructed, $V = 34$ MV	σ_t/fs reconstructed, $V = 20$ MV	σ_t/fs reconstructed, $V = 10$ MV
70 pC	54.2	54.2		54.6
38 pC	19.2	19.2	19.3	
20 pC A	12.1	12.2	16.6	
20 pC B	13.8	13.8	13.8	
1 nC	135.3		135.4	135.6

Table 8: Comparison of the Energy Spread at the Undulator End and the Reconstructed One Using the TDSs.

	$\langle\sigma_E\rangle$/keV at undulator	$\langle\sigma_E\rangle$/keV reconstructed, $V = 34$ MV	$\langle\sigma_E\rangle$/keV reconstructed, $V = 20$ MV	$\langle\sigma_E\rangle$/keV reconstructed, $V = 10$ MV
70 pC	82	1038		269
38 pC	328	1247	746	
20 pC A	212	1495	1039	
20 pC B	181	790	790	
1 nC	359		819	636

The previously shown tracking simulations demonstrate the feasibility of longitudinal phase space density measurements at FLASH2. Although the induced energy spread at high deflecting voltages is clearly visible, most of the main features of the electron bunches can be recon-

structed. The high resolution of the TDSs permits to accurately measure the longitudinal phase space density even of ultra-short electron bunches.

6.3.2 Reconstruction of Photon Pulses

The FEL process is simulated using Genesis 1.3 [132]. The particle distribution at the end of the exponential regime is then extracted and used to perform the photon pulse reconstruction. Additional to each lasing bunch, one bunch is tracked through the opened undulators to obtain the lasing-off particle distribution at the end of the undulator section. This lasing-off electron bunch serves then as comparison for both, the energy loss and energy spread method, c.f. Section 4.3.3.

The goal of the photon pulse reconstruction is to retrieve the temporal photon pulse distribution given by Genesis 1.3. In the following figures, this is plotted using a black line.

Firstly, the photon pulses are reconstructed directly at the end of the undulators. The energy loss and the energy spread increase of the bunches are calculated from the actual phase space density. The temporal power profiles are then calculated by means of Eqs. (4.38) and (4.39). In the following figures, these are plotted using a red solid line. This is the limit of what the reconstruction using the TDSs (see below) could achieve with a perfect temporal and energy resolution, as no additional information about the X-ray power profile can be extracted from the longitudinal phase space density. It is possible, that this distribution does not perfectly resemble the photon pulse from the Genesis 1.3 simulation. This can happen due to slippage effects, meaning that the position where the energy of the electron bunch is transferred to the light wave does not match with the position in the final photon pulse, as the photon pulse slips ahead of the electron bunch. Additionally, the energy lost by the particles may be too small so that it cannot be distinguished from energy differences which occur due to jitter.

Secondly, for the actual photon pulse reconstruction using the TDS, the electron bunches are tracked using elegant [154] through the TDSs and the transverse distribution at the screen is analyzed. Both transverse coordinates are transformed to the arrival time Δt and the energy deviation ΔE as described in the previous section. These reconstructed longitudinal phase space densities are then used as input for the energy spread and energy loss method, c.f. Section 4.3.3. The respective photon pulse reconstructions at the screen are plotted using solid blue lines. With a perfect longitudinal and energy resolution, the reconstruction at the screen would perfectly resemble the reconstruction at the undulator exit. As this is not the case and also the induced energy spread and collective effects such as CSR deteriorate the reconstruction, differences will be observed.

To give comparable examples for long and short pulses, Gaussian bunches with a length of 100 fs and 23 fs at beam energies of 1200 MeV and 700 MeV are tracked. The corresponding wavelengths are 6.6 nm and 19.4 nm, respectively. Additionally, the photon pulses described in Section 5.2 are reconstructed to show possible limitations of the reconstruction. One example for all settings is shown in the following using the highest deflecting voltage and the short pulse

optics to obtain the highest resolution possible.

The results of photon pulse reconstructions for bunches of 100 fs rms are shown in Figs. 6.21 and 6.22 for electron beam energies of 1200 MeV and 700 MeV, respectively.

The reconstruction at the end of the undulator section with a perfect resolution for 1200 MeV, c.f. Fig. 6.21(a), closely resembles the actual photon pulse. For the reconstruction at the screen using the TDSs the influence of the limited temporal resolution is visible, although the effect is rather small. Most of the SASE spikes are still visible in the reconstruction, only the separation of spikes that are very close to one another is blurred. If the energy spread method is used, already the reconstruction at the undulator exit differs from the actual photon pulse, c.f. Fig. 6.21(b), as the energy spread increase due to the SASE process is larger than what one would expect from the model. As mentioned in [119], this is due to the fact that the wavelength in this case is higher than for the derivations leading to Eq. (4.39) given therein. This is especially evident at the outer edges of the photon pulse, where the photon pulse power is small, but the energy spread is increased largely. Nonetheless, the reconstruction at the screen is able to retrieve the reconstruction at the undulator exit, although of course again with a limited resolution.

The same is true for the reconstruction of the photon pulse for the electron bunch with an energy of 700 MeV and using the energy spread method. The energy spread at the outer edges of the photon pulses increases more than it is expected from the model [119], c.f. Fig. 6.22(b). Additionally, for this photon pulse the reconstruction using the energy loss method is also more difficult than for the 1200 MeV bunch, as can be seen in Fig. 6.22(a). As the spikes are very close to one another and slippage effects take place, already the reconstruction at the undulator exit is unable to retrieve the individual spikes. Of course, this is then also true for the reconstruction at the screen. The retrieved rms pulse duration is slightly higher for the energy spread method due to these effects. The actual rms pulse duration is 46.4 fs, the reconstructed ones at the undulator exit and the screen are 53.6 fs and 57.5 fs, respectively.

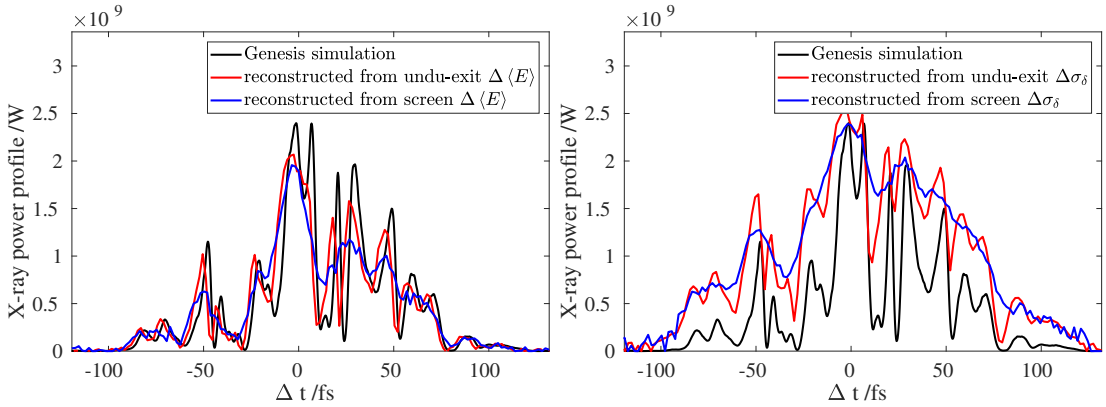

(a) Using the energy loss method.

(b) Using the energy spread method.

Figure 6.21: Photon pulse reconstruction of a Gaussian bunch with a bunch length of 100 fs rms at an energy of 1200 MeV using the regular optics without Delta undulator and a deflecting voltage of 20 MV. The wavelength is 6.6 nm.

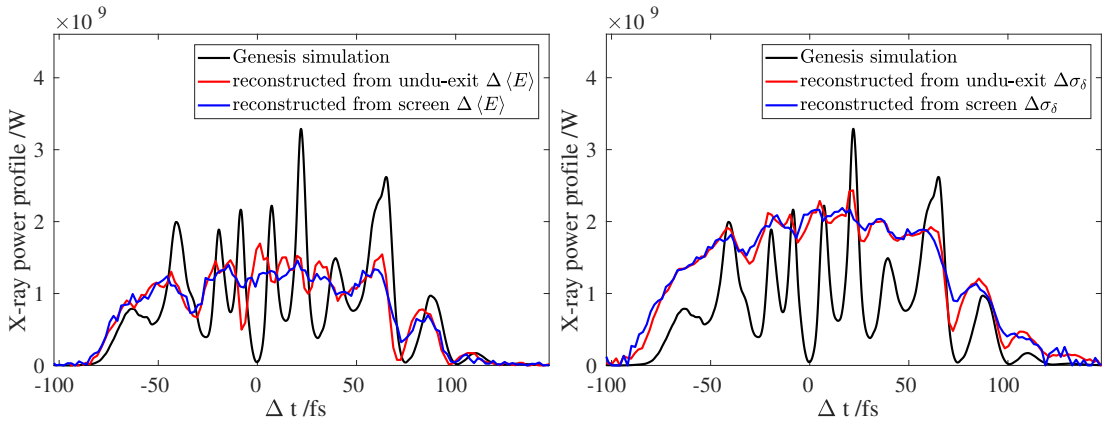

(a) Using the energy loss method.

(b) Using the energy spread method.

Figure 6.22: Photon pulse reconstruction of a Gaussian bunch with a bunch length of 100 fs rms at an energy of 700 MeV using the regular optics without Delta undulator and a deflecting voltage of 20 MV. The wavelength is 19.4 nm.

The reconstruction of two shorter pulses of 23 fs rms at electron energies of 1200 MeV and 700 MeV are shown in Figs. 6.23 and 6.24, respectively. If the energy loss method is used, the reconstruction at the undulator exit nearly perfectly resembles the actual photon pulse distribution, c.f. Fig. 6.23(a). The reconstruction at the screen also closely resembles the one at the undulator exit, but of course the limited resolution of 1.7 fs is again visible. If the energy spread method is used, the reconstruction overestimates the power of smaller, as again, the energy spread growth in this region is larger than expected from the model [119], c.f. Fig. 6.23(b). Also the reconstruction at the screen shows this behavior. The photon pulse for the electron bunch with an energy of 700 MeV shows a large single SASE spike with smaller side peaks, see Fig. 6.24. Using the energy spread method, the photon pulse shape at the undulator exit is a little different to the actual photon pulse, c.f. Fig. 6.24(a). The power of the main spike is also drawn from electrons which are now a little behind the main spike due to slippage effects. Therefore, the main spike is reconstructed with less power and the trailing spike with a little more power at the undulator exit. Nonetheless, the reconstruction at the screen perfectly resembles the reconstruction at the undulator due to the very high resolution of 1.3 fs. Also when the energy spread method is used, the main spike is reconstructed with less power, due to the same slippage effects, c.f. Fig. 6.24(b), and the aforementioned higher increase of the energy spread than it is expected by the model [119]. Yet, the reconstruction at the screen again perfectly resembles the reconstruction at the undulator exit due to the high resolution.

The reconstruction results for one of the ten statistical seed for the 70 pC bunch are shown in Fig. 6.25. For both methods, it can be observed that the reconstructed photon pulse is shifted slightly to the left, as the photon pulse slips ahead of the position where it withdrew energy from the electron bunch. Using the energy loss method the reconstruction is able to retrieve the photon pulse very accurately, c.f. Fig. 6.25(a). The right spike between −25 fs and 0 fs resembles the reconstructed one closely. For the large left spike and the smaller adjacent one between −60 fs and −25 fs the reconstruction looks slightly different. For the small adjacent

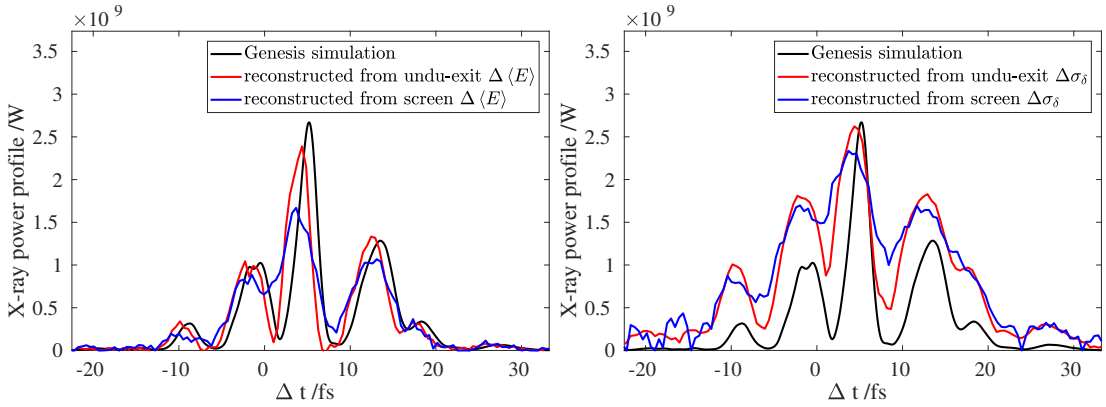

(a) Using the energy loss method. (b) Using the energy spread method.

Figure 6.23: Photon pulse reconstruction of a Gaussian bunch with a bunch length of 23 fs rms at an energy of 1200 MeV using the short pulse optics and a deflecting voltage of 34 MV. The wavelength is 6.6 nm.

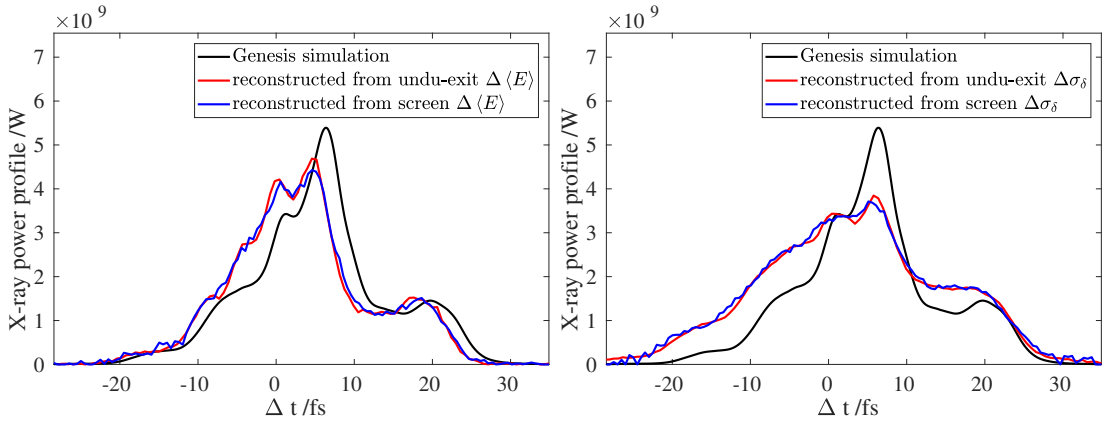

(a) Using the energy loss method. (b) Using the energy spread method.

Figure 6.24: Photon pulse reconstruction of a Gaussian bunch with a bunch length of 23 fs rms at an energy of 700 MeV using the short pulse optics and a deflecting voltage of 34 MV. The wavelength is 19.4 nm.

spike more power is reconstructed than there actually is in the photon pulse and less power is reconstructed for the large spike. This happens, because the large spike starts to grow early and slips ahead in the electron bunch. Therefore, the power in this part of the photon pulse is withdrawn at the position where the second smaller spike arises, but this reconstruction method is unable to retrieve this difference as explained before. Nonetheless, due to the high resolution of 1.4 fs the reconstruction at the screen is the same as the one at the undulator exit. The reconstruction using the energy spread method is more blurred, c.f. Fig. 6.25(b). This is again due to slippage effects and the high wavelength leading to a higher induced energy spread by the FEL process in regions, where the radiation process is started.

The reconstruction results for one of the ten statistical seed for the 38 pC bunch are shown in Fig. 6.26. The peak power of this photon pulse is roughly three times lower than for the 70 pC bunch, therefore the reconstruction is harder as less energy is lost by the electrons. Slight energy deviations for the electrons not induced by the lasing process but for example just due to

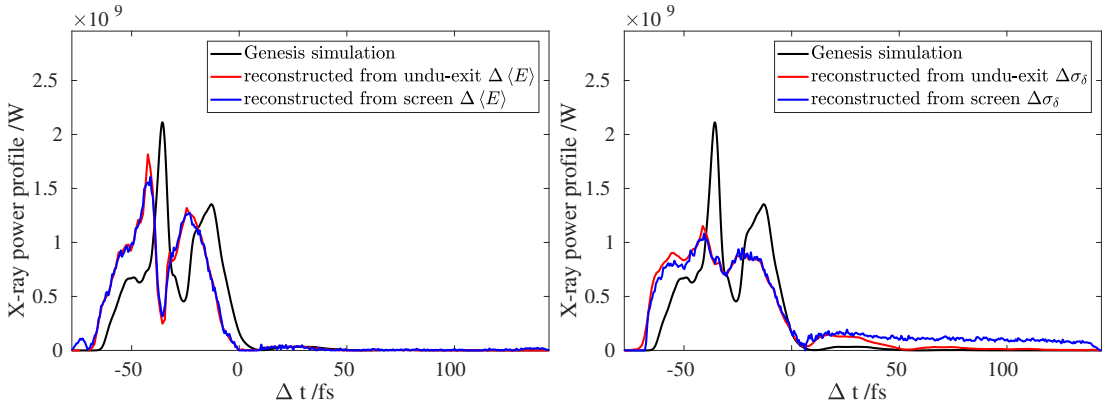

(a) Using the energy loss method. (b) Using the energy spread method.

Figure 6.25: Photon pulse reconstruction of the 70 pC electron bunch described in Section 5.2.2 using the short pulse optics and a deflecting voltage of 34 MV. This is Seed -11 from Fig. 5.10.

jitter might play a role and also the energy resolution affects the measurement. As can be seen in Fig. 6.26, these effects are still only minor for the 38 pC bunch. The reconstruction using the energy loss method resembles the photon pulse closely, c.f. Fig. 6.26(a), although again due to slippage, the photon pulse is reconstructed at another position within the bunch. The large main spike is retrieved by the reconstruction at the screen, the smaller side peak is reconstructed closer to the main spike due to the limited energy resolution of the measurement. For the reconstruction using energy spread method, c.f. Fig. 6.26(b), the same slippage effects as described before impact the reconstruction. The retrieved power of the smaller side peak is higher than the actual power in the photon pulse. Also here, differences between the reconstruction at the screen and at the undulator exit can be observed due to the limited energy resolution.

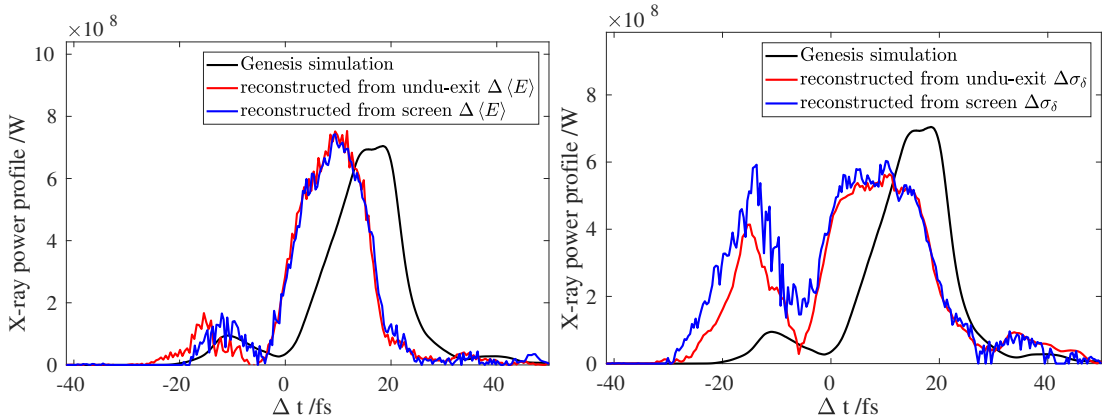

(a) Using the energy loss method. (b) Using the energy spread method.

Figure 6.26: Photon pulse reconstruction of the 38 pC electron bunch described in Section 5.2.2 using the short pulse optics and a deflecting voltage of 34 MV. This is Seed -21 from Fig. 5.15.

The reconstructions for one of the ten statistical seeds of the 20 pC bunch at wavelengths of 35.64 nm and 16.95 nm can be seen in Figs. 6.27 and 6.28, respectively. The aforementioned effects are even more severe for these bunches, as the energy lost by the electrons is even below the energy resolution of the measurement. Also, as both methods scale the energy loss

and the induced energy spread due to the FEL process by the current of the electron bunch, c.f. Eqs. (4.38) and (4.39), the large main spike with a peak current of more than 2 kA, that does not contribute to the lasing process, c.f. Section 5.3, deteriorates the reconstruction. Slight changes in the energy and the energy spread in the region of the spike due to jitter lead to large spikes in the reconstruction. For the photon pulse with a wavelength of 35.64 nm this effect is strongly visible for both, the reconstruction at the undulator exit and at the screen using both methods, c.f. Fig. 6.27. For the photon pulse with a wavelength of 16.95 nm the reconstruction at the screen is able to retrieve the single spike using both, the energy loss and the energy spread method, c.f. Fig. 6.28, as the peak power is higher than for the 35.64 nm case and therefore also the lost energy by the electrons and the induced energy spread in the electron bunch are higher. Unfortunately, the reconstruction at the screen is still not possible. Although the spike can be retrieved using the energy loss method, c.f. Fig. 6.28(a), energy differences in the region of the current peak are retrieved as a large photon pulse peak which is nonexistent in the actual photon pulse. The reconstruction using the energy spread method at the screen does not work, as the induced energy spread by the TDSs is too high and renders the reconstruction impossible.

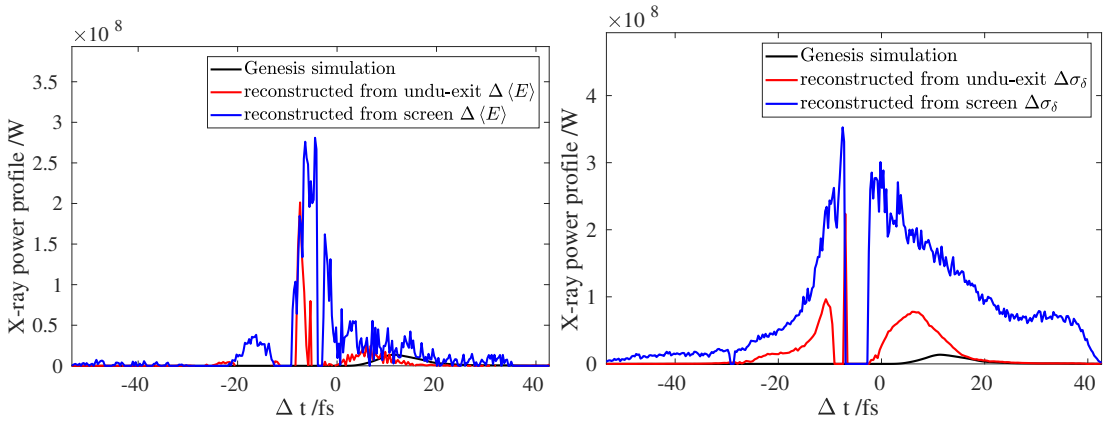

(a) Using the energy loss method.

(b) Using the energy spread method.

Figure 6.27: Photon pulse reconstruction of the 20 pC electron bunch at a wavelength of 35.64 nm described in Section 5.3 using the short pulse optics and a deflecting voltage of 34 MV. This is Seed -11 from Fig. 5.20.

To conclude, the tracking results indicate that using the PolariX TDSs at FLASH2 it is possible to reconstruct the temporal profile of photon pulses. An overview of the rms bunch lengths of the photon pulses from the Genesis 1.3 simulation and the reconstruction using the energy loss and the energy spread method at the undulator exit and at the screen, respectively, is shown in Table 9. Different cases for different wavelengths and bunch lengths were studied. In most of the studied cases, the energy loss method proves to be superior to the energy spread method, accurately reconstructing the temporal profile of the photon pulse and also the photon pulse duration. The energy spread method overestimates the power at the edges of the photon pulse leading to an increase of the reconstructed photon pulse duration. This effect can be observed at both, the reconstruction at the undulator exit and the reconstruction at the screen, as the derivations given in [119] leading to Eq. (4.39) for the higher wavelengths at FLASH do not

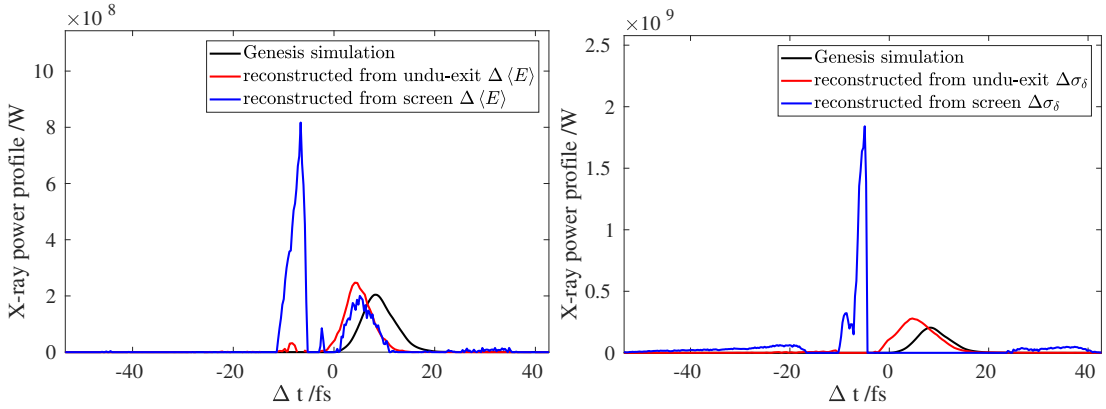

(a) Using the energy loss method.

(b) Using the energy spread method.

Figure 6.28: Photon pulse reconstruction of the 20 pC electron bunch at a wavelength of 16.95 nm described in Section 5.3 using the short pulse optics and a deflecting voltage of 34 MV. This is Seed -11 from Fig. 5.25.

Table 9: Comparison of rms Photon Pulse Duration Given by Genesis 1.3 and the Reconstruction at the Undulator Exit and the Screen.

	$\sigma_{t,\mathrm{ph}}$/fs actual Genesis	$\sigma_{t,\mathrm{ph}}$/fs recons. undu-exit $\Delta\langle E\rangle$	$\sigma_{t,\mathrm{ph}}$/fs recons. screen $\Delta\langle E\rangle$	$\sigma_{t,\mathrm{ph}}$/fs recons. undu-exit $\Delta\sigma_\delta$	$\sigma_{t,\mathrm{ph}}$/fs recons. screen $\Delta\sigma_\delta$
1200 MeV, 100 fs	37.6	37.3	38.6	52.2	56.5
700 MeV, 100 fs	46.4	45.8	46.5	53.8	57.5
1200 MeV, 23 fs	7.8	8.1	7.7	12.1	13.4
700 MeV, 23 fs	9.0	9.0	8.8	12.0	13.0
70 pC, 30 nm	17.9	17.9	21.8	29.2	48.7
38 pC, 30 nm	10.0	9.8	9.7	14.8	15.0
20 pC, 35 nm	7.0				
20 pC, 17 nm	3.4				

model the energy spread increase accurately. For future, actual measurements at FLASH2, only the energy loss method should therefore be considered. The reconstruction of the photon pulse is not possible, if the energy loss is in the order of the energy resolution and if large current spikes do not contribute to the lasing process. Therefore, for the two 20 pC bunches no bunch length is indicated in Table 9, since a meaningful reconstruction could not be achieved due to the low energy loss of the electrons.

6.3.3 Slice Emittance Measurement

The slice emittance measurement at FLASH2 is performed using a quadrupole scan as explained in Section 6.2.2, where also the optics used for this measurement are discussed. For the tracking simulations elegant [154] is used.

The input distributions are tracked from the emittance reconstruction point directly upstream

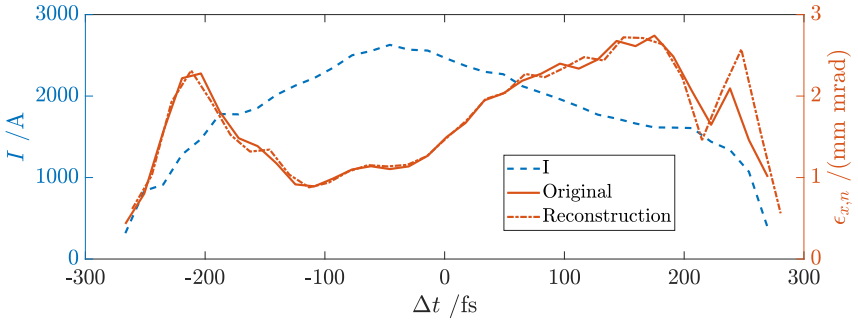

(a) $4R_t$.

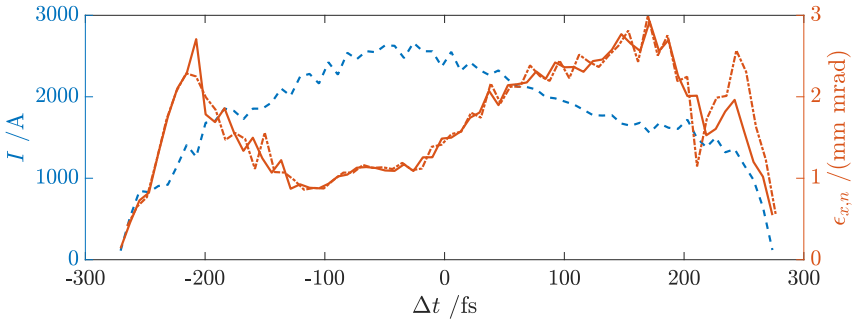

(b) $2R_t$.

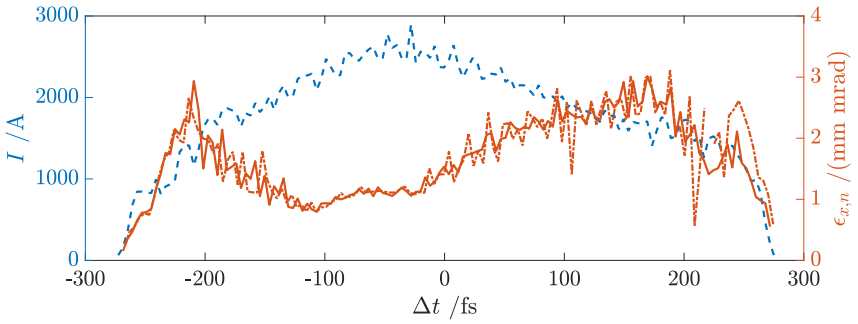

(c) R_t.

Figure 6.29: Horizontal slice emittance measurement of a 1 nC [155] bunch for three different slice widths. The longitudinal resolution is 4.5 fs, the TDS voltage is 34 MV.

of the first quadrupole used for the slice emittance measurement to the screen using all of the seven different optics for each transverse plane. The deflecting plane of the TDSs is set to the plane perpendicular to the plane in which the slice emittance is reconstructed. The screen image of each individual measurement is then sliced into slices with a fixed width depending on the longitudinal resolution R_t of $4R_t$, $2R_t$, and R_t, respectively. The central slice is defined as the slice comprising the mean of the distribution at its center [102]. For each individual slice the "rms beam size" is calculated as the square root of the variance of the beam profile [102]. Only slices containing more than 100 particles are considered as with fewer particles no reasonable calculation of the rms beam size can be achieved. The slices of the tracked bunches are then aligned and for each slice the emittance is calculated according to Eq. (4.43) [126, 127].

In the following figures, the current of the bunch is plotted using a blue dashed line for reference. The original slice emittance is plotted using a solid red line, the reconstruction at the screen is plotted using a dashed-dotted red line. For the simulations, the bunches with a charge

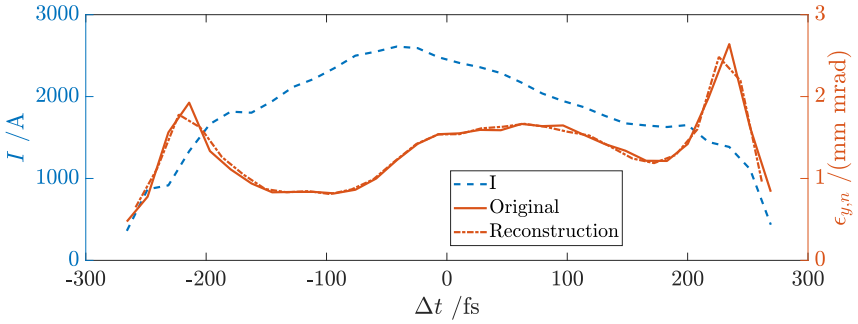

(a) $4R_t$.

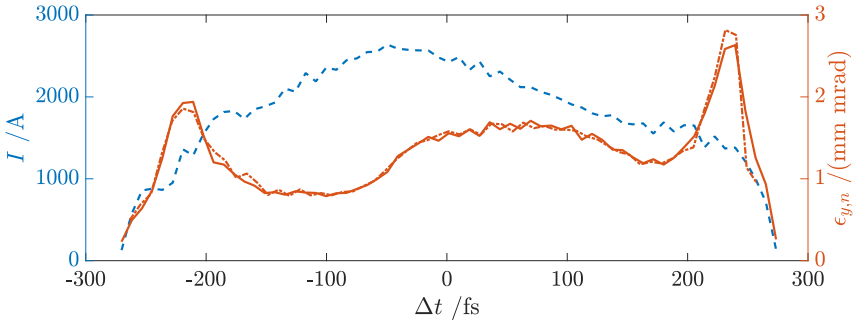

(b) $2R_t$.

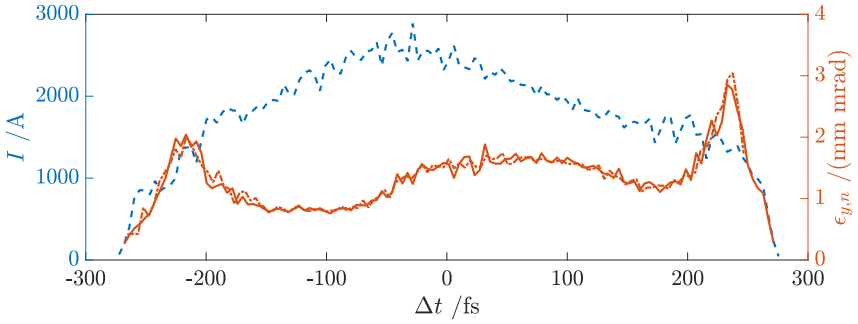

(c) R_t.

Figure 6.30: Vertical slice emittance measurement of a 1 nC [155] bunch for three different slice widths. The longitudinal resolution is 4.3 fs, the TDS voltage is 34 MV.

of 70 pC and 20 pC from Section 5.2 are tracked, as well as the bunch with a charge of 1 nC and 20 pC that were also used for the longitudinal phase space density reconstruction, c.f. Figs. 6.19 and 6.20. These examples were selected to show long and short bunches at FLASH, as well as optimized and not optimized cases.

Figures 6.29 and 6.30 show the reconstruction for a 1 nC bunch with a length of 135.2 fs rms in the horizontal and the vertical plane, respectively. For the largest slice width of $4R_t$ the original slice emittance and the reconstruction match perfectly in most parts of the bunch, c.f. Figs. 6.29(a) and 6.30(a). Only in the region of the head ($\Delta t \gtrsim 200$ fs) there are slight discrepancies, as in this region there are fewer particles for the calculation of the beam size and therefore outliers have a bigger influence. If the smallest slice width of just R_t is used for this rather long particle bunch, the reconstruction becomes very sensitive to outliers, as again fewer particles are found in each slice, c.f. Figs. 6.29(c) and 6.30(c). For long bunches it is therefore recommended to use larger slice widths to ensure a correct calculation of the slice beam size.

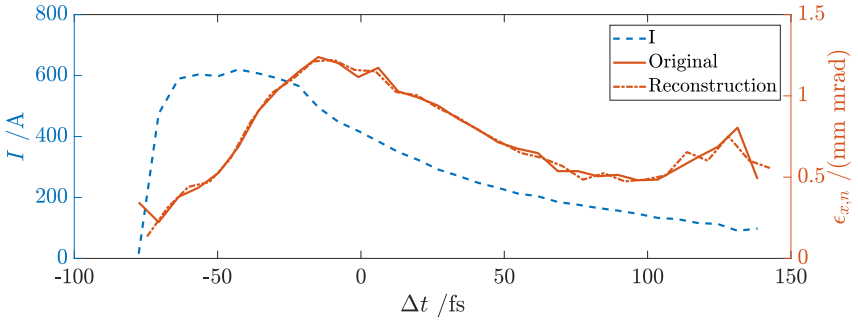

(a) $4R_t$.

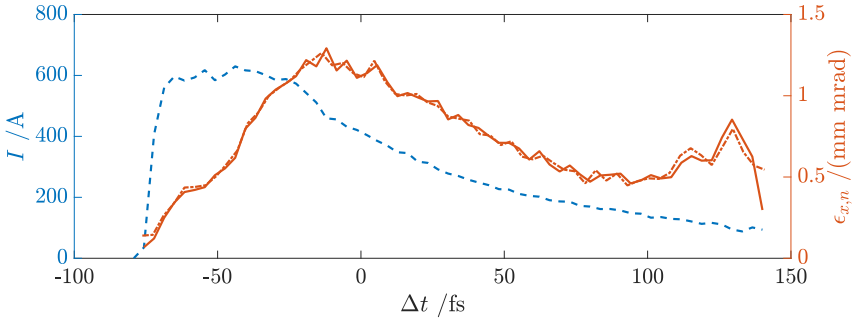

(b) $2R_t$.

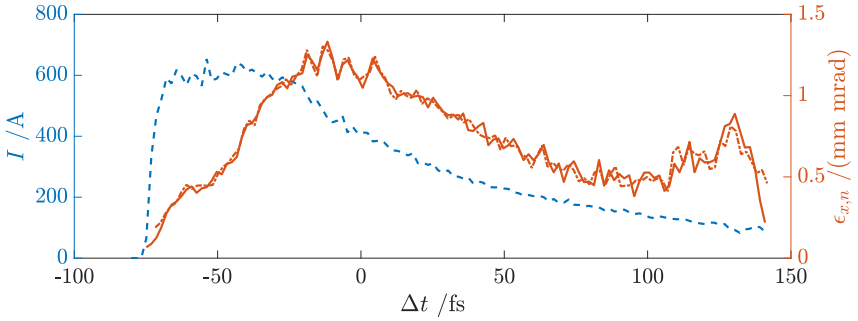

(c) R_t.

Figure 6.31: Horizontal slice emittance measurement of the 70 pC bunch described in Section 5.2.2 for three different slice widths. The longitudinal resolution is 1.8 fs, the TDS voltage is 34 MV.

The slice emittance reconstruction for the 70 pC bunch described in Section 5.2.2 are shown in Figs. 6.31 and 6.32 for the horizontal and the vertical plane, respectively. For a slice width of $4R_t$ the original and the reconstructed slice emittance match along the bunch in both planes, c.f. Figs. 6.31(a) and 6.32(a), as it was the case with the 1 nC bunch. For a slice width of $2R_t$, the reconstruction and the original slice emittance look again very similar, although already the original slice emittance shows a noisy behavior. Nonetheless, also this spiky behavior is retrieved by the reconstruction, c.f. Figs. 6.31(b) and 6.32(b). The same is true when applying the smallest slice width of R_t, c.f. Figs. 6.31(c) and 6.32(c).

Figures 6.33 and 6.34 show the slice emittance reconstruction for the 20 pC bunch described in Section 5.3 in both planes, respectively. Using a slice width of $4R_t$ for this particular electron bunch is not very reasonable, as adjacent particles with very different properties are mixed and minute features of the electron bunch are lost. This is already evident when looking at the current profiles in Figs. 6.33(a) and 6.34(a): The main current spike is blurred and looks very

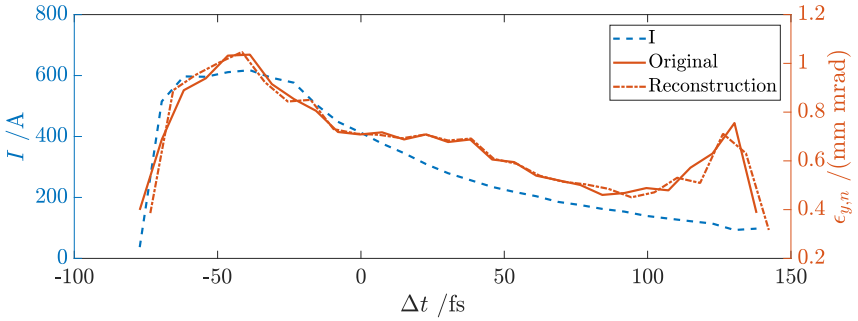

(a) $4R_t$.

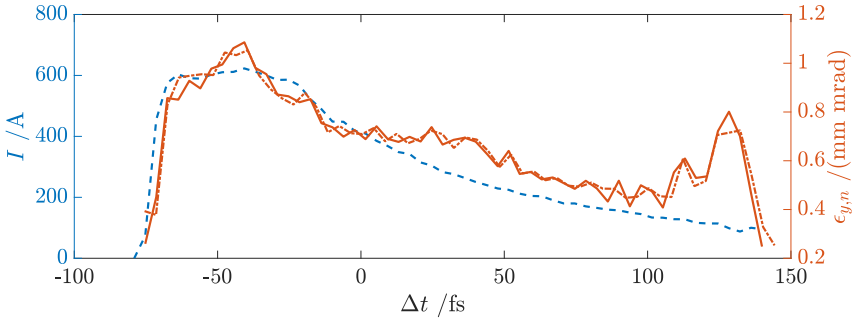

(b) $2R_t$.

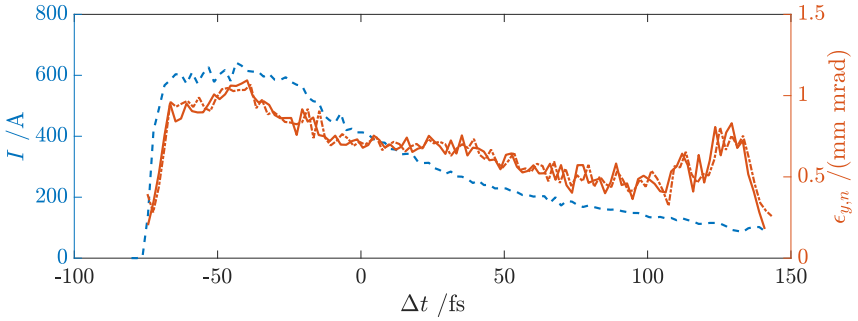

(c) R_t.

Figure 6.32: Vertical slice emittance measurement of the 70 pC bunch described in Section 5.2.2 for three different slice widths. The longitudinal resolution is 1.9 fs, the TDS voltage is 34 MV.

different to the one in Fig. 5.17. Nonetheless, comparing the slice emittances in the region of $\Delta t \geq 0\,\text{fs}$ shows, that they match very well, c.f. Fig. 6.33(a). In the region of $\Delta t \leq -20\,\text{fs}$ discrepancies can be observed in both planes as Fig. 5.17(b) reveals that the slices in this region are not matched very well to the design Twiss parameters of the beam line. The same observations can be also made when applying a slice width of R_t, c.f. Figs. 6.33(c) and 6.34(c). The original and the reconstructed slice emittance in the region of $\Delta t \geq 0\,\text{fs}$ match very well and in the region of $\Delta t \leq -10\,\text{fs}$ differences due to the unmatched slices are evident. In the region of the current spike between $-10\,\text{fs} > \Delta t > 0\,\text{fs}$, the limited resolution of this measurement is observable. As the slice emittance in this region changes rapidly, the measurement is unable to retrieve the exact value as the slices are mixed due to the limited resolution.

The slice emittance reconstruction for another short bunch with a charge of 20 pC is shown in Figs. 6.35 and 6.36. Also for this bunch, a slice width of R_t should be applied, as otherwise too much information is lost. Figures 6.35(c) and 6.36(c) reveal, that for the regions of $\Delta t \leq$

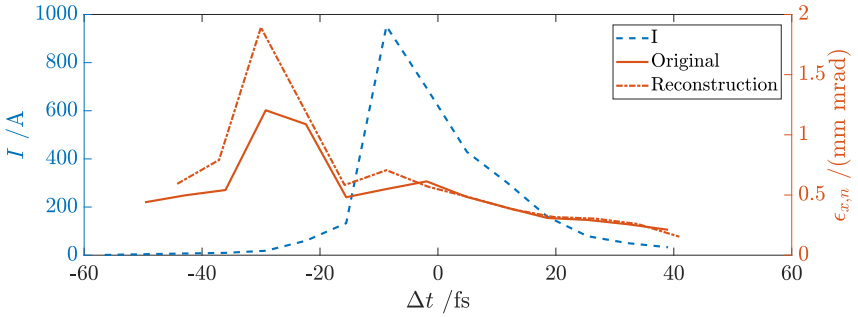

(a) $4R_t$.

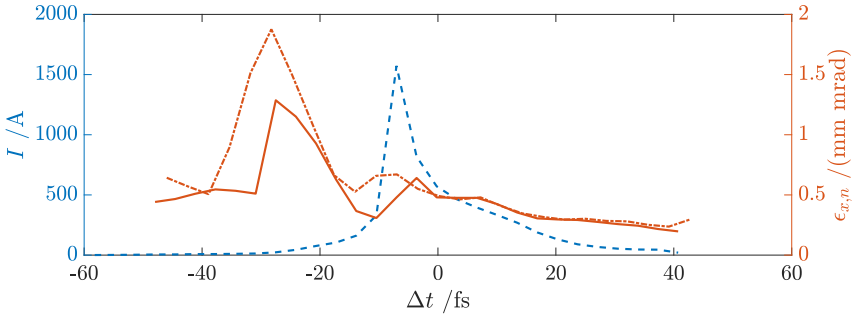

(b) $2R_t$.

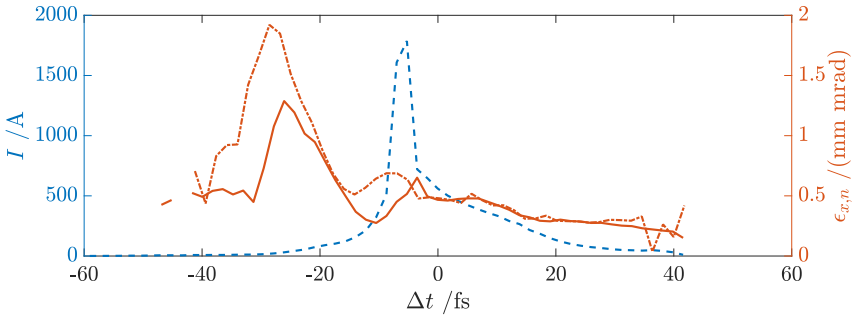

(c) R_t.

Figure 6.33: Horizontal slice emittance measurement of the 20 pC bunch described in Section 5.3 for three different slice widths. The longitudinal resolution is 1.7 fs, the TDS voltage is 34 MV.

-10 fs and $\Delta t \geq 10$ fs the reconstructed slice emittances in both planes match very nicely to the original one. Yet, in the region of the current spike, i.e. for $-10\,\text{fs} < \Delta t < 10\,\text{fs}$ again the influence of the limited resolution of this measurement is visible. Particles from adjacent slices mix in the reconstruction and the reconstructed value for the slice emittance is higher than the original one.

To summarize, the tracking results have shown that a meaningful slice emittance reconstruction in both planes using the same TDS are feasible using the PolariX TDSs at FLASH2. The dispersion created by the dipole between the TDSs and the screen station is compensated by optics matching as described in Section 6.2.2. The longitudinal resolution of the measurement is sufficient for most of the use cases. Even for very short electron bunches the slice emittance can be reconstructed in most parts of the bunch. Only when the slice emittance changes drastically on a scale close to the longitudinal resolution, the reconstruction shows some limitations as electrons leave their initial slices. In reality, the slice emittance reconstruction will of course be

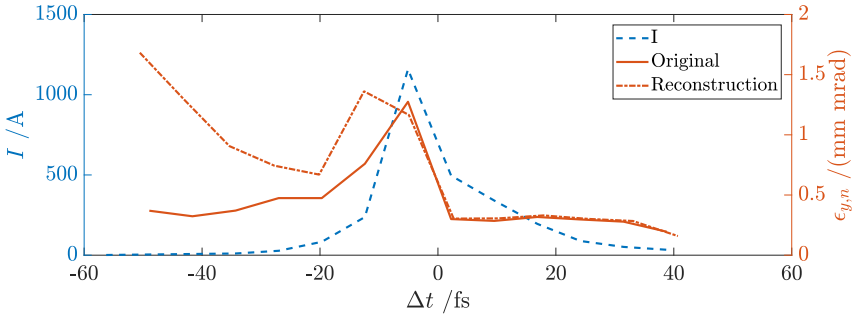

(a) $4R_t$.

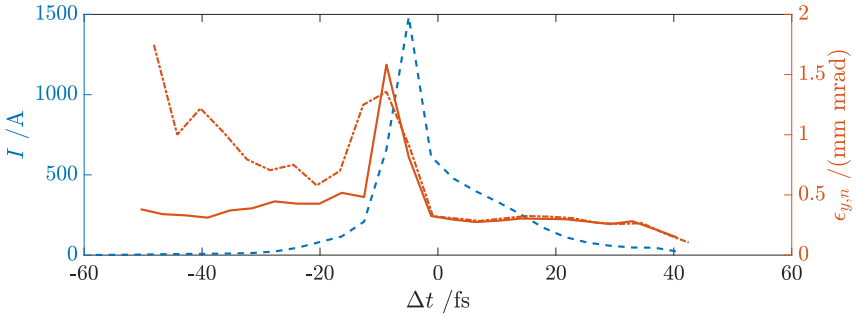

(b) $2R_t$.

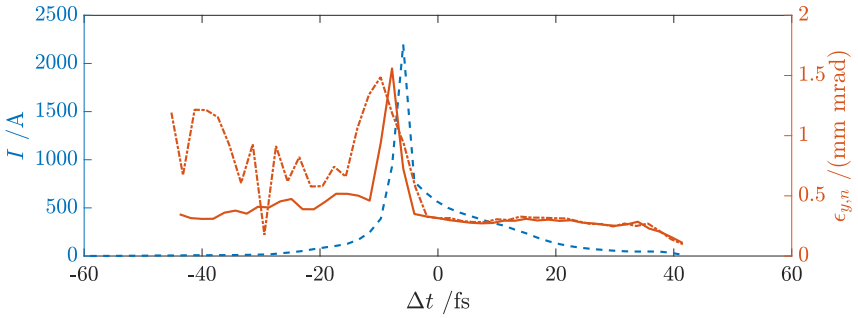

(c) R_t.

Figure 6.34: Vertical slice emittance measurement of the 20 pC bunch described in Section 5.3 for three different slice widths. The longitudinal resolution is 1.9 fs, the TDS voltage is 34 MV.

influenced by measurement errors, such as the imaging resolution. Also, a possible mismatch of the Twiss parameters is for now not considered for the tracking simulations, which is often the case in a real machine.

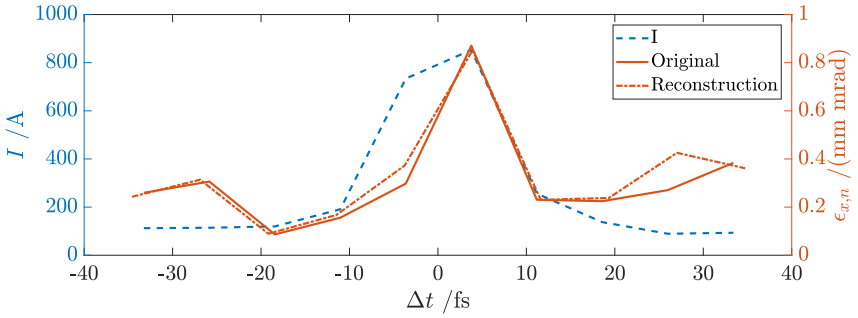

(a) $4R_t$.

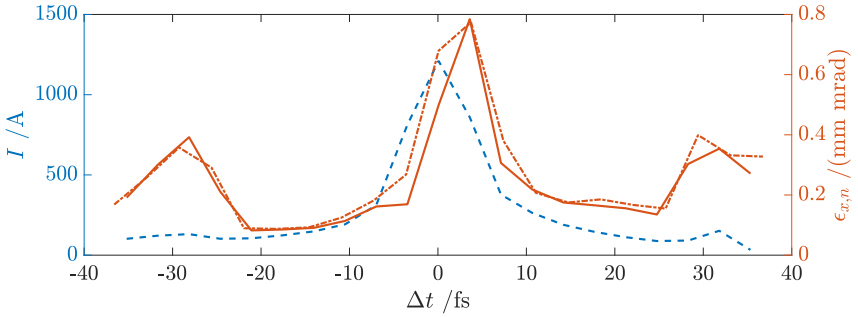

(b) $2R_t$.

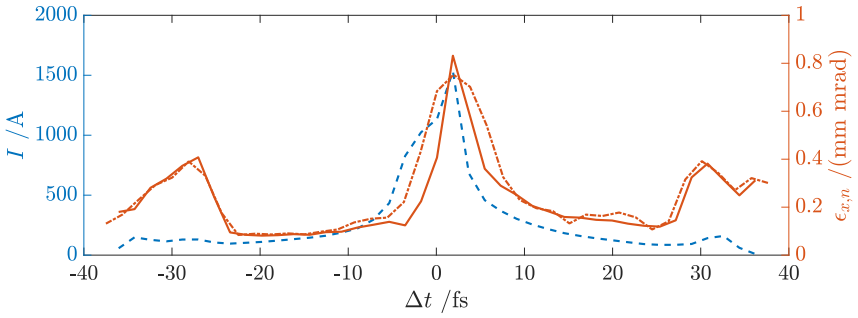

(c) R_t.

Figure 6.35: Horizontal slice emittance measurement of a 20 pC bunch [155] for three different slice widths. The longitudinal resolution is 1.8 fs, the TDS voltage is 34 MV.

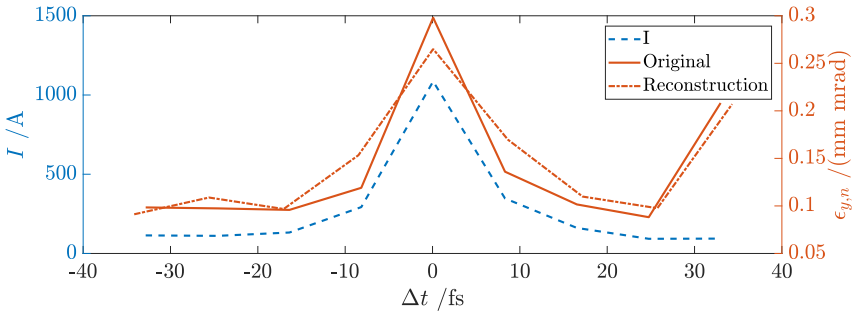

(a) $4R_t$.

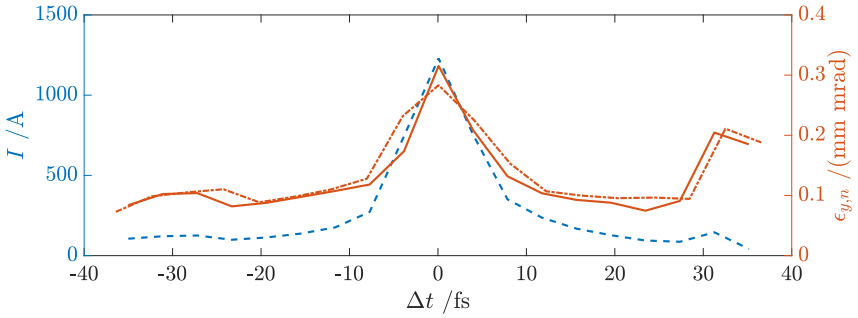

(b) $2R_t$.

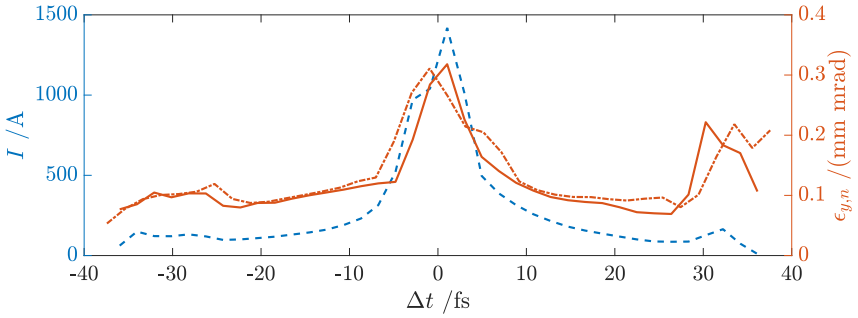

(c) R_t.

Figure 6.36: Vertical slice emittance measurement of a 20 pC bunch [155] for three different slice widths. The longitudinal resolution is 2.0 fs, the TDS voltage is 34 MV.

7 Temporal X-Ray Reconstruction Using Temporal and Spectral Measurements

As discussed in Sections 4 and 6, the limited resolution of a measurement using a TDS imposes an upper limit on the resolution of the temporal reconstruction of photon pulses. As the resolution of an X-band TDS used at an X-ray FEL is typically limited to around 1 fs rms, single SASE spikes, typically in the range of 0.1 fs to 3 fs, within one photon pulse can often not be resolved. However, the exact knowledge of the temporal structure of SASE radiation is interesting for applications such as "ghost imaging" [12, 13].

By combining the power spectrum from a high resolution photon spectrometer [156] and the temporal structure from the TDS, the overall resolution can be enhanced, thus allowing the observation of temporal, single SASE spikes in the X-ray range. The combined data from the spectrometer and the TDS is analyzed using an iterative algorithm to obtain an estimate of the actual intensity profile. This iterative reconstruction algorithm is published in [157, 158][18].

In this section both, the reconstruction algorithm as well as analyzed data obtained from simulations of LCLS, are presented and prove the reliability of this method. Additionally, real data taken at the LCLS which is analyzed using the reconstruction algorithm is shown.

7.1 Iterative Reconstruction Algorithm

The iterative reconstruction algorithm uses the blurred temporal profile $\tilde{P}(t)$ measured by a TDS and the blurred power spectrum $\tilde{\mathscr{P}}(\omega)$ measured by a spectrometer as starting points. The mechanism by which the finite TDS resolution blurs the actual temporal intensity profile $P(t)$ is modeled by a convolution with a Gaussian $G(t)$ of fixed standard deviation R_t

$$(P * G)(t) = \tilde{P}(t). \tag{7.1}$$

As the resolution of the spectrometer can be orders of magnitude lower than the width of single, spectral SASE spikes [156], in Section 7.2.1 we restrict ourselves to the testing of the algorithm with a perfect spectral resolution. The measured, blurred power spectrum is then the same as the actual power spectrum

$$\mathscr{P}(\omega) = \tilde{\mathscr{P}}(\omega). \tag{7.2}$$

However, if the spectrometer is not set up to the highest achievable resolution, the power spectrum can also be blurred through a convolution with a Gaussian $G(\omega)$ of fixed width R_ω

$$(\mathscr{P} * G)(\omega) = \tilde{\mathscr{P}}(\omega). \tag{7.3}$$

Simulated data for this case is tested in Section 7.2.2.

[18] The following sections contain excerpts from [157, 158].

7.1.1 Base Functions

The electric field is modeled as a sum of in principle arbitrary base functions $B_j(t)$ in time with varying complex coefficients $a_{j,m}$, where m is the iteration step, c.f. Section 7.1.2,

$$F_m(t) = \sum_{j=1}^{n} a_{j,m} B_j(t) \tag{7.4}$$

as is the field in the frequency domain

$$\mathscr{F}_m(\omega) = \sum_{j=1}^{n} a_{j,m} \mathscr{B}_j(\omega). \tag{7.5}$$

The complex coefficients $a_{j,0}$ are initialized randomly. It has proven advantageous for LCLS bunches to reduce the amplitude of every $a_{1+2p,0}$ coefficient with $p = 0, 1, 2, \ldots$ by 8 and every $a_{1+5p,0}$ coefficient by 16. This results in starting temporal intensity profiles and power spectra consisting of a few wider spikes instead of frequent narrower spikes, thereby resembling the nature of SASE more closely. The choice of this reduction is arbitrary but generally yields good results. Nonetheless, the method also works without this reduction. To match the integral of the blurred intensity profile, the coefficients are normalized so that $\int \tilde{P}(t)\mathrm{d}t = \int |F_m(t)|^2 \,\mathrm{d}t$. These normalized coefficients are then used to create the initial guess $F_0(t)$ and $\mathscr{F}_0(\omega)$.

In the following, two different choices for the base functions are presented.

Gaussian Base Functions

The first choice of base functions are Gaussians of fixed width σ_j centered at times t_j

$$B_j(t) = \left(\frac{1}{\sqrt{2\pi}\sigma_j}\right)^{\frac{1}{2}} e^{\frac{-\left(t-t_j\right)^2}{4\sigma_j^2}} e^{i\omega_j t}. \tag{7.6}$$

The ω_j can be initially calculated based on the energy profile of the electron phase space. For a linearly chirped electron bunch, we can for example set $\omega_j = \omega_0 + 2\frac{\gamma_j - \gamma_0}{\gamma_0}\omega_0$ [159], where ω_0 is the main radiation frequency created by electrons with an energy of γ_0 and γ_j is the mean energy of the electrons around t_j. Otherwise, they are initialized as $\omega_j = \omega_0$. The σ_j are chosen to be smaller than the expected width of the single SASE spikes. The t_j are chosen such that single SASE spikes can be modeled. Nonetheless, both σ_j and t_j have to be selected in a way that the matrix $\mathbf{T} + \mathbf{F}$ in Eq. (7.18) is not degenerate.

The B_j are chosen such that

$$\begin{aligned} \int_{-\infty}^{\infty} \left|B_j(t)\right|^2 \mathrm{d}t &= \int_{-\infty}^{\infty} \frac{1}{\sqrt{2\pi}\sigma_j} \cdot e^{-\frac{\left(t-t_j\right)^2}{2\sigma_j^2}} \,\mathrm{d}t \\ &= 1. \end{aligned} \tag{7.7}$$

By applying a Fourier transform, we obtain the base functions in the frequency domain

$$\mathscr{B}_j(\omega) = \left(\frac{\sigma_j}{\sqrt{\pi}}\right)^{\frac{1}{2}} e^{-it_j(\omega-\omega_j)} e^{\frac{-\sigma_j^2(\omega-\omega_j)^2}{2}}. \tag{7.8}$$

Linearly Chirped Base Functions

The Gaussian base functions described in the previous section are not chirped in time as suggested by [44, 50, 52]. To accommodate this we introduce an arbitrary linear chirp factor β_j to the base functions

$$B_j(t) = \left(\frac{1}{\sqrt{2\pi}\sigma_j}\right)^{\frac{1}{2}} e^{-\frac{\left(t-t_j\right)^2}{4\sigma_j^2}} e^{i\omega_j t} e^{i\left(t-t_j\right)^2\beta_j}. \tag{7.9}$$

These base functions are again chosen in a way that

$$\begin{aligned}\int_{-\infty}^{\infty} \left|B_j(t)\right|^2 \mathrm{d}t &= \int_{-\infty}^{\infty} \frac{1}{\sqrt{2\pi}\sigma_j} \cdot e^{-\frac{\left(t-t_j\right)^2}{2\sigma_j^2}} \mathrm{d}t \\ &= 1.\end{aligned} \tag{7.10}$$

By setting $C_j = \frac{1}{4\sigma_j^2} - i\beta_j$, Eq. (7.9) becomes

$$B_j(t) = \left(\frac{1}{\sqrt{2\pi}\sigma_j}\right)^{\frac{1}{2}} e^{-\left(t-t_j\right)^2 C_j} e^{i\omega_j t} \tag{7.11}$$

and we obtain the base functions in frequency domain

$$\mathscr{B}_j(\omega) = \left(\frac{1}{\sqrt{2\pi}\sigma_j}\right)^{\frac{1}{2}} \frac{1}{\sqrt{2C_j}} e^{-\frac{\left(\omega-\omega_j\right)\left(-4iC_j t_j+\omega+\omega_j\right)}{4C_j}}. \tag{7.12}$$

Following [44, 50] we set $\beta_j = -\frac{1}{4\sqrt{3}\sigma_j^2}$ for all base functions.

7.1.2 Iteration Process and Minimizing

Starting from the initial guesses for $F_0(t)$ and $\mathscr{F}_0(\omega)$, we apply the alternate projection method described in [160]. This is an iterative method, recalculating the complex coefficients $a_{j,m}$ at each iteration step $m \in [0, M]$. The maximum number of iterations M can be chosen arbitrarily.

Since in general $\left|\tilde{F}_m(t)\right|^2 \neq \tilde{P}(t)$, at each iteration step m the previously calculated field $F_m(t)$ is projected on the blurred intensity profile $\tilde{P}(t)$.

This is done by introducing the projected field

$$U_m(t) = F_m(t) \cdot \sqrt{\frac{\tilde{P}(t)}{\left|\tilde{F}_m(t)\right|^2}} \tag{7.13}$$

in each iteration step m which keeps the complex phases of $F_m(t)$ and satisfies $\left|\tilde{U}_m(t)\right|^2 = \tilde{P}(t)$. Additionally, we calculate the projected spectrum

$$V_m(\omega) = \mathscr{F}_m(\omega) \cdot \sqrt{\frac{\tilde{\mathscr{P}}(\omega)}{\left|\tilde{\mathscr{F}}_m(\omega)\right|^2}}. \tag{7.14}$$

Since $U_m(t)$ and $V_m(\omega)$ can in general not be written in the form of Eqs. (7.4) and (7.5), we try to find a new field $F_{m+1}(t)$ and its transform $\mathscr{F}_{m+1}(\omega)$, that minimize the distance from the projections

$$\begin{aligned} d &= \|F_{m+1} - U_m\|_{\mathscr{L}^2}^2 + \|\mathscr{F}_{m+1} - V_m\|_{\mathscr{L}^2}^2 \\ &= \left\| \sum_{j=1}^{n} a_{j,m+1} B_j - U_m \right\|_{\mathscr{L}^2}^2 + \left\| \sum_{j=1}^{n} a_{j,m+1} \mathscr{B}_j - V_m \right\|_{\mathscr{L}^2}^2 . \end{aligned} \tag{7.15}$$

Using the $\mathscr{L}^2$ scalar product [161]

$$\langle a, b \rangle = \int_{-\infty}^{\infty} a(x) b^*(x)\, \mathrm{d}x, \quad \langle a, a \rangle = \|a\|_{\mathscr{L}^2}^2 \tag{7.16}$$

we can rewrite Eq. (7.15)

$$\begin{aligned} d = &\sum_{i=1}^{n} \sum_{j=1}^{n} a_{i,m+1} a_{j,m+1}^* \left\langle B_i, B_j \right\rangle + \|U_m\|_{L^2}^2 \\ &- \sum_{i=1}^{n} a_{i,m+1} \left\langle B_i, U_m \right\rangle - \sum_{j=1}^{n} a_{j,m+1}^* \left\langle U_m, B_j \right\rangle \\ &+ \sum_{k=1}^{n} \sum_{l=1}^{n} a_{k,m+1} a_{l,m+1}^* \left\langle \mathscr{B}_k, \mathscr{B}_l \right\rangle + \|V_m\|_{L^2}^2 \\ &- \sum_{k=1}^{n} a_{k,m+1} \left\langle \mathscr{B}_k, V_m \right\rangle - \sum_{l=1}^{n} a_{l,m+1}^* \left\langle V_m, \mathscr{B}_l \right\rangle . \end{aligned} \tag{7.17}$$

d is minimized by finding $a_{j,m+1}$, so that the derivative of d with respect to all $a_{j,m+1}$ is equal to zero. After some simplifications and the application of the scalar product in Eq. (7.16), we obtain $k = 1, \ldots, n$ equations

$$\int U_m(t) B_k^*(t)\, \mathrm{d}t + \int V_m(\omega) \mathscr{B}_k^*(\omega)\, \mathrm{d}\omega = \sum_{j=1}^{n} a_{j,m+1} \left(T_{jk} + F_{jk} \right), \tag{7.18}$$

where $T_{jk} = \left\langle B_j, B_k \right\rangle$ and $F_{jk} = \left\langle \mathscr{B}_j, \mathscr{B}_k \right\rangle$. For the Gaussian base functions in Eqs. (7.6) and (7.8) this yields

$$T_{jk} = \sqrt{\frac{2\sigma_j \sigma_k}{\sigma_j^2 + \sigma_k^2}} \cdot e^{-\frac{(t_j - t_k)^2 - 2i(\omega_j - \omega_k)(t_j \sigma_k^2 + t_k \sigma_j^2) + \sigma_j^2 \sigma_k^2 (\omega_j - \omega_k)^2}{2(\sigma_j^2 + \sigma_k^2)}} \tag{7.19}$$

and $F_{jk} = T_{jk}$ due to the properties of the Fourier transform.

For the linearly chirped base functions in Eqs. (7.11) and (7.12) this yields

$$F_{jk} = T_{jk} = \frac{\sqrt{3}e^{-\frac{3i\sigma_j^2\sigma_k^2(\omega_j-\omega_k)^2+(3-i\sqrt{3})\sigma_j^2 t_k(\omega_j-\omega_k)+(3+i\sqrt{3})\sigma_k^2 t_j(\omega_j-\omega_k)+it_j^2-2it_jt_k+it_k^2}{(\sqrt{3}+3i)\sigma_j^2-(\sqrt{3}-3i)\sigma_k^2}}}{\sqrt{\frac{(3-i\sqrt{3})\sigma_j}{\sigma_k}+\frac{(3+i\sqrt{3})\sigma_k}{\sigma_j}}}. \tag{7.20}$$

In each iteration step new coefficients $a_{j,m+1}$ are calculated according to Eq. (7.18). Using those coefficients, the temporal and spectral fields are calculated according to Eqs. (7.6) and (7.8) and are fed back into the iteration algorithm.

7.2 Applying the Iterative Reconstruction Algorithm to SASE Simulations

To understand the capabilities and limitations of the iterative reconstruction algorithm, it is tested using simulations of the SASE process in the LCLS undulators at 1.5 nm. They are conducted using the leap-frog algorithm developed by Z. Huang [44]. To start, we simulate FEL pulses of bunches of 20 pC, 40 pC, and 150 pC charge, resulting in photon pulses of different lengths. These simulations are done using only one single random SASE seed per charge, resulting in only one intensity profile per charge. Further testing on the code is done using the intensity profiles of 50 different simulated SASE shots right before saturation (using the same input bunch but different initial conditions for the light wave due to the statistical nature of SASE) for a charge of 40 pC.

The temporal intensity profile and the power spectrum are taken at the end of the exponential regime, c.f. Section 4.3.3. The Gaussian blurrings used are in the range of 1.2 fs to 0.5 fs. Resolutions of up to ~ 1.0 fs are already demonstrated at LCLS, c.f. Section 7.3, higher resolutions will be possible with future upgrades of XTCAV. For each shot 50 reconstructions using different initial base functions are carried out. To obtain the final reconstruction, these 50 reconstructions are then averaged.

In order to assess the performance of the algorithm reconstructing the actual intensity profile the $1-R^2$ value known from statistics [162, 163] is used

$$1-R^2 = \frac{\sum_{i=1}^{n}(y_i-\hat{y}_i)^2}{\sum_{i=1}^{n}(y_i-\bar{y})^2}. \tag{7.21}$$

The sum $\sum_{i=1}^{n}(y_i-\bar{y})^2$, where the y_i are the observed data with their mean value $\bar{y}$, is called the total sum of squares and can be described as the total variation of the actual y_i values about their mean $\bar{y}$ [163]. The sum $\sum_{i=1}^{n}(y_i-\hat{y}_i)^2$, where the $\hat{y}_i$ are the predicted data, is called the residual sum of squares, since it is the residual or unexplained variation of the y_i values about the predicted values $\hat{y}_i$ [163]. A $1-R^2$ value of zero means a perfect agreement. In our case y is the actual intensity profile $P(t)$ and $\hat{y}$ is the obtained reconstructed intensity profile $F(t)$.

7.2.1 Blurred Temporal Measurement and Perfect Spectral Measurement

In this section, we assume only the temporal intensity profile to be blurred with Gaussian blurrings from 1.2 fs to 0.5 fs. The power spectrum is assumed to be perfect, and therefore $\mathscr{P}(\omega) = \tilde{\mathscr{P}}(\omega)$.

Figures 7.1 to 7.3 show the reconstructed temporal intensity for the three different bunch charges mentioned in the previous section. The blue solid line is the actual intensity profile from the simulation $P(t)$, the red solid line is the blurred intensity profile $\tilde{P}(t)$ using a resolution of R_t. The black solid line is the mean of the 50 reconstructions surrounded by a light gray shaded area that is one standard deviation. The $1-R^2$ value for the reconstruction is indicated at the top of the figures.

Figure 7.1 shows the actual photon pulse simulated for a bunch with 20 pC charge and the reconstructions for resolutions from 1.2 fs to 0.5 fs. The main intensity spike between 10 fs and 12 fs can be retrieved using all of the resolutions. The left spike between 6 fs and 8 fs as a whole is also reconstructed at any resolution, although the minute features within the spike cannot be resolved. The double spike in the region of 8 fs to 10 fs is difficult to retrieve, as both spikes are very close to one another and they are washed out too strongly by the resolution of the TDS. With a resolution of $R_t = 0.5$ fs the existence of a double spike in the center becomes visible in the reconstruction. All the reconstructions for this photon pulse show an $1-R^2$ value of below 0.1 meaning the algorithm is able to retrieve the photon pulse accurately.

The reconstructions for the 40 pC case are shown in Fig. 7.2. The two main spikes at 13 fs and 15 fs of this particular photon pulse can be retrieved using all resolutions. The smaller adjacent spikes are challenging to reconstruct, as they are obscured by the TDS resolution. This can also be seen in the $1-R^2$ values which are between 0.22 and 0.14 for resolutions in the range of 1.2 fs to 0.75 fs. However, using a resolution of $R_t = 0.5$ fs decreases the $1-R^2$ value to 0.04 and it can be seen in the bottom right image of Fig. 7.2 that most of the side peaks can be reconstructed by the algorithm.

The reconstructions for the 150 pC case displayed in Fig. 7.3 show a similar behavior. Small adjacent spikes are hard to retrieve for low resolutions. What can also be seen is that the ability of the algorithm to reconstruct the photon pulse does not depend on the charge but rather on how "complex" the photon pulse is as the $1-R^2$ values for this reconstruction are all well below those for the 40 pC reconstruction.

Further investigation of the algorithm robustness is performed by reconstructing the above mentioned 50 shots using different initial light wave conditions for a bunch charge of 40 pC. The $1-R^2$ values of the reconstruction for all of the 50 different photon pulses can be found in Fig. 7.4. For the best resolution of $R_t = 0.5$ fs the $1-R^2$ values are in the order of 0.1 for all shots. Assuming a TDS resolution of $R_t = 0.75$ fs most of the $1-R^2$ values are in the region of 0.1 to 0.2, while some of them are in the order of 0.3. For resolutions of $R_t = 1.0$ fs and $R_t = 1.2$ fs the algorithm reconstructs most of the shots with $1-R^2$ values between 0.1 and 0.3. A small number of shots show a $1-R^2$ value of 0.3 to 0.4 after the reconstruction for a

resolution of $R_t = 1.2\,\mathrm{fs}$.

To examine the capabilities of the algorithm further, we now take a look at two shots from Fig. 7.4. Shot 11 which shows a low $1 - R^2$ value among all TDS resolutions can be found including the respective reconstructions in Figure 7.5. This photon pulse consists of only three separated main spikes and can therefore be retrieved easily by the algorithm. Figure 7.6 showcases Shot 48 from Fig. 7.4. This photon pulse distribution is harder to reconstruct for the algorithm as there are many spikes of similar height close to one another. Since the algorithm matches for the blurred intensity profile (c.f. Eq. (7.13)) the spikes are washed out too strongly and the iterations from the 50 different starting points arrive at very diverse endpoints.

This section has argued that the reconstruction algorithm is able to retrieve the photon pulse very robustly for a blurred temporal and a perfect power spectrum. Better TDS temporal resolutions lead to better reconstruction results and photon pulses with sparse spikes can be retrieved more fittingly.

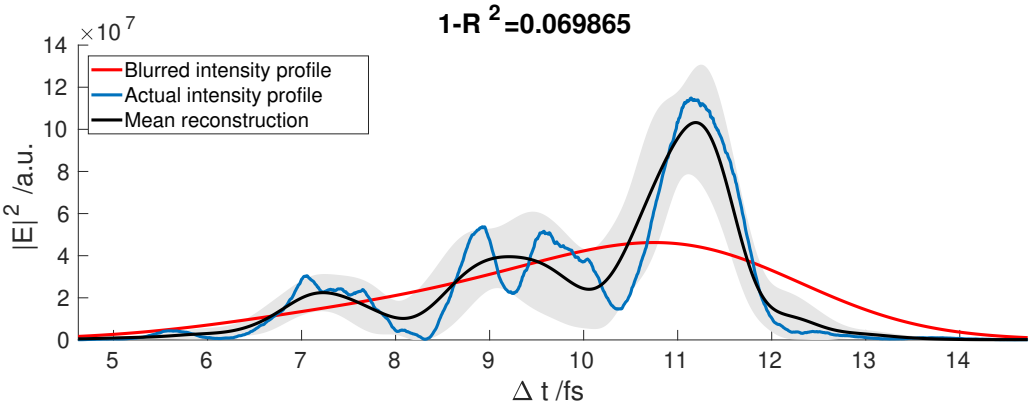

(a) $R_t = 1.2\,\mathrm{fs}$.

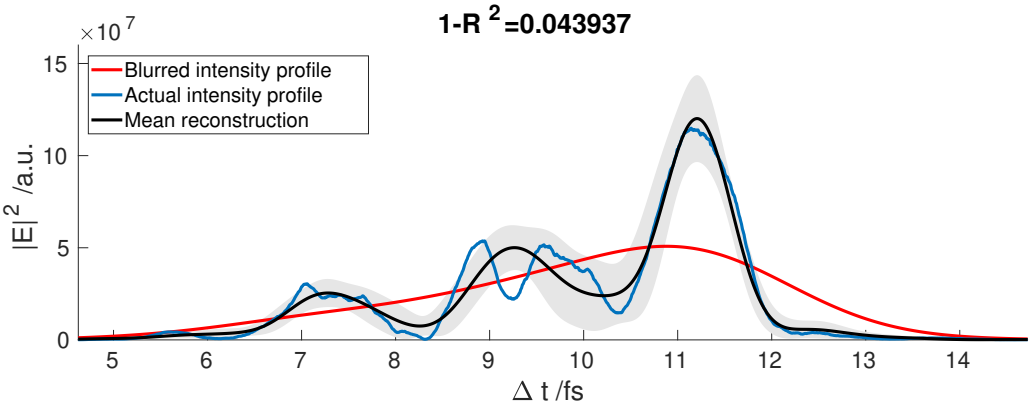

(b) $R_t = 1.0\,\mathrm{fs}$.

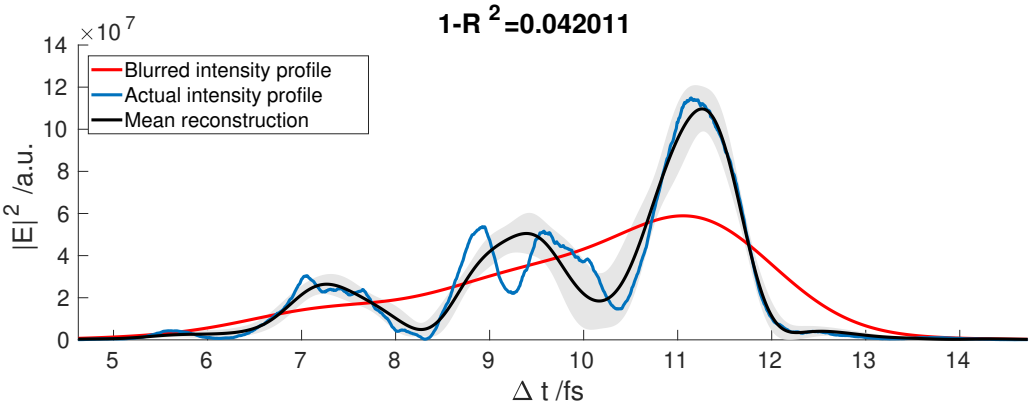

(c) $R_t = 0.75\,\mathrm{fs}$.

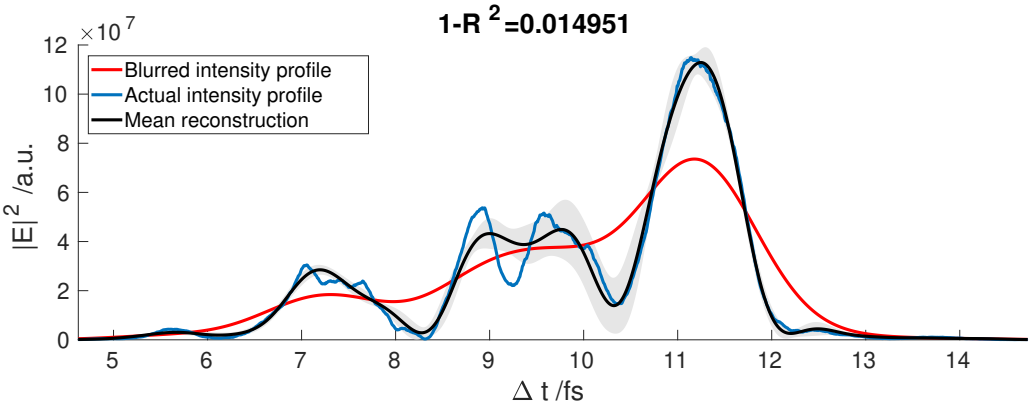

(d) $R_t = 0.5\,\mathrm{fs}$.

Figure 7.1: Four reconstructions for 20 pC. The TDS resolution is indicated below each figure.

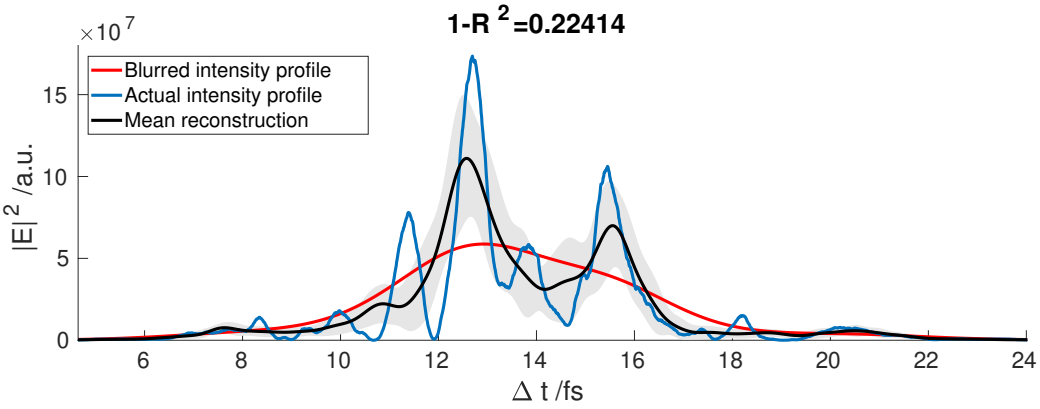

(a) $R_t = 1.2\,\mathrm{fs}$.

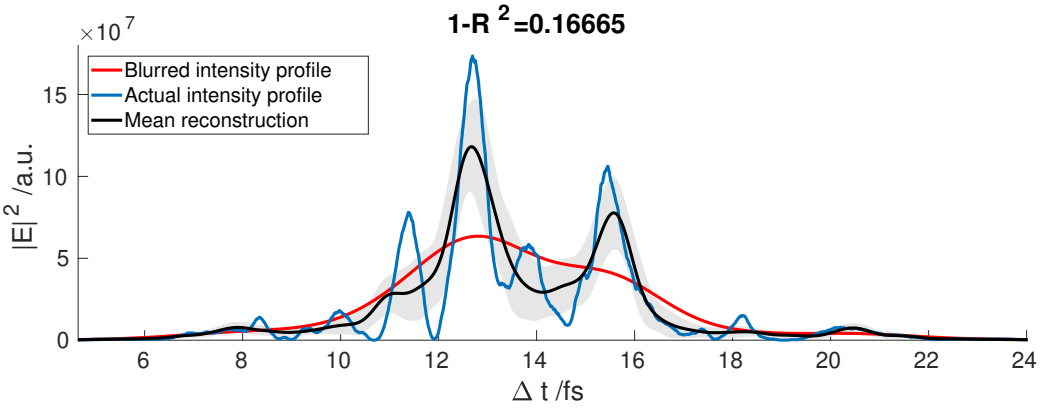

(b) $R_t = 1.0\,\mathrm{fs}$.

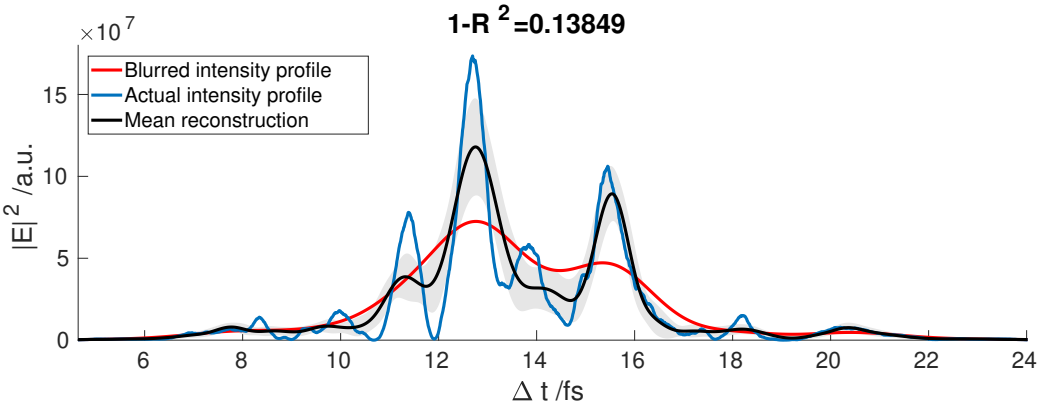

(c) $R_t = 0.75\,\mathrm{fs}$.

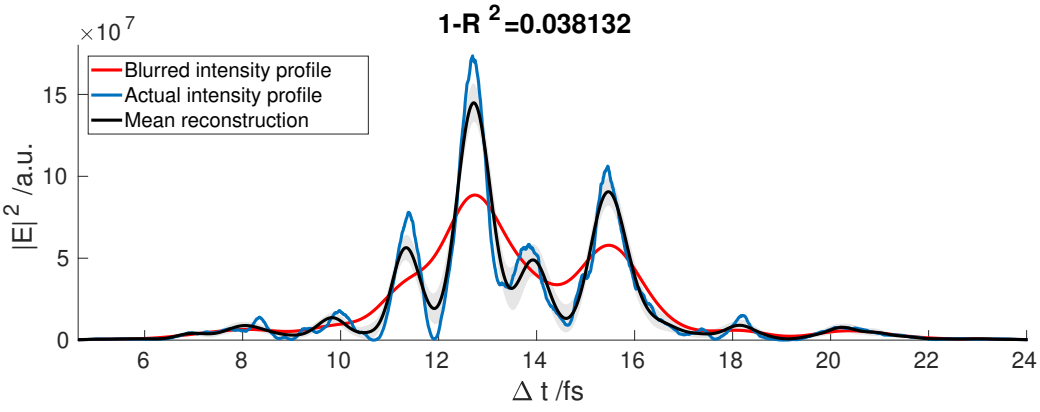

(d) $R_t = 0.5\,\mathrm{fs}$.

Figure 7.2: Four reconstructions for 40 pC. The TDS resolution is indicated below each figure. This shot is not included in Fig. 7.4.

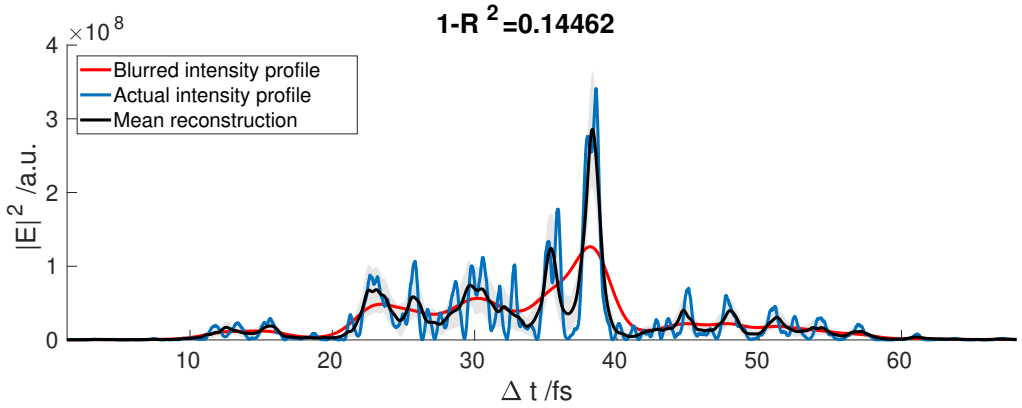

(a) $R_t = 1.2\,\mathrm{fs}$.

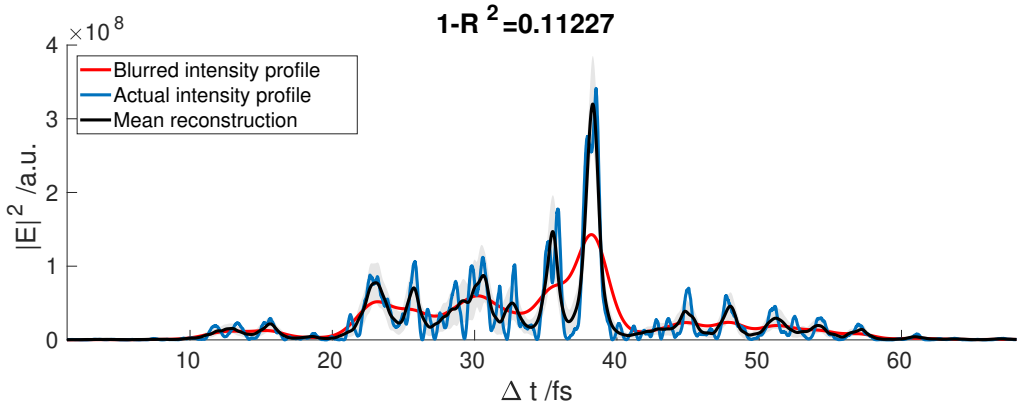

(b) $R_t = 1.0\,\mathrm{fs}$.

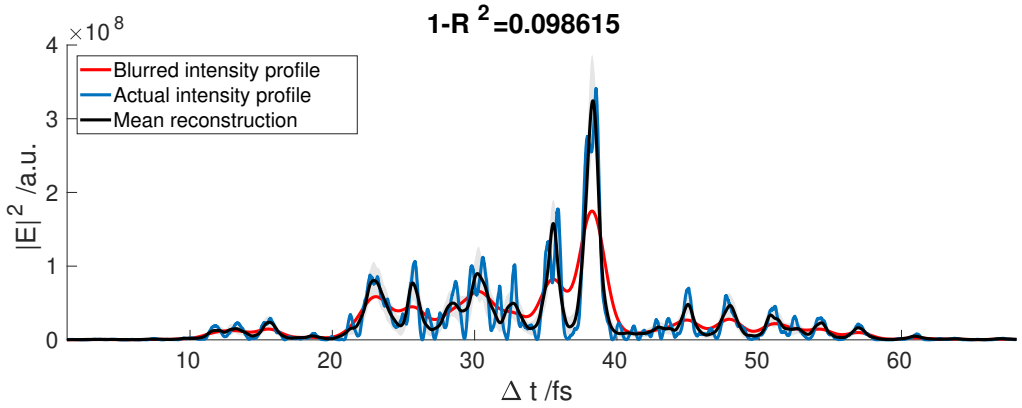

(c) $R_t = 0.75\,\mathrm{fs}$.

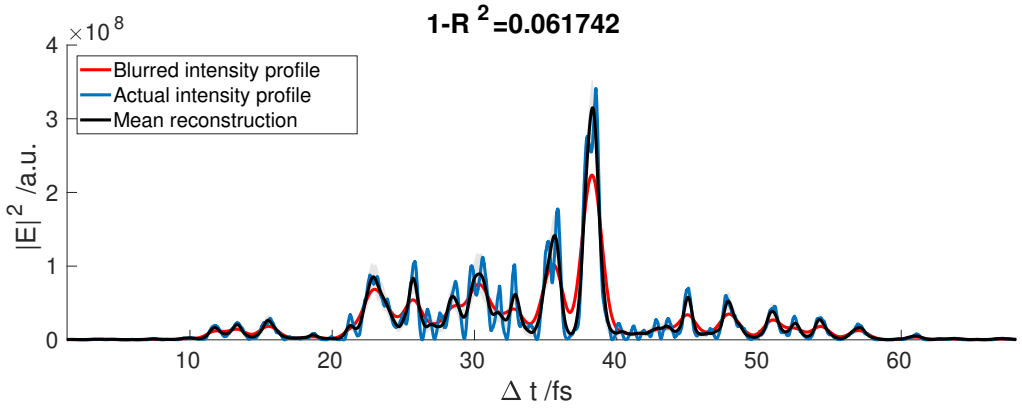

(d) $R_t = 0.5\,\mathrm{fs}$.

Figure 7.3: Four reconstructions for 150 pC. The TDS resolution is indicated below each figure.

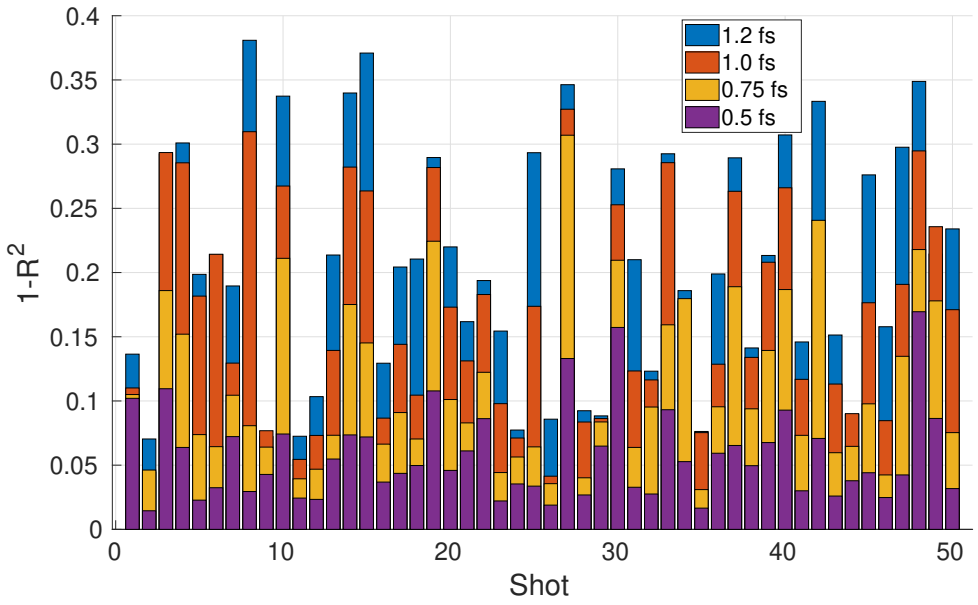

Figure 7.4: Results of the reconstruction of 50 different SASE shots for 40 pC bunches for different TDS resolutions shown in the legend. The $1 - R^2$ value is plotted against the shot number.

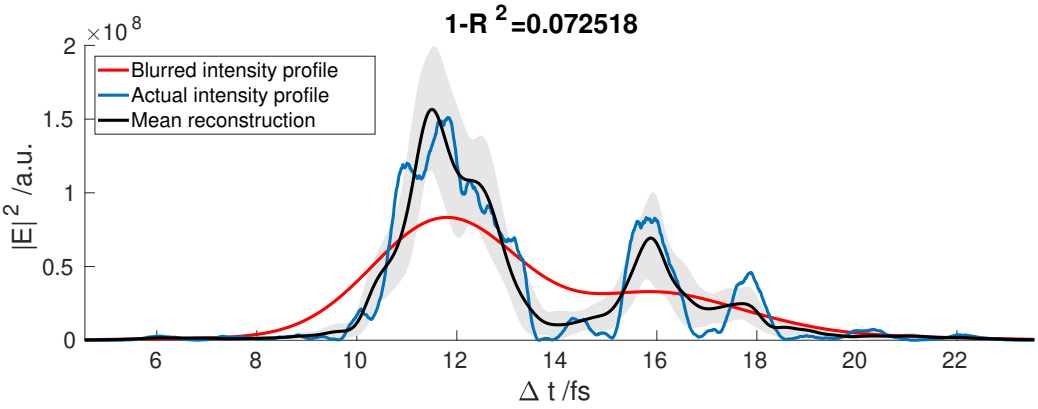

(a) $R_t = 1.2\,\mathrm{fs}$.

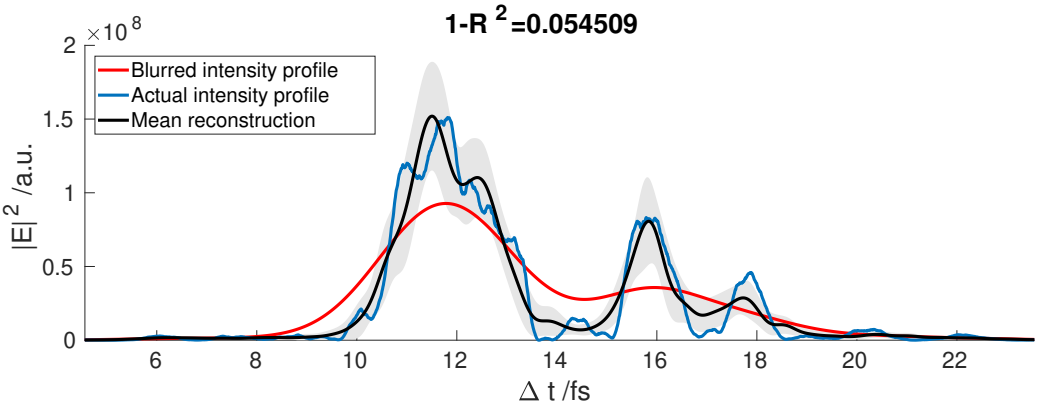

(b) $R_t = 1.0\,\mathrm{fs}$.

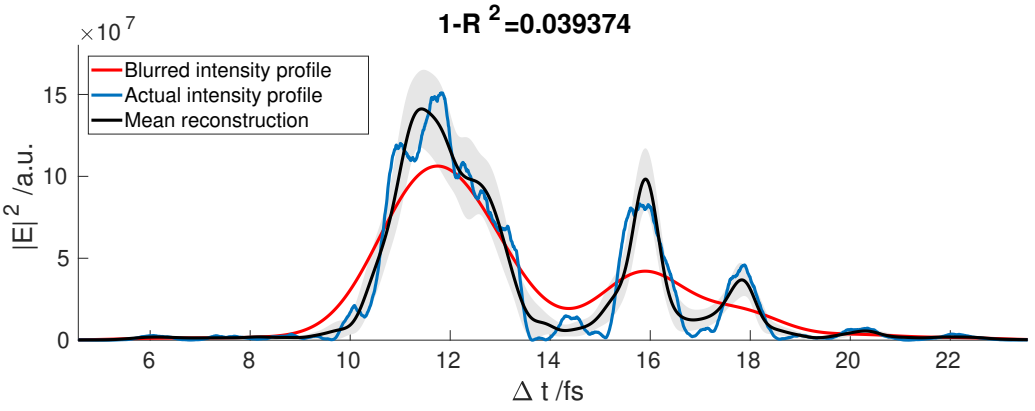

(c) $R_t = 0.75\,\mathrm{fs}$.

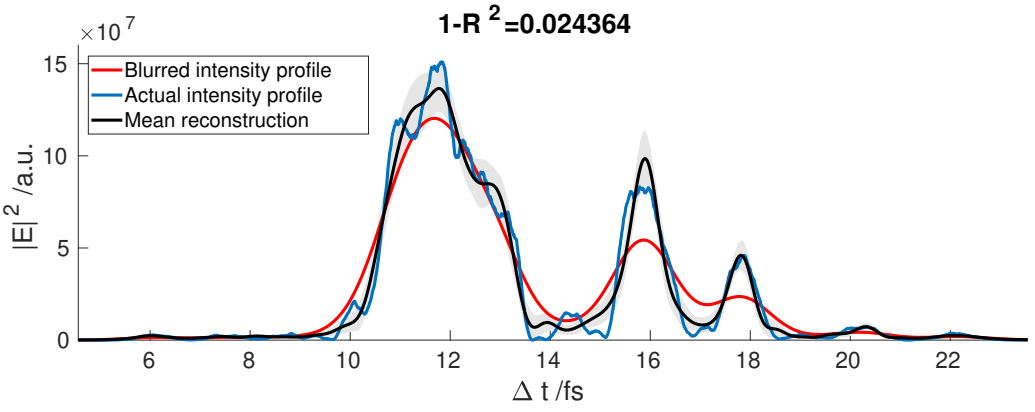

(d) $R_t = 0.5\,\mathrm{fs}$.

Figure 7.5: Four reconstructions for 40 pC. The TDS resolution is indicated below each figure. This is Shot 11 from Fig. 7.4.

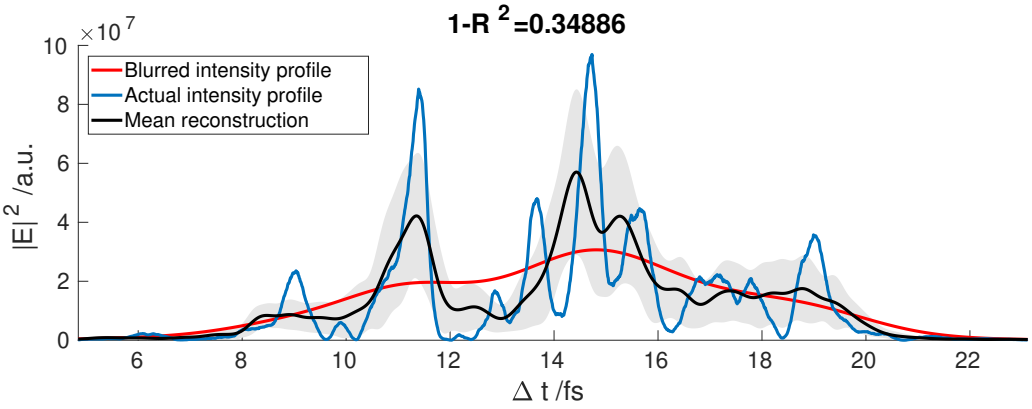

(a) $R_t = 1.2\,\mathrm{fs}$.

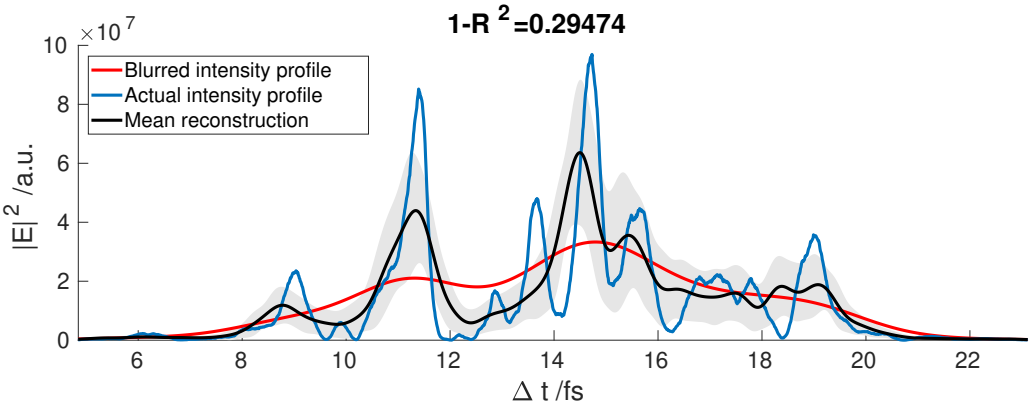

(b) $R_t = 1.0\,\mathrm{fs}$.

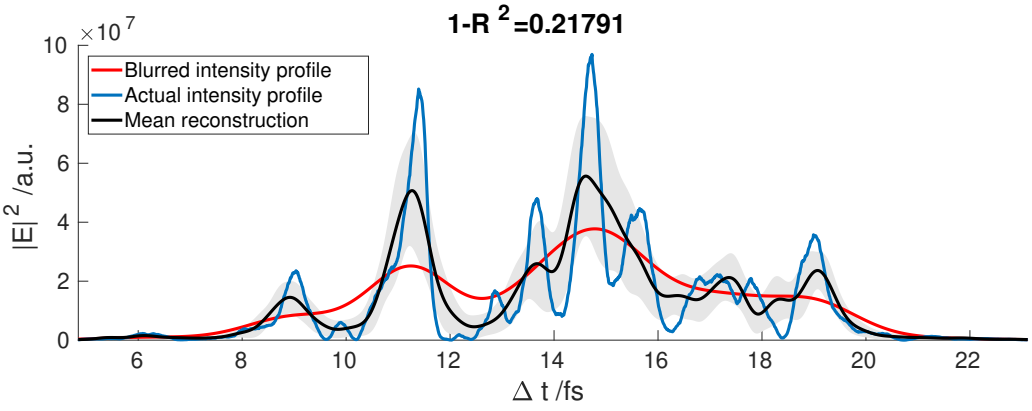

(c) $R_t = 0.75\,\mathrm{fs}$.

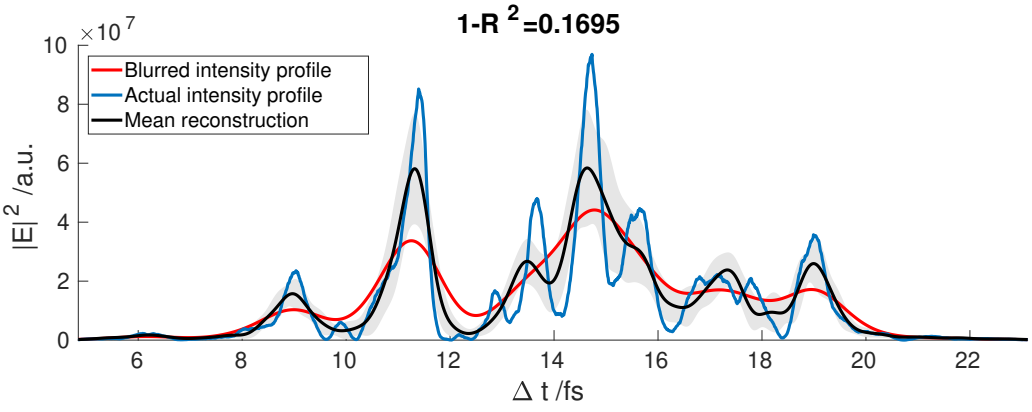

(d) $R_t = 0.5\,\mathrm{fs}$.

Figure 7.6: Four reconstructions for 40 pC. The TDS resolution is indicated below each figure. This is Shot 48 from Fig. 7.4.

7.2.2 Blurred Temporal Measurement and Blurred Spectral Measurement

In this section, the robustness of the reconstruction algorithm is tested if, contrarily to the section before, both the temporal intensity profile and the power spectrum are blurred. This is done as in principle spectrometers can have a nearly perfect resolution [156] yielding cases as described in the section before. However, during the measurements that were conducted at LCLS which are shown in Section 7.3 the spectrometer resolution was not perfect but rather in the order of 0.2 eV rms. Therefore, the same tests as in the section before are conducted and showcased in the following using a blurred power spectrum, $(\mathscr{P} * G)(\omega) = \tilde{\mathscr{P}}(\omega)$ with $R_\omega = 0.2\,\mathrm{eV}$.

To start with, again the temporal profiles for charges of 20 pC, 40 pC, and 150 pC are reconstructed. The reconstructed temporal profiles are shown in Figures 7.7 to 7.9. As can be observed, the reconstruction algorithm is still able to retrieve the actual intensity profile very similar to the cases without spectral blurring. The $1-R^2$ values are all in the same region as in Section 7.2.1 and also the capabilities and limitations of the algorithm remain the same as before. The algorithm excels at reconstructing single, isolated spikes and struggles to resolve multiple, adjacent spikes individually.

Figure 7.10 shows the $1-R^2$ values for the 50 different shots with a charge of 40 pC. Comparing to Fig. 7.4 it can be seen, that for every shot the $1-R^2$ value is in the same order for the perfect and the blurred spectrum, respectively. It can therefore be concluded, that the algorithm performs equally well for both spectral measurements.

Another test was conducted to see, if there is an upper limit on the spectral resolution at which the algorithm stops to work. In order to do so, we assumed that there is no spectral information at all, so the second term in Eq. (7.15) is neglected. The results are shown in Fig. 7.11. It can be seen, that although no spectral information is used, the initial temporal distribution can be retrieved for certain pulses. For most pulses, the $1-R^2$ value is in the order of 0.3 or below. Nonetheless, most of the $1-R^2$ values are higher than the ones with a perfect spectral resolution, c.f. Fig. 7.4, or a small spectral blurring of $R_\omega = 0.2\,\mathrm{eV}$, c.f. Fig. 7.10. Therefore, adding the spectral information is highly recommended, as the reliability and the accurateness of the reconstruction are greatly improved.

7.2.3 Capabilities and Limitations of the Reconstruction Algorithm

In summary, these results show that the algorithm excels at reconstructing single, isolated spikes and struggles to resolve multiple, adjacent spikes individually. The existence of adjoining spikes of similar height is retrieved, although the peak power cannot always be correctly determined, especially at lower resolutions. For high TDS resolutions in the order of 0.5 fs the algorithm reconstructs nearly all of the temporal power profiles accurately.

A small blurring of the spectral measurement has a negligible influence on the reconstruction ability of the algorithm. The algorithm even performs satisfyingly for most pulses, when no spectral information is used by simply trying to deconvolve the temporal blurring. Nonetheless, adding spectral information greatly improves the reliability and the accurateness of the

reconstruction and is therefore highly recommended.

As for measured data we cannot calculate a $1-R^2$ value, we use a different approach to see if the algorithm reconstructs the photon pulse correctly in the following sections. Both, the power profile obtained from the energy spread and the energy loss method, c.f. Section 4.3.3 are used as target power profiles for the reconstruction algorithm. By then comparing the reconstructed temporal power profiles one can observe the similarities and differences to check if even though the inputs might be slightly different the algorithm ends up with the same temporal power profile.

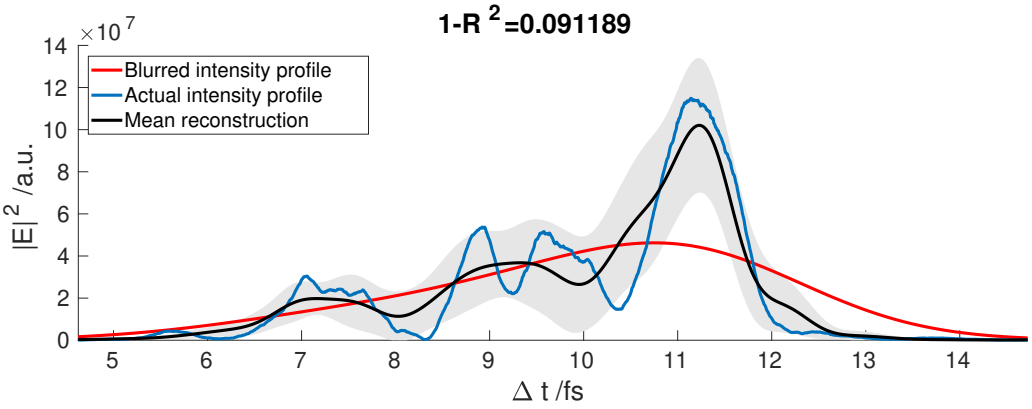

(a) $R_t = 1.2\,\mathrm{fs}$.

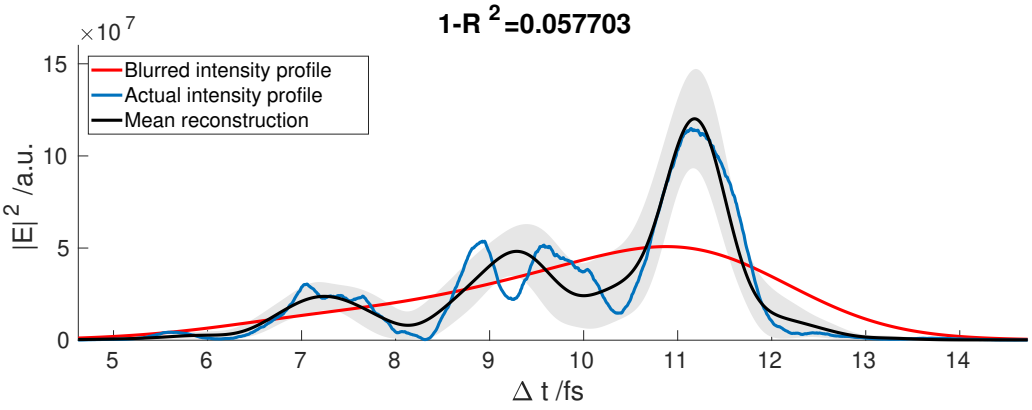

(b) $R_t = 1.0\,\mathrm{fs}$.

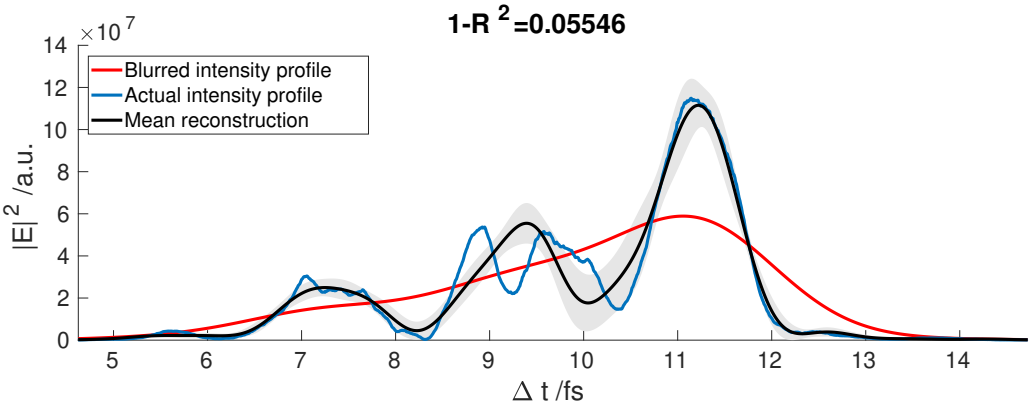

(c) $R_t = 0.75\,\mathrm{fs}$.

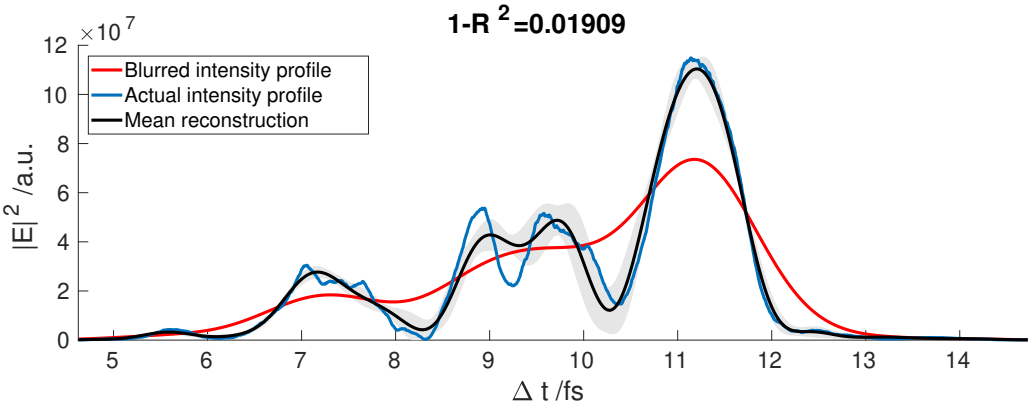

(d) $R_t = 0.5\,\mathrm{fs}$.

Figure 7.7: Four reconstructions for 20 pC. The TDS resolution is indicated below each figure. The power spectrum is blurred using a Gaussian blurring of $R_\omega = 0.2\,\mathrm{eV}$.

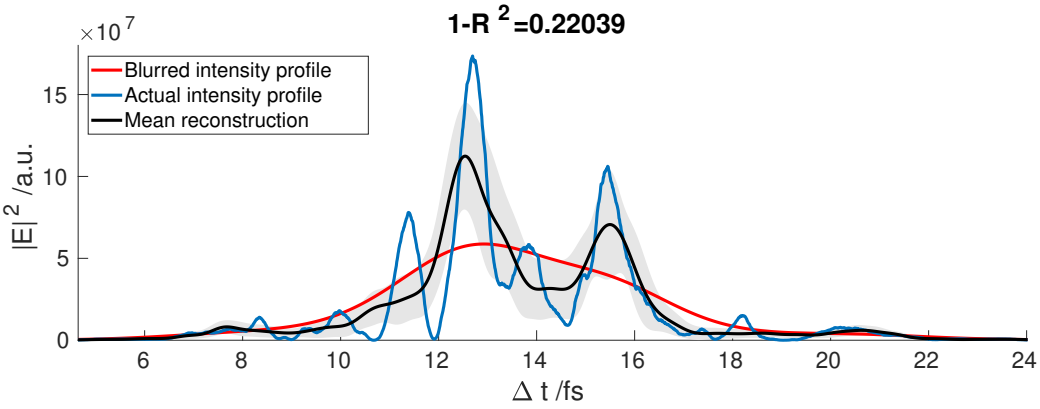

(a) $R_t = 1.2\,\mathrm{fs}$.

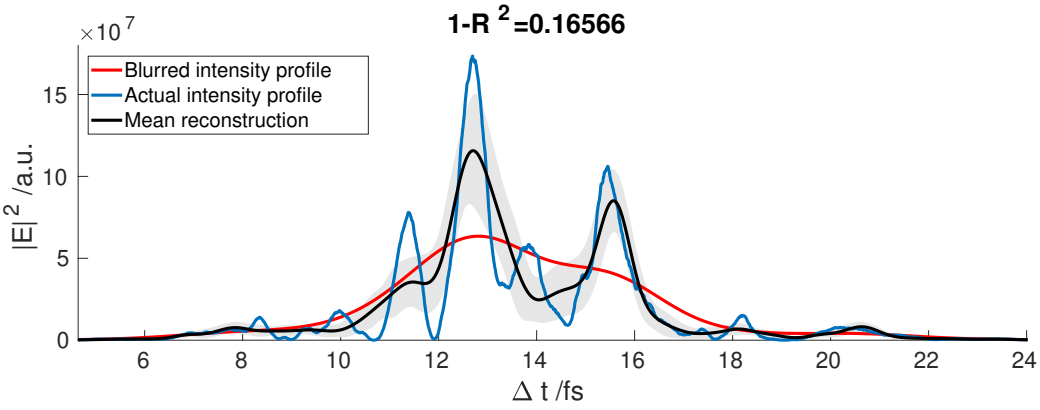

(b) $R_t = 1.0\,\mathrm{fs}$.

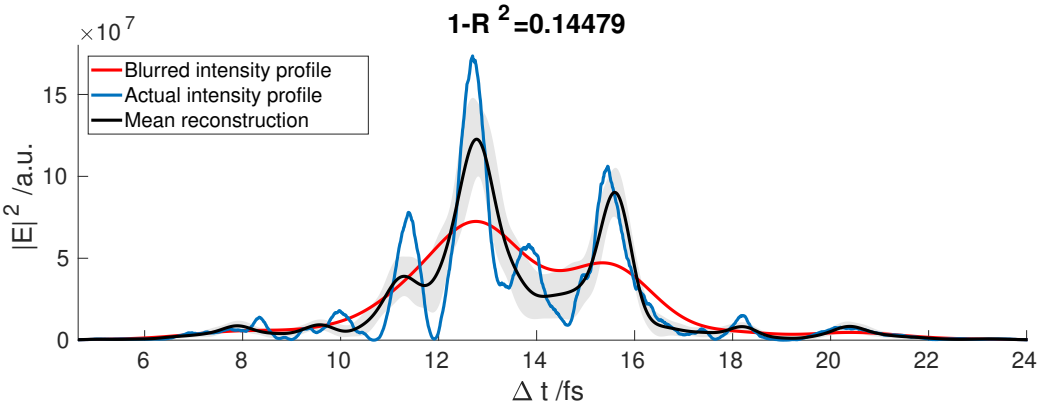

(c) $R_t = 0.75\,\mathrm{fs}$.

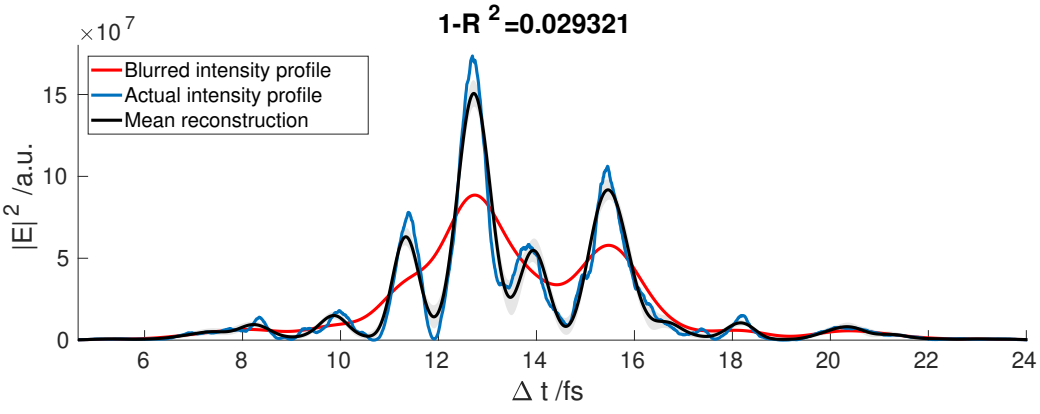

(d) $R_t = 0.5\,\mathrm{fs}$.

Figure 7.8: Four reconstructions for 40 pC. The TDS resolution is indicated below each figure. The power spectrum is blurred using a Gaussian blurring of $R_\omega = 0.2\,\mathrm{eV}$. This shot is not included in Fig. 7.10.

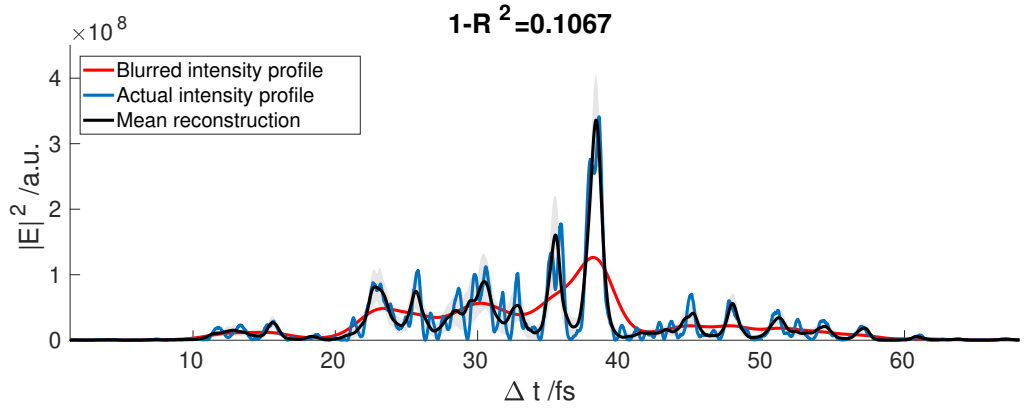

(a) $R_t = 1.2\,\mathrm{fs}$.

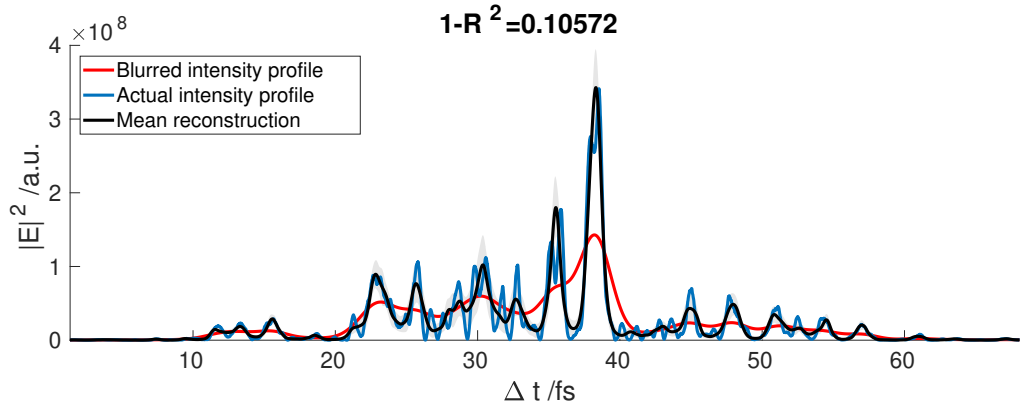

(b) $R_t = 1.0\,\mathrm{fs}$.

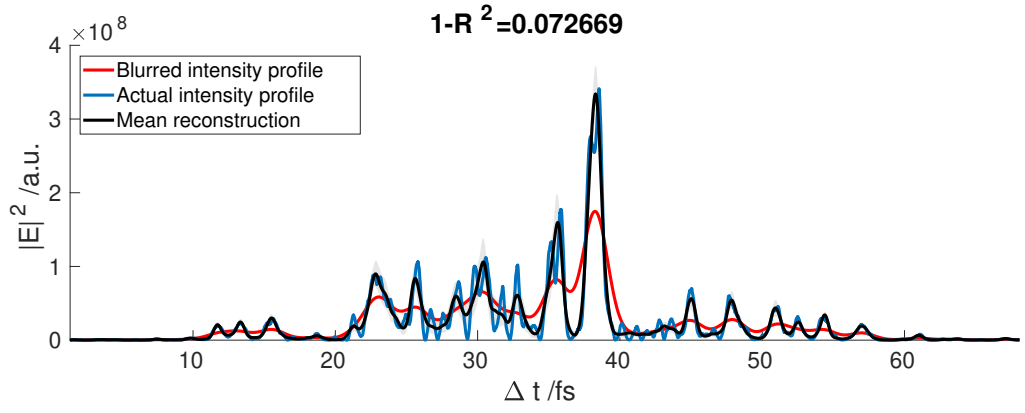

(c) $R_t = 0.75\,\mathrm{fs}$.

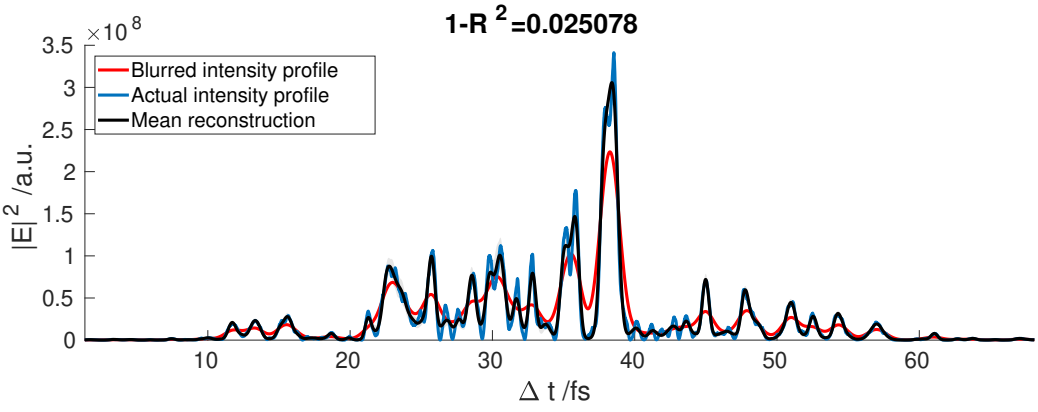

(d) $R_t = 0.5\,\mathrm{fs}$.

Figure 7.9: Four reconstructions for 150 pC. The TDS resolution is indicated below each figure. The power spectrum is blurred using a Gaussian blurring of $R_\omega = 0.2\,\mathrm{eV}$.

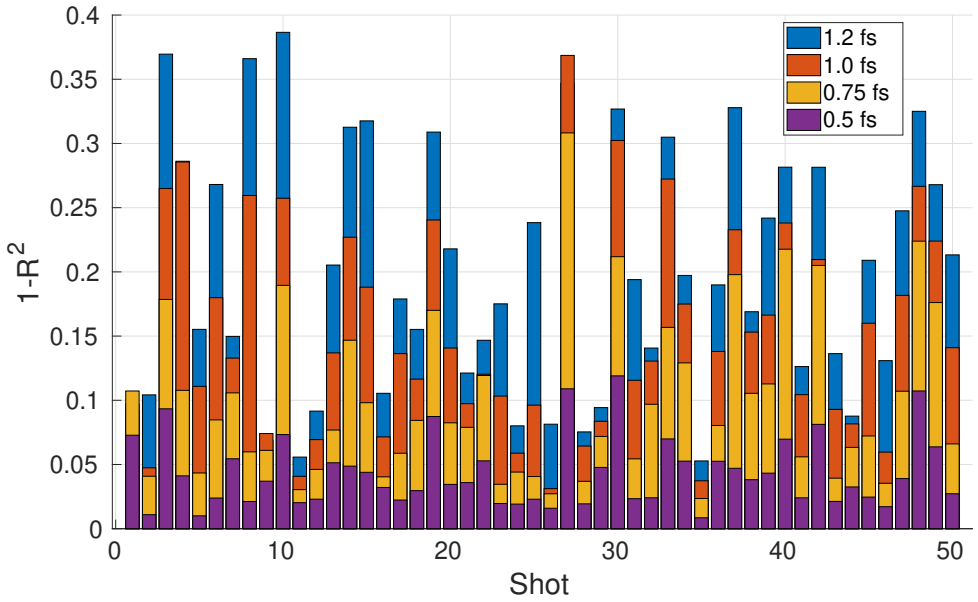

Figure 7.10: Results of the reconstruction of 50 different SASE shots for 40 pC bunches for different TDS resolutions shown in the legend. The $1 - R^2$ value is plotted against the shot number. The power spectrum is blurred using a Gaussian blurring of $R_\omega = 0.2\,\mathrm{eV}$.

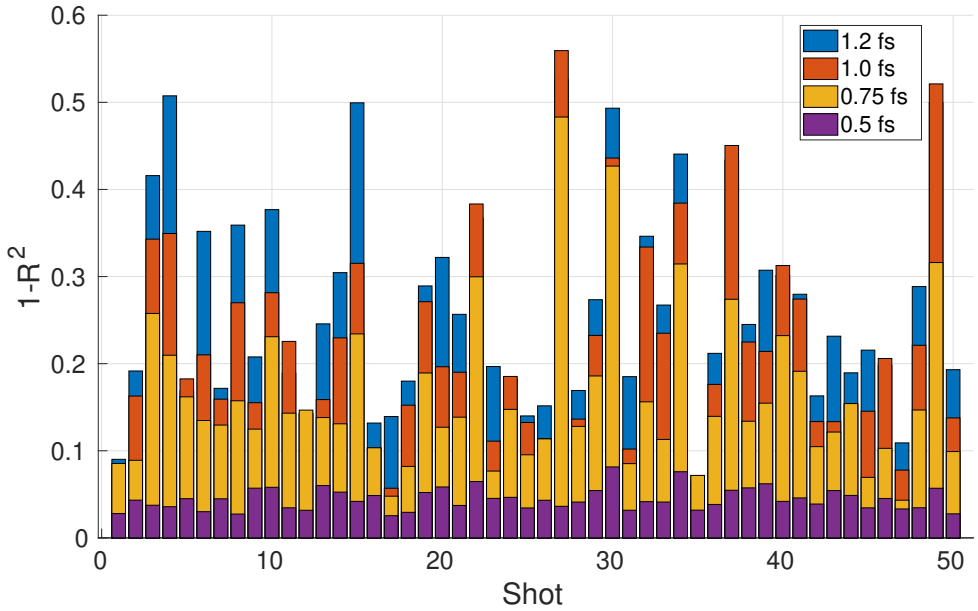

Figure 7.11: Results of the reconstruction of 50 different SASE shots for 40 pC bunches for different TDS resolutions shown in the legend. The $1 - R^2$ value is plotted against the shot number. No spectral information is used.

7.3 Iterative Reconstruction Algorithm Applied to Measurement Data Taken at LCLS

In a dedicated measurement shift data was taken at LCLS (c.f. Section 3.4) to be analyzed using the iterative reconstruction algorithm.

The measurements were taken at a beam energy of 4 GeV resulting in a wavelength of ~ 1.7 nm or a photon energy of ~ 730 eV. The initial charge at the cathode was 40 pC. Using energy collimators in the first bunch compressors, electrons with high energy deviations from the reference energy were truncated. An overview of the parameters for the measurements shown in the following can be found in Table 10.

Table 10: Parameter Overview of Measurements for Iterative Reconstruction Algorithm at LCLS

Charge at undulator	30 pC	20 pC
Bunch length σ_t	12 fs	5 fs
Peak current I_e	2.2 kA	2.2 kA
TDS deflecting voltage V	80 MV	80 MV
Temporal resolution R_t	1.2 fs	1.0 fs
Spectral resolution R_ω	0.2 eV	0.2 eV

As the reconstruction has to be performed using bunches that are not yet saturated, c.f. Section 4.3.3, a gain curve was recorded, see Fig. 7.12. For this reason the beam was kicked behind the 20$^{\text{th}}$ undulator (at $z = 67$ m) to suppress lasing in the downstream undulators. This configuration provided sufficient signal for the spectrometer to work and fulfilled the requirement of pre-saturation. The orbit downstream of the undulator section was restored stable by using a closed three bump [19, 22, 164]. This offset the orbit in the remaining undulators to cancel the overlap between the light wave and the electron bunch.

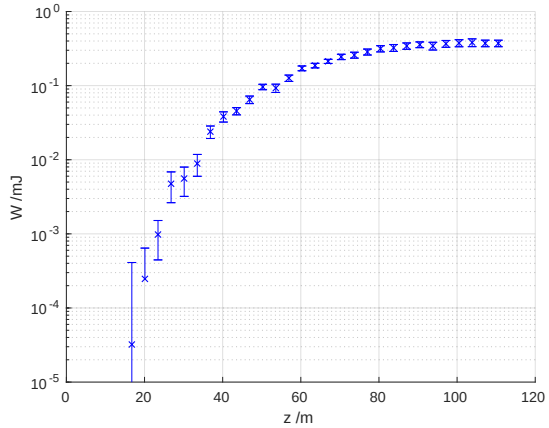

Figure 7.12: Gain curve measured at LCLS in the course of recording data for the reconstruction algorithm showing the gas detector signal over the distance traveled in the undulators. The beam was kicked behind the 20$^{\text{th}}$ undulator (at $z = 67$ m) to sustain the unsaturated condition of the bunches, but still provided sufficient signal for the spectrometer.

To obtain the photon pulse power, the data taken is analyzed using both the energy loss and the energy spread method [117], c.f. Section 4.3.3. Only shots which have an agreement of more than 92 % between both methods are considered for further evaluation using the iterative reconstruction algorithm. This allows for having a sufficient number of shots for reconstruction while maintaining a good agreement between the two methods. Each shot is reconstructed twice using the photon pulse power obtained by both, the energy loss and the energy spread method as target power profile.

In the following, the photon pulses obtained from the reconstruction using only the XTCAV and the according reconstruction methods are displayed as dashed-dotted lines. The reconstructions using the energy loss method are plotted in black and those using the energy spread method are plotted in blue. Identical to the reconstruction of the simulations, 50 different initial guesses serve as starting points for the reconstruction algorithm. These 50 reconstructions are averaged to obtain the final reconstructed photon pulses (solid lines). The mean reconstruction is surrounded by a dark gray and a light gray shaded area which is one standard deviation for the energy loss and the energy spread method, respectively.

7.3.1 Reconstruction of Photon Pulses from Bunches with 30 pC Charge

Firstly, bunches with a charge of 30 pC at the undulator entrance are used for the reconstruction. The parameter overview can be found in the left column of Table 10. Example images of the longitudinal phase space density measured using the XTCAV downstream of the undulators for lasing off and lasing on can be found in Fig. 7.13.

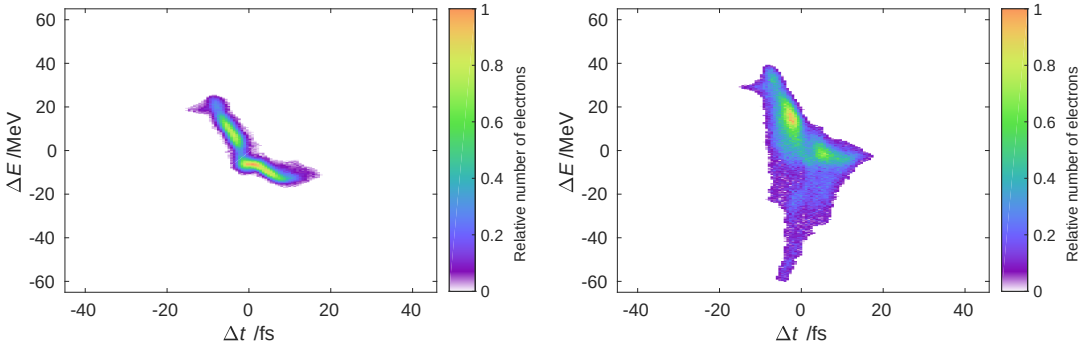

(a) Lasing off.

(b) Lasing on.

Figure 7.13: Longitudinal phase space density of two bunches with a charge of 30 pC, one for lasing off and one for lasing on. The energy deviation of the electrons from the central energy is plotted against their longitudinal position within the bunch.

The longitudinal phase space density is measured using the XTCAV and the resulting images are analyzed according to Section 4.3.3. Both, the energy loss and the energy spread method [117], are used to obtain the temporal profile of the photon pulse.

As discussed in the previous section, the photon pulse is then reconstructed using the iterative reconstruction algorithm described in Section 7.1.

Examples of reconstructed photon pulses can be found in Figs. 7.14 to 7.16, demonstrating the capabilities and the limitations of the algorithm when applied to measured data. As can be seen in these figures, the photon pulse obtained from the energy loss and the energy spread method differ lightly at a deviation of less than 8 %.

For the power profiles in Fig. 7.14 the position of most of the larger SASE spikes is the same for both reconstructions. The maximum power of the highest spike is ~ 1.36 times higher if the energy spread method is used as the target profile. This is because the power obtained from the XTCAV reconstruction at the position of the spike is ~ 1.30 times higher if the energy spread method is used. The smaller SASE spikes agree very well in position and also in height. The reconstruction works well, as the main SASE spikes are separated, which according to Section 7.2 facilitates the reconstruction for the algorithm.

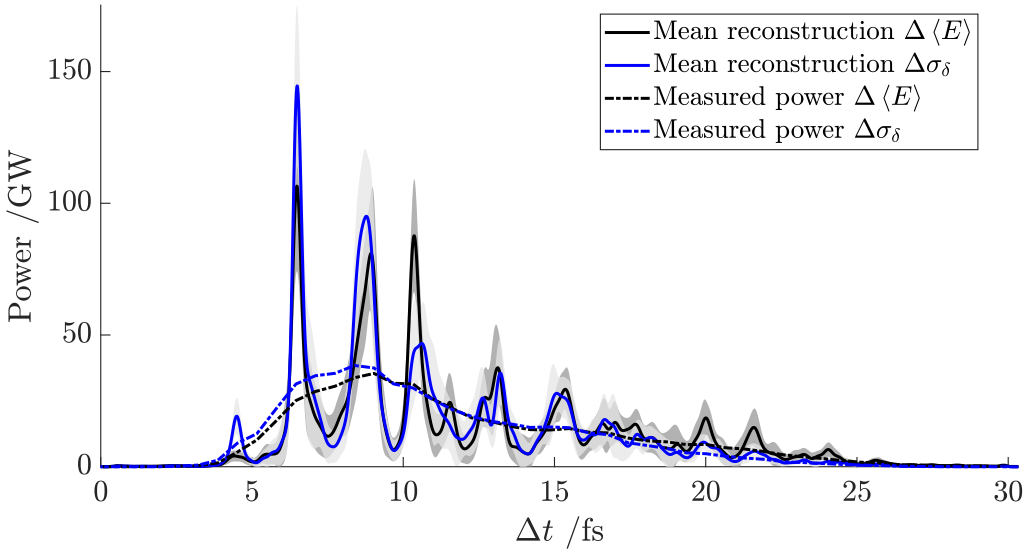

Figure 7.14: Reconstruction of a photon pulse measured at LCLS obtained using the iterative reconstruction algorithm, Shot 1. The total bunch charge at the undulator is 30 pC, the XTCAV resolution is 1.2 fs.

The position and height of most of the main SASE spikes is also very similar for both target profiles shown in Fig. 7.15. The maximum power of the main spike differs by less than 7 %. There is a slight difference in the reconstruction on the left side of the main spike. Here, multiple spikes are very close to one another and the reconstruction algorithm reaches its limitations providing slightly different results for the two target profiles. It can be observed that the power profile contains two spikes between 2 fs and 4.5 fs and three between 4.5 fs and 8 fs. The position can be reconstructed, yet the exact maximum power for each single spike remains unknown. The isolated spikes in the region of 10 fs and 20 fs can be retrieved efficiently by the algorithm.

Figure 7.16 shows a reconstruction where the algorithm reaches the limitations for reconstructing the main features of the photon pulse. These limitations were noted in Section 7.2. In the central part of the photon pulse (between 6 fs and 10 fs) the SASE spikes are too close

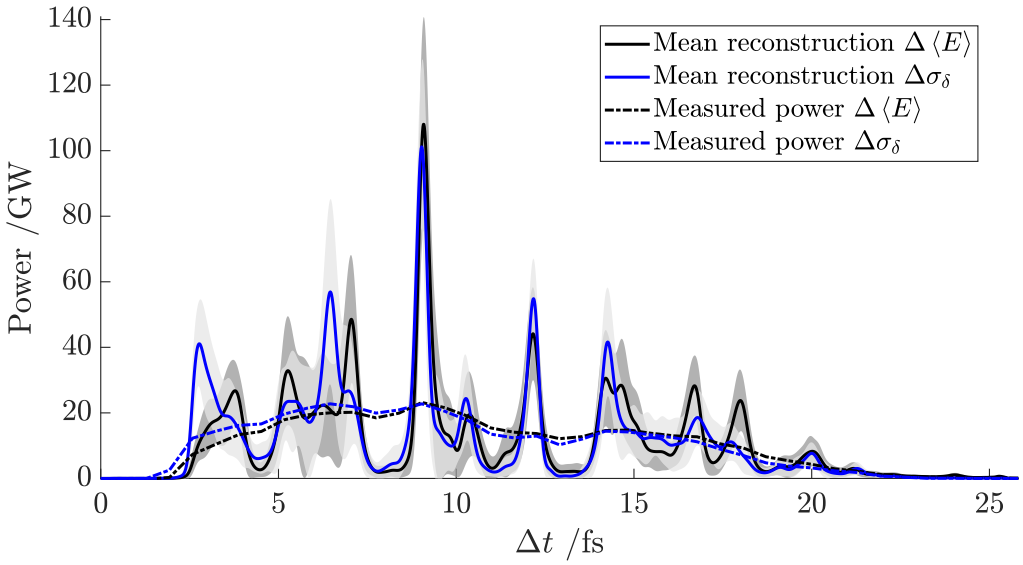

Figure 7.15: Reconstruction of a photon pulse measured at LCLS obtained using the iterative reconstruction algorithm, Shot 2. The total bunch charge at the undulator is 30 pC, the XTCAV resolution is 1.2 fs.

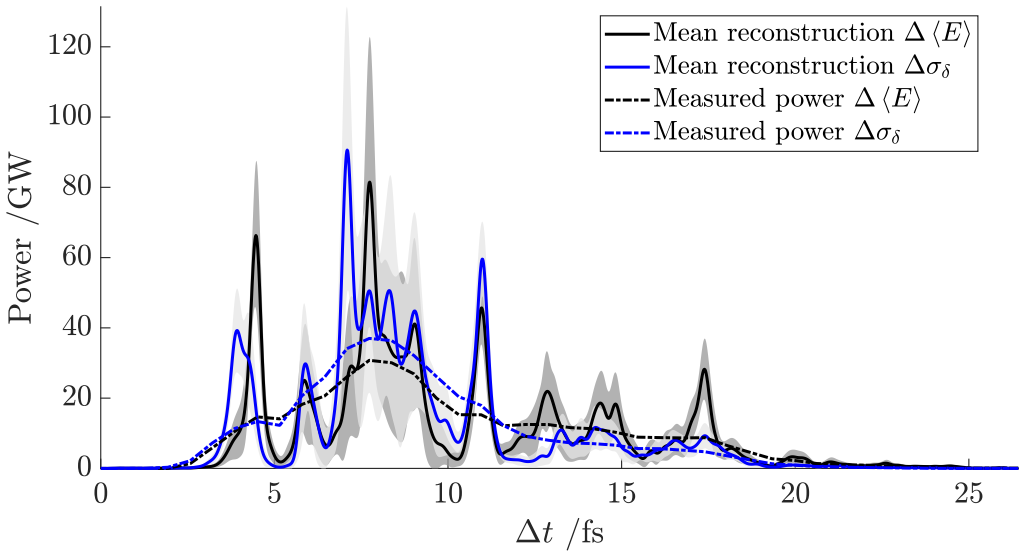

Figure 7.16: Reconstruction of a photon pulse measured at LCLS obtained using the iterative reconstruction algorithm, Shot 3. The total bunch charge at the undulator is 30 pC, the XTCAV resolution is 1.2 fs.

to one another to be retrieved by the algorithm. A similar situation can be seen in Fig. 7.6. Nonetheless, the smaller, isolated side peaks to the left and right of the central part are retrieved adequately by the algorithm.

7.3.2 Reconstruction of Photon Pulses from Bunches with 20 pC Charge

Secondly, bunches with a charge of 20 pC at the undulator entrance are used for the reconstruction. The settings are the same as in Section 7.3.1, but the bunches are truncated even further

using energy collimators in the first bunch compressor. The resulting parameters can be found in the right column of Table 10. Example images of the longitudinal phase space density measured using the XTCAV downstream of the undulators for lasing off and lasing on can be found in Fig. 7.17.

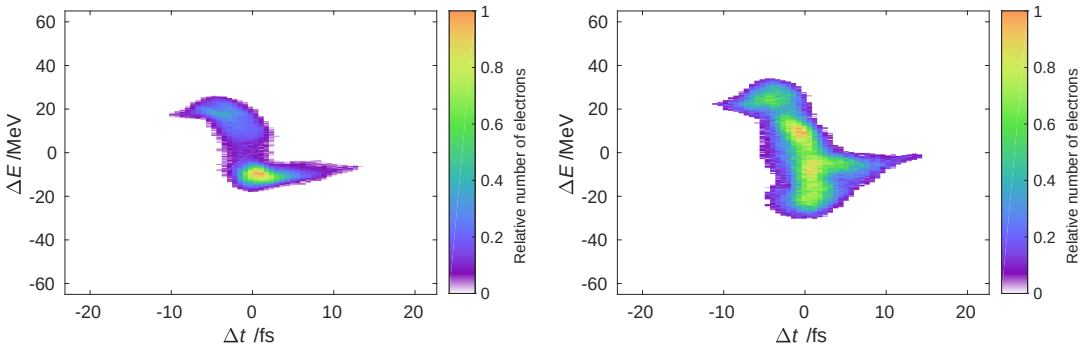

(a) Lasing off. (b) Lasing on.

Figure 7.17: Longitudinal phase space density of two bunches with a charge of 20 pC, one for lasing off and one for lasing on. The energy deviation of the electrons from the central energy is plotted against their longitudinal position within the bunch.

For this setting the longitudinal phase space density is also measured using the XTCAV and the images are analyzed according to Section 4.3.3. Both, the energy loss and the energy spread method [117], are used to obtain the temporal profile of the photon pulse and finally it is reconstructed using the iterative reconstruction algorithm described in Section 7.1.

Figures 7.18 to 7.20 show examples of reconstructed photon pulses for these settings demonstrating the capabilities and the limitations of the algorithm when applied to measured data. As in the previous section, the deviation between the photon pulse reconstructions using the energy difference and the energy spread method is less than 8 %.

The reconstruction found in Fig. 7.18 shows a dominant spike at the beginning of the photon pulse. Both methods reconstruct the spike at 2 fs but with a different maximum power. With the energy difference method the power is ~ 1.35 times higher, in good agreement with the blurred power, which is ~ 1.34 times higher. The rest of the photon pulse consists of smaller, adjacent spikes which can only partly be retrieved by the algorithm. In the region between 8 fs and 10 fs the photon pulse power reconstructed using the energy difference method is close to zero. As a result the algorithm does not reconstruct any power in that region. On the contrary, the energy spread method yields power in this region which results in the reconstruction algorithm showing spikes here. Hence, the difference in the reconstruction is not caused by the algorithm but rather by the differing outputs of the two different methods.

The second example for this setting can be found in Fig. 7.19. The main spikes between 6 fs and 8 fs and 4 fs and 6 fs of the photon pulse are retrieved using both methods as starting points. The small spike between 2 fs and 3 fs of the photon pulse is higher if the energy spread method is used, as the photon pulse power reconstructed using this method is also higher. Several adjacent spikes in the region of 8 fs to 10 fs, cannot be clearly distinguished by the reconstruction

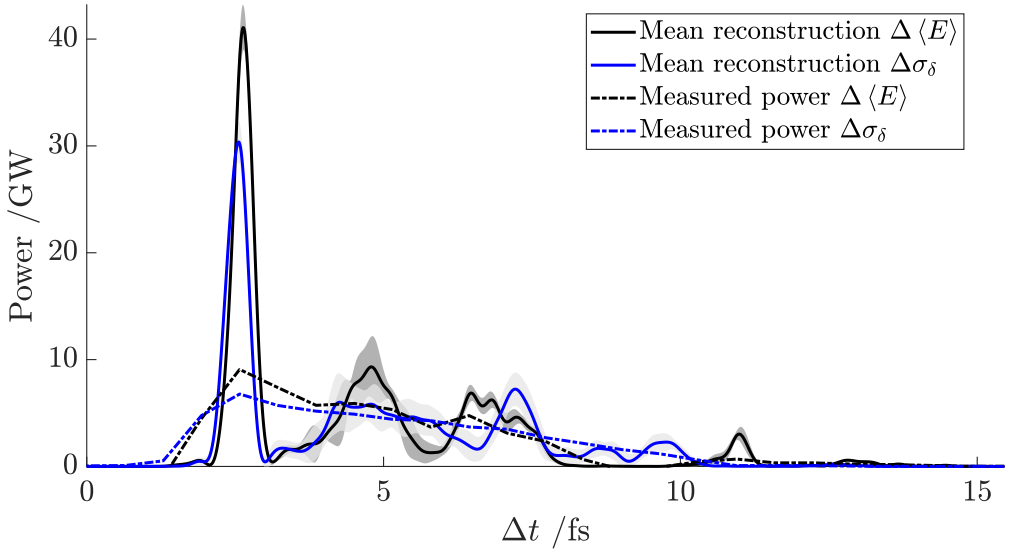

Figure 7.18: Reconstruction of a photon pulse measured at LCLS obtained using the iterative reconstruction algorithm, Shot 1. The total bunch charge at the undulator is 20 pC, the XTCAV resolution is 1.0 fs.

algorithm. Additionally, the power obtained by the energy difference method is higher in this region, leading to a higher power retrieved by the algorithm.

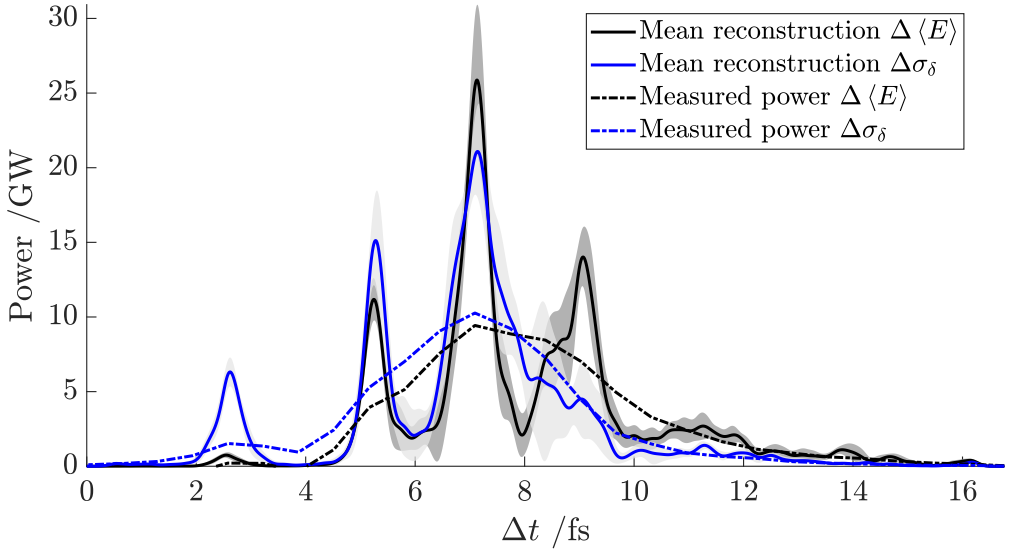

Figure 7.19: Reconstruction of a photon pulse measured at LCLS obtained using the iterative reconstruction algorithm, Shot 2. The total bunch charge at the undulator is 20 pC, the XTCAV resolution is 1.0 fs.

An example where the iterative algorithm did not reconstruct successfully can be found in Fig. 7.20. Here, the central part of the photon pulse comprises many adjacent SASE spikes that cannot be distinguished by the algorithm, c.f. Figs. 7.6 and 7.16. This is expected since the initial reconstruction using the two methods differs in the region of 7 fs to 11 fs both in height and shape and thus, the algorithm ends up with different solutions in this region.

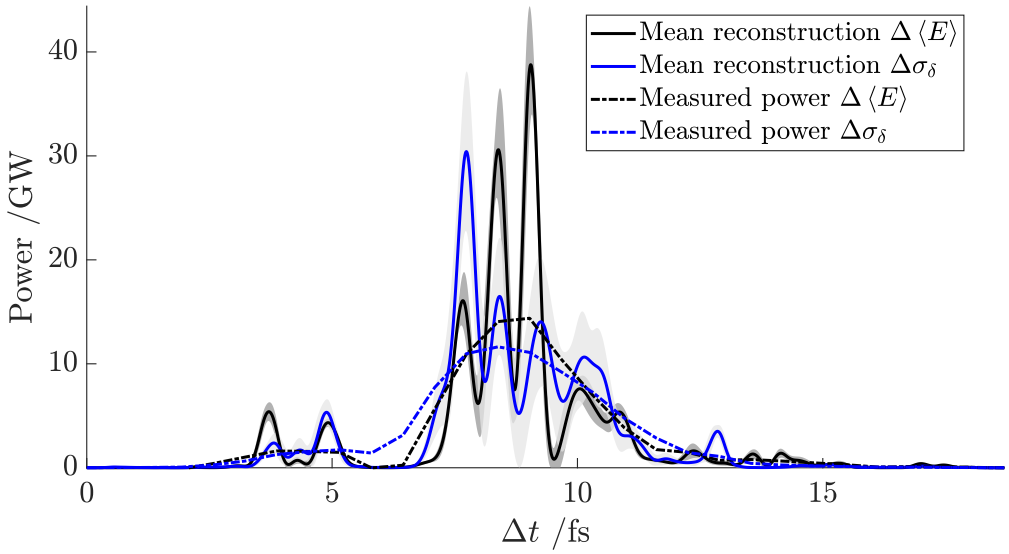

Figure 7.20: Reconstruction of a photon pulse measured at LCLS obtained using the iterative reconstruction algorithm, Shot 3. The total bunch charge at the undulator is 20 pC, the XTCAV resolution is 1.0 fs.

8 Summary

In this thesis, we have investigated the generation of ultra-short electron bunches and FEL pulses at FLASH2. At a wavelength of 40.5 nm 1.1 ± 0.2 modes could be demonstrated using statistics measurements corresponding to a minimum photon pulse duration of (14.7 ± 2.8) fs. An even shorter photon pulse duration was achieved at a wavelength of 15 nm with (13.0 ± 1.5) fs corresponding to 2.0 ± 0.2 modes in this case. Tracking simulations of two measurement shifts were conducted and presented to show the underlying processes of the generation of ultra-short electron bunches. The possibility to produce single-spike radiation at wavelengths of 35.64 nm and 16.95 nm was demonstrated using simulations.

Furthermore, the integration of two PolariX TDSs downstream of the FLASH2 undulators was investigated in this thesis. The beam optics and beam line layout were redesigned yielding resolutions of down to 2.7 fs for standard operation and 1.5 fs for low charge operation with an energy resolution of $3.0 \cdot 10^{-4}$ and $1.7 \cdot 10^{-4}$, respectively. With these PolariX TDSs in the FLASH2 beam line it will be possible to measure the longitudinal phase space density, reconstruct the photon pulse profile, and perform slice emittance measurements in both planes, as was shown using tracking simulations.

Finally, an iterative reconstruction algorithm to enhance the temporal resolution of photon pulse reconstructions was developed and presented in this thesis. This reconstruction algorithm retrieves the square of the absolute value of the electric field of the light wave by combining spectral and temporal measurements. It was tested using simulation data and showed excellent reconstruction abilities among multiple beam settings. Furthermore, it was successfully applied to measurement data taken at LCLS.

A Momentum Compaction in Straight Beam Line Elements

The coordinates in MAD8 [165] for the fifth and sixth coordinate are given by

$$t = -c\Delta t \tag{A.1}$$

$$p_t = \frac{\Delta E}{p_s c}, \tag{A.2}$$

where t is the longitudinal coordinate, c is the speed of light, Δt is the actual time difference between the particle and the synchronous particle, p_t is the momentum in t direction, E is the total energy, and p_s is the synchronous momentum. In a drift space, the momentum p_t changes the coordinate t according to Eq. (5.3) in [165] to

$$t = -c\Delta t = \frac{L}{\beta_s^2 \gamma_s^2} \frac{\Delta E}{p_s c}, \tag{A.3}$$

where $\beta = v/c$, v is the velocity, $\gamma = \sqrt{\frac{1}{1-\beta^2}}$, and the index s refers to the synchronous particle.

The coordinates given in Eq. (2.38) for the fifth and sixth coordinate are

$$\tau = -\Delta t \cdot \frac{T_s}{p_s} \tag{A.4}$$

$$\delta = \frac{T - T_s}{T_s}, \tag{A.5}$$

where $T = E - m_e c^2$ is the kinetic energy an m_e is the electron mass. In a drift space, the energy deviation δ changes the coordinate τ according to Eq. (2.55) to

$$\begin{aligned} -\Delta t \cdot \frac{T_s}{p_s} &= \frac{L}{(\gamma_s + 1)^2} \frac{T - T_s}{T_s} \\ \Rightarrow -c\Delta t &= \frac{L}{(\gamma_s + 1)^2} \frac{T - T_s}{T_s^2} \cdot p_s c. \end{aligned} \tag{A.6}$$

In the following, we will apply some useful formulas from special relativity:

$$T = E - m_e c^2 = (\gamma - 1) m_e c^2 \tag{A.7}$$

$$E = T + m_e c^2 = \gamma m_e c^2 \tag{A.8}$$

$$p = \beta \gamma m_e c \tag{A.9}$$

$$\gamma^2 = \frac{1}{1 - \beta^2} \tag{A.10}$$

$$\beta^2 = 1 - \frac{1}{\gamma^2} \tag{A.11}$$

$$\beta^2 \gamma^2 = \gamma^2 - 1. \tag{A.12}$$

We will now show that Eqs. (A.3) and (A.6) are in fact equal. Starting from Eq. (A.6), we

see:

$$
\begin{aligned}
-c\Delta t &= \frac{L}{(\gamma_s+1)^2}\cdot\frac{(\gamma-1)m_ec^2-(\gamma_s-1)m_ec^2}{(\gamma_s-1)^2m_e^2c^4}\cdot\beta_s\gamma_s m_ec^2\\
&= \frac{L}{(\gamma_s+1)^2}\cdot\frac{\Delta E}{(\gamma_s-1)^2m_ec^2}\cdot\beta_s\gamma_s\\
&= \frac{L}{(\gamma_s^2-1)}\cdot\frac{\Delta E}{(\gamma_s^2-1)m_ec^2}\cdot\beta_s\gamma_s\\
&= \frac{L}{(\gamma_s^2-1)}\cdot\frac{\beta_s\gamma_s}{(\gamma_s^2-1)}\cdot\frac{\Delta E}{\frac{p_sc}{\beta_s\gamma_s}}\\
&= \frac{L}{(\gamma_s^2-1)}\cdot\frac{\beta_s^2\gamma_s^2}{(\gamma_s^2-1)}\cdot\frac{\Delta E}{p_sc}\\
&\overset{(A.12)}{=} \frac{L}{\beta_s^2\gamma_s^2}\frac{\Delta E}{p_sc}. \qquad \square
\end{aligned}
\tag{A.13}
$$

References

[1] J. M. J. Madey, "Stimulated Emission of Bremsstrahlung in a Periodic Magnetic Field", *Journal of Applied Physics*, vol. 42, no. 5, pp. 1906–1913, 1971. DOI:10.1063/1.1660466

[2] P. Emma *et al.*, "Femtosecond and Subfemtosecond X-Ray Pulses from a Self-Amplified Spontaneous-Emission–Based Free-Electron Laser", *Phys. Rev. Lett.*, vol. 92, p. 074801, 2004. DOI:10.1103/PhysRevLett.92.074801

[3] R. Neutze, R. Wouts, D. van der Spoel, E. Weckert, and J. Hajdu, "Potential for biomolecular imaging with femtosecond X-ray pulses", *Nature*, vol. 406, no. 6797, pp. 752–757, 2000. DOI:10.1038/35021099

[4] M. Drescher *et al.*, "Time-resolved atomic inner-shell spectroscopy", *Nature*, vol. 419, no. 6909, pp. 803–807, 2002. DOI:10.1038/nature01143

[5] M. Levantino *et al.*, "Ultrafast myoglobin structural dynamics observed with an X-ray free-electron laser", *Nature Communications*, vol. 6, p. 6772, 2015. DOI:10.1038/ncomms7772

[6] P. Emma, J. Frisch, and P. Krejcik, "A Transverse RF Deflecting Structure for Bunch Length and Phase Space Diagnostics", SLAC National Accelerator Laboratory, CA, USA, Tech. Rep. LCLS-TN-00-12, 2000.

[7] M. Vogt, K. Honkavaara, J. Rönsch-Schulenburg, S. Schreiber, and J. Zemella, "Upgrade Plans for FLASH for the Years After 2020", in *Proceedings of IPAC2019*, Melbourne, Australia, 2019, paper TUPRB027, pp. 1748–1751. DOI:10.18429/JACoW-IPAC2019-TUPRB027

[8] A. Grudiev, "Design of Compact High Power RF Components at X-Band", CERN, Geneva, Switzerland, CLIC - Note 1067, 2016.

[9] B. Marchetti *et al.*, "X-Band TDS Project", in *Proceedings of IPAC2017*, Copenhagen, Denmark, 2017, paper MOPAB044, pp. 184–187. DOI:10.18429/JACoW-IPAC2017-MOPAB044

[10] P. Craievich *et al.*, "Status of the Polarix-TDS Project", in *Proceedings of IPAC2018*, Vancouver, BC, Canada, 2018, paper THPAL068, pp. 3808–3811. DOI:10.18429/JACoW-IPAC2018-THPAL068

[11] C. Behrens *et al.*, "Few-femtosecond time-resolved measurements of X-ray free-electron lasers", *Nature Communications*, vol. 5, p. 3762, 2014. DOI:10.1038/ncomms4762

[12] S. Li *et al.*, "Electron Ghost Imaging", *Phys. Rev. Lett.*, vol. 121, p. 114801, 2018. DOI:10.1103/PhysRevLett.121.114801

[13] D. Ratner, J. P. Cryan, T. J. Lane, S. Li, and G. Stupakov, "Pump-Probe Ghost Imaging with SASE FELs", *Phys. Rev. X*, vol. 9, p. 011045, 2019. DOI:10.1103/PhysRevX.9.011045

[14] K. R. Meyer, G. R. Hall, and D. Offin, *Introduction to Hamiltonian Dynamical Systems and the N-Body Problem*. Springer, 2009. DOI:10.1007/978-3-319-53691-0

[15] M. Vogt, "Bounds on the Maximum Attainable Equilibrium Spin Polarization of Protons at High Energy in HERA", Ph.D. dissertation, Universität Hamburg, 2000.

[16] G. H. Hofstätter, "Rigorous Bounds on Survival Times in Circular Accelerators and Efficient Computation of Fringe-Field Transfer-Maps", Ph.D. dissertation, Michigan State University, 1994.

[17] W. Hein, *Einführung in die Struktur- und Darstellungstheorie der klassischen Gruppen*. Springer-Verlag Berlin Heidelberg, 1990. DOI:10.1007/978-3-642-74340-5

[18] J. Hilgert and K.-H. Neeb, *Lie-Gruppen und Lie-Algebren*. Vieweg, 1991. DOI:10.1007/978-3-322-80270-5

[19] F. Müller, "Compensation of Steerer Crosstalk between FLASH1 and FLASH2", Master's thesis, Universität Hamburg, 2015.

[20] H. Mais, "Some Topics in Beam Dynamics of Storage Rings", *DESY Report 96-119*, 1996.

[21] H. Wiedemann, *Particle Accelerator Physics*. Springer-Verlag Berlin Heidelberg, 2007. DOI:10.1007/978-3-540-49045-6

[22] K. Wille, *The Physics of Particle Accelerators: An Introduction*. Oxford University Press, 2000.

[23] E. Courant and H. Snyder, "Theory of the alternating-gradient synchrotron", *Annals of Physics*, vol. 3, no. 1, pp. 1 – 48, 1958. DOI:10.1016/0003-4916(58)90012-5

[24] F. Schwabl, *Statistical Mechanics*. Springer-Verlag Berlin Heidelberg, 2006. DOI:10.1007/3-540-36217-7

[25] R. Duvenhage, "Recurrence in Quantum Mechanics", *International Journal of Theoretical Physics*, vol. 41, no. 1, pp. 45–61, 2002. DOI:10.1023/A:1013217415677

[26] L. Spentzouris, "Fundamentals of Accelerator Physics and Technology with Simulations and Measurements Lab: Emittance", in *Course Materials - U.S. Particle Accelerator School*, MIT, Cambridge, MA, USA, 2010.

[27] S. Di Mitri, "Bunch Length Compressors", *CERN Yellow Rep. School Proc.*, vol. 1, pp. 363–380, 2018. DOI:10.23730/CYRSP-2018-001.363

[28] M. Rehders, “Generation of ultra-short low-charge electron bunches for single spike SASE radiation at the Free-Electron Laser in Hamburg”, Ph.D. dissertation, Universität Hamburg, Hamburg, Germany, 2017.

[29] M. Reiser, *Theory and Design of Charged Particle Beams*. Weihnheim, Germany: WILEY-VCH Verlag GmbH & Co. KGaA, 2008. DOI:10.1002/9783527622047

[30] M. Ferrario, “Space Charge Mitigation”, *CERN Yellow Reports: School Proceedings*, vol. 1, pp. 177–194, 2018. DOI:10.23730/CYRSP-2018-005.89

[31] H. Freund, “Space-charge effects in free-electron lasers”, *Nuclear Instruments and Methods in Physics Research Section A: Accelerators, Spectrometers, Detectors and Associated Equipment*, vol. 331, no. 1, pp. 496 – 500, 1993. DOI:10.1016/0168-9002(93)90096-Z

[32] P. Schmüser, M. Dohlus, J. Rossbach, and C. Behrens, *Free-Electron Lasers in the Ultraviolet and X-Ray Regime*. Cham, Switzerland: Springer, 2014. DOI:10.1007/978-3-319-04081-3

[33] K. Schindl, “Space Charge”, in *Proceedings, CAS - CERN Accelerator School: Intermediate Course on Accelerator Physics, Zeuthen, Germany, 15 - 26 Sep, 2003*, 2006, pp. 305–320. DOI:10.5170/CERN-2006-002.305

[34] N. Chauvin, “Space-Charge Effect”, in *Proceedings, CAS - CERN Accelerator School: Ion Sources, Senec, Slovakia, May 29-June 8, 2012*, 2013, pp. 63–83. DOI:10.5170/CERN-2013-007.63

[35] M. Dohlus, A. Kabel, and T. Limberg, “Coherent effects of a macro-bunch in an undulator”, *Nuclear Instruments and Methods in Physics Research Section A: Accelerators, Spectrometers, Detectors and Associated Equipment*, vol. 445, no. 1, pp. 84 – 89, 2000. DOI:10.1016/S0168-9002(00)00118-2

[36] J. Schwinger, “On the Classical Radiation of Accelerated Electrons”, *Phys. Rev.*, vol. 75, pp. 1912–1925, 1949. DOI:10.1103/PhysRev.75.1912

[37] M. Dohlus and T. Limberg, “Emittance growth due to wake fields on curved bunch trajectories”, *Nuclear Instruments and Methods in Physics Research Section A: Accelerators, Spectrometers, Detectors and Associated Equipment*, vol. 393, no. 1, pp. 494 – 499, 1997. DOI:10.1016/S0168-9002(97)00552-4

[38] M. Dohlus, T. Limberg, and P. Emma, “Electron Bunch Length Compression”, in *Proc. Int. Committee for Future Accelerator Beam Dynamics Newsletter*, I. Ko and W. Chou, Eds., no. 38, 2005, pp. 15–37.

[39] S. Di Mitri, “Coherent Synchrotron Radiation and Microbunching Instability”, *CERN Yellow Reports: School Proceedings*, vol. 1, pp. 381–400, 2018. DOI:10.23730/CYRSP-2018-001.381

[40] E. L. Saldin, E. A. Schneidmiller, and M. V. Yurkov, “Coherent radiation of an electron bunch moving in an arc of a circle”, *AIP Conference Proceedings*, vol. 413, no. 1, pp. 291–297, 1997. DOI:10.1063/1.54410

[41] M. Scholz, “Design of the Extraction Arc for the 2nd Beam Line of the Free-Electron Laser FLASH”, Ph.D. dissertation, Universität Hamburg, 2013.

[42] J. Schwinger, “On Radiation by Electrons in a Betatron”, 1945, unpublished.

[43] E. Saldin, E. Schneidmiller, and M. Yurkov, *The Physics of Free Electron Lasers*. Springer, 2000. DOI:10.1007/978-3-662-04066-9

[44] K.-J. Kim, Z. Huang, and R. Lindberg, *Synchrotron Radiation and Free-Electron Lasers: Principles of Coherent X-Ray Generation*. Cambridge University Press, 2017. DOI:10.1017/9781316677377

[45] Z. Huang and K.-J. Kim, “Review of x-ray free-electron laser theory”, *Phys. Rev. ST Accel. Beams*, vol. 10, p. 034801, 2007. DOI:10.1103/PhysRevSTAB.10.034801

[46] D. A. G. Deacon, L. R. Elias, J. M. J. Madey, G. J. Ramian, H. A. Schwettman, and T. I. Smith, “First Operation of a Free-Electron Laser”, *Phys. Rev. Lett.*, vol. 38, pp. 892–894, 1977. DOI:10.1103/PhysRevLett.38.892

[47] R. Bonifacio, C. Pellegrini, and L. Narducci, “Collective instabilities and high-gain regime in a free electron laser”, *Optics Communications*, vol. 50, no. 6, pp. 373 – 378, 1984. DOI:10.1016/0030-4018(84)90105-6

[48] M. Xie, “Design optimization for an X-ray free electron laser driven by SLAC linac”, in *Proceedings of PAC1995*, vol. 1, 1995, pp. 183–185 vol.1. DOI:10.1109/PAC.1995.504603

[49] E. Saldin, E. Schneidmiller, and M. Yurkov, “Coherence properties of the radiation from SASE FEL”, in *Free Electron Lasers 2002*, K.-J. Kim, S. Milton, and E. Gluskin, Eds. Amsterdam: Elsevier, 2003, pp. 106 – 109. DOI:10.1016/B978-0-444-51417-2.50031-6

[50] K.-J. Kim, “Temporal and transverse coherence of self-amplified spontaneous emission”, *AIP Conference Proceedings*, vol. 413, no. 1, pp. 3–13, 1997. DOI:10.1063/1.54421

[51] H. Freund and T. Antonsen, *Principles of Free-Electron Lasers*. Dordrecht, Netherlands: Springer, 1992, ch. Optical Guiding. DOI:10.1007/978-3-319-75106-1

[52] R. Bonifacio, L. De Salvo, P. Pierini, N. Piovella, and C. Pellegrini, "Spectrum, temporal structure, and fluctuations in a high-gain free-electron laser starting from noise", *Phys. Rev. Lett.*, vol. 73, pp. 70–73, 1994. DOI:10.1103/PhysRevLett.73.70

[53] E. Saldin, E. Schneidmiller, and M. Yurkov, "Statistical properties of the radiation from VUV FEL at DESY operating at 30nm wavelength in the femtosecond regime", *Nuclear Instruments and Methods in Physics Research Section A: Accelerators, Spectrometers, Detectors and Associated Equipment*, vol. 562, no. 1, pp. 472 – 486, 2006. DOI:10.1016/j.nima.2006.02.166

[54] E. A. Schneidmiller and M. V. Yurkov, "Application of Statistical Methods for Measurements of the Coherence Properties of the Radiation from SASE FEL", in *Proceedings of IPAC2016*, Busan, Korea, 2016, paper MOPOW013, pp. 738–740. DOI:10.18429/JACoW-IPAC2016-MOPOW013

[55] S. Ackermann *et al.*, "Generation of Coherent 19- and 38-nm Radiation at a Free-Electron Laser Directly Seeded at 38 nm", *Phys. Rev. Lett.*, vol. 111, p. 114801, 2013. DOI:10.1103/PhysRevLett.111.114801

[56] L. DiMauro *et al.*, "First SASE and seeded FEL lasing of the NSLS DUV FEL at 266 and 400nm", *Nuclear Instruments and Methods in Physics Research Section A: Accelerators, Spectrometers, Detectors and Associated Equipment*, vol. 507, no. 1, pp. 15 – 18, 2003. DOI:10.1016/S0168-9002(03)00825-8

[57] S. Reiche, P. Musumeci, C. Pellegrini, and J. Rosenzweig, "Development of ultra-short pulse, single coherent spike for SASE X-ray FELs", *Nuclear Instruments and Methods in Physics Research Section A: Accelerators, Spectrometers, Detectors and Associated Equipment*, vol. 593, no. 1, pp. 45 – 48, 2008. DOI:10.1016/j.nima.2008.04.061

[58] J. Feldhaus, "FLASH—the first soft x-ray free electron laser (FEL) user facility", *Journal of Physics B: Atomic, Molecular and Optical Physics*, vol. 43, no. 19, p. 194002, 2010. DOI:10.1088/0953-4075/43/19/194002

[59] V. Ayvazyan *et al.*, "First operation of a free-electron laser generating GW power radiation at 32 nm wavelength", *The European Physical Journal D - Atomic, Molecular, Optical and Plasma Physics*, vol. 37, no. 2, pp. 297–303, 2006. DOI:10.1140/epjd/e2005-00308-1

[60] W. Ackermann *et al.*, "Operation of a free-electron laser from the extreme ultraviolet to the water window", *Nature Photonics*, vol. 1, pp. 336 – 342, 2007. DOI:10.1038/nphoton.2007.76

[61] B. Faatz *et al.*, "Simultaneous operation of two soft x-ray free-electron lasers driven by one linear accelerator", *New Journal of Physics*, vol. 18, no. 6, p. 062002, 2016. DOI:10.1088/1367-2630/18/6/062002

[62] M. Vogt, B. Faatz, J. Feldhaus, K. Honkavaara, S. Schreiber, and R. Treusch, "Status of the Soft X-ray Free Electron Laser FLASH", in *Proceedings of IPAC2015*, Richmond, VA, USA, 2015, paper TUPWA033, pp. 1482–1484. DOI:10.18429/JACoW-IPAC2015-TUPWA033

[63] M. Scholz, B. Faatz, S. Schreiber, and J. Zemella, "First Simultaneous Operation of Two Sase Beamlines in FLASH", in *Proceedings of FEL2015*, Daejeon, Korea, 2015, paper TUA04, pp. 297–300. DOI:10.18429/JACoW-FEL2015-TUA04

[64] J. Rönsch-Schulenburg *et al.*, "Experience with Multi-Beam and Multi-Beamline FEL-Operation", *Journal of Physics: Conference Series*, vol. 874, p. 012023, 2017. DOI:10.1088/1742-6596/874/1/012023

[65] A. Aschikhin *et al.*, "The FLASHForward facility at DESY", *Nuclear Instruments and Methods in Physics Research Section A: Accelerators, Spectrometers, Detectors and Associated Equipment*, vol. 806, pp. 175 – 183, 2016. DOI:10.1016/j.nima.2015.10.005

[66] S. Schreiber, S. Lederer, P. Michelato, L. Monaco, and D. Sertore, "Update on the Lifetime of Cs2Te Photocathodes Operated at FLASH", in *Proceedings of FEL2017*, Santa Fe, NM, USA, 2017, paper WEP003, pp. 415–418. DOI:10.18429/JACoW-FEL2017-WEP003

[67] S. Schreiber, J. Rönsch-Schulenburg, B. Steffen, C. Grün, and K. Klose, "Simultaneous Operation of Three Laser Systems at the FLASH Photoinjector", in *Proceedings of FEL2015*, Daejeon, Korea, 2015, paper TUP041, pp. 459–463. DOI:10.18429/JACoW-FEL2015-TUP041

[68] M. Vogt, K. Honkavaara, M. Kuhlmann, J. Rönsch-Schulenburg, S. Schreiber, and R. Treusch, "Status of the Superconducting Soft X-Ray Free-Electron Laser FLASH at DESY", in *Proceedings of IPAC2018*, Vancouver, BC, Canada, 2018, paper TUPMF090, pp. 1481–1484. DOI:doi:10.18429/JACoW-IPAC2018-TUPMF090

[69] J. Rönsch-Schulenburg *et al.*, "Short SASE-FEL Pulses at FLASH", in *Proceedings of FEL2013*, New York, NY, USA, 2013, paper TUPSO64, pp. 379–382.

[70] T. Plath, J. Rönsch-Schulenburg, J. Roßbach, H. Schlarb, S. Schreiber, and B. Steffen, "Commissioning and Diagnostics Development for the New Short-Pulse Injector Laser at FLASH", in *Proceedings of IBIC2013*, Oxford, UK, 2013, paper TUPC03, pp. 353–356.

[71] J. Rönsch-Schulenburg, private communication, 2019.

[72] S. Schreiber and B. Faatz, "The free-electron laser FLASH", *High Power Laser Science and Engineering*, vol. 3, p. e20, 2015. DOI:10.1017/hpl.2015.16

[73] F. Stulle, “A Bunch Compressor for small Emittances and high Peak Currents at the VUV Free-Electron Laser”, Ph.D. dissertation, Universität Hamburg, 2004.

[74] J. Zemella and M. Vogt, “Optics & Compression Schemes for a Possible FLASH Upgrade”, in *Proceedings of IPAC2019*, Melbourne, Australia, 2019, paper TUPRB026, pp. 1744–1747. DOI:10.18429/JACoW-IPAC2019-TUPRB026

[75] B. Faatz *et al.*, “Flash II: Perspectives and challenges”, *Nuclear Instruments and Methods in Physics Research Section A: Accelerators, Spectrometers, Detectors and Associated Equipment*, vol. 635, no. 1, Supplement, pp. S2 – S5, 2011. DOI:10.1016/j.nima.2010.10.065

[76] M. Vogt, B. Faatz, J. Feldhaus, K. Honkavaara, S. Schreiber, and R. Treusch, “Status of the Free Electron Laser User Facility FLASH”, in *Proceedings of IPAC2014*, Dresden, Germany, 2014, paper TUOCA02, pp. 938–940. DOI:10.18429/JACoW-IPAC2014-TUOCA02

[77] K. Honkavaara, B. Faatz, J. Feldhaus, S. Schreiber, R. Treusch, and M. Vogt, “FLASH: First Soft X-ray FEL Operating Two Undulator Beamlines Simultaneously”, in *Proceedings of FEL2014*, Basel, Switzerland, 2014, paper WEB05, pp. 635–639.

[78] M. Vogt, J. Feldhaus, K. Honkavaara, J. Rönsch-Schulenburg, S. Schreiber, and R. Treusch, “The Superconducting Soft X-ray Free-Electron Laser User Facility FLASH”, in *Proceedings of IPAC2016*, Busan, Korea, 2016, paper MOPOW010, pp. 729–731. DOI:10.18429/JACoW-IPAC2016-MOPOW010

[79] T. Maltezopoulos *et al.*, “A high-harmonic generation source for seeding a free-electron laser at 38 nm”, *Applied Physics B*, vol. 115, no. 1, pp. 45–54, 2014. DOI:10.1007/s00340-013-5571-6

[80] T. Plath *et al.*, “Free-electron laser multiplex driven by a superconducting linear accelerator”, *Journal of Synchrotron Radiation*, vol. 23, no. 5, pp. 1070–1075, 2016. DOI:10.1107/S1600577516009620

[81] S. Düsterer *et al.*, “Development of experimental techniques for the characterization of ultrashort photon pulses of extreme ultraviolet free-electron lasers”, *Phys. Rev. ST Accel. Beams*, vol. 17, p. 120702, 2014. DOI:10.1103/PhysRevSTAB.17.120702

[82] P. Emma *et al.*, “First lasing and operation of an ångstrom-wavelength free-electron laser”, *Nature Photonics*, vol. 4, pp. 641–647, 2010. DOI:10.1038/nphoton.2010.176

[83] R. B. Neal, Ed., *The Stanford Two-Mile Accelerator*. New York, NY, USA: W.A. Benjamin, Inc., 1968.

[84] R. Akre *et al.*, "Commissioning the Linac Coherent Light Source injector", *Phys. Rev. ST Accel. Beams*, vol. 11, p. 030703, 2008. DOI:10.1103/PhysRevSTAB.11.030703

[85] D. H. Dowell *et al.*, "The LCLS Injector Drive Laser", in *Proceedings of PAC2007*, Albuquerque, New Mexico, USA, 2007, paper TUPMS058, pp. 1317–1319. DOI:10.1109/PAC.2007.4441068

[86] D. H. Dowell *et al.*, "Results of the SLAC LCLS Gun High-Power RF Tests", in *Proceedings of PAC2007*, Albuquerque, New Mexico, USA, 2007, paper TUPMS058, pp. 1296–1298. DOI:10.1109/PAC.2007.4441061

[87] E. Saldin, E. Schneidmiller, and M. Yurkov, "Longitudinal space charge-driven microbunching instability in the TESLA Test Facility linac", *Nuclear Instruments and Methods in Physics Research Section A: Accelerators, Spectrometers, Detectors and Associated Equipment*, vol. 528, no. 1, pp. 355 – 359, 2004. DOI:10.1016/j.nima.2004.04.067

[88] Z. Huang *et al.*, "Suppression of microbunching instability in the linac coherent light source", *Phys. Rev. ST Accel. Beams*, vol. 7, p. 074401, 2004. DOI:10.1103/PhysRevSTAB.7.074401

[89] Z. Huang *et al.*, "Measurements of the linac coherent light source laser heater and its impact on the x-ray free-electron laser performance", *Phys. Rev. ST Accel. Beams*, vol. 13, p. 020703, 2010. DOI:10.1103/PhysRevSTAB.13.020703

[90] P. Emma *et al.*, "Measurements of Compression and Emittance Growth after the First LCLS Bunch Compressor Chicane", in *Proceedings of PAC2007*, Albuquerque, NM, USA, 2007, paper TUOCAB02. DOI:10.1109/PAC.2007.4440746

[91] P. Emma *et al.*, "Commissioning of the LCLS Linac and Bunch Compressors", in *Proceedings of FEL2008*, Gyeongju, Korea, 2008, paper FRAAU04, pp. 548–551.

[92] K. L. F. Bane *et al.*, "Measurements and modeling of coherent synchrotron radiation and its impact on the Linac Coherent Light Source electron beam", *Phys. Rev. ST Accel. Beams*, vol. 12, p. 030704, 2009. DOI:10.1103/PhysRevSTAB.12.030704

[93] H.-D. Nuhn, "LCLS undulator commissioning, alignment, and performance", in *Proceedings of FEL2009*, Liverpool, UK, 2009, paper THOA02, pp. 714–721.

[94] I. Vasserman *et al.*, "LCLS Undulator Design Development ", in *Proceedings of FEL2004*, Trieste, Italy, 2004, paper TUBOS04, pp. 367–370.

[95] Z. Wolf, V. Kaplounenko, Y. Levashov, and A. Weidemann, "LCLS undulator tuning and fiducialization", in *Proceedings of PAC2007*, Albuquerque, New Mexico, USA, 2007, paper TUPMS059, pp. 1320–1322. DOI:10.1109/PAC.2007.4441069

[96] Y. Ding *et al.*, "Femtosecond x-ray pulse temporal characterization in free-electron lasers using a transverse deflector", *Phys. Rev. ST Accel. Beams*, vol. 14, p. 120701, 2011. DOI:10.1103/PhysRevSTAB.14.120701

[97] W. K. H. Panofsky and W. A. Wenzel, "Some Considerations Concerning the Transverse Deflection of Charged Particles in Radio-Frequency Fields", *Review of Scientific Instruments*, vol. 27, no. 11, pp. 967–967, 1956. DOI:10.1063/1.1715427

[98] P. R. Phillips, "Microwave Separator for High Energy Particle Beams", *Review of Scientific Instruments*, vol. 32, no. 1, pp. 13–16, 1961. DOI:10.1063/1.1717133

[99] O. H. Altenmueller, R. R. Larsen, and G. A. Loew, "Investigations of Traveling-Wave Separators for the Stanford Two-Mile Linear Accelerator", *Review of Scientific Instruments*, vol. 35, no. 4, pp. 438–442, 1964. DOI:10.1063/1.1718840

[100] M. Röhrs, "Investigation of the Phase Space Distribution of Electron Bunches at the FLASH-Linac Using a Transverse Deflecting Structure", Ph.D. dissertation, Universität Hamburg, 2008.

[101] P. Craievich *et al.*, "Fermi Low-energy Transverse RF Deflector Cavity", in *Proceedings of EPAC2008*, Genoa, Italy, 2008, paper TUPC080, pp. 1239–1241.

[102] M. Yan, "Online diagnostics of time-resolved electron beam properties with femtosecond resolution for X-ray FELs", Ph.D. dissertation, Universität Hamburg, 2015.

[103] P. Craievich, R. Ischebeck, F. Löhl, G. Orlandi, and E. Prat, "Transverse Deflecting Structures for Bunch Length and Slice Emittance Measurements on SwissFEL", in *Proceedings of FEL2013*, New York, NY, USA, 2013, paper TUPSO14, pp. 236–241.

[104] C. Behrens and C. Gerth, "On the Limitations of Longitudinal Phase Space Measurements using a Transverse Deflecting Structure", in *Proceedings of DIPAC2009*, Basel, Switzerland, 2009, paper TUPB44, pp. 269–271.

[105] C. Behrens and C. Gerth, "Measurement of the Slice Energy Spread Induced by a Transverse Deflecting RF Structure at FLASH", in *Proceedings of DIPAC2011*, Hamburg, Germany, 2011, paper TUPD31, pp. 371–373.

[106] M. Cornacchia and P. Emma, "Transverse to longitudinal emittance exchange", *Phys. Rev. ST Accel. Beams*, vol. 5, p. 084001, 2002. DOI:10.1103/PhysRevSTAB.5.084001

[107] G. Kube, C. Behrens, and W. Lauth, "Resolution Studies of Inorganic Scintillation Screens for High Energy and High Brilliance Electron Beams", in *Proceedings of IPAC2010*, Kyoto, Japan, 2010, paper MOPD088, pp. 906–908.

[108] K. Honkavaara *et al.*, "Design of OTR beam profile monitors for the TESLA Test Facility, Phase 2 (TTF2)", in *Proceedings of PAC2003*, Portland, OR, USA, 2003, pp. 2476–2478. DOI:10.1109/PAC.2003.1289159

[109] B. Steffen, "Electro-Optic Methods for Longitudinal Bunch Diagnostics at FLASH", Ph.D. dissertation, Universität Hamburg, 2007.

[110] X. Yan *et al.*, "Subpicosecond Electro-optic Measurement of Relativistic Electron Pulses", *Phys. Rev. Lett.*, vol. 85, pp. 3404–3407, 2000. DOI:10.1103/PhysRevLett.85.3404

[111] S. Wesch, "Echtzeitbestimmung longitudinaler Elektronenstrahlparameter mittels absoluter Intensitäts- und Spektralmessung einzelner kohärenter THz Strahlungspulse", Ph.D. dissertation, Universität Hamburg, 2012.

[112] T. J. Maxwell *et al.*, "Coherent-Radiation Spectroscopy of Few-Femtosecond Electron Bunches Using a Middle-Infrared Prism Spectrometer", *Phys. Rev. Lett.*, vol. 111, p. 184801, 2013. DOI:10.1103/PhysRevLett.111.184801

[113] C. Behrens *et al.*, "Constraints on photon pulse duration from longitudinal electron beam diagnostics at a soft x-ray free-electron laser", *Phys. Rev. ST Accel. Beams*, vol. 15, p. 030707, 2012. DOI:10.1103/PhysRevSTAB.15.030707

[114] H. Loos *et al.*, "Experimental Studies of Temporal Electron Beam Shaping at the DUV-FEL Accelerator", in *Proceedings of FEL2005*, Stanford, CA, USA, 2005, paper THPP066, pp. 632–635.

[115] D. Marx, R. Assmann, P. Craievich, U. Dorda, A. Grudiev, and B. Marchetti, "Longitudinal phase space reconstruction simulation studies using a novel X-band transverse deflecting structure at the SINBAD facility at DESY", *Nuclear Instruments and Methods in Physics Research Section A: Accelerators, Spectrometers, Detectors and Associated Equipment*, vol. 909, pp. 374 – 378, 2018. DOI:10.1016/j.nima.2018.02.037

[116] M. Röhrs, C. Gerth, H. Schlarb, B. Schmidt, and P. Schmüser, "Time-resolved electron beam phase space tomography at a soft x-ray free-electron laser", *Phys. Rev. ST Accel. Beams*, vol. 12, p. 050704, 2009. DOI:10.1103/PhysRevSTAB.12.050704

[117] T. J. Maxwell *et al.*, "Femtosecond-scale X-ray FEL diagnostics with the LCLS X-band transverse deflector", in *Proc.SPIE*, vol. 9210, 2014. DOI:10.1117/12.2065252

[118] T. Plath *et al.*, "Mapping few-femtosecond slices of ultra-relativistic electron bunches", *Scientific Reports*, vol. 7, no. 1, p. 2431, 2017. DOI:10.1038/s41598-017-02184-3

[119] Z. Huang, K. Bane, Y. Cai, A. Chao, R. Hettel, and C. Pellegrini, "Steady-state analysis of short-wavelength, high-gain FELs in a large storage ring", *Nuclear Instruments and Methods in Physics Research Section A: Accelerators, Spectrometers, Detectors and Associated Equipment*, vol. 593, no. 1, pp. 120 – 124, 2008. DOI:10.1016/j.nima.2008.04.070

[120] K. Tiedtke *et al.*, "The soft x-ray free-electron laser FLASH at DESY: beamlines, diagnostics and end-stations", *New Journal of Physics*, vol. 11, no. 2, p. 023029, 2009. DOI:10.1088/1367-2630/11/2/023029

[121] K. Tiedtke *et al.*, "Gas detectors for X-ray lasers", *Journal of Applied Physics*, vol. 103, no. 9, p. 094511, 2008. DOI:10.1063/1.2913328

[122] S. Moeller *et al.*, "Photon beamlines and diagnostics at LCLS", *Nuclear Instruments and Methods in Physics Research Section A: Accelerators, Spectrometers, Detectors and Associated Equipment*, vol. 635, no. 1, Supplement, pp. S6 – S11, 2011. DOI:10.1016/j.nima.2010.10.125

[123] F. Löhl, "Measurements of the Transverse Emittance at the VUV-FEL", Diploma thesis, Universität Hamburg, 2005.

[124] C. Behrens, C. Gerth, G. Kube, B. Schmidt, S. Wesch, and M. Yan, "Electron beam profile imaging in the presence of coherent optical radiation effects", *Phys. Rev. ST Accel. Beams*, vol. 15, p. 062801, 2012. DOI:10.1103/PhysRevSTAB.15.062801

[125] U. Hahn *et al.*, "Wire scanner system for FLASH at DESY", *Nuclear Instruments and Methods in Physics Research Section A: Accelerators, Spectrometers, Detectors and Associated Equipment*, vol. 592, no. 3, pp. 189 – 196, 2008. DOI:10.1016/j.nima.2008.04.018

[126] J. Zemella, T. Hellert, M. Scholz, and M. Vogt, "Measurements of the Optical Functions at FLASH", in *Proceedings of IPAC2014*, Dresden, Germany, 2014, paper TUPRO050, pp. 1141–1143. DOI:10.18429/JACoW-IPAC2014-TUPRO050

[127] J. Zemella and M. Vogt, "Progress in FLASH Optics Consolidation", in *Proceedings of IPAC2017*, Copenhagen, Denmark, 2017, paper MOPAB051, pp. 211–214. DOI:10.18429/JACoW-IPAC2017-MOPAB051

[128] M. G. Minty and F. Zimmermann, *Measurement and control of charged particle beams*. Springer: Berlin, 2003. DOI:10.1007/978-3-662-08581-3

[129] E. Prat *et al.*, "Slice Emittance Optimization at the SwissFEL Injector Test Facility", in *Proceedings of FEL2013*, New York, NY, USA, 2013, paper TUOCNO06, pp. 200–204.

[130] K. Flöttmann, “ASTRA - A Space Charge Tracking Algorithm”, www.desy.de/~mpyflo/, 1997.

[131] M. Dohlus and T. Limberg, “CSRtrack”, http://www.desy.de/fel-beam/csrtrack/, 2012.

[132] S. Reiche, “Numerical Studies for a Single Pass High Gain Free-Electron Laser”, Ph.D. dissertation, Universität Hamburg, Hamburg, Germany, 1999.

[133] F. Christie, J. Rönsch-Schulenburg, S. Schreiber, and M. Vogt, “Generation of Ultra-Short Electron Bunches and FEL Pulses and Characterization of Their Longitudinal Properties at FLASH2”, in *Proceedings of IPAC2017*, Copenhagen, Denmark, 2017, paper WEPAB17, pp. 2600–2603. DOI:10.18429/JACoW-IPAC2017-WEPAB017

[134] L. Bittner *et al.*, “MCP-Based Photon Detector with Extended Wavelength Range for FLASH”, in *Proceedings of FEL2007*, Novosibirsk, Russia, 2007, pp. 334–337.

[135] B. Beutner, M. Dohlus, and H. Dinter, “RFTweak 5 - An Efficient Longitudinal Beam Dynamics Code”, in *Proceedings of FEL2015*, Daejeon, Korea, 2015, paper MOP060, pp. 176–180. DOI:10.18429/JACoW-FEL2015-MOP060

[136] V. Wacker, “Sub-Femtosecond Single-Spike X-Ray Pulse from Electron Bunches with Very Low Charge at LCLS”, Master’s thesis, Universität Hamburg, 2014.

[137] B. Schmidt *et al.*, “Longitudinal Bunch Diagnostics using Coherent Transition Radiation Spectroscopy”, Deutsches Elektronen-Synchrotron, Hamburg, Germany, DESY reports 027, 2018. DOI:10.3204/PUBDB-2018-01372

[138] M. Vogt, “FLASH Status”, in *DESY Beschleuniger-Betriebsseminar*, Travemünde, Germany, 2019.

[139] N. Catalán Lasheras *et al.*, “Commissioning of XBox-3: A very high capacity X-band test stand”, in *Proceedings of LINAC2016*, East Lansing, MI, USA, 2016, paper TUPLR047, pp. 568–571. DOI:10.18429/JACoW-LINAC2016-TUPLR047

[140] I. Syratchev, “Status of high-power X-band RF systems development at CERN”, in *LCWS14*, Belgrade, Serbia, 2014.

[141] P. Wang, H. Chen, J. Shi, I. Syratchev, W. Wuensch, and H. Zha, “The RF Design of a Compact, High Power Pulse Compressor with a Flat Output Pulse”, in *Proceedings of IPAC2016*, Busan, Korea, 2016, paper THPMW022, pp. 3591–3593. DOI:10.18429/JACoW-IPAC2016-THPMW022

[142] R. Zennaro, M. Bopp, A. Citterio, R. Reiser, and T. Stapf, “C-band RF Pulse Compressor for SwissFEL”, in *Proceedings of IPAC2013*, Shanghai, China, 2013, paper WEPFI059, pp. 2827–2829.

[143] R. D'Arcy, A. Aschikhin, P. González Caminal, V. Libov, and J. Osterhoff, "Longitudinal Phase Space Reconstruction at FLASHForward Using a Novel Transverse Deflection Cavity, PolariX-TDS", in *Proceedings of IPAC2018*, Vancouver, BC, Canada, 2018, paper TUPML017, pp. 1567–1570. DOI:10.18429/JACoW-IPAC2018-TUPML017

[144] D. Marx, R. Assmann, U. Dorda, B. Marchetti, and F. Mayet, "Lattice considerations for the use of an X-band transverse deflecting structure (TDS) at SINBAD, DESY", *Journal of Physics: Conference Series*, vol. 874, p. 012078, 2017. DOI:10.1088/1742-6596/874/1/012078

[145] P. Craievich *et al.*, "Sub-Femtosecond Time-Resolved Measurements Based on a Variable Polarization X-Band Transverse Deflecting Structures for SwissFEL", in *Proceedings of FEL2017*, Santa Fe, NM, USA, 2017, paper WEP040, pp. 499–502. DOI:10.18429/JACoW-FEL2017-WEP040

[146] D. Marx, R. Assmann, P. Craievich, U. Dorda, A. Grudiev, and B. Marchetti, "Reconstruction of the 3D charge distribution of an electron bunch using a novel variable-polarization transverse deflecting structure (TDS)", *Journal of Physics: Conference Series*, vol. 874, p. 012077, 2017. DOI:10.1088/1742-6596/874/1/012077

[147] D. Marx, R. Assmann, R. D'Arcy, and B. Marchetti, "Simulations of 3D charge density measurements for commissioning of the PolariX-TDS", *Journal of Physics: Conference Series*, vol. 1067, p. 072012, 2018. DOI:10.1088/1742-6596/1067/7/072012

[148] U. Ellenberger *et al.*, "Status of the Manufacturing Process for the SwissFEL C-Band Accelerating Structures", in *Proceedings of FEL2013*, New York, NY, USA, 2013, paper TUPSO17, pp. 245–249.

[149] C. Wiebers, M. Holz, G. Kube, D. Nölle, G. Priebe, and H.-C. Schröder, "Scintillating Screen Monitors for Transverse Electron Beam Profile Diagnostics at the European XFEL", in *Proceedings of IBIC2013*, Oxford, UK, 2013, paper WEPF03, pp. 807–810.

[150] G. Kube, S. Liu, A. Novokshonov, and M. Scholz, "A Simple Model to Describe Smoke Ring Shaped Beam Profile Measurements With Scintillating Screens at the European XFEL", in *Proceedings of IBIC2018*, Shanghai, China, 2018, paper WEOC03, pp. 366–370. DOI:10.18429/JACoW-IBIC2018-WEOC03

[151] T. Scheimpflug, "Method of Distorting Plane Images by means of Lenses or Mirrors", U.S. Patent 751 347, 1904.

[152] H. Grote and F. C. Iselin, "The MAD Program - User's Reference Manual", CERN, Geneva, Switzerland, Tech. Rep. CERN/SL/90-13 (AP) (Rev. 5), 1996.

[153] H. Grote, E. Keil, T. O. Raubenheimer, and M. Woodley, “Extension of MAD Version 8 to include Beam Acceleration”, in *Proceedings of EPAC2000*, Vienna, Austria, 2000, paper TUP3A02, pp. 1390–1392.

[154] M. Borland, “elegant: A Flexible SDDS-Compliant Code for Accelerator Simulation”, *Advanced Photon Source LS-287*, 2000.

[155] I. Zagorodnov, “FLASH Beam Daynamics Simulations”, www.desy.de/fel-beam/s2e/flash.html, 2013.

[156] D. Zhu *et al.*, “A single-shot transmissive spectrometer for hard x-ray free electron lasers”, *Applied Physics Letters*, vol. 101, no. 3, p. 034103, 2012. DOI:10.1063/1.4736725

[157] F. Christie *et al.*, “Temporal X-ray Reconstruction Using Temporal and Spectral Measurements”, in *Proceedings of IPAC2018*, Vancouver, BC, Canada, 2018, paper TUPMF076, pp. 1440–1443. DOI:10.18429/JACoW-IPAC2018-TUPMF076

[158] F. Christie *et al.*, “Temporal X-ray reconstruction using temporal and spectral measurements”, *Journal of Physics: Conference Series*, vol. 1067, no. 3, p. 032011, 2018. DOI:10.1088/1742-6596/1067/3/032011

[159] S. Krinsky and Z. Huang, “Frequency chirped self-amplified spontaneous-emission free-electron lasers”, *Phys. Rev. ST Accel. Beams*, vol. 6, p. 050702, 2003. DOI:10.1103/PhysRevSTAB.6.050702

[160] L. Gubin, B. Polyak, and E. Raik, “The method of projections for finding the common point of convex sets”, *USSR Computational Mathematics and Mathematical Physics*, vol. 7, no. 6, pp. 1 – 24, 1967. DOI:10.1016/0041-5553(67)90113-9

[161] O. Forster, *Analysis 3*. Wiesbaden, Germany: Springer Spektrum, 2017. DOI:10.1007/978-3-8348-2374-8

[162] H.-J. Mittag, *Statistik: eine Einführung mit interaktiven Elementen*. Berlin, Germany: Springer Spektrum, 2017. DOI:10.1007/978-3-642-54387-6

[163] D. Gujarati, *Basic Econometrics*. Boston, MA, United States: McGraw Hill, 2003.

[164] D. Ratner *et al.*, “FEL Gain length and Taper Measurements at LCLS”, in *Proceedings of FEL2009*, Liverpool, UK, 2009, paper TUOA03, pp. 221–224.

[165] H. Grote and F. C. Iselin, “The MAD Program (Methodical Accelerator Design) Version 8.13 Physical Methods Manual”, CERN, Geneva, Switzerland, Tech. Rep. CERN/SL/92-?? (AP), 1996.

Acknowledgments

This thesis is dedicated to Prof. Dr. Wilfried Wurth who sadly passed away before the final version was completed. You will be deeply missed.

I would like to thank my two super supervisors Dr. Mathias Vogt and Dr. Juliane Rönsch-Schulenburg for their support, advice, and effort during my work on this thesis. Without their knowledge and guidance, this thesis would not have been possible. Thank you for always helping me out!

Many thanks are due to Prof. Dr. Wolfgang Hillert who accepted to act as a referee for my thesis on very short notice.

A big thank you to Dr. Bolko Beutner, Dr. Marie Rehders, Dr. Matthias Scholz, and Dr. Johann Zemella for introducing me to the complicated world of numerical accelerator physics studies and guiding me through all of the simulation programs.

Special thanks are due to the DESY accelerator division, namely Dr. Klaus Balewski, Dr. Reinhard Brinkmann, and Dr. Wim Leemans for offering me the possibility to work on this subject, supporting my travels to various conferences, SLAC, and other business trips. Swantje Mette and Christel Övermann always helped me with a smile while guiding me through the bureaucratic procedures, for which I am very grateful.

Many thanks to the whole FLASH team and especially to Dr. Siggi Schreiber, Dr. Katja Honkavaara, and Dr. Bart Faatz for making measurement shifts possible and trusting me not to screw up "their" machine.

For many hours of useful discussions, joint work, and constant exchange of ideas I am much obliged to my "evil antagonists" at FLASHForward and SINBAD, Dr. Richard D'Arcy, Pau González Caminal, and Daniel Marx.

I really appreciated the work in the PolariX TDS collaboration including but not limited to Dr. Barbara Marchetti, Dr. Paolo Craievich, Dr. Alexej Grudiev, and Dr. Nuria Catalan Lasheras.

I very much enjoyed my stay at SLAC during which I really enjoyed working with Dr. Yuantao Ding, Dr. Jacek Krzywinski, Dr. Marc Guetg, Dr. Alberto Lutman, Dr. Timothy Maxwell, Dr. Daniel Ratner, and Prof. Dr. Zhirong Huang.

Without the technical staff DESY would probably be a lot darker. Thank you, for providing so much knowledge, Manon Föse, Jan Kuhlmann, Rolf Jonas, Daniel Meißner, Frauke Poblotzki, and Dr. Markus Hüning (and many more!).

During three years of academic writing, Louise Kennedy and the rest of the course never struggled to put on their editor's cap and nitpicked every tiniest sentence I ever wrote. I really enjoyed our sessions!

A big thank you to the whole PR department and especially Antje Brandes and Dr. Thomas Zoufal for making DESY appreciated by the public.

For always making DESY a better place to work for PhD students I would like to thank DOIT and especially Nicole Stefanov and Ulrich Einhaus. The same goes for the PIER Helmholtz Graduate School and especially their coordinators Mirko Siemssen, Stefanie Tepaß, and

Jennifer Vix.

I really enjoyed the time in the best office on campus and during the best lunch and coffee (and other ...) sessions due to Philipp Amstutz, Immo Bahns, Dr. Thorsten Hellert, Christian Henkel, Max Kellermeier, Willi Kuropka, Jan Oliver Rieger, and Patrick Rauer.

Last but not least, I would like to thank my friends and family and my wife Kim Christie for their support and understanding during this very busy time.

Eidesstattliche Versicherung

Hiermit versichere ich an Eides statt, die vorliegende Dissertationsschrift selbst verfasst und keine anderen als die angegebenen Hilfsmittel und Quellen benutzt zu haben.

Die eingereichte schriftliche Fassung entspricht der auf dem elektronischen Speichermedium.

Die Dissertation wurde in der vorgelegten oder einer ähnlichen Form nicht schon einmal in einem früheren Promotionsverfahren angenommen oder als ungenügend beurteilt.

Hamburg, den 1.7.2019

_____

Florian Christie